Development and Experimental Validation of a New Control Strategy Considering Device Dynamics for Large-Scale MR Dampers using Real-Time Hybrid Simulation

Anthony J. Friedman and Shirley J. Dyke

{afriedman, sdyke} @ purdue.edu

Report IISL – 003, May 2013

Abstract

As MR control devices increase in scale for use in real-world civil engineering applications, their dynamics become increasingly complicated. Control designs that are able to take these characteristics into account will be more effective in achieving good performance. A new control algorithm, ODCOC, which utilizes over- and back-driving current control to increase the efficacy of the control device, is proposed. To validate the performance of the new controller under general earthquake excitation and uncertain conditions, a series of three large-scale validation experiments (using large-scale 200kN MR Dampers and steel frames) are performed, including: (1) a three-story linear structure real-time hybrid simulation (RTHS), with a large-scale steel frame and MR damper as tbe physical substructure; (2) a nine-story linear structure real-time hybrid simulation, with a large-scale steel frame and MR damper(s) as the physical substructure; and (3) a non-linear nine-story structure numerical simulation analysis. The performance of the proposed controller is compared to several establish MR damper control methods in each experiment. Through these studies, RTHS is verified as a viable testing technique for large-scale applications, as comparisons to numerical simulations and repeatability testing demonstrate the reliability of this method, and the controller experiments demonstrate the improved structural performance that results when using the ODCOC algorithm compared to other established methods. Any projects, including both academic and professional engineering applications, that utilize devices at these scales will benefit from employing this control method.

Acknowledgement: Financial support for this research was provided from several sources, including the Graduate Assistance in Areas of National Need (GAANN) Fellowship (CFDA Grant No. 84.200) and the Graduate STEM Fellows in K-12 Education (GK12) Program (DGE Grant No. 1007911). This research is also funded by National Science Foundation's Division of Civil, Mechanical and Manufacturing Innovation (CMMI) Grant No. 1011534

Data presented herein will be available for download in the NEEShub(nees.org).

TABLE OF CONTENTS

CHAPTER 1: INTRODUCTION

In recent years, the expectations of civil engineering as a discipline have begun to change. Civil infrastructure has always played a key role in the ability of any society to function efficiently. Buildings, bridges, roads and other edifices are all necessities for the general public at large. The loss of any key structure in the network can have severe consequences on the regional and national economies, in terms of recovery and business costs, social and cultural impacts, and time and life losses.

As such, safeguards for these structures are paramount to reduce the overall burden imposed by natural hazards and extreme loading. Earthquakes, in particular, are of major concern to structural engineering. Protection is becoming more of a concern to communities around the globe, given the recent devastation that occurred as a result of earthquakes in Haiti (Jibson et al., 2011), Chile (ARC, 2011), Japan, Turkey (Erguven et al., 2011), and China (Klinger et al., 2010), and earthquake awareness is rising. More importance is being placed on sophisticated design, with an emphasis on sustainability and resiliency. To put it simply, society is demanding more of its structures.

To accommodate these demands, new approaches to design that incorporate advanced technologies must be sought and developed. National guidelines (FEMA P695) have been implemented that identify design criteria to achieve varying levels of structural performance in the wake of a seismic event. Specifically, new design methodologies incorporating the capabilities of controllable devices must consider (1) the definition and quantification of the performance for a building and (2) how the device will be controlled to bring the performance of the structure within the specified range. In the first category, for many applications, performance objectives are typically specified by acceptable damage levels, which are categorized with terms like "Immediate Occupancy", "Life Safety", and "Collapse Prevention". The expected severity of the seismic input, which must also be quantified for analysis, affects the damage tolerance associated with each of these levels. These tolerances may be expressed as allowable stress, inter-story displacement, or a myriad of other measurements. Concerning the second category, the key to realizing the performance goal of structures is the ability to modify the responses of the structure to increase effectiveness and function. Dissipative damping devices coupled with control strategies that optimize performance and efficiency are the key to influencing the behavior of the structure and decreasing damage that may result from the event in question.

Figure 1.1: Earthquake damage in (a) Sichuan Province, China and (b) Santiago, Chile

Seismic code requirements have changed over time, arising from events that exposed noted deficiencies in structures like adequate design for lateral strength and ductility. However, these requirements are still rooted in traditional design methodologies, which are based on a demand-to-capacity relationship with little regard for more demanding structural performance parameters. The structure is designed with the capability to withstand certain amounts of stress, deformation, etc., but will fail if that capacity is exceeded. Given the unpredictable and stochastic nature of an event like an earthquake, one can imagine that events may easily occur for which the design is insufficient. Earthquakes, such as the Northridge (1994) and Kobe (1995), taught designers that code-compliant structures can still suffer catastrophic damage and losses.

As civil engineering and design continue to evolve around the world, perspectives on the design and subsequent performance of a structure must also change. New edifices must be able to withstand natural hazards, ensure occupant safety, and remain operational after the event. Downtime, due to reconstruction or repair, as a result of a disaster can prove costly, in terms of recovery and time lost.

As such, innovative approaches to design and mitigation, which may cover multiple objectives, including owner-specified, economic or performance goals, must be sought and developed. One idea which is gaining traction in the engineering community is the concept of Performance-Based Design (PBD). Many engineers, in both academia and the professional community, have proposed PBD methodologies to improve resilience against seismic hazards [Bertero and Zagajeski (1979), Hatamoto et al (1990), Paulay and Priestley (1992), SEAOC (1999)]. Additionally, national guidelines [FEMA 349, SANZ 1994] have been implemented that identify design criteria to achieve varying levels of seismic performance. The primary objective of this approach is to establish a desired performance level for a structure, based on the probabilistic hazard levels that

exist for the region. The design for the structure is iterated until the performance objectives are met, using rigorous analysis methods.

Applications of advanced damping systems and proper control algorithms are expected to facilitate major advances in our ability to achieve performance-based design of structures. Steel structures, in particular, will be benefit from this technology due to their flexibility while stiffer structures, like reinforced concrete or masonry, may not see as much improvement in response reduction. In addition, smaller structures like residential or single-story commercial facilities may not require this technology as much as their taller or more massive counterparts. Currently, implementation of control systems in civil structures has been slow, due to acceptance from the professional engineering community regarding implementability, stability, reliability, cost, maintenance and operation, etc. By addressing these issues with the development of new devices and design strategies for combined structure-damping systems, the practicing engineering community can be convinced to utilize these devices in real-world projects (such as mid- to high-rise office/residential/manufacturing facilities or other tall flexible structures which would benefit from the addition of these devices) and structures will ultimately become safer for their occupants.

This report centers on the design of a new control strategy for use with large-scale magnetorheological damper(s), semi-active energy dissipation devices. The proposed control algorithm, which consists of an over-/back-driving clipped optimal controller, is demonstrated herein to improve structural performance under seismic loading and ultimately, lead to improved design methodologies which utilize these devices. A series of large-scale validation experiments using 200kN MR Dampers and a steel frame are performed for evaluating the performance of the proposed control algorithm. Using different evaluation techniques, including pure numerical simulation and real-time hybrid simulation (RTHS), which combines aspects of numerical simulation and physical testing in a single experiment, the proposed controller will be evaluated for a series of seismic ground motions and device configurations.

1.1 Literature Review

The effects of control on structures have been investigated by many researchers, using many different structures and devices. As stated before, structural control is typically divided up into four categories, based on the type of device being utilized: (1) passive, (2) active, (3) hybrid and (4) semi-active. For the remainder of this section, each of these control devices, with corresponding previous research efforts, will be discussed.

1.1.1 Passive Control Devices

The first, and perhaps most common energy dissipation device, is referred to as a *passive* device. These systems can include a range of materials and devices and, in general, augment the stiffness or damping of a structural system. Typically, passive systems

make use of concepts such as plastic deformation or yielding, friction, visco- elastic fluids and solids, etc. These devices are simple, inherently stable and dissipative, and they require no auxiliary power source. However, because the response of the device is limited to the motion of the system, they are unable to adapt to structural/loading changes or vary their usage patterns.

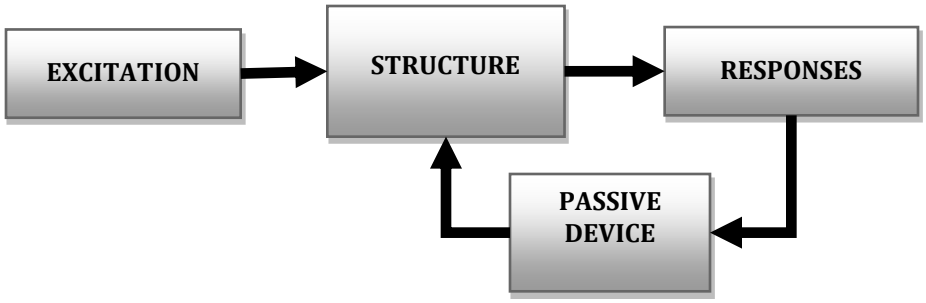

Figure 1.2: Passive Control Block Diagram

Passive control has been explored by many researchers over the years, and is well understood by the engineering community as a whole. Yield devices, also referred to as "additional damping and stiffness" (ADAS), have been explored by Fierro and Perry, (1993) and Tena-Colunga et al., (1997) for a seismic retrofit projects in San Francisco and Mexico City, respectively. In both cases, the addition of the ADAS devices to the structural system improved the performance. Another popular passive device is the base-isolator (Skinner et al, 1974). The concept behind this device is to decouple the structure from the ground such that in a seismic event, the ground will move under the structure without disturbing it.

Many researchers have studied base isoloation systems and design. Viscoelastic dampers, utilizing material with viscous and elastic properties and the ability to dissipate energy during deformation (Chang et al., 2004), have been employed in several different instances. Rao (2001) explored the use of VE for noise control in automobiles and airplanes and Lee et al., (2005) devised a simplified design procedure for designing frames equipped with VE dampers. Some alternative passive devices include the elastomeric damper (Kottapalli et al., 2010), which have been implemented in many engineering projects ranging in disciplines from civil to aerospace; tuned-mass dampers, which use a lighter mass component to mitigate the harsher vibrations to which a structure is subjected (Kaynia et al., 1981; Ural 1995); and tuned-liquid column dampers (TLCD) (Fediw et al., 1995), which uses liquid wave motion in a partially-filled tank to absorb energy through viscous action.

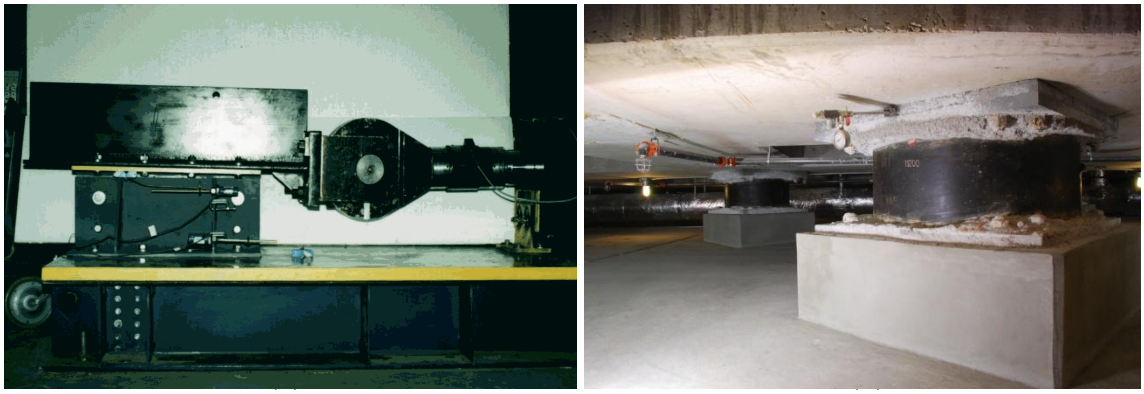

Figure 1.3: Examples of (a) visco-elastic dampers and (b) base isolators

There are several examples of passive control systems implemented in full-scale civil engineering applications. TMDs were applied to the Zhengzhou International Conference and Exhibition Center in China (Li and Huo 2010) and in the John Hancock Tower in Boston, MA (ENR 1977). Base isolation was used in the retrofit of the San Francisco City Hall building (SFCH), and the Higashi-Kobe cable-stayed bridge was outfitted with TLCDs to mitigate the effects of wind-induced vibration (Kareem et al 1999).

1.1.2 Active Control Devices

Active control systems (Abdel-Rohman and Leipholz, 1979), in contrast, can adapt to changing loading conditions and apply control measures in real-time. For an active system, there are three main components: (1) sensors, to measure the inputs and responses of the system; (2) a central processor station to determine an appropriate restoring force based on the measured responses; and (3) actuators, to impart the desired force to the structure.

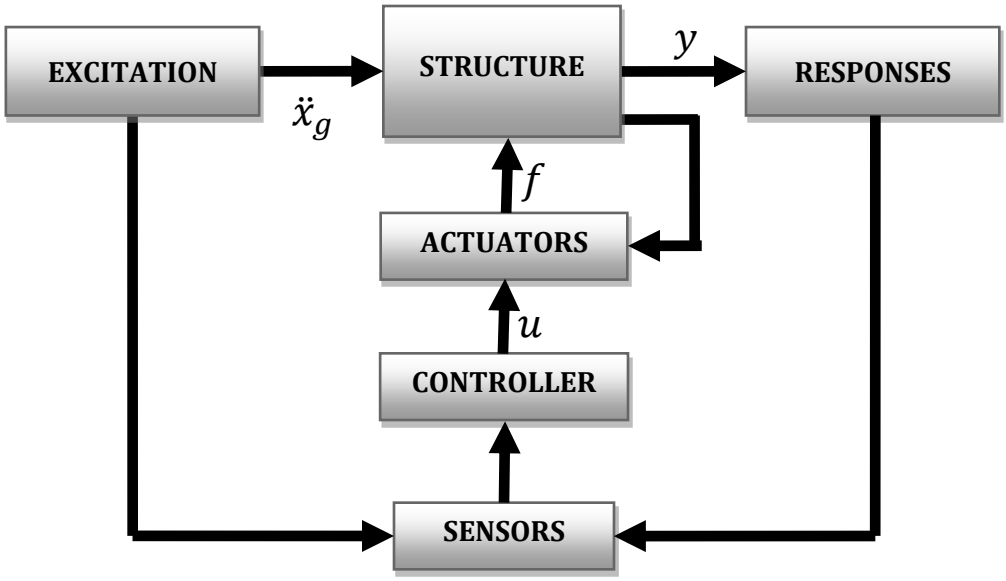

Figure 1.4: Active Control Block Diagram

Active control covers a wide variety of devices and control approaches. One of the first examples of active control is the active tendon system (ATS) uses pre-stressed tendons attached the structure to control responses. Actuators can vary the tension in the tendons depending on the measured behavior of the structure to decrease the overall response to the excitation (Warnitchai et al 1993). Another active control method is the active mass damper/driver (AMD). An AMD is an alternative take on the passive TMD, where, as before, a lighter mass element is specifically designed to mitigate the vibratory response of a structure at a certain frequency. However, for an AMD, the mass element is attached to actuators which directly control its motion to oppose the motion of the structure (Chang 1995).

Figure 1.5: TMD installed in Taipei 101 in Taiwan

There are many different control approaches for active systems. Linear methods, including output feedback control utilizing acceleration feedback (Dyke 1996) and stroke/force limitations (Asano and Nakagawa 1993) have been explored by many researchers. More recently, nonlinear methods have been considered, including neural methods (Ghaboussi and Joghataie 1995), fuzzy-logic based methods (Yoshimura et al, 1999), genetic algorithms (Jiang and Adeli, 2008) and adaptive methods (Suresh et al., 2012) and combinations thereof. Each method of control is designed to increase the efficacy of the overall control system.

There are many applications of active control in real world structures, though focused mainly in Asia. One of the more famous applications of an AMD control system is in Taipei 101 (Li et al., 2011), as shown in Figure 1.5. A 730-ton mass damper, with motion controlled by eight separate actuators, is installed in the top portion of the structure to help mitigate the damage due to typhoon winds and earthquakes that are common in that region. Implementation in the United States and elsewhere has been slow due to many reasons, including a lack of accepted design/analysis procedures in codes. As research and technology progresses, implementation on a national level should increase.

There are several advantages to active control. Because of the real-time nature of this control approach, these systems are quite versatile, with the ability to adapt to changing situations and alter loading patterns. With this adaptability, active control systems can often provide response reductions far superior to that of passive systems. Also, because the control system is flexible, multiple objectives for performance can be achieved. Emphasis can be placed on the inter-story drift response, if the primary focus of the owner is on the structure retaining usability after a seismic event. Conversely, if the structure is full of delicate equipment, reducing the acceleration response of the structure could be paramount. Each of these objectives is possible when using active control. However, there are also some limitations and drawbacks to this approach. Actuators require power to deliver the control forces, and as such, a large external power

source is necessary for operation. Natural hazards may disrupt that power source, and limit the effectiveness of the control system. Modeling errors, uncertainties in structural parameters, noise in sensors, etc. can lead to ineffective control or unstable control signals. Because of the ability to inject energy into the system, proper consideration is needed to ensure that instabilities do not occur. Furthermore, because of the need for controller hardware, sensors, power supply, and actuator size (in larger engineering applications), the cost of active systems are typically large compared to passive systems.

1.1.3 Hybrid Control Devices

An alternative to active control is hybrid control. Hybrid control systems utilize at least two different types of devices. By utilizing both types of devices, the drawbacks and limitations of each system operating independently are lessened. Because a part of the control force is supplied by the passive device, less force and power are required from the active devices. In addition, because less active control force is required, there is less chance of an instability occurring within the control system. By alleviating the shortcomings of both systems, high performance is usually achieved, though the system as a whole is more complex than either system by themselves.

Hybrid control systems typically use one of two types of devices: (1) hybrid mass dampers and (2) active base isolation systems. Hybrid mass dampers (HMD) combine a passive control tuned-mass damper and an active control actuator. The TMD is responsible for most of the control force, while the active actuator serves to increase the robustness of the total control system, allowing for better control along a higher range of frequencies of excitation (Nagashima et al., 2011). Active base isolation (ABI) combines a passive base isolation system with hydraulic actuators to mitigate the displacement of the base while simultaneously decreasing the acceleration. The addition of the actuator allows the normally passive system to adapt to changing loads without increasing cost significantly.

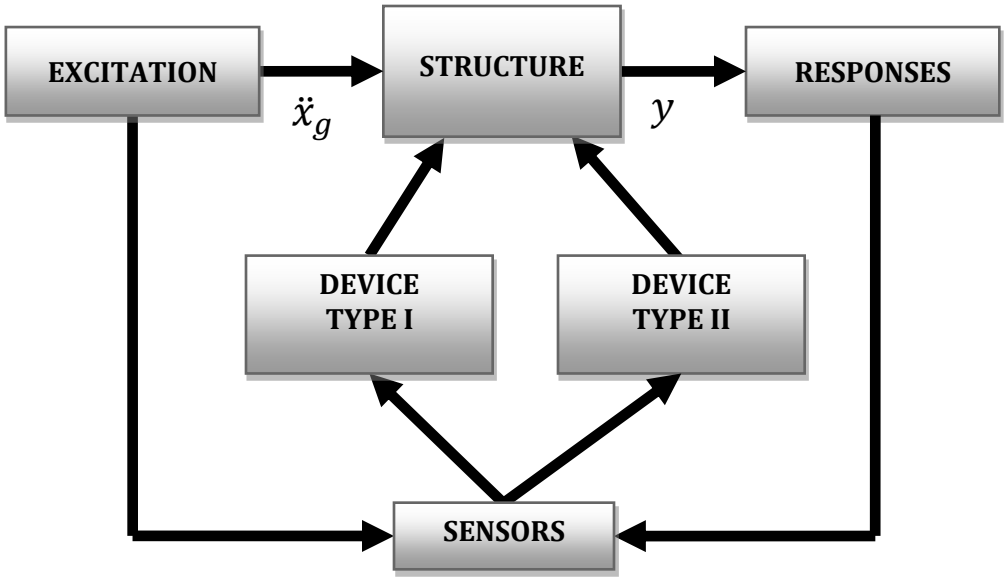

Figure 1.6: Hybrid Control Block Diagram

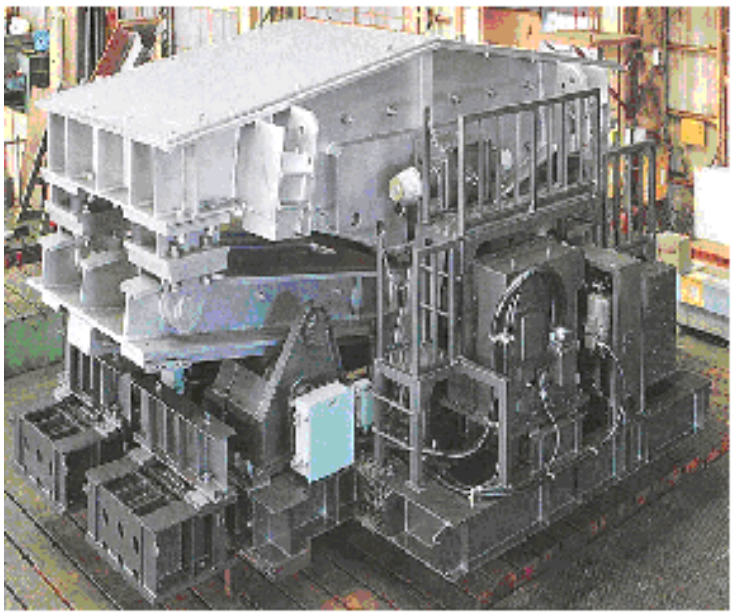

Figure 1.7: HMD in the Shinjuku Tower

In general, control approaches for both classes of hybrid devices include many of the same techniques as active control. Additionally, there are many applications of these hybrid control systems, including the V-shaped HMD (Figure 1.7) installed in the

Shinjuku Park Tower (Nishitani 2000) in Tokyo, the Sotetsu Takashimaya Kyoto Building (Soong and Spencer, 2002) in Yokohama, and the TC Tower Office Building (Spencer and Sain, 1997), in Kaosiung, Taiwan. The installation of control systems in each of these cases led to improved responses for the structure.

1.1.4 Semi-Active Control Devices

Semi-active control (Karnopp and Allen, 1975) combines aspects of both passive and active control, possessing large force capacity and adaptability without the need for large power sources (Symans and Constantinou 1996). Semi-active devices include variable friction/stiffness dampers, variable orifice dampers, controllable fluid dampers, etc. Specifically, two controllable-fluid devices which have recently seen a rising interest for control applications are electro-rheological (ER) and magneto-rheological (MR) dampers (Carlson 1995). These dampers can act as energy dissipation devices that are capable of changing their characteristics in a nearly instantaneous manner. They have large force capacities but require low power levels to achieve them and they possess a large dynamic range, making them very reliable. Their adaptability and controllability stemming from the variable-yield stress of the fluid makes them uniquely suited for many possible control-based strategies dealing with events of a stochastic nature, such as earthquakes.

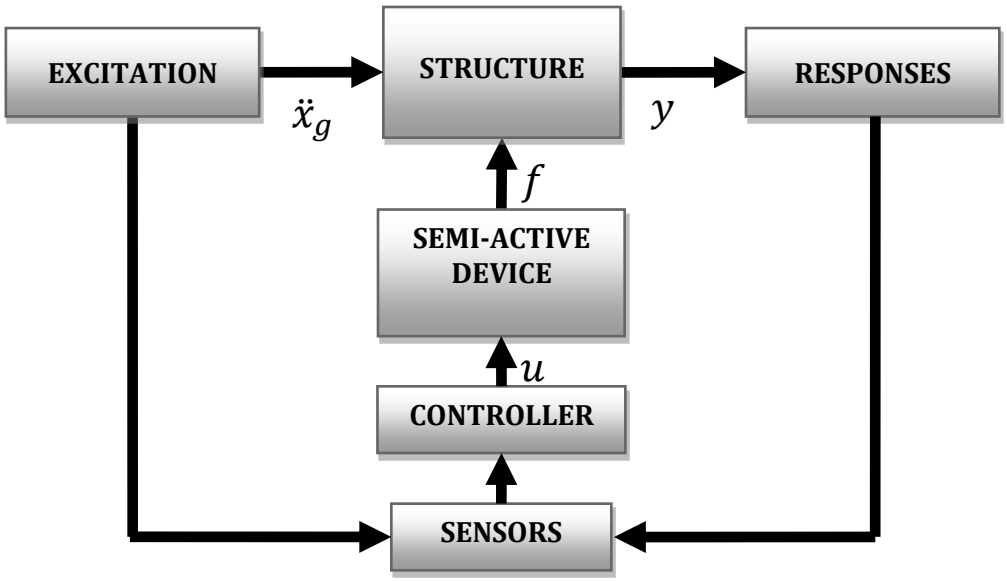

Figure 1.8: Semi-active Control Block Diagram

Several effective semi-active control methods have been developed during recent decades, and typically fall into two categories: (1) model-based control and (2) soft computing-based control. Categories of model-based control include bang-bang control,

backstepping control, sliding mode control, H_2 and $H\infty$ control, adaptive/non-linear control and bilinear control. Categories of soft computing-based control include neural network-based control, fuzzy logic control, and genetic algorithm-based control. McClamroch and Gavin (1995) proposed a decentralized bang-bang controller for ER dampers, where the current commanded to the damper is switched on and off depending upon state feedback from the structure. Dyke (1995) proposed the clipped optimal controller, a variation of bang-bang control, for use with MR dampers. Yoshida (2004) proposed a modified version of the clipped optimal control, to avoid the high accelerations generated by rapidly switching the voltage on and off. More recently, research has focused on methods such as backstepping control (Zapatiero 2009), where recursive methods are used to gain stability in the system under investigation. Sliding mode control (Chae et al 2010, TY Lee et al 2011) has also gained some traction within the research community, by utilizing MR/ER dampers to alter the dynamics of structures under seismic loading to mitigate damage. Kane et al (2009) proposed a non-linear market- based control approach for MR Dampers, using theories for resource allocation in microeconomics as a parallel for distributed control in structural systems to obtain an optimal control solution. Non-linear/adaptive control approaches, using time-varying systems and parameter estimation, have been proposed by Bitaraf et al (2010) and Nilkhamhang et al (2008). For soft computing-based control methods, neural networks

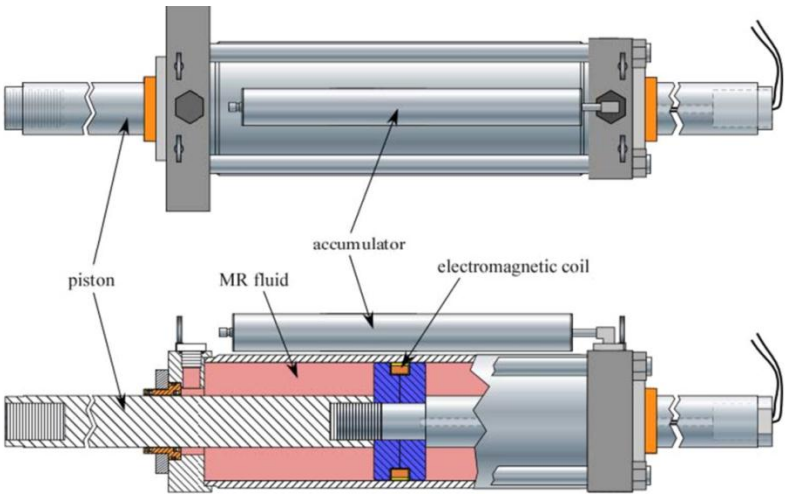

Figure 1.9: MR Damper schematic

are being utilized for both modeling of MR/ER devices (Boada et al 2009) and control designs (Kim et al, 2003, Xu et al 2003, Wang and Liao 2005, Shook D., et al 2007). Methods to identify a model of an MR damper and control a structure equipped with them based on genetic algorithms were offered by Liu et al (2011) and Xue et al (2011), respectively. Fuzzy logic controllers combining several other control methods, such as sliding mode and genetic algorithm control, with rules based on uncertain parameters (Al-Dawod et al 2004, Hu et al 2009, Kim et al 2010, Gu et al 2008) have also been proposed.

As with active control, implementation in the U.S. has been slow. Though, MR dampers have been implemented successfully in several real-world civil engineering applications around the world, including the Dongting Lake Bridge in China for cable vibration control (Chen et al., 2003) and the Nihon-Kagaku-Miraikan Museum in Japan for seismic mitigation.

1.1.5 Real-Time Hybrid Testing

To validate these concepts and controller applications, sophisticated experimental techniques are required. One method that is gaining traction in the experimental community is real-time hybrid simulation (RTHS). RTHS is based on the concept of separating a structure into experimental substructures and analytical substructures. The experimental substructures are tested physically, while the analytical substructures are modeled computationally, with both components interfacing with each other in real time as the test progresses.

Traditional structural testing methodologies include many different approaches, from monitoring full-scale prototype structures and shake table testing to conventional hybrid testing and real-time hybrid testing (Blakeborough et al, 2001). The ideal test case is the full-scale structure testing/monitoring, as this eliminates errors associated with modeling and reproduces the behavior of the structure at full scale. However, this type of testing is extremely time- and cost-prohibitive. Shake table testing allows the test structure to undergo inertial forces as well, but unless a large-scale table is used, full- and large-scale test specimens cannot be tested. Conventional hybrid simulation [Dermitzakis et al 1985], or pseudo-dynamic testing, combines physical and analytical models to test specimens over an extended period of time (i.e. tests using a 30 second earthquake excitation may take 3 hours to complete, etc.). This type of testing can capture the inertial effects of the excitation on the structure well. However, it is not suited for testing rate-dependent devices, due to the expanded time scale. Real-time hybrid simulation enforces the real-time constraint for command displacements to be applied to the experimental specimen. There are several advantages to this type of testing, including reduced costs as a result of not requiring full-scale models to test structures, not requiring high fidelity models for components that may be quite difficult to effectively model (i.e. highly non-linear devices, etc.), and the ability to effectively capture the behavior of rate-dependent devices.

There are also several challenges to this type of testing, including the requirement that the integration algorithm generate smooth, continuous, and stable displacement commands that can be realized by servo-hydraulic actuators which are imposing the displacements onto the test structure. In addition, hardware and software platforms must be able to conduct iterative calculations within the required time step to converge on the command for the next step, as well as interface with data acquisition systems, etc. and the lag between the command and the actuator achieving the desired displacement must be minimized.

In addressing the demands of the displacement input to the actuators, many integration algorithms have been proposed. Bonnet et al. (2007), Carrion et al. (2006), Nakashima et al (1992), and Chen et al (2008) have proposed explicit integration algorithms, which utilize the current measured state of a system to calculate the state at a future time. In contrast, Shing (2002) and Wu (2007) have proposed implicit methods, which solve equations using both current a future systems states. In general, implicit algorithms require more computation time but can be facilitated using larger time steps. Explicit algorithms use less computation, but also require significantly smaller time steps to retain stability, which is detrimental to achieving real-time testing. However, each type of algorithm has been applied with success for real-time hybrid simulation.

Another critical component of RTHS is achieving accurate tracking of a desired displacement command signal using servo-hydraulic actuators. Because actuators are dynamic systems, time lags may result due to the physical dynamics/limitations of the servo-hydraulic actuators and can with both the excitation and specimen (Dyke et al., 1995). To overcome this lag, several compensation methods have been proposed. After lumping all systematic time lags into a single value, Horiuchi et al. (1996) proposed the polynomial extrapolation delay compensation method. Modern approaches (Wallace et al. 2007, Chen and Ricles 2010) include creating inverse transfer function of low-order models which represent the dynamics of the actuator. Further, model-based controllers (Carrion and Spencer (2007), Carrion et al. (2009)) address the tracking issue using feedforward-feedback controllers. While, currently, displacement command and tracking is accepted and has been implemented, other methods including force control (Chantranuwathana 1999) and acceleration control (Nakata 2010) may also prove useful in future endeavors.

Although conceptually very attractive, further research is needed to identify and meet the challenges associated with the use of RTHS in large-scale experiments to assess these complicated physical phenomena. Progress in this cutting-edge research field requires expertise from interdisciplinary research teams. Moreover, numerous practical challenges, including those on the physical side (e.g., time delays/lags, sensor noise, actuator dynamics, control-structure interaction) and on the computational side (e.g., real-time execution, numerical modeling errors, robust actuator control, integration algorithms) need to be considered and understood. Though there have been tests using several types of isolated physical components (e.g., MR dampers), very few have utilized a significant structural component, such as a large-scale frame (Gao et al., 2012; Nakata and Stehman, 2012 As part of this research, several new enabling technologies have been developed and successfully employed in a real-time hybrid simulation. Several new novel actuator tracking controllers, for use with single/multiple large-scale actuators attached to a large-scale steel frame, were developed and validated through experimental testing. In addition, several newly developed semi-active control methods for large-scale MR dampers were implemented and tested using real-time hybrid simulation. Using a three-story steel frame, RTHS, 3-Story Prototype Structure, 9-Story Benchmark Structure

1.2 Overview

This report focuses on the development and experimental validation of a new semi-active control strategy for use with large-scale magnetorheological dampers in civil engineering applications.

In Chapter 2, a number of topics vital to the design, development and validation of the semi-active control strategies are introduced and discussed at length. These topics include: current relevant research related to semi-active devices and control, modeling and basic behavior of magnetorheological dampers, and a summary of the fundamentals of control theory and design approaches.

The proposed semi-active control algorithm is offered in Chapter 3. First, the motivation behind this control approach, including large-scale device dynamics and behavior is discussed. Next, the process to exploit these device-specific traits is laid out in the control design. Finally, through simulation and experimental results, the performance gains in tracking a desired force by using this controller are demonstrated.

Chapters 4-6 demonstrate the experimental validation of this proposed controller using two different structures. In the first experiment, a three-story prototype structure (representing a low-rise office building in Los Angeles) is tested through real-time hybrid simulation using large-scale physical substructures at the NEES@Lehigh RTMD facility at Lehigh University (Chapter 4). The second experiment builds upon the previous results, and utilizes the same large-scale physical components to test a 9-story benchmark structure. Testing is carried out at two different facilities for different phases of the testing: RTHS using only a large-scale damper at the SSTL facility at the University of Illinois – Urbana/Champaign and RTHS using a large-scale steel frame and large-scale MR damper at Lehigh University (Chapter 5). Finally, non-linear time history analysis of the 9-story benchmark structure under seismic loading is performed with numerical simulation using the RT-Frame2D computational tool in MATLAB (Chapter 6). In each phase of testing, various damper deployment schemes are considered and several controllers are tested for robust performance under unknown conditions. These tests mark the first instance of successfully implementing RTHS using a large-scale frame as the physical substructure.

Finally, in Chapter 7, general conclusions from the body of experimental work conducted for this report are drawn and presented. In addition, several avenues of future research are discussed.

CHAPTER 2: BACKGROUND

In this chapter, an overview of relevant research is summarized. Magneto-rheological damping devices are discussed, including basic behavior and theory for modeling. A synopsis of the basic tenets of modern control theory is offered, and the problem formulation for conducting a real-time hybrid simulation is discussed.

2.1 Magnetorheological Dampers

Magnetorheological dampers are semi-active devices that utilize magneto-rheological fluid to dissipate energy in dynamic systems. Magneto-rheological fluid consists of magnetically polarized particles suspended in a carrier fluid (typically a mineral or silicone oil). When a magnetic field is applied to the fluid (as shown in Figure 2.1), the magnetic particles connect and form chains, morphing the fluid from a viscous state to a semi-solid state and increasing the yield strength of the fluid. The transitioning to rheological equilibrium, which occurs when the particles are fully-aligned in chains, can happen within milliseconds and is dependent on the strength of the magnetic field applied to the fluid. In like manner, when the application of the magnetic field ends, the fluid reverts back to a viscous state and the yield strength of the fluid decreases. The ability of the damper fluid to quickly respond to the magnetic field and change states makes it suited for potential high-bandwidth applications like structural control. Additionally, the power levels required for adequate control over the MR fluid the damper are low compared to active devices, and the operational temperature range of the damper fluid is large without loss of yield strength in the fluid.

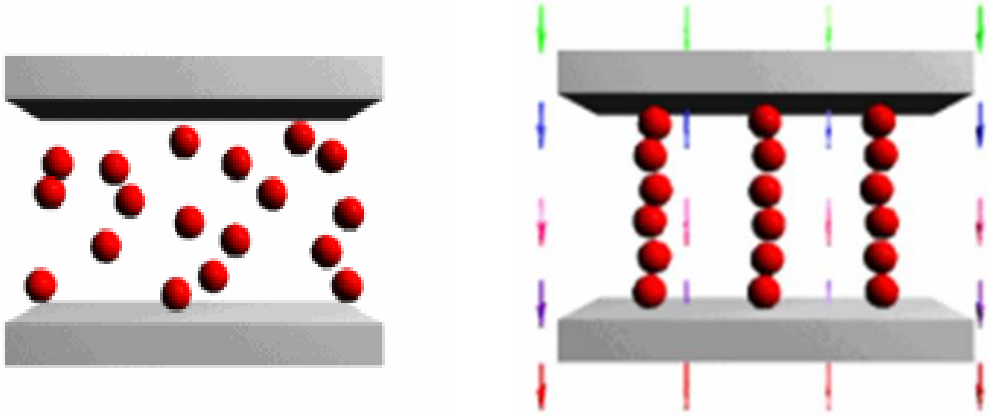

Figure 2.1: MR fluid particle chain development

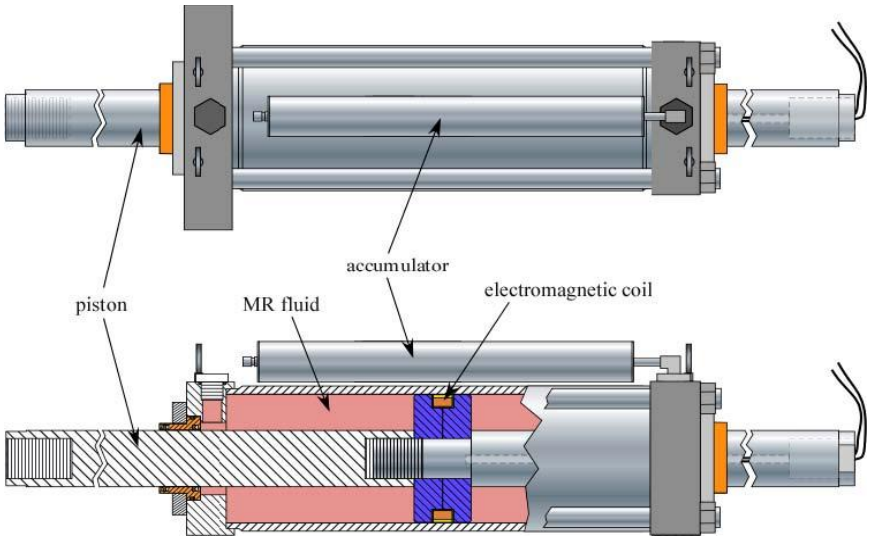

Figure 2.2: Schematic of a magneto-rheological fluid damper

The focus of this report concerns the use of a large-scale MR damper. The large-scale MR dampers are manufactured by Lord Corporation in Cary, NC, and a schematic of is shown in Figure 2.2. The damper is 1.47 m (58 inches) in length, weighs approximately 2.734 kN (615 lbs), and has a maximum stroke of ±292 mm (±12.5 inches). The MR damper contains a fixed-orifice damper filled with a MR fluid, which consists of micron-sized, magnetized iron particles randomly dispersed in a synthetic oil along with additives that promote homogeneity and inhibit gravitational settling. The damper's accumulator can accommodate a temperature change in the fluid of 80°F (27°C). The damper can provide control forces of over 200 kN (45 kip).

The MR damper is controlled with a low voltage, current driven command signal. The coil resistance is approximately 4.8 ohms, while the inductance is approximately 5 Henrys at 1 amp and 3 Henrys at 2 amps. An Advanced Motion Controls PWM Servo-Amplifier (30A8DDE) is powered by an 80 volt DC, 5 amp unregulated linear power supply. The servo-amplifier is used to provide the command signal that controls the electromagnetic field for each damper. The PWM Servo-Amplifier is controlled by a 0-5 volt DC signal and utilizes pulse width modulation for current control. The input control signal can be switched at a rate of up to 1 kHz, although the rise time of the current signal is limited by the inductance of the MR damper. Each damper has been fitted with a 1.5KE75A transient voltage suppressor to protect the MR damper electromagnetic coils from unintended and damaging voltage peaks, limiting the peak voltage to 75 volts.

To take advantage of the unique features and attributes associated with the MR dampers in control applications, development of a high fidelity model is necessary. In order to test the damper and ascertain prominent characteristics, the damper must be driven under various loadings and applied currents. To this end, the damper is attached in series to a hydraulic actuator and load cell, and secured to a test frame. From this

setup, the damper behavior under a wide variety of loading patterns, including sinusoidal, triangular, step, etc.

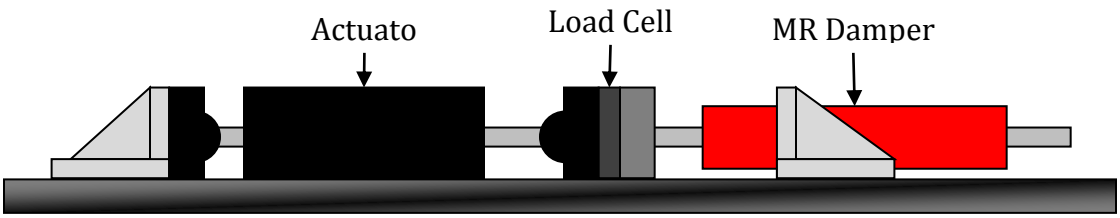

Figure 2.3: MR Damper Characterization Testing Frame

Typically, characterization of a MR damper is performed with triangle and sinusoidal tests, using a fixed frequency and amplitude for each run. A constant voltage is applied during the duration of the test, and ultimately, a variety of amplitudes, frequencies, and voltage levels are used.

The results for a subset of typical characterization tests are shown in Figure 2.4 and there are several items of interest to note. All data was sampled at 1024 Hz, and velocities were calculated from the measured displacements using the derivative function in SIMULINK. The excitation signal is a 0.5 Hz sinusoid with an amplitude of 25.4 mm for six voltage levels, 0 V, 0.5 V, 1.0 V, 1.5 V, 2.0V, and 2.5V. Three plots are shown, including the force generated as a function of time, force versus displacement (clockwise progression) and force versus velocity (counter-clockwise progression). When the applied voltage is 0 V, the MR damper demonstrates behavior consistent with a viscous device (*i.e.*, the force-displacement relationship is approximately elliptical, and the force-velocity relationship is approximately linear). However, as the voltage increases, the force required to yield the bonds of the particles in the MR fluid in the damper also increases. The increase in force for a given increase in the applied voltage is approximately linear for voltages between 0–2.5 V, and for this damper in specific, saturation of the MR effect (occurs when increasing the applied voltage no longer incurs an increase in the force required to break the particle bonds) occurs above 2.5 V.

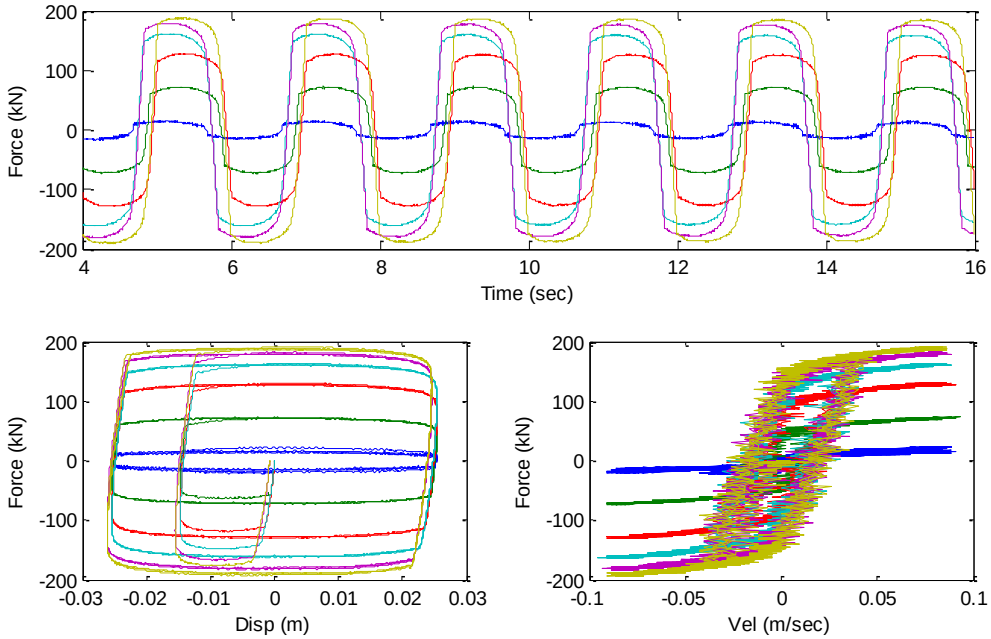

Figure 2.4: MR damper characterization behavior (0.5 Hz sine displacement input)

For the purposes of this study, characterization of the MR dampers was carried out at two different locations: the University of Illinois – Urbana/Champaign (UIUC) and Lehigh University (LU). At the UIUC Smart Structures Technology Laboratory (http://sstl.cee.illinois.edu), the testing setup utilizes a 125 kip actuator, manufactured by the Shore Western Corporation. A three-stage servo-valve is used to control the actuator, built up by integrating a Schenck-Pegasus model 1800 servo-valve rated at 80 gpm as the main-spool-valve with a Schenck-Pegasus model 20B two-stage servo-valve rated at 0.86 gpm as the pilot-valve. The actuator and specimen (MR damper) are both mounted in a test frame designed to minimize backlash and elastic deformation under the high forces expected during testing. A Shore Western model 1104 digital servo-controller is used to control the actuator in displacement feedback mode. Actuator lag is minimized using a model-based feed-forward feed-back control strategy (Phillips et al, 2011). The servo-controller accepts externally generated commands from a dSPACE model 1103 digital signal processing (DSP) board.

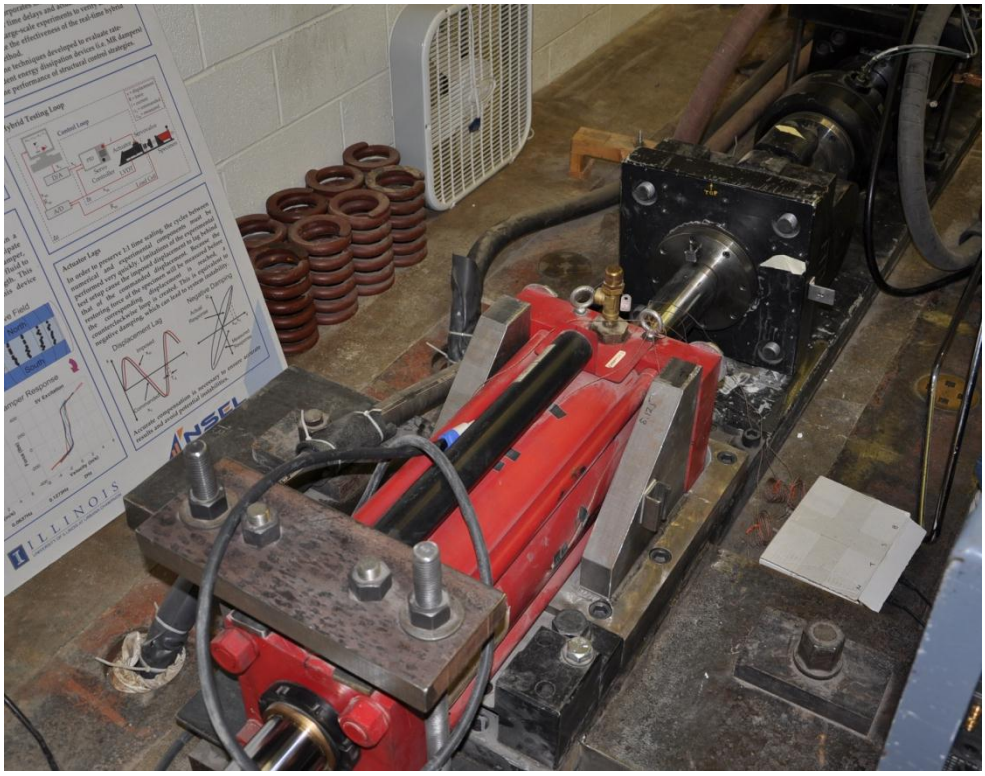

Figure 2.5: UIUC MR damper test setup

At the NEES@Lehigh Real-Time Multi-Directional (RTMD) Large-scale testing facility (http://www.nees.lehigh.edu/), the actuator is a Servotest Systems Ltd. 2300 kN hydraulic actuator (designated as Actuator 4, Model # 200-1000-1700KN, Serial # 6173). This actuator is controlled by two three-stage servo-valves, built through the integration of a Servotest SV1200 servo valve with a Moog G772-204 pilot valve, rated at 550 gpm and designated as "F" and "G". Each servo valve is connected to the hydraulic supply system (manufactured by Parker Hannifin Corp.) via a hydraulic service manifold (HSM). Each HSM provides high/low pressure and shutoff operations. To control the actuator

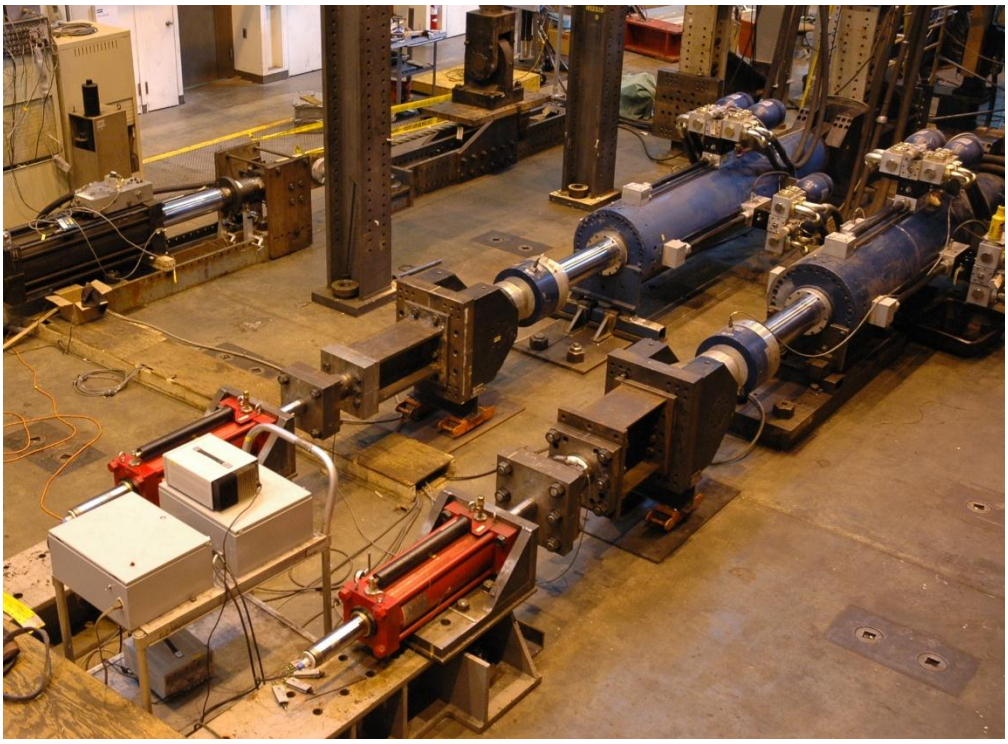

Figure 2.6: Lehigh MR damper test setup

with displacement/force feedback, a Servotest Systems Ltd. DCS 2000 servocontroller is used. The servocontroller accepts commands from a 2203 1-channel servo drive card, which can drive multiple two-stage or 1 off three stage servovalves. To apply the desired actuator input and current for the MR damper, xPC Target (Mathworks) real-time software is utilized. Data acquisition is carried out using a DAS 6000 DAQ system from Pacific Instruments Inc. (Model # 6000DAS, Serial # 6000s), with data logged as separate channels specified within the Simulink model.

Ultimately, to develop a comprehensive model of the MR damper control system, each component (PWM amplifier and the MR Damper) must be characterized independently and modeled. Several methods have been proposed for each element.

2.1.1. PWM Amplifier Model

The dynamics associated with commanding current and achieving rheological equilibrium have a large impact on the performance of the MR damper, and as such, must be taken into account and included with any damper model (Jiang, 2012). The PWM current driver is represented by a first-order filter combined with a constant time delay of 0.0006 seconds.

$$H(s) = \frac{I_{PWM}}{U} = \frac{1}{1+\tau s} \tag{2.1}$$

where $\boldsymbol{I_{PWM}}$ is the Laplace transform of the current output from the PWM, $\boldsymbol{U}$ is the Laplace transform of the command current sent to the PWM, and τ is a time constant.

The dynamics associated with the damper reaching rheological equilibrium as a result of the application of a magnetic field are related to the current within the electromagnetic coil inside the damper. This current will experience dynamics due to the inductance within this coil, and is modeled as

$$\boldsymbol{G(s) = \frac{I}{I_{PWM}} = \frac{1}{1 + \frac{L}{R}s}} \tag{2.2}$$

where $\boldsymbol{R}$ is the resistance of the damper, and $\boldsymbol{L}$ is the inductance in the coil which, as a function of current, is defined as the following

$$\boldsymbol{L(i) = \frac{R \cdot i}{di/dt} + L_0} \tag{2.3}$$

where $\boldsymbol{L_0}$ is the inductance constant and i is the time-varying current.

2.1.2. Dahl + Viscous MR Damper Model

Originally proposed by Dahl (1968) to describe frictional behavior, Aguirre (2008) proposed a modified version which included a dashpot element to better represent the viscous behavior of the damper. A schematic diagram is shown in Figure 2.7.

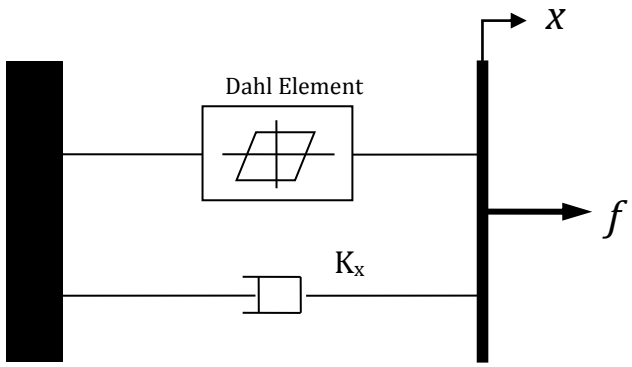

Figure 2.7: Viscous + Dahl MR damper model

The governing equations of the model are,

$$\dot{z} = \rho\,(\dot{x} - |\dot{x}|\,z\,) \tag{2.4}$$

$$f = \kappa_x \dot{x} + \kappa_\omega \omega \tag{2.5}$$

where $\dot{x}$ is the damper piston velocity, κ_x is the viscous friction coefficient, κ_ω is the static friction coefficient, z represent the nonlinear behavior of the damper characterized by the Dahl element, and f is the force generated by the MR damper. Thus, three parameters $(\rho,\ \kappa_x, \kappa_\omega)$ must be identified to fully characterize this model.

2.1.3. Hyperbolic Tangent MR Damper Model

Gavin (2001) proposed a simplified model for an 8-kN ER damper, dubbed the Hyperbolic Tangent Model. Christenson and Bass (2007) adapted this model for use with a 200 kN MR damper.

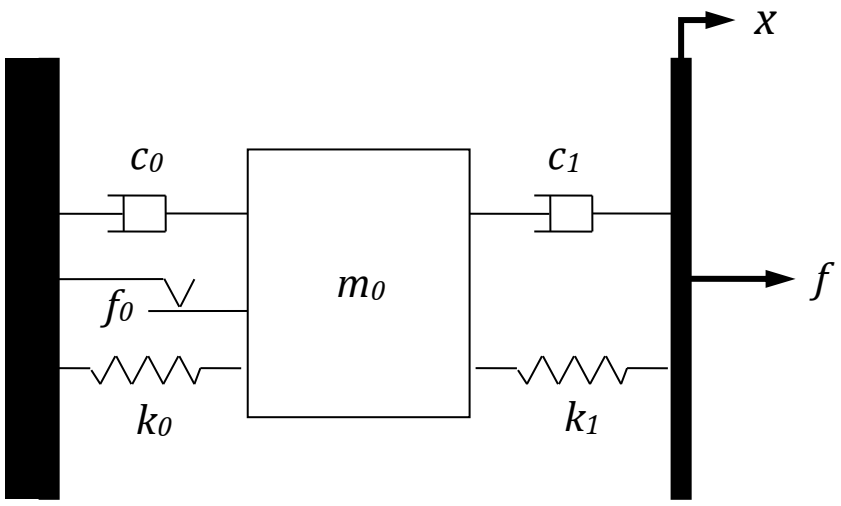

Figure 2.8: Hyperbolic Tangent MR damper model

The governing equations of this model are defined as

$$\begin{aligned} &m_0\ddot{x}_0 + (c_0 + c_1)\dot{x}_0 + (k_0 + k_1)x_0 \\ &= k_1 x + c_1 \dot{x} - f_0 \tanh\left(\frac{\dot{x}_0}{V_{ref}}\right) \end{aligned} \tag{2.6}$$

$$f = -k_0 x_0 - c_0 \dot{x}_0 + k_1 x + c_1 \dot{x} \tag{2.7}$$

where k_0 and c_0 represent the post-yield, visco-elastic stiffness and damping of the damper, k_1 and c_1 represent the pre-yield, visco-elastic stiffness and damping of the

damper, $\boldsymbol{m_0}$ represents the inertial mass of the damper piston and fluid, $\boldsymbol{x_0}$ and $\boldsymbol{\dot{x}_0}$ are displacement and velocity, respectively, of the inertial mass relative to the fixed base**,** $\boldsymbol{x}$ and $\boldsymbol{\dot{x}}$ are the summary of $\boldsymbol{x_0}$ and $\boldsymbol{\dot{x}_0}$ and the displacement and velocity of the damper piston relative to the inertial mass, $\boldsymbol{f_0}$ is the yield force of the damper, $\boldsymbol{V_{ref}}$ is a constant reference velocity, and $\boldsymbol{f}$ is the MR damper force. To parameterize this model, identification of seven variables ($\boldsymbol{m_1, c_0, c_1, k_0, k_1, f_0, V_{ref}}$) is required.

2.1.4. Bouc Wen MR Damper Model

Another approach was taken by Bouc (1971) and generalized by Wen (1976) to create the Bouc-Wen Model. Consisting of a spring and dashpot in parallel with a Bouc-Wen element, the model has been shown to be applicable for modeling hysteretic behavior. Spencer et al. (1997) proposed a modified version of this model, the phenomenological Bouc-Wen model, which has been demonstrated to capture the behavior of MR dampers very well and can be evaluated with little computational effort. As such, this model was chosen for this experimental study. The mechanical idealization of the model is shown in Figure 2.9 below.

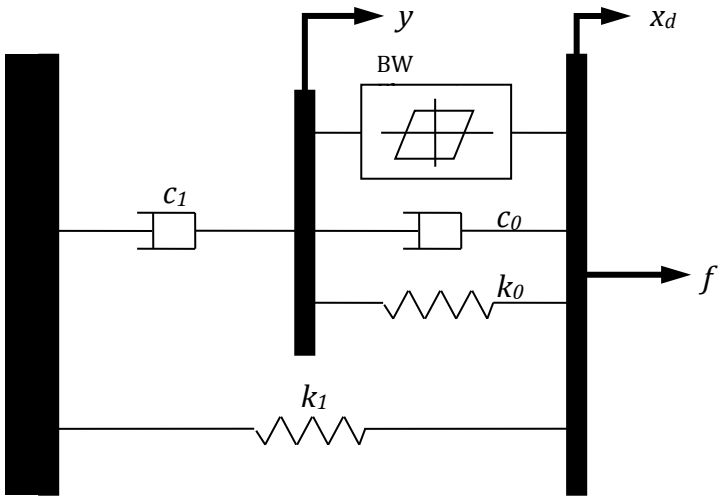

Figure 2.9: Phenomenological Bouc-Wen MR damper model

The governing equations of the model are

$$\boldsymbol{f = \alpha z + c_0(\dot{x}_d - \dot{y}) + k_0(x_d - y) + k_1(x_d - x_0)} \quad \textbf{(2.8)}$$

$$\boldsymbol{c_1\dot{y} = \alpha z + k_0(x_d - y) + c_0(\dot{x}_d - \dot{y})} \quad \textbf{(2.9)}$$

$$\boldsymbol{\dot{z} = -\gamma|\dot{x}_d - \dot{y}||z|z|^{n-1} - \beta(\dot{x}_d - \dot{y})|z|^n + A(\dot{x}_d - \dot{y})} \quad \textbf{(2.10)}$$

where $\boldsymbol{f}$ represents the damper force, $\boldsymbol{c_0}$ represents the viscous damping observed at large velocities, $\boldsymbol{c_1}$ is included to produce the roll-off observed at low velocities, $\boldsymbol{k_0}$ represents the stiffness at large velocities, $\boldsymbol{k_1}$ represents the accumulator stiffness, $\boldsymbol{x_0}$ is the initial displacement of the spring $\boldsymbol{k_1}$ associated with the nominal damper force due to the accumulator, and $\boldsymbol{z}$ is the evolutionary variable of the Bouc Wen element.

In order to ensure the model can capute the behavior of the device as it is implemented, the damper model must be able to account for fluctuating current levels. To establish such a model, certain parameters must be modeled as functions of current. For the phenomenological Bouc-Wen model, the three parameters are identified as functions of current, as

$$\boldsymbol{\alpha = \alpha_A e^{(\alpha_B i)} + \alpha_C e^{(\alpha_D i)}} \tag{2.11}$$

$$\boldsymbol{c_o = c_{0A} e^{(c_{0B} i)} + c_{0C} e^{(c_{0D} i)}} \tag{2.12}$$

$$\boldsymbol{c_1 = c_{1A}\sqrt{|i|} + c_{1B}} \tag{2.13}$$

where $\boldsymbol{i}$ is the current applied to damper from the current driver. In total, optimal values of 17 parameters ($\boldsymbol{\alpha_A\ \alpha_B\ \alpha_C\ \alpha_D\ c_{0A}\ c_{0B}\ c_{0C}\ c_{0D}\ c_{1A}\ c_{1B}\ k_0\ k_1\ x_0\ \beta\ \gamma\ \eta\ A}$) must be determined to model the MR damper.

In addition, the dynamics associated with commanding current and achieving rheological equilibrium have a large impact on the performance of the MR damper, and as such, must be taken into account and included with any damper model (Jiang et al. 2010, Jiang and Christenson, 2012). These dynamics are related to the current within the electromagnetic coil inside the damper. This current will experience dynamics due to the inductance within this coil, and is modeled as

$$\boldsymbol{G(s) = \frac{I}{I_{PWM}} = \frac{1}{1 + \frac{L}{R}s}} \tag{2.14}$$

where $\boldsymbol{R}$ is the resistance of the damper, and $\boldsymbol{L}$ is the inductance in the coil which, as a function of current, is defined as

$$\boldsymbol{L(i) = \frac{R \cdot i}{di/dt} + L_0} \tag{2.15}$$

where $\boldsymbol{L_0}$ is the inductance constant and $\boldsymbol{i}$ is the time-varying current.

Finally, the PWM current driver is modeled as a first-order filter combined with a constant time delay of 0.0006 seconds.

$$\boldsymbol{H(s) = \frac{I_{PWM}}{U} = \frac{1}{1 + \tau s}} \qquad \textbf{(2.16)}$$

where $\boldsymbol{I_{PWM}}$ is the Laplace transform of the current output from the PWM, $\boldsymbol{U}$ is the Laplace transform of the command current sent to the PWM, and $\boldsymbol{\tau}$ is a time constant.

2.2. Structural Control

Perhaps one of the more important technological advances in the field of structural engineering is the development and application of control to civil infrastructure. In the last couple of decades, extensive effort has been committed to the development of control theory and practical control applications/devices, both in academia and professional settings. More than two decades have passed since the completion of the Kyobashi Seiwa building, in Tokyo Japan (Kobori, 1996), which featured the first instance of active control in a structure. In the intervening years, much progress has been made on the integration of sensors and digital control systems within the confines of a structure to enhance the life safety of the occupants, serviceability/comfort, and overall global responses of the structure.

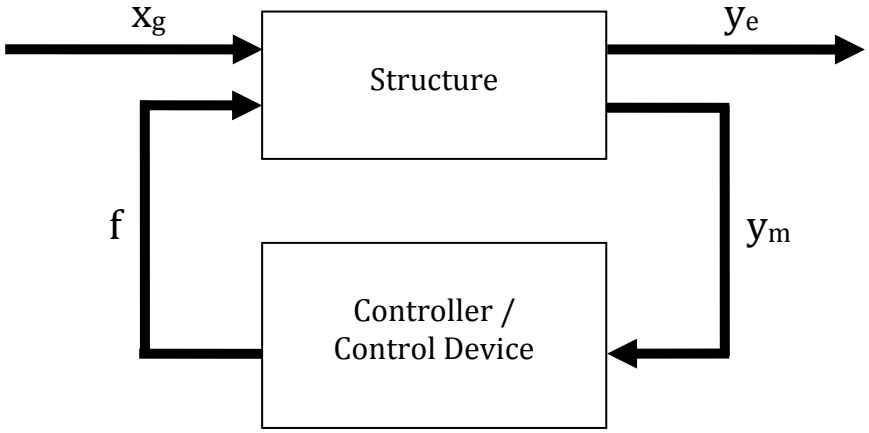

Figure 2.10: General Structural Control Block Diagram

Consider a seismically excited structure being controlled with *n* devices placed between the floors of the structure. A block diagram of this problem is shown in Figure 2.10, where $\ddot{x}_g$ is the ground excitation to the structure, f is the vector of forces input to the structure from the control devices, y_m is the vector of measured outputs from the structure (full-state feedback is not usually obtainable in a real-world scenario and as

such, y_m is typically a subset of a certain type of measurement, be it acceleration, displacement, etc.), and y_e is the vector of measurements used to evaluate the performance of the structure with control. Assuming that the forces from these devices are sufficient to keep the responses of the structure within a linear region, the equations of motion can be written as

$$\boldsymbol{M_s\ddot{x} + C_s\dot{x} + K_s x = \Lambda f - M_s \Gamma \ddot{x}_g} \tag{2.17}$$

where the mass and stiffness matrices ($\boldsymbol{M_s}$ and $\boldsymbol{K_s}$ respectively) are defined using finite-element modeling techniques, the damping matrix, $\boldsymbol{C_s}$, is determined based on an assumption of Rayleigh damping, $\boldsymbol{x}$ is a vector representing the displacements of the floors of the structure, $\boldsymbol{\ddot{x}_g}$ is a vector representing the earthquake excitation record, $\boldsymbol{f} = [\boldsymbol{f_1}, \boldsymbol{f_2}, \dots, \boldsymbol{f_n}]^{\boldsymbol{T}}$ is a vector representing the measured control forces generated by the MR dampers, $\boldsymbol{\Lambda}$ is a matrix determined by the number and placement of the MR dampers within the structure, and $\boldsymbol{\Gamma}$ is a column vector of ones.

This equation can be rewritten in state-space form as

$$\boldsymbol{\dot{x} = Ax + B}\begin{bmatrix}\boldsymbol{\ddot{x}_g}\\ \boldsymbol{f}\end{bmatrix} \tag{2.18}$$

$$\boldsymbol{y_m = C_m x + D_m}\begin{bmatrix}\boldsymbol{\ddot{x}_g}\\ \boldsymbol{f}\end{bmatrix} \tag{2.19}$$

$$\boldsymbol{y_e = C_e x + D_e}\begin{bmatrix}\boldsymbol{\ddot{x}_g}\\ \boldsymbol{f}\end{bmatrix} \tag{2.20}$$

$$\boldsymbol{y_c = C_c x + D_c}\begin{bmatrix}\boldsymbol{\ddot{x}_g}\\ \boldsymbol{f}\end{bmatrix} \tag{2.21}$$

where $\boldsymbol{x}$ is the state vector, $\boldsymbol{y_m}$ is the vector corresponding to the measured outputs, $\boldsymbol{y_e}$ is the vector corresponding to the outputs used for evaluation, and $\boldsymbol{y_c}$ is the vector corresponding to the connection outputs that are used as input for control device models. The state space matrices of the system are given as

$$\boldsymbol{A} = \begin{bmatrix}\boldsymbol{0} & \boldsymbol{I}\\ \boldsymbol{-M^{-1}K} & \boldsymbol{-M^{-1}C}\end{bmatrix}, \qquad \boldsymbol{B} = \begin{bmatrix}\boldsymbol{0} & \boldsymbol{0}\\ \boldsymbol{\Gamma} & \boldsymbol{M^{-1}\Lambda}\end{bmatrix} \tag{2.22}$$

where $\boldsymbol{C_m, C_e, C_c, D_m, D_e, D_c, F_m, F_e}$ and $\boldsymbol{F_c}$ are appropriate matrices corresponding to the measured, evaluation, and connection (used as inputs for the damper) outputs.

Many control strategies have been studied for civil engineering. However, due to practical limitation of being unable to obtain full-state (i.e. displacement, velocity and acceleration) measurement of the system, and the stochastic nature of earthquake ground excitations, LQG methods are advocated herein. In Dyke (1996), Spencer et al., (1994) and Suhardjo et al. (1992), output feedback control strategies based on using measured structural accelerations in determining a desired control force have been systematically developed based on LQG methods. An overview of the LQG control design is given in this section.

The LQG utilizes feedback (both measured responses and damper force), to generate a desired control force, f_c. To design the optimal regulator, the quadratic cost function

$$\boldsymbol{J(u) = \int_0^\infty (y^T Q y + u^T R u) dt} \quad \textbf{(2.23)}$$

must be minimized. Q and R are matrices that define the tradeoff between response regulation and control effort. The optimal control and observer gains,

$$\boldsymbol{K = R^{-1} B^T P} \quad \textbf{(2.24)}$$

$$\boldsymbol{L = (SC^T + GUH^T)(W + HUH^T)^{-1}} \quad \textbf{(2.25)}$$

are obtained by solving the respective algebraic Ricatti equations, given as

$$\boldsymbol{PA + A^T P - PBRB^T P + C^T QC = 0} \ \textbf{(K)} \quad \textbf{(2.26)}$$

$$\boldsymbol{AS + SA^T - SC^T CS + W^{-1} UGG^T = 0} \ \textbf{(L)} \quad \textbf{(2.27)}$$

where $\boldsymbol{U}$ is the disturbance covariance, $\boldsymbol{W}$ is the measurement noise covariance, $\boldsymbol{G}$ is the column of the $\boldsymbol{B}$ matrix that corresponds to the ground acceleration input, and $\boldsymbol{H}$ is the corresponding part of the $\boldsymbol{D}$ matrix.

As stated before, it is not always feasible to obtain full state feedback for a given system, thus, a Kalman state estimator is formed to minimize the steady-state error covariance and combined with the control law to produce the LQG regulator. The equations of motion for this regulator are represented as

$$\boldsymbol{\dot{\hat{x}} = (A - LC)\hat{x} + L y_m + (B - LD) f_m} \quad \textbf{(2.28)}$$

$$\boldsymbol{f_D = -K\hat{x}} \quad \textbf{(2.29)}$$

where $\boldsymbol{f_D}$ is a vector of desired restoring forces for the structure, $\boldsymbol{\hat{x}}$ are the estimated states of the system, $\boldsymbol{y_m}$ are the measured states of the system, and $\boldsymbol{f_m}$ are the measured

forces from the dampers. Calculations to determine $\boldsymbol{K}$ and $\boldsymbol{L}$ are performed using the Control System Toolbox in MATLAB.

Oftentimes, the model of the structure used for control design has fewer DOFs while still remaining accurate at the lower natural frequencies. It is feasible that modeling errors could occur due to unmodeled dynamics. However, if one tries to use aggressive controllers with emphasis at frequencies where the accuracy of system model is poor, instabilities and poor performance may occur. Thus, for the structural system under consideration, no significant control effort is allowed above any frequency related to the primary horizontal displacement modes. More details regarding the specific considerations used to design the controllers are provided in subsequent chapters

2.3. Real-Time Hybrid Simulation

To conduct a real-time hybrid simulation of a structural system, the structure is divided into two parts: the analytical (or computational) substructure and the physical (or experimental) substructure (shown in Figure 2.11). The physical substructure is tested in the lab while the analytical substructure is simulated on a computer. Displacements calculated using the analytical model are imposed on physical system using hydraulic actuators, and the resulting measured restoring forces from the physical system are fed back into the analytical model. This feedback relationship is outlined in the subsequent equations.

Consider an MDOF mass-spring-dashpot system with the associated free body diagrams (FBD):

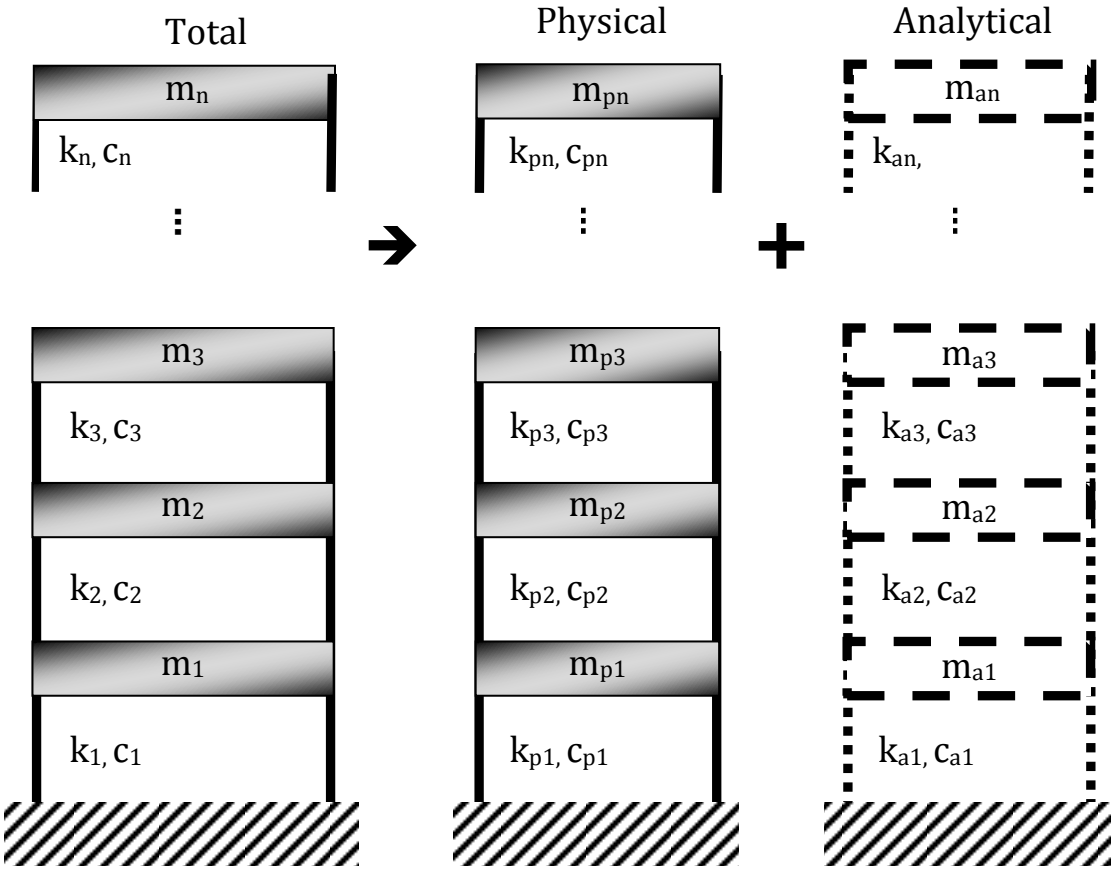

Figure 2.11: MDOF Frame model and associated substructures

The equations of motion for the total MDOF system under a seismic excitation are

$$\underline{\boldsymbol{F}}_{\ddot{x}_g} = \underline{\boldsymbol{m}}\,\underline{\ddot{\boldsymbol{x}}} + \underline{\boldsymbol{c}}\,\underline{\dot{\boldsymbol{x}}} + \underline{\boldsymbol{k}}\,\underline{\boldsymbol{x}} \qquad \textbf{(2.30)}$$

where $\underline{\boldsymbol{m}}$ is the mass matrix, $\underline{\boldsymbol{c}}$ is the damping matrix, $\underline{\boldsymbol{k}}$ is the stiffness matrix, $\underline{\boldsymbol{F}}_{\ddot{x}_g} = \left[\underline{F}_{\ddot{x}_{g_1}}, \ldots, \underline{F}_{\ddot{x}_{g_n}}\right]^{\boldsymbol{T}}$ is the vector force due to the ground excitation, $\underline{\ddot{\boldsymbol{x}}} = \left[\underline{\ddot{x}}_1, \ldots, \underline{\ddot{x}}_n\right]^{\boldsymbol{T}}$ is the vector of floor accelerations, $\underline{\dot{\boldsymbol{x}}} = \left[\underline{\dot{x}}_1, \ldots, \underline{\dot{x}}_n\right]^{\boldsymbol{T}}$ is the vector of floor velocities, and $\underline{\boldsymbol{x}} = \left[\underline{x}_1, \ldots, \underline{x}_n\right]^{\boldsymbol{T}}$ is the vector of floor displacements, respectively. The mass, stiffness,

and damping coefficients of each floor can be divided into analytical and physical components

$$m_i = m_{ai} + m_{pi}\,, \qquad c_i = c_{ai} + c_{pi}\,, \qquad k_i = k_{ai} + k_{pi} \tag{2.31}$$

where i = 1..n. Additionally, the restoring forces from the physical substructure (which incorporate the internal forces due to any control devices present within the physical substructure) are defined as

$$\underline{\boldsymbol{F}}_{\boldsymbol{R}} = \underline{\boldsymbol{m}}_{\boldsymbol{p}}\,\underline{\ddot{\boldsymbol{x}}} + \underline{\boldsymbol{c}}_{\boldsymbol{p}}\,\underline{\dot{\boldsymbol{x}}} + \underline{\boldsymbol{k}}_{\boldsymbol{p}}\,\underline{\boldsymbol{x}} \tag{2.32}$$

where $\underline{\boldsymbol{F}}_{\boldsymbol{R}}, \underline{\boldsymbol{m}}_{\boldsymbol{p}}, \underline{\boldsymbol{c}}_{\boldsymbol{p}}$ and $\underline{\boldsymbol{k}}_{\boldsymbol{p}}$ are the vector of restoring forces, and the mass, damping and stiffness matrices for the physical substructure, respectively. Substituting Eqs. 2.31 and 2.32 into Eq. 2.30 yields the equations of motion for the analytical substructure

$$\underline{\boldsymbol{F}}_{\ddot{x}_g} = \underline{\boldsymbol{m}}_{\boldsymbol{a}}\,\underline{\ddot{\boldsymbol{x}}} + \underline{\boldsymbol{c}}_{\boldsymbol{a}}\,\underline{\dot{\boldsymbol{x}}} + \underline{\boldsymbol{k}}_{\boldsymbol{a}}\,\underline{\boldsymbol{x}} + \underline{\boldsymbol{F}}_{\boldsymbol{R}} \tag{2.33}$$

where $\underline{\boldsymbol{m}}_{\boldsymbol{a}}, \underline{\boldsymbol{c}}_{\boldsymbol{a}}$ and $\underline{\boldsymbol{k}}_{\boldsymbol{a}}$ are the mass, damping and stiffness matrices, respectively, of the analytical substructure.

In the implementation of the RTHS, the restoring force is measured using load cells attached to the actuators driving the physical substructure. This quantity is necessary to compute the displacement in the analytical substructure (using a numerical solver) for the next time step. The resulting calculated displacement is then imposed on the physical substructure, and the restoring force is measured again. This cycle repeats at every time step in real-time for the duration of the experiment.

This system is represented visually in Figure 2.12.

.

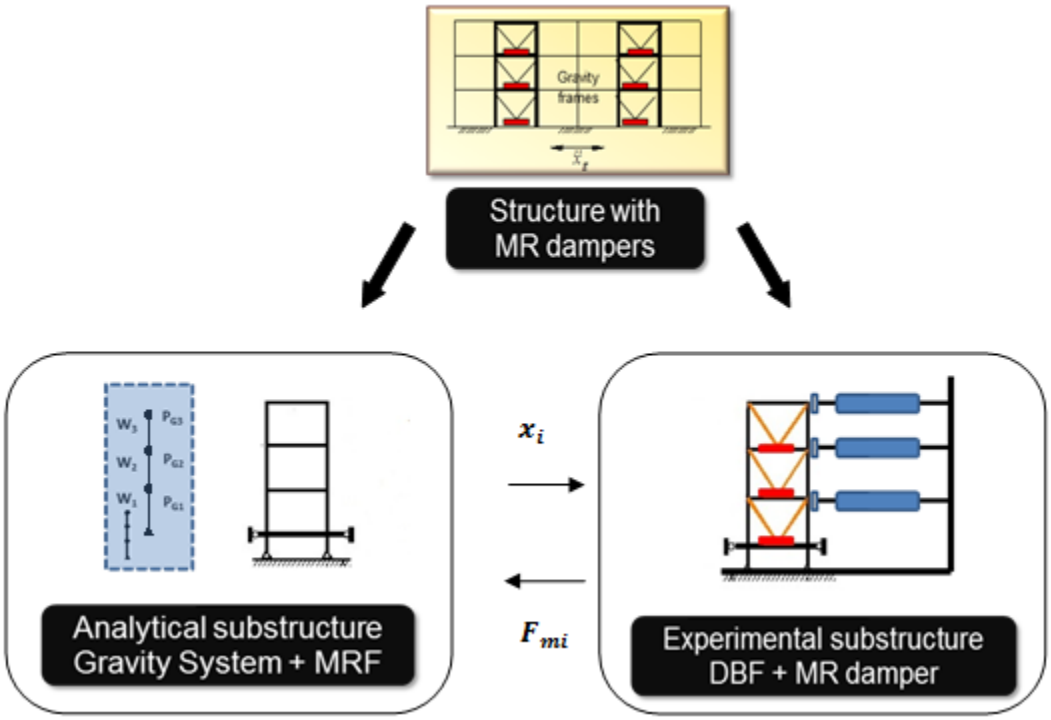

2.4. Summary

In this chapter, the background concepts related to the research presented in this report and discussed. The current state-of-the-art for semi-active magneto-rheological damping devices, including behavior and modeling, is summarized, the guiding principles of modern control theory are illustrated, and problem formulation for conducting a real-time hybrid simulation is presented.

CHAPTER 3: OVER-DRIVEN CLIPPED OPTIMAL CONTROL

As certain semi-active control devices increase in scale the dynamics become increasingly complicated. Control designs must take these characteristics into account to obtain systems that utilize these devices to their full potential. In this chapter, a new control algorithm is presented that is intended to exploit the unique behaviors of the large-scale magnetorheological (MR) to mitigate seismic response.

3.1 Over-/Back-driving Concept

Magnetorheological dampers are semi-active devices that utilize MR fluid to dissipate the energy in systems. MR fluid consists of magnetically polarized particles suspended in a carrier fluid (typically a mineral or silicone oil). When a magnetic field is applied to the fluid, the magnetic particles connect and form chains, morphing the fluid from a viscous state to a semi-solid state and increasing the yield strength of the fluid. The transitioning to rheological equilibrium, which occurs when the particles are fully-aligned in chains, is dependent on the strength of the magnetic field applied to the fluid. In like manner, when the application of the magnetic field ends, the fluid reverts back to a viscous state and the yield strength of the fluid decreases. The ability of the damper fluid to quickly respond to the magnetic field and change states makes it suitable for applications like structural control. Additionally, the power levels required for adequate control over the MR fluid the damper are low compared to active devices, and the operational temperature range of the damper fluid is large without loss of yield strength in the fluid.

This study uses a 200 kN MR damper developed by the Lord Corporation. The damper is 1.47 m in length, weighs approximately 2.7 kN, and has an available stroke of 584 mm. The damper's accumulator can accommodate a temperature change in the fluid of 80^{o}F and the damper is controlled with a low-voltage, current-driven command signal (Jiang, 2012). The coil resistance is approximately 4.8 Watts, while the inductance is approximately 5 H at 1 amp and 3 H at 2 amps. An Advanced Motion Controls PWM Servo-Amplifier (30A8DDE) is used to provide the command signal that controls the electromagnetic field for each damper and utilizes pulse width modulation for current control. The input control signal can be switched at a rate of up to 1 kHz, although the rise time of the current signal is limited by the inductance of the MR damper. Each damper has been fitted with a 1.5KE75A transient voltage suppressor to protect the MR damper electromagnetic coils from unintended and damaging voltage peaks.

The concepts of over-driving and back-driving are perhaps best explained using a simple analogy. Consider a person driving a boat on a lake. Initially the boat is at rest, but the driver desires to go the fastest speed that the boat is capable of. To achieve this speed as quickly as possible, the driver would open the throttle as far as possible, and then throttle back once the desired speed has been reached. Now consider the boat moving at maximum speed, while the driver desires to come to a complete stop as

quickly as possible. Setting the throttle to zero would cause the boat to simply coast to a stop. Instead, the best course would be to put the engine in full reverse, until the boat has stopped, and then switch to zero. These same principles are applied to the over-driven clipped optimal controller (ODCOC) developed for use with MR dampers.

When controlling an MR Damper, it is not possible to directly command the damper to generate a specified force, because the response of the MR damper is dependent on the displacement/velocity of the MR damper piston. However, the forces produced by the MR damper may be increased or decreased by adjusting the value of the current applied by the current driver. Given the dynamic nature of the current driver and the MR fluid inside of the damper, there is a time lag between the voltage being commanded to the damper and the damper reaching a desired force. However, as shown in Figure 3.1, by commanding a higher level of voltage than the normal level of operation (or *over-driving* the damper) the response time of the damper can be reduced. For to the safety of the electronics inside the damper, this amplified voltage level can only be sustained for a brief period of time.

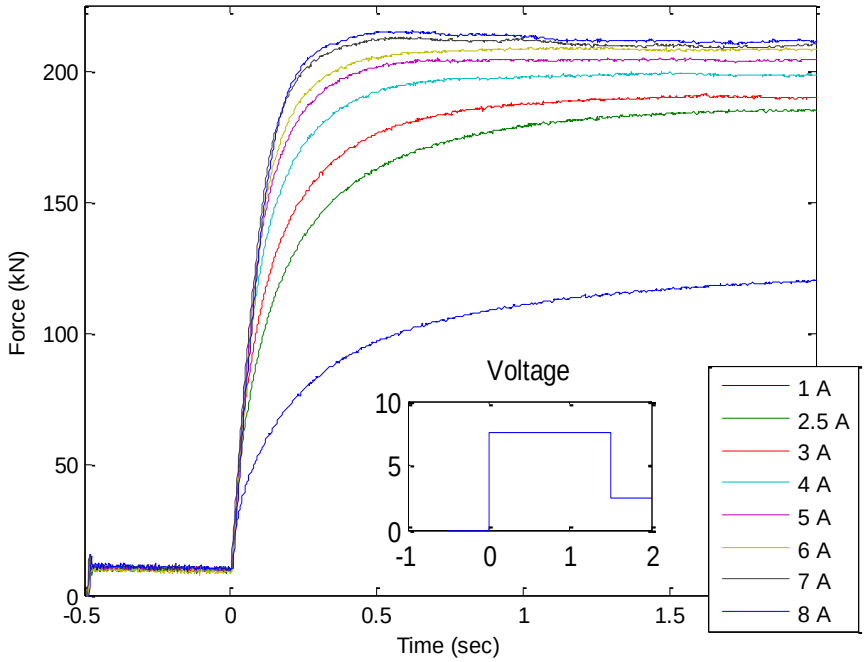

Figure 3.1: MR damper force rise time in response to various current (step up) input patterns

Back-driving the damper is similar in concept to over-driving. If the desired force is lower than the measured force, a negative voltage can applied to the damper for a brief period of time until the desired force is reached. The negative voltage serves to induce a magnetic field in the opposite direction to that of a positive voltage, and as such, the magnetic bonds between the particles in the MR fluid are forcibly broken. This effect decreases the fall time of the force in the MR damper, as illustrated in Figure 3.2

.

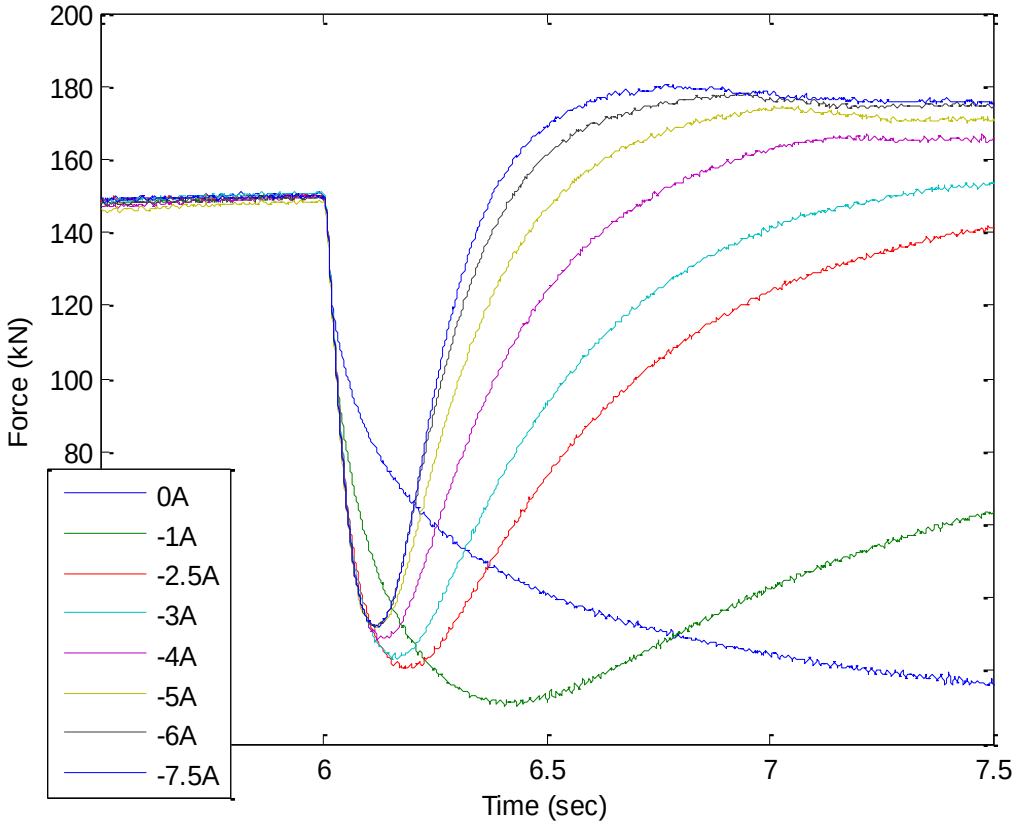

Figure 3.2: MR damper force fall time in response to various current (step down) input patterns

However, if the negative current is applied for a long duration and the magnetic field in the positive direction is completely dissipated, the magnetic field begins to build up in the opposite direction, and the damper force begins to rise again. Thus, the duration of time that the negative current is applied is also a factor to consider in design. As shown in Figure 3.3, applying a negative current for an optimal time before the magnetic field starts building up in the opposite direction is crucial to optimizing the damper performance.

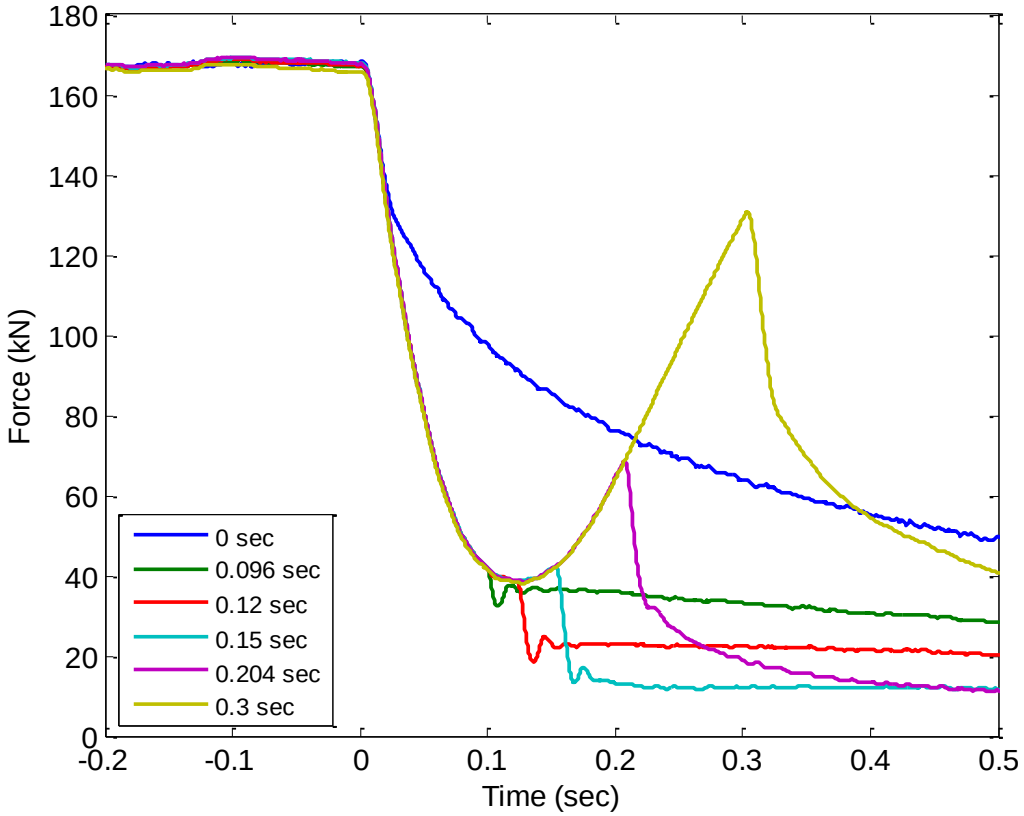

Figure 3.3: Force response as a function of negative current application duration

Given the greater impact of this behavior in the large-scale damper (as the size of the damper and amount of fluid therein increases, the time required to achieve/break rheological equilibrium also increases), it is in the interest of the control designer to devise a strategy that can account for and also exploit this behavior to increase the effectiveness of the devices.

3.2 Over-Driven Clipped Optimal Control Algorithm Development

A new controller is proposed in this report to effectively exploit the above characteristics of the large MR damper. This controller is referred to as the Over-Driven Clipped Optimal Controller (ODCOC). The ODCOC begins with the concepts of the clipped optimal controller (COC - Dyke 1996), while adding effects to make use of over-driving and back-driving current commands, suggested by Yang (2001) and previously discussed. This control approach consists of two parts: a linear quadratic Gaussian (LQG) regulator used to estimate unmeasured states and determine an optimal restoring force to be applied the structure, and a control law designed to select an appropriate

voltage to be applied to the damper based on the relationship between this desired force and the measured damper force, with the intention of inducing the MR damper to reach the desired force.

The LQG utilizes acceleration feedback (due to ease and reliability of measurement) and measured damper force, to generate a desired control force, f_c. To design the optimal regulator, the quadratic cost function

$$\boldsymbol{J(u) = \int_0^\infty (y^T Q y + u^T R u) dt} \quad \textbf{(3.1)}$$

must be minimized. Q and R are matrices that define the tradeoff between response regulation and control effort. The optimal control and observer gains,

$$\boldsymbol{K = R^{-1} B^T P} \quad \textbf{(3.2)}$$

$$\boldsymbol{L = (SC^T + GUH^T)(W + HUH^T)^{-1}} \quad \textbf{(3.3)}$$

are obtained by solving the associated respective algebraic Ricatti equations, given as

$$\boldsymbol{PA + A^T P - PBRB^T P + C^T QC = 0} \ \textbf{(K)} \quad \textbf{(3.4)}$$

$$\boldsymbol{AS + SA^T - SC^T CS + W^{-1} UGG^T = 0} \ \textbf{(L)} \quad \textbf{(3.5)}$$

where $\boldsymbol{U}$ is the disturbance covariance, $\boldsymbol{W}$ is the measurement noise covariance, $\boldsymbol{G}$ is the column of the B matrix that corresponds to the ground acceleration input, and $\boldsymbol{H}$ is the corresponding part of the D matrix.

It is not always feasible to obtain full state feedback for a given system, thus, a Kalman state estimator is formed to minimize the steady-state error covariance and combined with the control law to produce the LQG regulator. The equations of motion for this regulator are represented as

$$\boldsymbol{\dot{\hat{x}} = (A - LC)\hat{x} + Ly_m + (B - LD)f_m} \quad \textbf{(3.6)}$$

$$\boldsymbol{f_D = -K\hat{x}} \quad \textbf{(3.7)}$$

where $\boldsymbol{f_D}$ is a vector of desired restoring forces for the structure, $\boldsymbol{\hat{x}}$ are the estimated states of the system, $\boldsymbol{y_m}$ are the measured states of the system, and $\boldsymbol{f_m}$ are the measured forces from the dampers. Calculations to determine $\boldsymbol{K}$ and $\boldsymbol{L}$ are performed using the Control System Toolbox in MATLAB.

The regulator is coupled with a control law that determines the voltage to be applied to the damper. Based on the damper behavior previously described, the process for the selecting the applied voltage is as follows. The possible voltage values used in this controller are 7.5, 2.5, 0 and -7.5 volts. In the control law, the selection of the voltage depends on four variables: $f_{D,}$ the desired force output from the LQG regulator; $f_{M,}$ the measured force feedback from the MR dampers; $f_{MAX,}$ the maximum force capacity of the MR damper; $f_{MIN,}$ the minimum force capacity of the MR damper, defined as the force present when the damper is in an "off-state", or when the input voltage is set to 0 volts. The control law is separated into separate regions of over-driving and back-driving, and there are several conditions that must be fulfilled to activate each block.

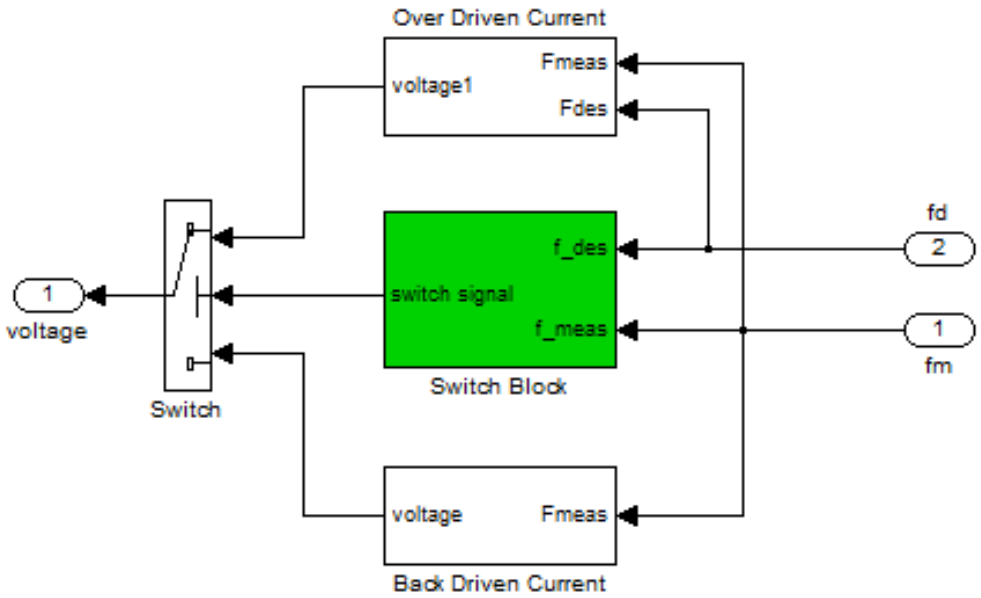

Figure 3.4: SIMULINK diagram of ODCOC controller

The over-arching physically-motivated condition of the control system is that the absolute values of the desired force must be greater than f_{MIN} or, because it is not possible to control the damper forces below this threshold, the voltage is set to zero.

When over-driving the damper, the amplified voltage is applied only when two conditions are met: (1) f_M is less than f_D and (2) the error between the two is large enough. For both over- and back-driving currents, the large amplitude current is limited to a specific application time. This restriction is made based on two issues: (i) safety concerns for the damper, as applying amplified voltage to the damper for extended periods may cause damage to the internal electronic circuit, and (ii) limitations on the ability of the current driver to sustain ±7.5 amps for an extended period of time. For the damper considered herein, the appropriate application time, based on the test data shown in Figure 3.3, is 0.1 seconds.

Alternatively, three conditions must be met for the back-driving current command block to be activated: (1) the desired and measured forces must have opposite signs, (2) the desired force must be on the downside, which occurs when the desired force is trending toward zero and (3) the difference between the desired and measured forces must be sufficiently large to warrant the additional voltage levels. Additionally, when back-driving the damper, while the negative voltage can cause the force to dissipate quickly, eventually the force will rise again as the magnetic field magnitude increases in the opposite direction. Thus, it is necessary to cutoff the voltage before the force beings to rise again. For this controller, the amplified voltage levels are ±7.5 volts. A visual representation of this control algorithm is shown in Figure 3.5.

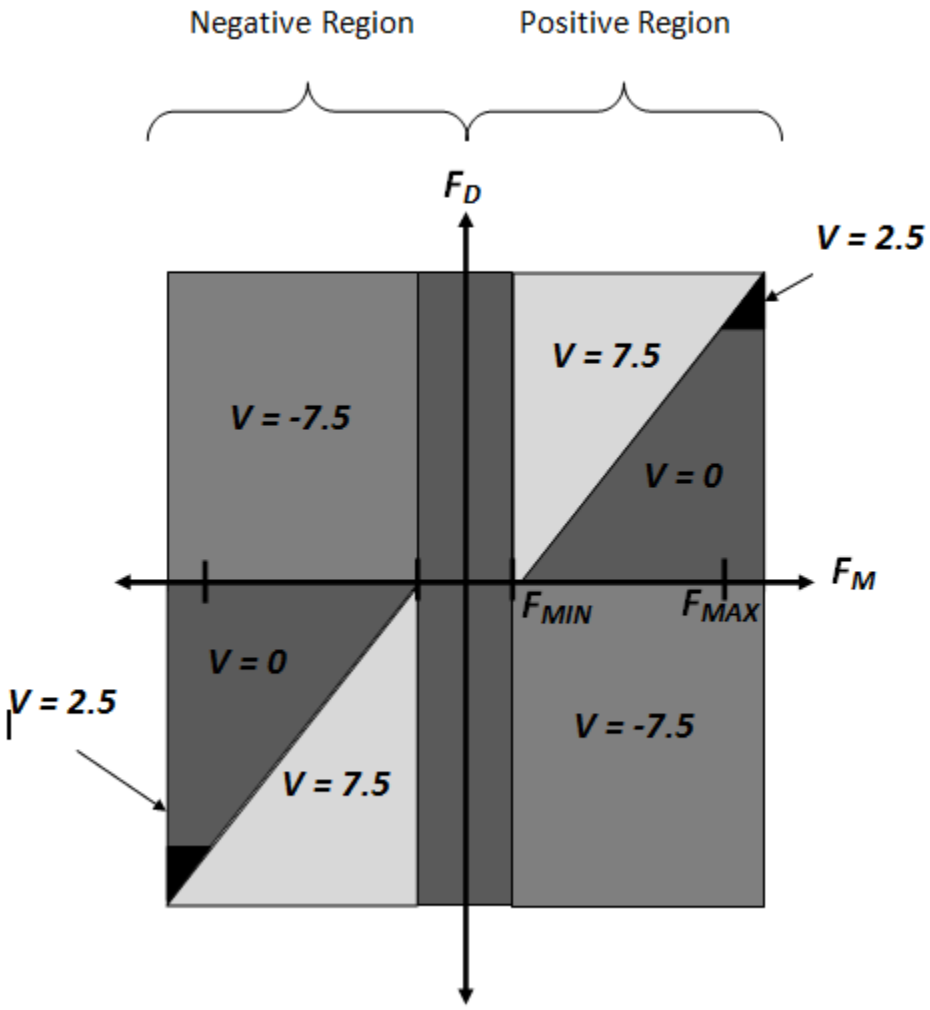

Figure 3.5: Visualization of ODCOC Control Law

3.3 Force Tracking Validation

Ultimately, the goal of any optimal controller is to achieve a desired performance, and in this case, that is to track a desired force response. In this case, the control law needs to induce the MR damper into tracking the desired restoring force as closely as possible, by regulating the voltage output to damper.

To evaluate the ability of the ODCOC algorithm to track a desired force, a numerical simulation is performed. For the purposes of this validation, a model of a nine story structure with a single MR damper installed the 1st floor is developed. The

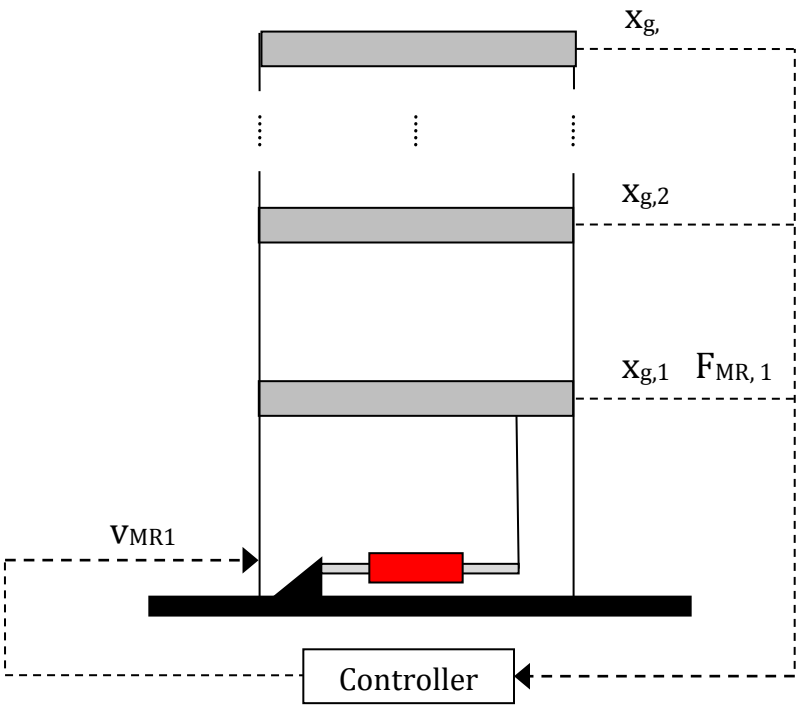

Figure 3.6: Numerical Simulation Representation

damper is connected between the bracing and floor, and a diagram of the implementation is shown in Figure 3.6. The equations of motion for this structure are

$$\boldsymbol{M\ddot{x} + C\dot{x} + Kx = \Lambda f - \Gamma M\ddot{x}_g} \tag{3.8}$$

where $\boldsymbol{f}$ is the vector of measured damper control forces and $\boldsymbol{x} = [\boldsymbol{x_1} \quad \cdots \quad \boldsymbol{x_9}]^{\boldsymbol{T}}$ is the vector of displacements (relative to the ground) of the nine floors of the structure.

Acceleration feedback from the system and measured damper forces are fed into an optimal LQG controller to generate the optimal (or, desired) restoring force. The excitation used to determine the building responses for inputs to the damper model is the

EW component of the 1940 El Centro, shown in Figure 3.7. The control weighting on the responses is set to 5e4 on all floor accelerations, as this value limits the desired force to the maximum force capacity of the damper (200 kN). The baseline responses of the structure are obtained (required as inputs to the damper model in simulation) and used as a basis for comparison between the semi-active control algorithms.

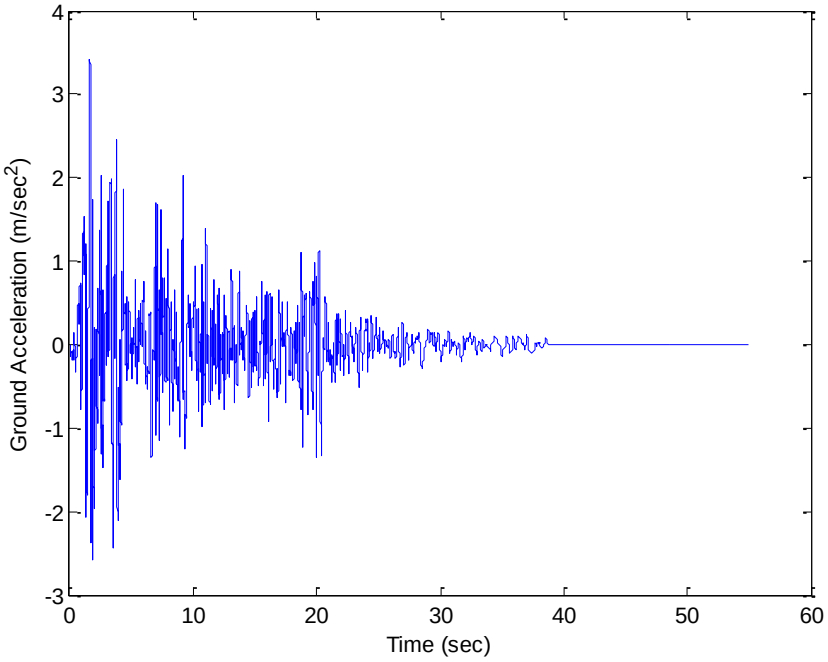

Figure 3.7: El Centro Earthquake Time History

To assess the ability of the controllers to track the optimal control forces when applied to the large scale MR damper model, two different semi-active controllers are considered. Both the clipped optimal controller (COC), as proposed by Dyke (1996) and ODCOC are considered in simulation. Based on the results of the simulation (shown in Figure 3.9a-b), both controllers achieve a reasonable level of force tracking. In terms of the peak error, the ODCOC achieves a 16% reduction with 146.3 kN, as compared to 173.8 kN for the COC. The RMS error between the desired force and the measured damper force for the COC is 38.1 kN. For the ODCOC, the RMS error is 29.9 kN, which is a 22% reduction in error as compared to the COC. In Figure 3.8a-b, notice that the COC is able to track the desired force in a general sense, whereas the ODCOC is able to track the desired force in a precise manner. The better tracking capability is due to the overdriving and back-driving nature of the ODCOC controller, coupled with the dynamics of the large-scale MR damper. This controller is better able to command the MR damper to quickly respond to changes in the desired force being tracked. Note that neither controller allows for exact, continuous tracking, as evidenced by the small oscillations in the measured damper force around the desired force.

Table 3.1: Simulation Force Tracking Error Results

Controller	Peak Error (kN)	RMS Error (kN)
COC	173.8	38.1
ODCOC	146.3	29.9

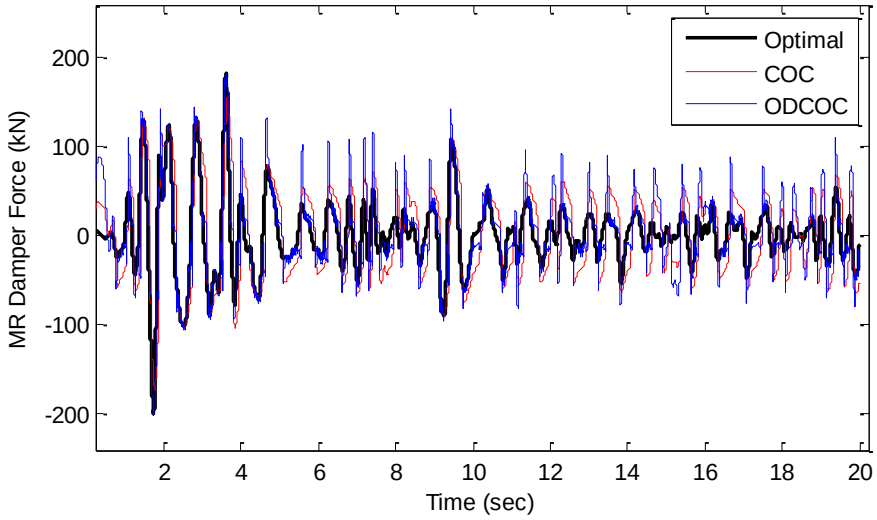

(a)

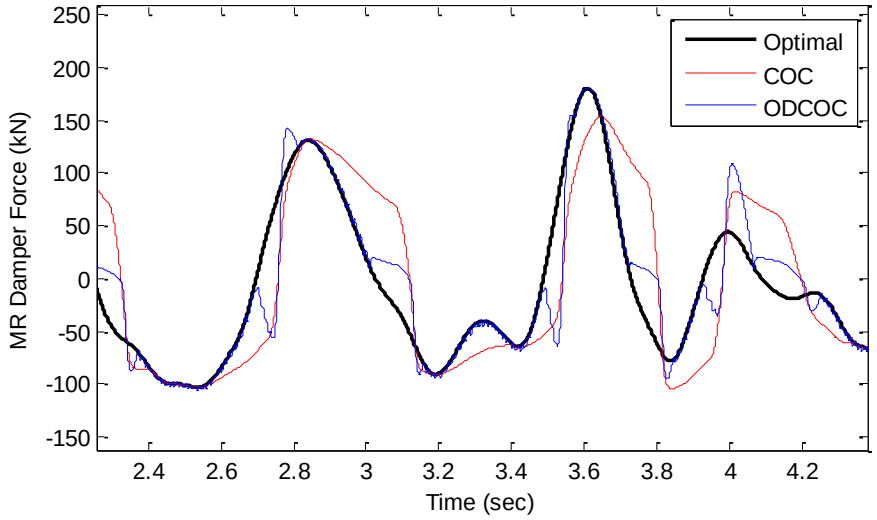

(b)

Figure 3.8a-b: Simulation Force Tracking Comparison (a) Full View and (b) Zoom

To further validate the performance of the controllers, a real-time hybrid simulation was performed at the University of Illinois – Urbana/Champaign Smart Structures Technology Laboratory (SSTL) using a large-scale MR damper. The damper was tested as the physical substructure using a hydraulic actuator, while the nine story structure was modeled computationally as the analytical substructure. Acceleration and MR damper force feedback were again used to determine the optimal restoring force, with an equal weighting value of 5e4 placed on all floor accelerations for both controllers. A summary of the error results is shown Table 3.2 and a comparison of the measured damper force for each controller and the desired tracking force for the RTHS is shown in Figure 3.9a-b.

Table 3.2: UIUC RTHS Force Tracking Error Results

Controller	Peak Error (kN)	RMS Error (kN)
COC	145.2	28.6
ODCOC	102.9	25.6

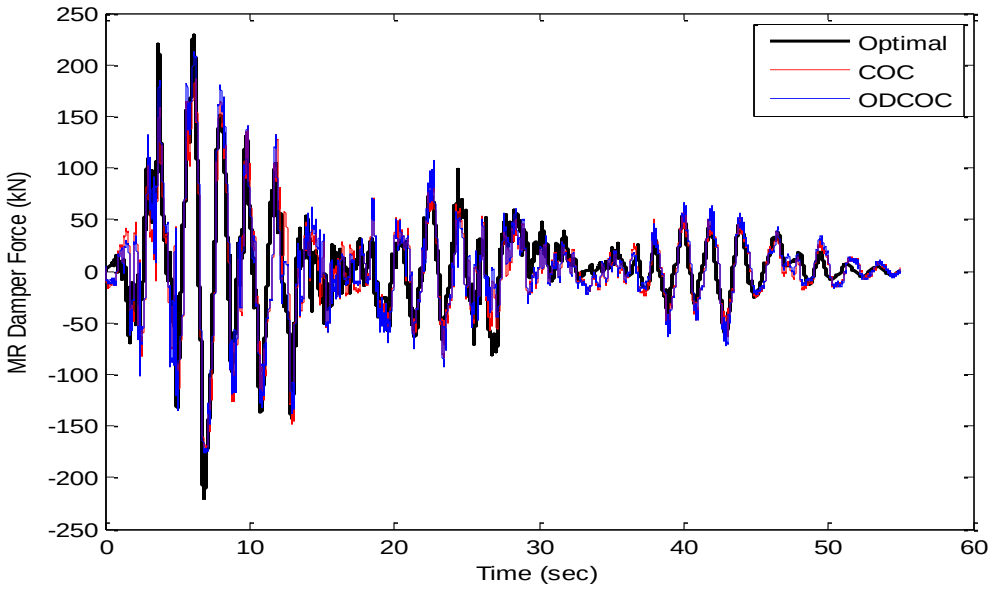

(a)

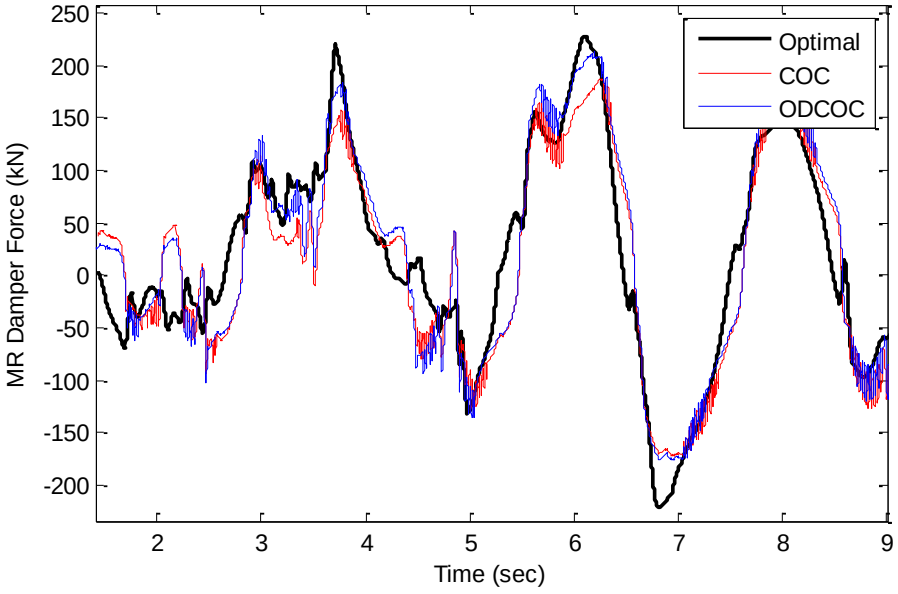

(b)

Figure 3.9a-b: RTHS Force Tracking Comparison (a) Full View and (b) Zoom

The results of the RTHS show the same patterns as the simulation. The ODCOC has a peak error (the difference between the desired tracking force and the measured MR damper force) of 102.9 kN, a 30% reduction compared to COC, which has a peak error of 145.2 kN. The RMS error for the ODCOC is 25.6 kN, which is a 10% reduction in error as compared to the COC, with 28.6 kN. In both cases, the ODCOC outperforms the COC approach in both peak and RMS error, which effectively demonstrates that the size of these devices and corresponding dynamics should be considered in the design of control laws.

It should be noted that the amplified voltage values used for this damper are not universal. The concepts of over- and back-driving will hold true to all large and full-scale MR devices, but the actual voltage command values used for control will need to be determined on a case-by-case basis. The exact device that the designer/engineer will use in a given application should be analyzed using the step voltage command pattern shown in Figures 3.1-3.3. Many factors will influence the selection of the larger voltage commands, including: (1) the required response time for the device to gain adequate control of the structure, (2) consideration of the internal electronics of the damper, which may be compromised if the amplified voltage is too large, and (3) the amount of power available to generate the voltage command for a sustained period of time. Control designers will need to consider all of these aspects when selecting the voltage command levels to be applied to specific dampers.

3.4 Summary

The motivation and concepts of over-driving and back-driving the large-scale MR damper are introduced. The necessity of employing these techniques in conjunction with large-scale devices is demonstrated through several experimental tests. A new control strategy using these strategies is proposed for use large-scale MR dampers, and the effectiveness of this strategy in tracking a desired force is demonstrated through numerical simulation and experimental tests. In the simulations, a comparison was made between an established semi-active control method, and the ODCOC approach showed marked improvement over the other controller. In the experimental test involving a real MR damper, the enhanced force tracking capability of the ODCOC is confirmed. In the following chapters, the proposed control algorithm will be employed in several simulations and experiments to demonstrate its ability to reduce the global responses of the structure.

CHAPTER 4: THREE-STORY PROTOTYPE STRUCTURE EXPERIMENT

In this chapter, an overview of an experimental study to assess various control algorithms for use with magneto-rheological (MR) dampers through real-time hybrid simulation (RTHS) is presented. With an emphasis on practical implementation, a code-compliant example structure equipped with multiple dampers is considered, and readily available acceleration feedback is used to determine the control input to the damper. The performance of each control algorithm is evaluated and compared using a variety of earthquake inputs through both numerical simulation and real-time hybrid simulation. Following this characterization, the best controller is selected and evaluated using a single earthquake input with varying masses, to analyze the robust performance ability. In all cases, the reduction in relative displacement, inter-story drift, and absolute acceleration in the global sense of the structure is examined.

4.1 Experimental Setup and Procedure

In order to perform the experiment, several steps must be taken, including: selection/ modeling/construction of a representative structure to serve as a portion of the physical substructure in the RTHS testing using the experimental setup at the NEES@Lehigh facility, identification of the various components utilized in testing the physical substructure of the RTHS (large-scale steel frame, large-scale MR damper, hydraulic actuators, etc.). These steps are described in the following sections.

4.1.1 Prototype Structure Description

The 3-story prototype structure used in this study was designed by collaborators at Lehigh University (Chae, 2011). Although not actually constructed, the structure adheres to provisions in the seismic code and is meant to exemplify a typical low-rise building office building (for general commercial use) designed for the Los Angeles, California region. A structure is shown in Figure 4.1

The full-scale prototype structure is 150 ft by 150 ft in plan, and 37.5 ft in elevation. The bays are 25 ft on-center, in both directions, with six bays each in the E–W direction and the N–S direction. Typical floor-to-floor heights (for analysis purposes measured from center of beam to center of beam) are 12.5 ft. Lateral load resistance is achieved through the use of perimeter steel moment-resisting frames (MRFs) in combination with damped-braced frames (DBFs) that house the MR dampers. The interior bays of the structure contain simple framing. The levels of the 3-story building are numbered with respect to the base level, which is located at the ground level. The third level is the roof.

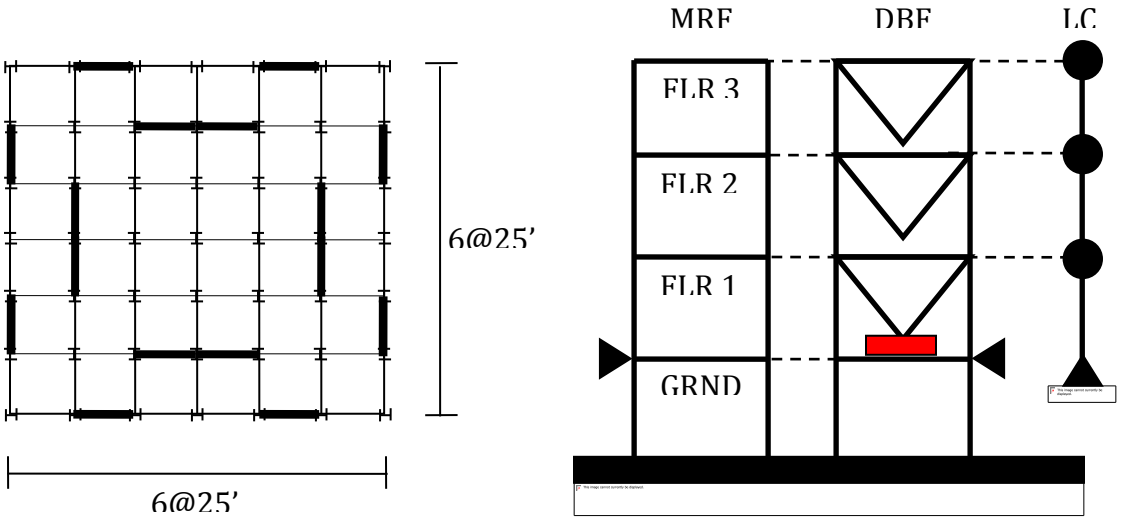

(a) **(b)**

Figure 4.1: (a) Plan View of Structure and (b) Elevation View of MRF+DBF+LC

Due to height restrictions in the NEES@Lehigh facility, a full-scale version of this frame system cannot be constructed. Thus, a scaled, representative prototype of the structure is necessary to conduct testing and controller performance analysis. The length scaling factor is selected as 0.6, and the various resulting relationships between the prototype structure and the testing structure are outlined in Table 4.1.

The prototype consists of two separate frames: (1) a moment-resisting frame that supplies the bulk of the lateral resistance for the structure, and (2) a damped braced frame (DBF) which houses the MR dampers deployed within the structure. Both frames are constructed using A992 steel, and consists of a ground floor, 5ft. in height, and three additional floors, measuring 7.5 ft. in height. The frames are restrained from lateral movement at the ground floor by way of rigid links at each end (effects of the surrounding soil and foundation walls), and loading frames are used to impose equivalent displacement on both frames. Instrumentation, consisting of accelerometers, strain gages, LVDTs, etc. is placed on each frame prior to installation within the test area. Due to time constraints, the large-scale MRF was not connected to the DBF with the loading beams, and so it was not considered in the physical substructure portion of the RTHS. Schematics of the test setup and design drawings of the DBF are shown in Figures 4.2 and 4.3, respectively.

Table 4.1: Scaling parameters for the DBF

Quantity	Units	Scaling Relationship	Scaling Value
Length	L	Λ	0.6
Area	L^2	Λ^2	0.36
Section Modulus	L^3	Λ^3	0.22
Moment of Inertia	L^4	Λ^4	0.13
Stress	S	1	1
Force	F = S•L	Λ^2	0.36
Moment	F•L = S•L^2	Λ^3	0-22
Time	T	$\Lambda^{1/2}$	0.77
Acceleration	A = L/T^2	1	1
Velocity	V = L/T	$\Lambda^{1/2}$	0.77
Mass	F/A = S•L•T^2	Λ^2	0.36

To conduct analysis on the prototype structure, a representative model must be developed. The floor systems are assumed to be rigid in the horizontal plane. The inertial effects of the floor slab are assumed to be evenly distributed among the MRFs, and thus, each MRF accounts for one quarter of the seismic weight associated with each floor of the entire structure. The column bases are modeled as pinned and secured to the ground at the basement level. Since structural responses are considered only in the horizontal plane, the structure will be modeled a system composed of a MRF, DBF and a lean-on column (LC) joined with rigid links at each floor level (as shown in Figure 4.2). The LC represents the additional seismic mass and stiffness of the structure not present in the MRF and DBF.

Using OpenSEES (McKenna et al., 2006), a finite element model of the prototype structure is developed. Through a series of model reductions (boundary conditions, Ritz reductions for rigid slab assumptions, Guyan reductions for vertical/rotation DOF reductions, static condensation for the unused bracing DOF, etc.), a 3DOF model is distilled. Damping in the structure is assumed to 2%, and the natural frequencies for the model are 1.3, 4.0, and 8.2 Hz.

$$\boldsymbol{M_T} = \begin{bmatrix} \mathbf{102} & \mathbf{0.04} & \mathbf{0} \\ \mathbf{0.04} & \mathbf{102} & \mathbf{0.008} \\ \mathbf{0} & \mathbf{0.008} & \mathbf{74} \end{bmatrix} \left(\frac{\boldsymbol{kN * s^2}}{\boldsymbol{m}} \right)$$

$$C_T = \begin{bmatrix} 582 & -258 & 28 \\ -258 & 443 & -182 \\ 28 & -182 & 209 \end{bmatrix} \left(\frac{kN * s}{m}\right)$$

$$K_T = \begin{bmatrix} 1.68e5 & -1.04e5 & 2.26e4 \\ -1.04e5 & 1.29e5 & -5.07e4 \\ 2.26e4 & -5.07e4 & 3.14e4 \end{bmatrix} \left(\frac{kN}{m}\right)$$

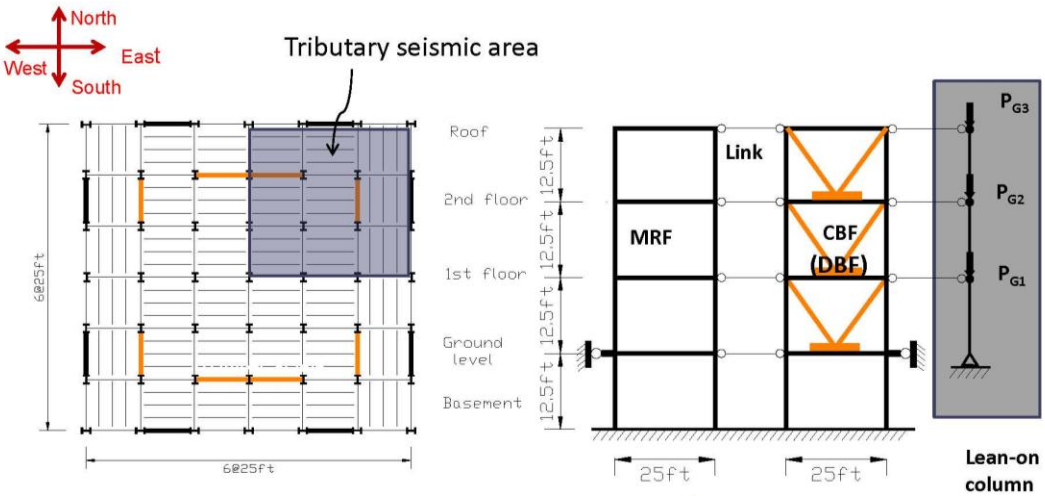

Figure 4.2: Prototype Test Structure

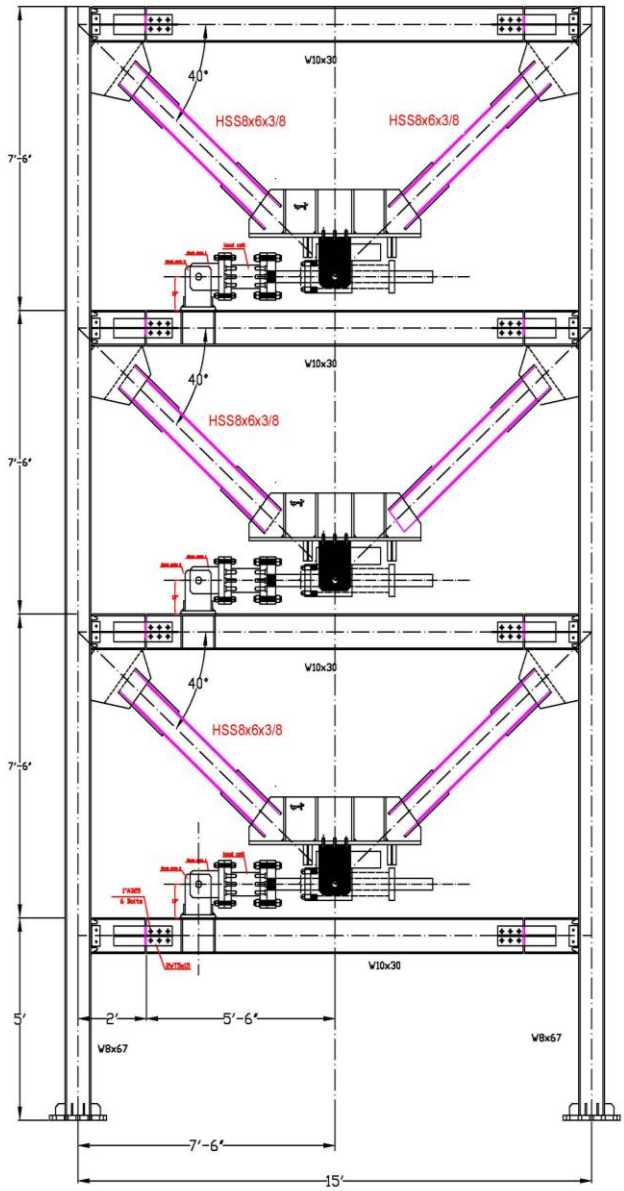

Figure 4.3: Scaled DBF Design Drawing

4.1.2 Testing Facility Description

At the NEES@Lehigh Real-Time Multi-Directional (RTMD) Large-scale testing facility (http://www.nees.lehigh.edu/), the RTHS setup (Figure 4.4) uses three actuators to displace the scaled prototype frame. The actuator attached to the first floor of the structure is a Servotest Systems Ltd. 2300 kN hydraulic actuator (designated as Actuator 4, Model # 200-1000-1700KN, Serial # 6173). This actuator is controlled by two three-stage servo-valves, built up from Servotest SV1200 servo valve and a Moog G772-204 pilot valve, rated at 550 gpm and designated as "F" and "G". The actuators attached to second and third floor are Servotest Systems Ltd. 1695 kN hydraulic actuators (designated as Actuator 2/3, Model # 200-1000-1250kN, Serial #s 6177/6176, respectively). Actuator 2 and 3 are controlled by three stage servo valves, identical to the first floor actuator (valves "C" and "D" control Actuator 2 and valve "E" controls Actuator 3). Each servo valve is connected to the hydraulic supply system (manufactured by Parker Hannifin Corp.) via a hydraulic service manifold (HSM). To control the actuator with displacement/force feedback, a Servotest Systems Ltd. DCS 2000 servocontroller is used. The servocontroller accepts commands from a 2203 1-channel servo drive card. The integration of the equations of motion for the analytical substructure and commands for the actuators are carried out using the xPC Target (Mathworks, 2012) real-time software.

A model, which includes the analytical substructure, required hardware/software drivers for interface with the physical substructure, etc. is constructed in SIMULINK (Figure 4.5) and compiled into an executable form. This code is transferred to a target computer to conduct the RTHS (Castaneda, 2012). Data acquisition is carried out using a DAS 6000 data acquisition system from Pacific Instruments Inc. (Model # 6000DAS, Serial # 6000s), with data logged as separate channels specified within the SIMULINK model.

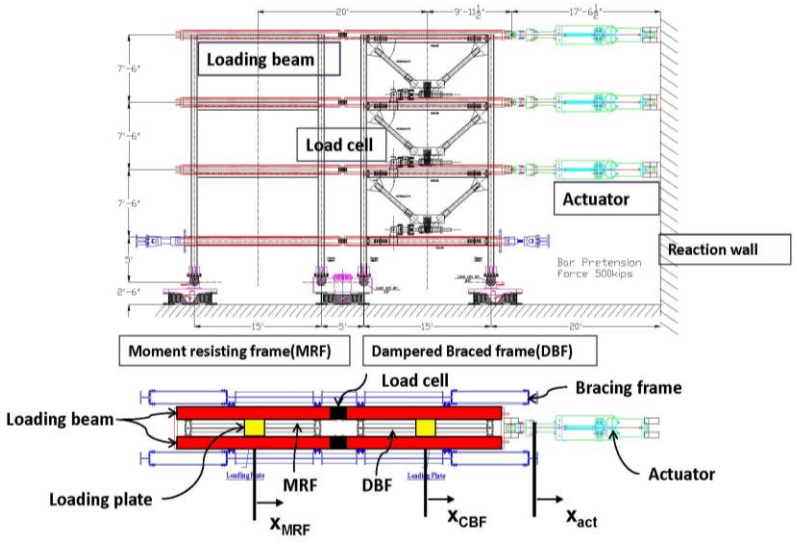

Figure 4.4: RTHS Test Schematic

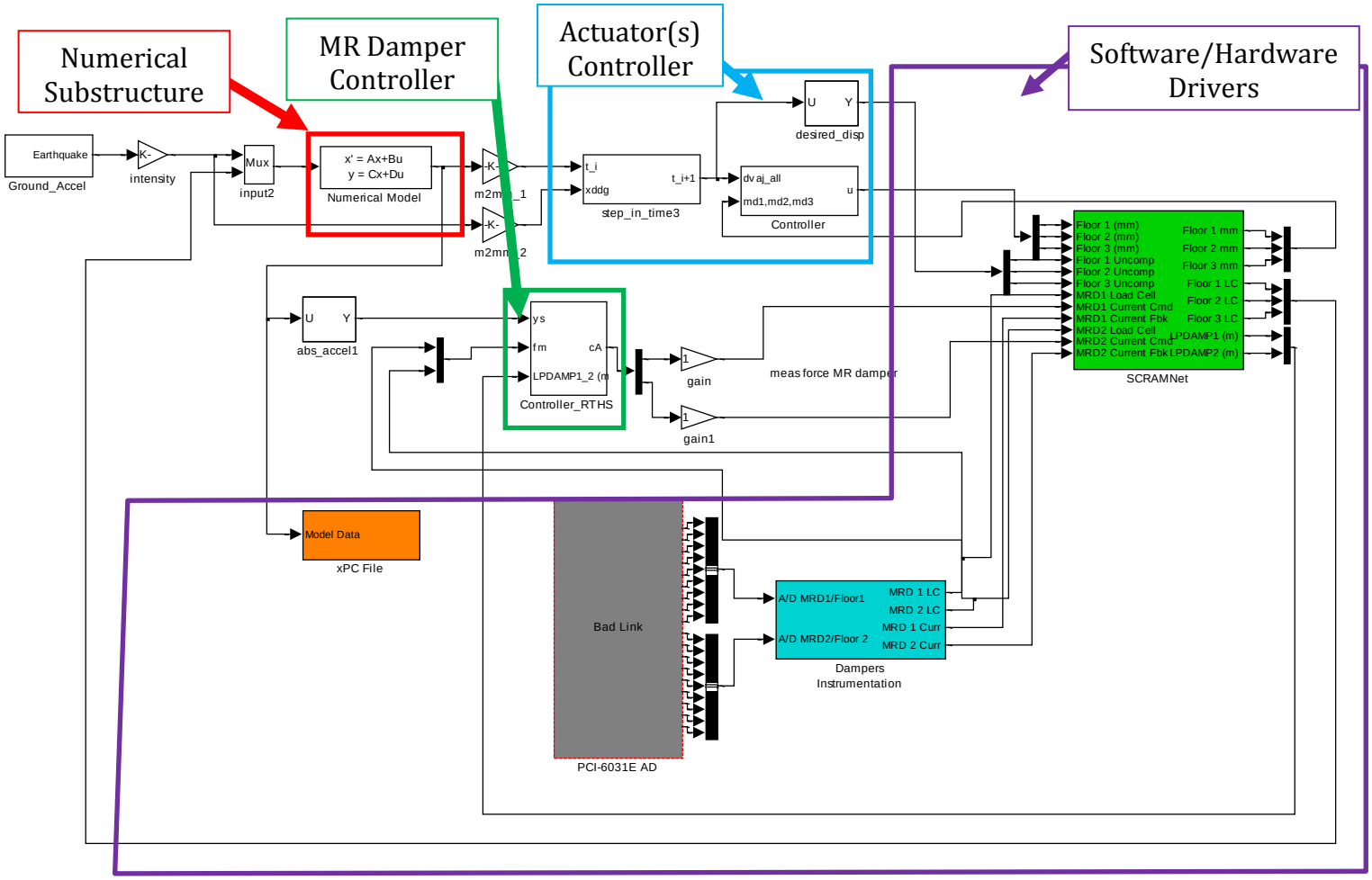

Figure 4.5: Example SIMULINK Model for Real-Time Hybrid Testing

A Scramnet system (SC150e) is used at the Lehigh NEES laboratory to facilitate shared memory between the various computers, allowing each computer to have access to all measurements and calculations needed to perform the test and acquire data.

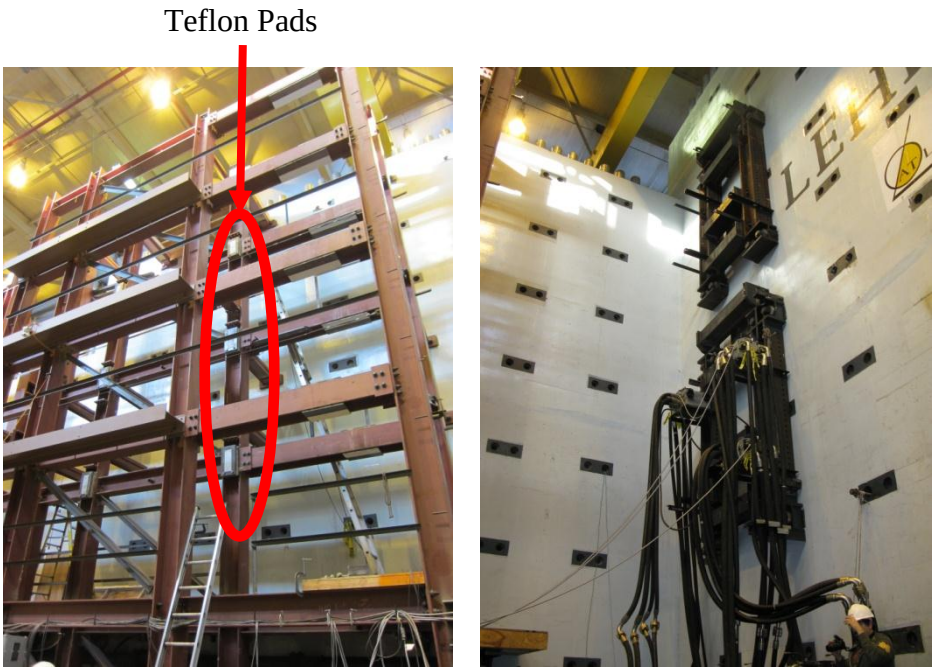

(a) **(b)**

Figure 4.6a-b: (a) Braced reaction frame and (b) Actuator mount for the concrete reaction wall

Within the testing facility, a concrete L-shaped reaction wall (measuring 15.2 m, at the highest point, and 1.5 m, at the thickest point, Figure 4.7) is used as the primary reaction surface for the three actuators and an actuator mount (Figure 4.6b) is used to lock the actuators to the reaction wall. The test specimen is mounted within a braced frame system (Figure 4.6a), consisting of two large-scale steel frames in parallel to each other. The system is constructed along the long side of the concrete reaction wall and is securely bolted to it, restraining the test specimen against unintended out-of-plane motion. To minimize friction between the test specimens and the braced frame, teflon pads are installed at various points for each floor.

Figure 4.7: NEES@Lehigh Testing Facility and Reaction Wall

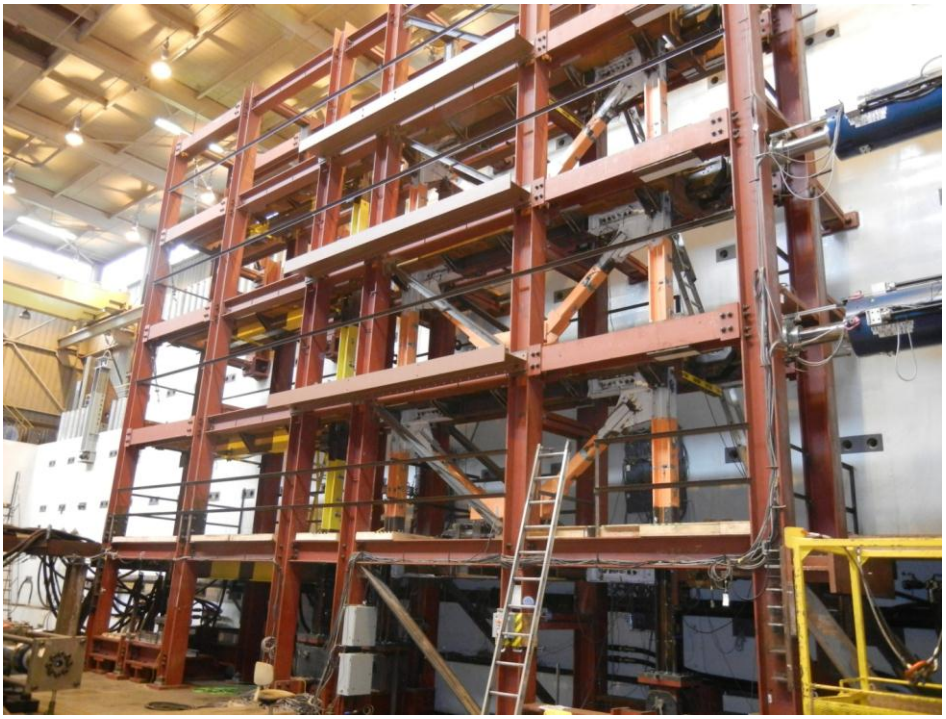

Figure 4.8: RTHS Large-scale Frame Testing Setup at Lehigh University

4.1.3. System Identification

This section considers the steps necessary to identify the physical substructures used in the RTHS, including the large-scale steel damped-braced frame (DBF), the 200 kN MR damper, and the actuator control system used to impose displacements on the steel frame.

4.1.3.1. Frame Identification

To successfully conduct the RTHS, it is necessary to identify the characteristics of the DBF constructed in the laboratory. Specifically, the structure as built in the laboratory will not have exactly the stiffness predicted using idealization and modeling assumptions. A stiffness matrix for the laboratory DBF must be identified.

Quasi-static testing is used to identify the stiffness of the frame and to evaluate individual frame components (Figure 4.9). In this approach, each floor is loaded individually while the two remaining floors are allowed to displace with no external force from the corresponding actuators. Experimental testing is performed with the frame in several different configurations, including actuators attached at single/multiple floor levels, rigid links attached/detached, MR damper installed in the frame, etc.

Using an OpenSEES analysis, the applied force in testing is determined to be half of the force necessary to induce yielding in the frame (for both attached/detached rigid links). This force level allows for most frame phenomena to occur and be cataloged while remaining low enough so as to not damage the frame. While a majority of the characterization testing utilizes actuators at every story, several additional tests are conducted with an actuator located at the specifically at the third floor, as loading the frame at this point engaged all of the T-section connections on the frame. Each test is sampled at 128 Hz, as the relatively low velocities produced sufficiently dense data plots.

For the DBF specimen used here, a three-by-three stiffness matrix, representing the lateral displacements of each floor level, is developed using data from a series of single-actuator tests.

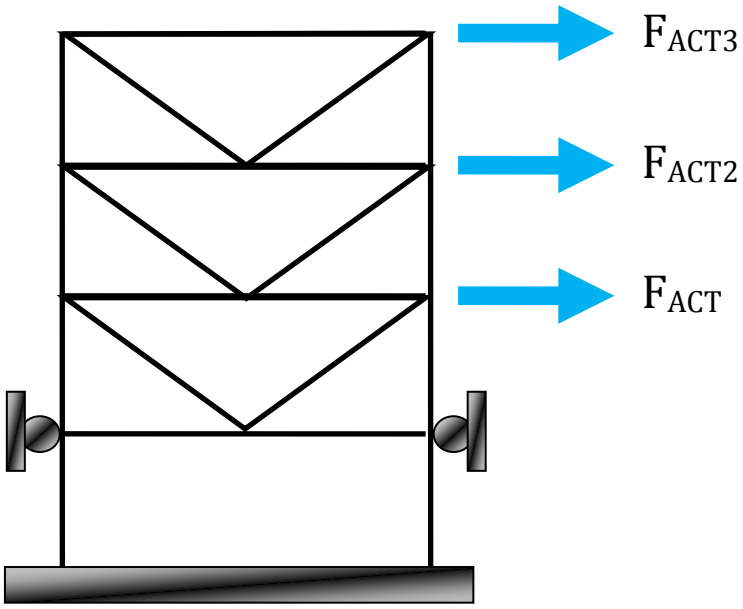

Figure 4.9: DBF Identification Diagram

The first step is finding the flexibility matrix of the structure. By plotting the displacement of each floor versus the applied load from the actuator, the flexibility coefficient for the floor/force combination (and corresponding matrix element) can be determined using the formula:

$$\boldsymbol{f_{ij}} = \frac{\Delta_{max} - \Delta_{min}}{\boldsymbol{F_{max}} - \boldsymbol{F_{min}}} \qquad \textbf{(4.1)}$$

where $\boldsymbol{f_{ij}}$ is the flexibility coefficient (i.e. the deformation at the i^{th} DOF due to a unit deformation at the j^{th} DOF), Δ_{max} is the maximum deformation, Δ_{min} is the minimum deformation, $\boldsymbol{F_{max}}$ is the maximum force, and $\boldsymbol{F_{min}}$ is the minimum force.

For any test that has a significant amount of hysteresis, an average slope is taken for both the loading and unloading curves, as shown in Figure 4.10. From a set of three tests, nine flexibility coefficients are determined and the 3x3 matrix can be formed. The symmetric stiffness matrix is then be calculated by inverting the flexibility matrix and averaging the off diagonal terms. Using MATLAB, the entire process was automated.

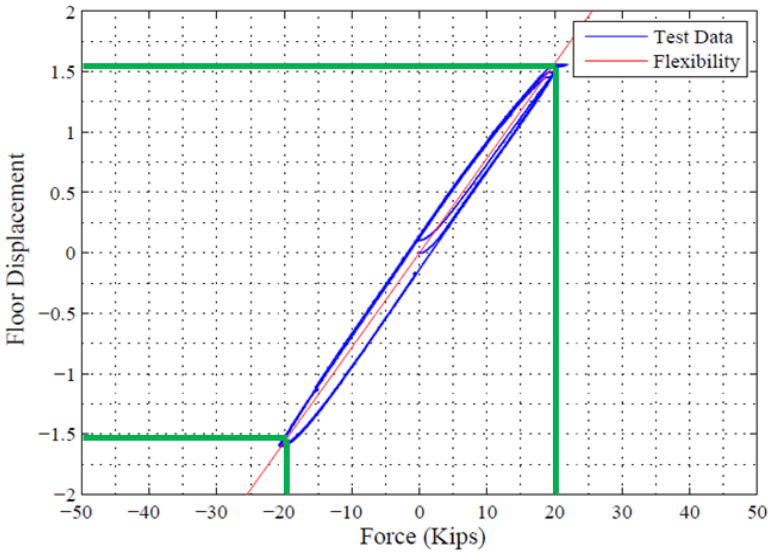

Figure 4.10: Flexibility determination from quasi-static test data

In addition to the experimentally-identified interstory stiffness for the physical DBF, the effective stiffness of each bracing system that houses the MR damper also needs to be identified to accurately model the structure. Through observations, it is clear that there is a differential between the displacement of the first floor of the DBF induced by the actuators and the displacement of the damper piston. This differential arises from several sources, including compliance within the clevis plate attachment to the MR damper and the imperfect rigidity with the resulting displacement/rotation of the beam representing the ground floor. Thus, the bracing system must be treated as an additional DOF, and the effective properties are identified to include the associated dynamics, as shown in Figure 4.11.

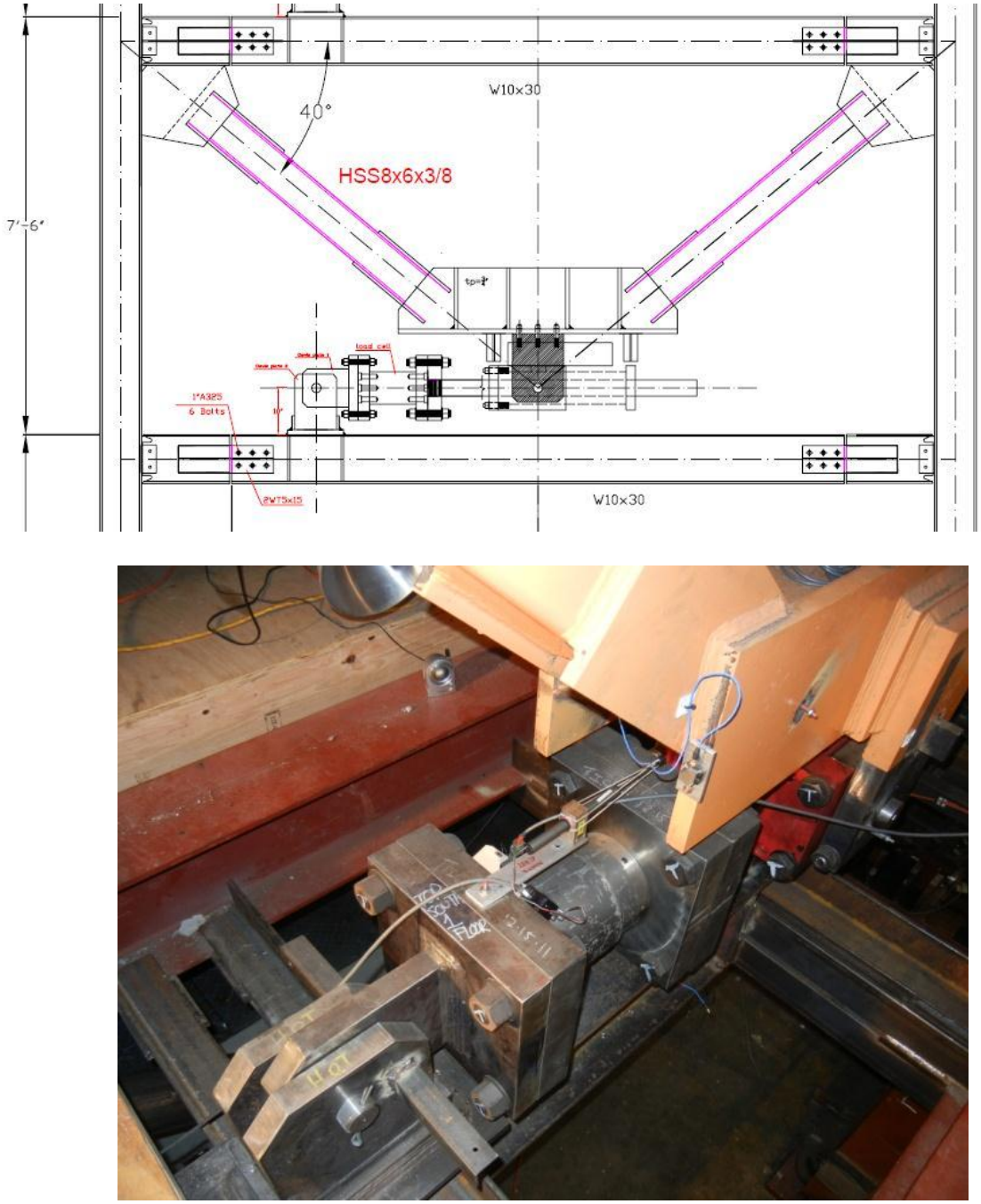

Figure 4.11: First Floor Bracing System in the DBF

Accurate modeling of this compliance is important for several reasons, including effective controller design. Due to the fact that control design is based on the model of the structure, if the model does not accurately reflect the actual structure, performance will suffer.

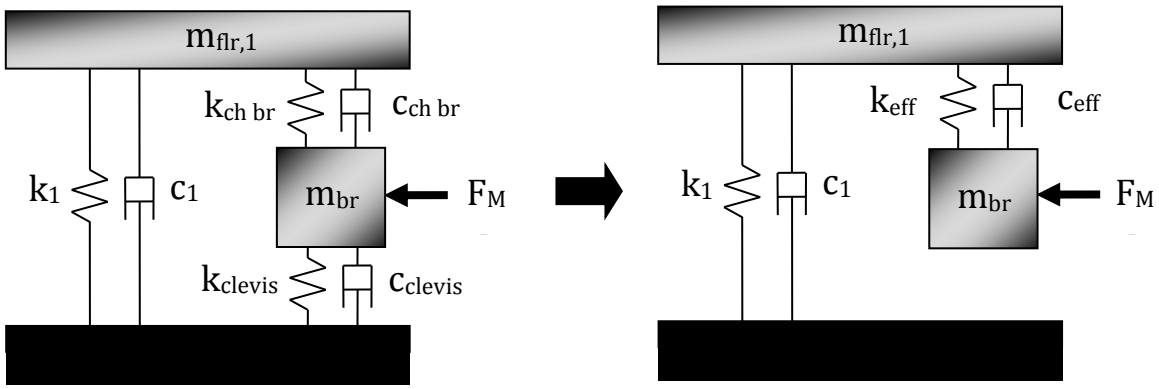

Figure 4.12: Modeling of the Bracing System

During various different tests, the displacement of the ground floor, the first floor, and the MR damper piston, as well as the force from the MR damper, are all measured. Using the assumption that

$$\boldsymbol{F_{MR} = k_{br} * x_{br}} \tag{4.2}$$

where $\boldsymbol{F_{MR}}$ is the measured damper force, $\boldsymbol{k_{br}}$ is the effective stiffness of the bracing system within the floor level and $\boldsymbol{x_{br}}$ is the effective displacement of the bracing system, as defined as

$$\boldsymbol{x_{br} = \left(x_{1,act} - x_{gr}\right) - x_{mr\ piston}} \tag{4.3}$$

where $\boldsymbol{x_{1,act}}$ is the measured displacement of the first floor actuator, $\boldsymbol{x_{gr}}$ is the measured ground floor displacement, and $\boldsymbol{x_{mr\ piston}}$ is the displacement of the MR damper piston. Substituting Eq. 4.3 into Eq. 4.2 and rearranging yields a solution for the effective bracing stiffness

$$\boldsymbol{k_{br} = F_{MR} \,/\, s_{(x_{1,act} - x_{gr}) - x_{mr\ piston}}} \tag{4.4}$$

Because $\boldsymbol{F_{MR}}$ and $\boldsymbol{x_{br}}$ are both vectors in time, the resulting stiffness is also computed at each time step during the test, as shown in Figure 4.13a.

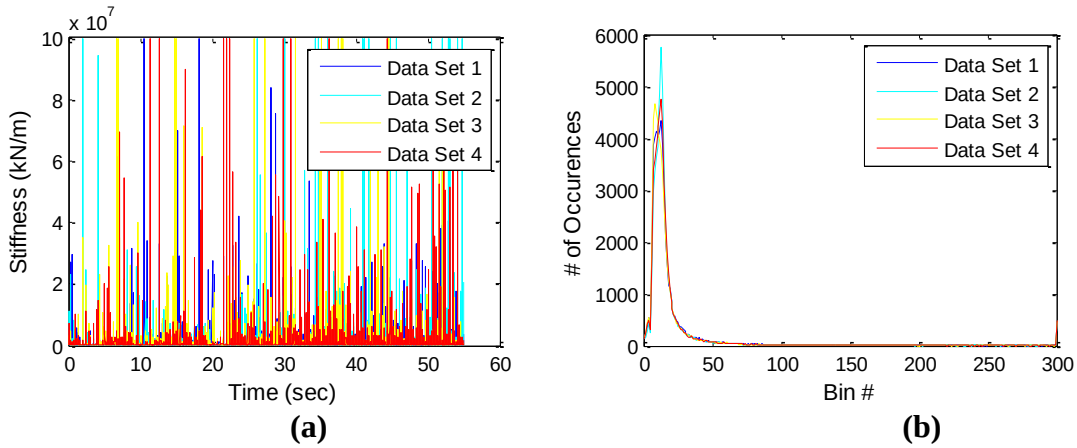

Figure 4.13a-b: (a) Bracing stiffness computed at each time step and (b) computed stiffness data histogram

To determine the appropriate stiffness value to represent the bracing at the floor, a histogram of the stiffness vector is plotted and the value with the highest occurrence is taken as the identified bracing stiffness value. Four sets of data are used to make this determination, and the histograms for each data set are shown in Figure 4.13b. Based on the histogram plot, the bracing stiffness is identified as 48,615 kN/m. The mass of the bracing system is estimated as 0.299 $\frac{kN*s^2}{m}$ based on the member sizes. The damping ratio for the bracing DOF is assumed to be 0.5%.

4.1.3.2. MR Damper Identification

To identify the parameters for the phenomenological Bouc Wen model, a series of tests is conducted using three different experimental 200 kN MR damper (Christenson et al. 2008, Jiang et al., 2011) at the Smart Structures Technology Lab (SSTL) at the University of Illinois – Urbana/Champaign and the Real-Time Multi-Directional (RTMD) Facility at the NEES@Lehigh Laboratory (Figure 4.14a-b).

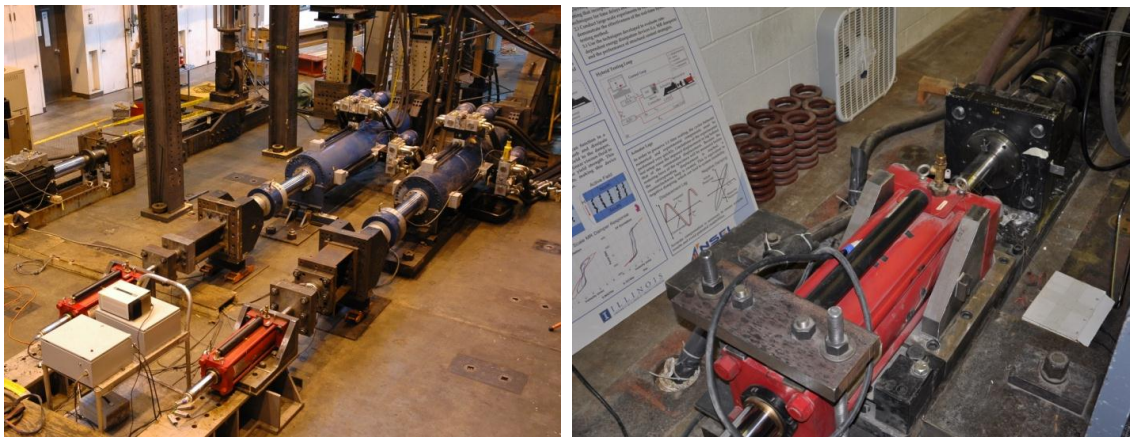

(a) **(b)**

Figure 4.14: Damper characterization testing setup at (a) Lehigh (Damper #1 and #2) and (b) UIUC (Damper #3)

A hydraulic actuator (125 kips at the SSTL Facility, 500 kips at the NEES@Lehigh Facility) is used to drive each of the dampers, and the damper displacement and force are measured. For each test, a sinusoidal displacement input, having a fixed amplitude and frequency, is applied to drive the MR damper by the actuator. A current input to the MR damper was held at various constant levels. A wide range of frequencies and current values were selected during testing, and the resulting experimental data was used to identify the parameters of the MR damper model. A constrained nonlinear optimization was performed using MATLAB to identify the needed model parameters from the experimental data. The parameters and a comparison of the analytical model and the experimental damper are summarized in Table 4.2 and Figure 4.15.

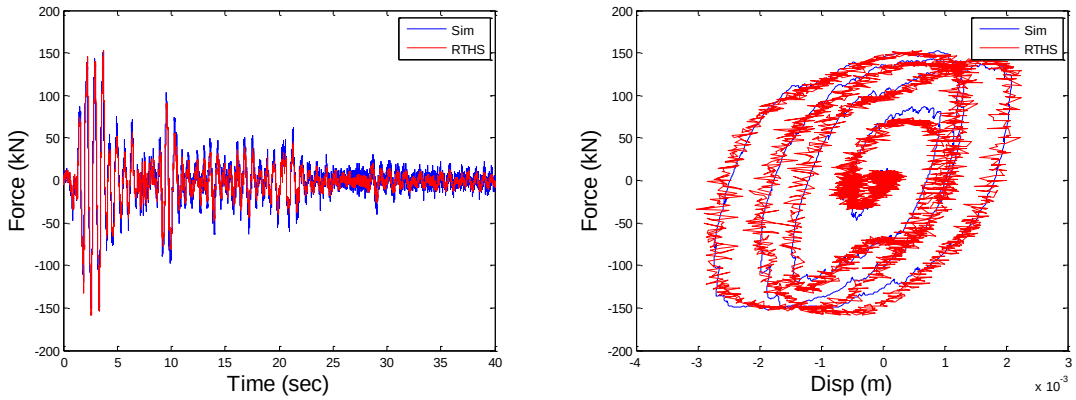

(a) **(b)**

Figure 4.15: Comparison of (a) force time history and (b) force vs. displacement for the experimental damper and the analytical model

Table 4.2: MR Damper model parameters

Parameter	Value	Parameter	Value
α_A	687.7 kN	c_{1A}	100 kN·sec/m
α_B	0.006 kN	c_{1B}	15000 kN·sec/m
α_C	-697.6 kN	k_0	0.0559 kN/m
α_D	-0.91 kN	k_1	0.0641 kN/m
c_{0A}	201.3 kN·sec/m	x_0	0.01 m
c_{0B}	0.113 kN·sec/m	β	3000 m^{-1}
c_{0C}	-109 kN·sec/m	γ	3000 m^{-1}
c_{0D}	-2.116 kN·sec/m	A	336.56
L_0	0.8 H	n	2
L	2 H	R	4.8 Ω

4.1.3.3. Actuator Motion Control

Another step for performing a successful RTHS is the design of the actuator motion control scheme (Phillips and Spencer, 2012; Gao et al., 2012). When multiple actuators are connected to the same specimen, the dynamics of the actuators become coupled through the specimen, leading to a complex control challenge (i.e., when an actuator applies a force to the structure, the other actuators will also experience this force; Phillips and Spencer 2012). Consider the input-output transfer function model $\mathbf{G}_{du}(s)$ of the linearized servo-hydraulic system, including the actuator, servo-valve, servo-controller, and specimen as represented in Figure 4.17 (Dyke et al. 1995). In this

diagram, ***u*** is the command vector, ***f*** is the force imparted by the actuator, and ***d*** is the displacement vector as realized by the actuator and specimen. The servo-hydraulic system contains inner-loop feedback control, which provides nominal tracking of ***u*** as measured by ***d***. However, this inner loop control alone is inadequate for actuator control to be successful in RTHS applications.

,

Fig 4.16: Actuator setup for RTHS at NEES@Lehigh facility

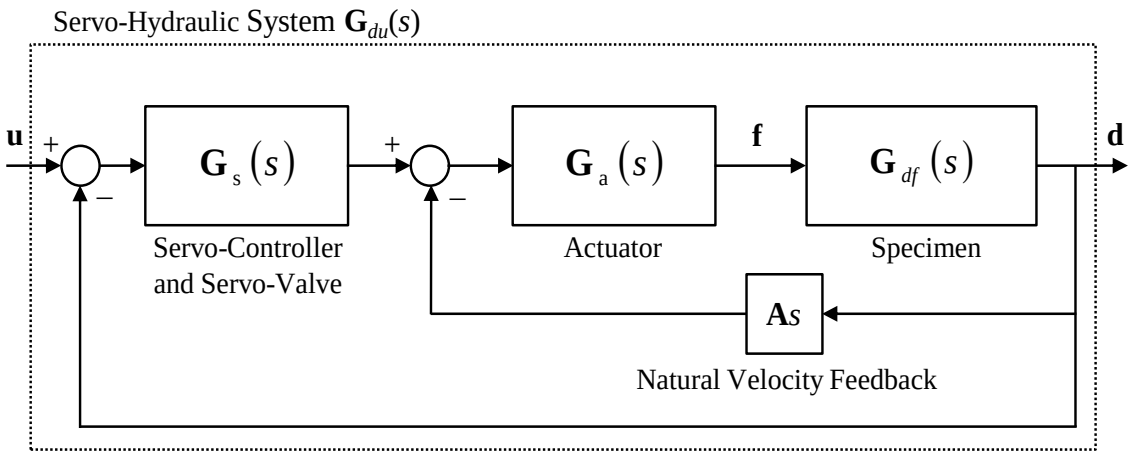

Figure 4.17: Servo-hydraulic system block diagram

The dynamics of the servo-controller and servo-valve, actuator, and specimen have been condensed into transfer functions $\mathbf{G}_{\mathrm{s}}(s)$, $\mathbf{G}_{\mathrm{a}}(s)$, and $\mathbf{G}_{df}(s)$, respectively. The parameter **A** represents the effective cross-sectional area of the actuator piston. The input-output transfer function can be written in the Laplace domain as:

$$\mathbf{G}_{du}(s) = \frac{\mathbf{D}(s)}{\mathbf{U}(s)} = \frac{\mathbf{G}_{\mathrm{s}}(s)\mathbf{G}_{\mathrm{a}}(s)\mathbf{G}_{df}(s)}{\mathbf{I} + (\mathbf{G}_{\mathrm{s}}(s) + \mathbf{A}s)\mathbf{G}_{\mathrm{a}}(s)\mathbf{G}_{df}(s)} \tag{4.5}$$

In multi-actuator systems, the servo-hydraulic components operate independently, thus $\mathbf{G}_{\mathrm{s}}(s)$, $\mathbf{G}_{\mathrm{a}}(s)$, and **A** are diagonal. The source of actuator coupling is the specimen, namely the off-diagonals of $\mathbf{G}_{df}(s)$.

In model-based control, an outer-loop controller is created to cancel the modeled dynamics of the servo-hydraulic system, including specimen dependency through the natural velocity feedback loop. This feedback leads to actuator coupling in the system. The model-based control approach used in this study is based on a linearized model of the servo-hydraulic system, as in Fig. 4.14.

The tracking error ***e*** is defined as the difference between the desired displacement vector ***r*** and measured displacement vector ***d***. Through regulator redesign, the tracking problem can be defined as a regulator problem about a setpoint. The resulting model-based controller, incorporating both feedforward and feedback links, is represented in Fig. 4.15. The servo-hydraulic system of Fig. 4.15 has been condensed to show the details of the model-based controller, which acts as an outer-loop controller around the system.

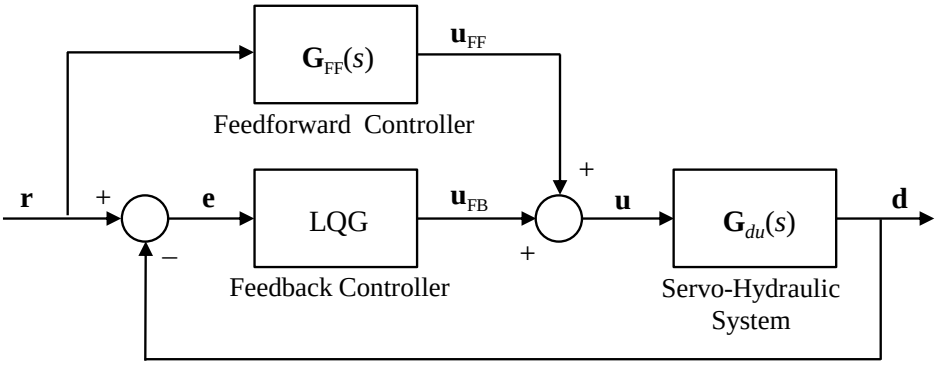

Figure 4.18: Model-based actuator control with feedforward and feedback links

The feedforward controller is designed to cancel the modeled dynamics of the servo-hydraulic system. Placed in series with the servo-hydraulic system, the inverse of the servo-hydraulic system model will serve as the feedforward controller:

$$\mathbf{G}_{\mathrm{FF}}(s)=\mathbf{G}_{xu}(s)^{-1}=\frac{\mathbf{U}_{\mathrm{FF}}(s)}{\mathbf{X}^{\mathrm{I}}(s)}=\mathbf{I}+\mathbf{G}_{xu}(s)^{-1}\mathbf{G}_{\mathrm{a}}(s)^{-1}\mathbf{G}_{\mathrm{s}}(s)^{-1}+\mathbf{A}s\mathbf{G}_{\mathrm{s}}(s)^{-1} \quad \textbf{(4.6)}$$

In the presence of changing specimen conditions, modeling errors, nonlinearities, and disturbances, feedback control can be applied to reduce further the tracking error. Evoking the separation principal, an LQG controller can be designed from independent LQR and Kalman filter designs (Stengel, 1986). The feedback controller is designed based on a state space representation of Eq.4.13.

In the case that the parameters of the servo-hydraulic system are unknown, nonparametric system identification can be used to obtain the servo-hydraulic system transfer function model of Eq. 4.13 and the inverse model of Eq. 4.14. The process includes experimentally determining the servo-hydraulic system transfer function from input command to measured displacement and subsequently fitting the data to a model. The details of model-based control strategy are found in Phillips and Spencer (2011), and are extended to multi-actuator systems in Phillips and Spencer (2012).

4.2. RTHS Implementation

In this section, the implementation of the RTHS is discussed. The prototype system is broken down into the physical and analytical components following the RTHS convention presented in Chapter 2. The total scaled prototype structure is represented by the following mass, damping and stiffness matrices:

$$\boldsymbol{M_T} = \begin{bmatrix} \mathbf{102} & \mathbf{0} & \mathbf{0} & \mathbf{0} \\ \mathbf{0} & \mathbf{102} & \mathbf{0} & \mathbf{0} \\ \mathbf{0} & \mathbf{0} & \mathbf{74} & \mathbf{0} \\ \mathbf{0} & \mathbf{0} & \mathbf{0} & \mathbf{0.299} \end{bmatrix} \left(\frac{\boldsymbol{kN * s^2}}{\boldsymbol{m}}\right)$$

$$\boldsymbol{C_T} = \begin{bmatrix} \mathbf{385} & \mathbf{-158} & \mathbf{11.2} & \mathbf{-76.1} \\ \mathbf{-158} & \mathbf{328} & \mathbf{-178} & \mathbf{-42.4} \\ \mathbf{11.2} & \mathbf{-178} & \mathbf{164} & \mathbf{5.02} \\ \mathbf{76.1} & \mathbf{-42.4} & \mathbf{5.02} & \mathbf{57.8} \end{bmatrix} \left(\frac{\boldsymbol{kN * s}}{\boldsymbol{m}}\right)$$

$$\boldsymbol{K_T} = \begin{bmatrix} \mathbf{1.89e5} & \mathbf{-9.50e4} & \mathbf{1.89e3} & \mathbf{-4.86e4} \\ \mathbf{-9.50e4} & \mathbf{1.29e5} & \mathbf{-5.08e4} & \mathbf{0} \\ \mathbf{1.89e4} & \mathbf{-5.08e4} & \mathbf{3.14e4e4} & \mathbf{0} \\ \mathbf{-4.86e4} & \mathbf{0} & \mathbf{0} & \mathbf{4.86e4} \end{bmatrix} \left(\frac{\boldsymbol{kN}}{\boldsymbol{m}}\right)$$

The 4DOF characteristic matrices, representing the DBF as the physical substructure in the RTHS using the identified and estimated parameters, are defined as:

$$\boldsymbol{M_P} = \begin{bmatrix} \mathbf{3.15} & \mathbf{0} & \mathbf{0} & \mathbf{0} \\ \mathbf{0} & \mathbf{3.15} & \mathbf{0} & \mathbf{0} \\ \mathbf{0} & \mathbf{0} & \mathbf{3.15} & \mathbf{0} \\ \mathbf{0} & \mathbf{0} & \mathbf{0} & \mathbf{0.299} \end{bmatrix} \left(\frac{\boldsymbol{kN * s^2}}{\boldsymbol{m}}\right)$$

$$\boldsymbol{C_P} = \begin{bmatrix} \mathbf{161} & \mathbf{-59.3} & \mathbf{3.38} & \mathbf{-76.1} \\ \mathbf{-59.3} & \mathbf{152} & \mathbf{-53.2} & \mathbf{-42.4} \\ \mathbf{3.38} & \mathbf{-53.2} & \mathbf{80.5} & \mathbf{5.02} \\ \mathbf{76.1} & \mathbf{-42.4} & \mathbf{5.02} & \mathbf{57.8} \end{bmatrix} \left(\frac{\boldsymbol{kN * s}}{\boldsymbol{m}}\right)$$

$$\boldsymbol{K_P} = \begin{bmatrix} \mathbf{1.09e5} & \mathbf{-3.87e4} & \mathbf{9.37e3} & \mathbf{-4.86e4} \\ \mathbf{-3.87e4} & \mathbf{4.75e4} & \mathbf{-2.00e4} & \mathbf{0} \\ \mathbf{9.37e3} & \mathbf{-2.00e4} & \mathbf{1.23e4} & \mathbf{0} \\ \mathbf{-4.86e4} & \mathbf{0} & \mathbf{0} & \mathbf{4.86e4} \end{bmatrix} \left(\frac{\boldsymbol{kN}}{\boldsymbol{m}}\right)$$

Similarly, the 4DOF characteristic matrices representing the analytical substructure in the RTHS (the rest of the structure not represented by the DBF) are defined as:

$$\boldsymbol{M_N} = \begin{bmatrix} \mathbf{98.1} & \mathbf{0} & \mathbf{0} & \mathbf{0} \\ \mathbf{0} & \mathbf{98.1} & \mathbf{0} & \mathbf{0} \\ \mathbf{0} & \mathbf{0} & \mathbf{70.8} & \mathbf{0} \\ \mathbf{0} & \mathbf{0} & \mathbf{0} & \mathbf{0} \end{bmatrix} \left(\frac{\boldsymbol{kN * s^2}}{\boldsymbol{m}}\right)$$

$$C_N = \begin{bmatrix} 224.4 & -100 & 3.8 & 0 \\ -100 & 175.5 & -80.9 & 0 \\ 3.8 & -80.9 & 83.5 & 0 \\ 0 & 0 & 0 & 0 \end{bmatrix} \left(\frac{kN * s}{m}\right)$$

$$K_N = \begin{bmatrix} 7.97e4 & -5.62e4 & 9.49e3 & 0 \\ -5.62e4 & 8.16e4 & -3.08e4 & 0 \\ 9.49e3 & -3.08e4 & 1.91e4 & 0 \\ 0 & 0 & 0 & 0 \end{bmatrix} \left(\frac{kN}{m}\right)$$

The fourth row and column of each matrix correspond to the 4th DOF of the system, which is the first floor bracing system. Because the bracing is entirely physical, each matrix has a row and column consisting of zeros to account for this DOF. In the RTHS, these rows and columns are eliminated before constructing a SS model representing the analytical substructure.

4.3. Experimental Results

In this section, the results from the RTHS evaluation of the controllers are presented and evaluated. The controllers considered for the MR damper are listed and discussed. Two separate types of experimental testing are conducted: (1) evaluation/ validation of large-scale RTHS testing and (2) evaluation/validation of MR damper controller performance. The MR damper controller performances are evaluated under two conditions: (1) performance under general earthquake excitation, using seismic inputs of varying magnitudes, and (2) robust performance in the face of uncertainties in the structural system. The uncertainties are manifested by varying the mass of the structure in several increments.

4.3.1. Considered Control Approaches

Passive On Control (PON)

The first method for control used in this study places the MR damper in a passive state, where the voltage is held at a constant level, regardless of the building response. Designated as *Passive On (PON)* control, the command voltage to the MR damper is held at the maximum operational level, 2.5 V.

Clipped Optimal Control (COC)

The second control approach, designated as *Clipped Optimal Control (COC)*, was proposed by Dyke (1996). This controller combines an LQG regulator with a control law to select the proper voltage level, v_i and has been shown to be effective when used in conjunction with MR dampers. The control law for COC can be written as

$$\boldsymbol{v_i = V_{max} H(\{f_{ci} - f_i\} f_i)} \quad \textbf{(4.7)}$$

where $\boldsymbol{V_{max}}$ is the maximum voltage applied to the current driver (2.5 volts) and $\boldsymbol{H}(\cdot)$ is the Heaviside step function.

Over-Driven Clipped Optimal Control (ODCOC)

The third controller utilized in this study is the ODCOC, as previously discussed in Chapter 3. This control approach consists of two parts: an linear quadratic Gaussian (LQG) regulator used to determine an optimal restoring force to be applied the structure (as described previously), and a control law incorporating the concepts of over-/back-driving which is designed to select an appropriate voltage to be applied to the damper. With over-/back-driving, the operating range of the damper is extended. As previously shown, incorporating these features into the controller has led to an increase in the ability to track a desired force trajectory in large-scale devices.

4.3.2 RTHS Validation

To validate the RTHS testing, a comparison of test results for a RTHS test and an equivalent numerical simulation is made. In both cases, tests using the 3-story prototype structure with a single MR damper in the first floor (ODCOC control) are performed. The RTHS utilizes a time step of 1/1024 seconds, with a linear state-space model for the analytical substructure and a Runga-Kutta numerical solver. Model-based feedforward-feedback control was utilized for all actuators. To validate the RTHS method, the global responses of the structure are compared as time histories.

Figures 4.20 and 4.21 show the comparison of several structural responses, including the 1st floor displacement, velocity, and acceleration, for numerical simulation and RTHS. From these figures, it is clear that the RTHS simulation compares very well with the numerical simulation.

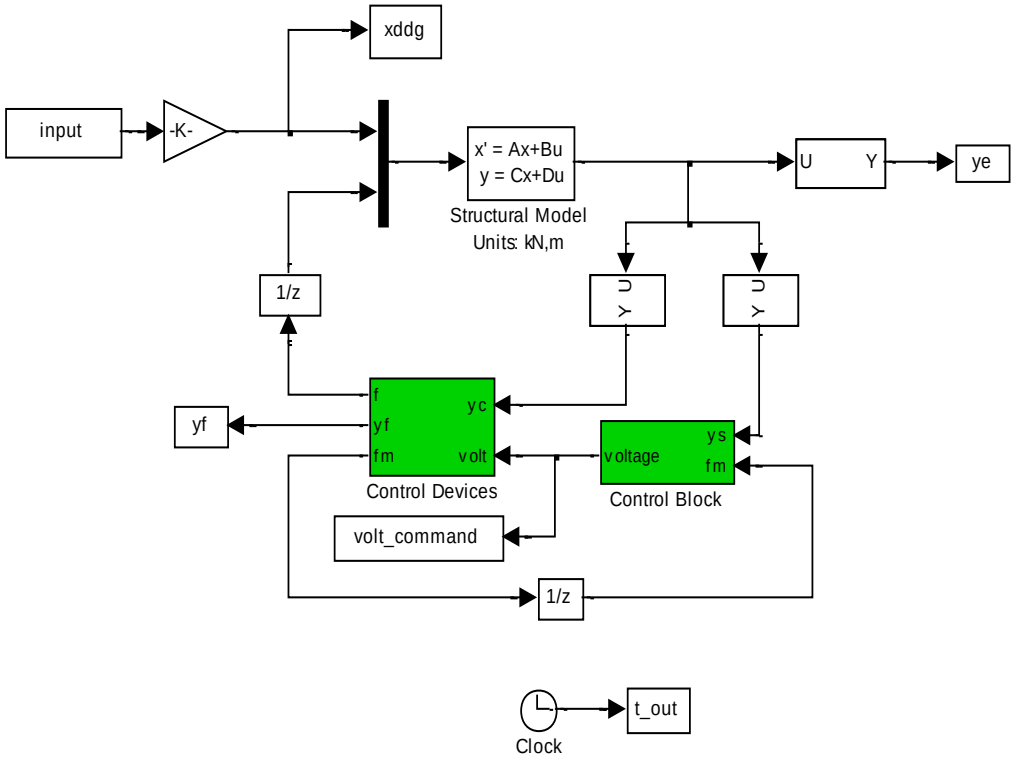

Figure 4.19: SIMULINK model for numerical simulation

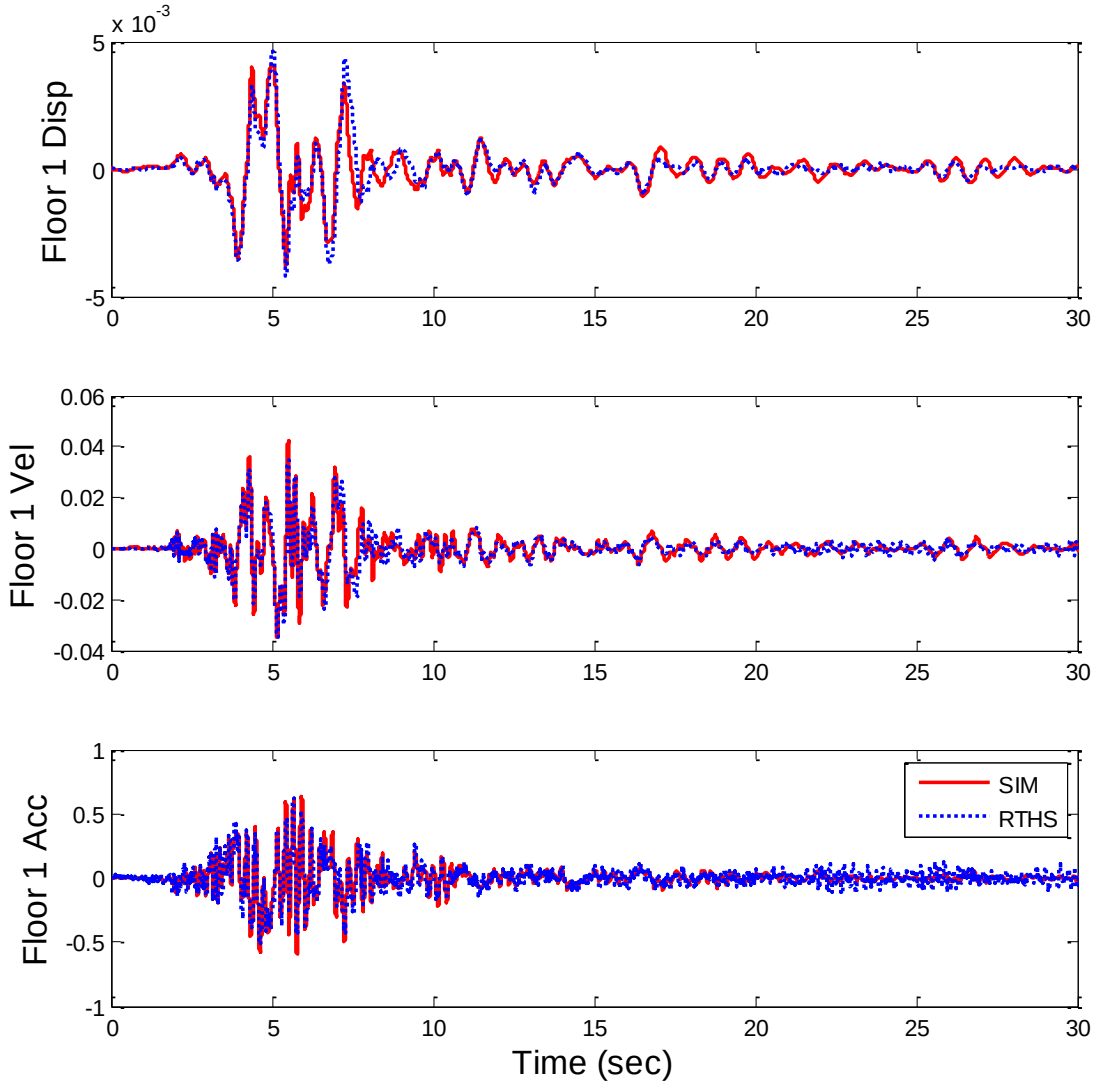

Figure 4.20: Time History Comparison of Simulation/RTHS Structure Responses

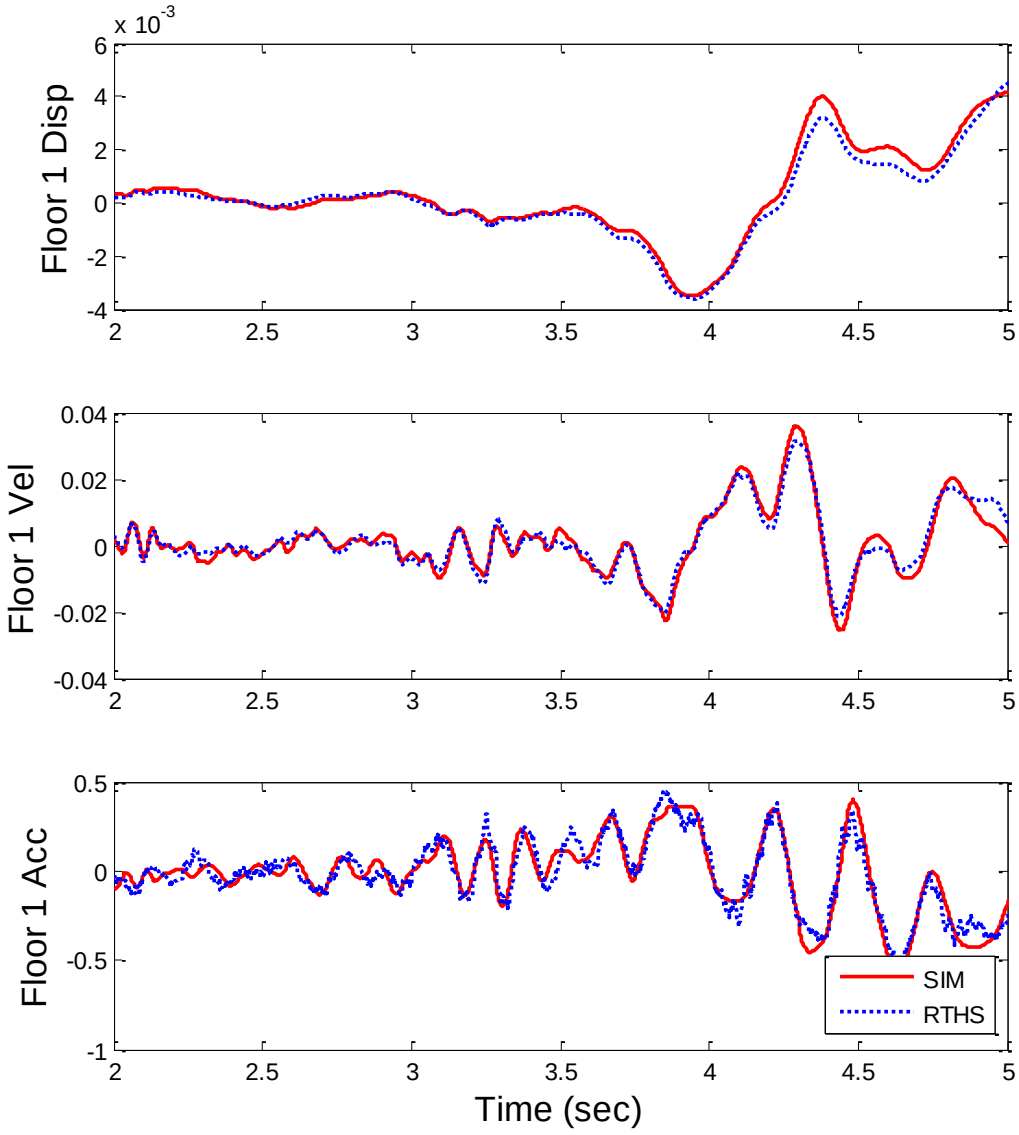

Figure 4.21: Time History Comparison of Simulation/RTHS Structure Responses

4.3.3 MR Damper Controller Evaluation

To validate the MR damper controller performance, a RTHS test using the 3-story prototype structure equipped with a single damper is used. As before, the RTHS utilizes a time step of 1/1024 seconds, with a linear state-space model for the analytical substructure, a Runga-Kutta numerical solver, and model-based feedforward-feedback control for all actuators. The large-scale steel frame equipped with a single MR damper between the ground and 1st floor is used as the experimental substructure. The rest of the prototype structure (the portion of mass, damping, and stiffness not accounted for with the steel frame) is modeled as the analytical substructure, using a linear, finite element-based 3DOF model.

4.3.3.1. Evaluation Criteria

To evaluate the efficiency of the proposed controllers, several input excitations, $\ddot{x}_g$, are used in simulation, including: (i) *SAC Small I Earthquake*, (ii) *SAC II Small Earthquake*, (iii) the NS component of the 1940 *El Centro* Earthquake, (iv) *SAC Medium I Earthquake*, (v) the *Superstition Hills Earthquake*, and (vi) *SAC Large Earthquake.* The SAC ground motions are generated time histories for use in topical investigations, case studies, and trial applications in the SAC Phase 2 Steel Project (Los Angeles area, corresponding to seismic Zone 4). Due to safety limitations of the frame, the maximum applied interstory drift was limited to 1% of the story height, or 23 mm. Thus, each earthquake was scaled to 50% intensity, to maintain this limitation. In addition, as a 0.6-scaled model of the frame is being tested, each SAC ground motion (designed for use with another structure) is scaled appropriately in time, by a factor of $\sqrt{0.6}$.

Focusing on global structural performance, the controller evaluation criteria are divided into two categories: peak responses and RMS responses. Since most criteria are normalized with respect to the uncontrolled simulation value (no uncontrolled RTHS testing was performed, so the uncontrolled simulation results are used as the basis of comparison for both controlled numerical simulation and RTHS), in general, smaller values for the evaluation measures are indicative of better performance. A summary of these criteria is presented in Table 4.3.

Table 4.3: Controller Evaluation Criteria

J Value	Equation	Description	J Value	Equation	Description
$\mathbf{J_1}$	$max_{EQ}\left\{\frac{\max_{t,i}\lvert x_i(t)\rvert}{x^{max}}\right\}$	Peak Floor Displacement Ratio of controlled maximum relative displacement to the uncontrolled value	$\mathbf{J_5}$	$max_{EQ}\left\{\frac{\max_{t,i}\lvert x_{RMS_i}(t)\rvert}{x_{RMS}{}^{max}}\right\}$	RMS Floor Displacement Ratio of controlled root mean square relative displacement to the uncontrolled value
$\mathbf{J_2}$	$max_{EQ}\left\{\frac{\max_{t,i}\frac{\lvert d_i(t)\rvert}{h_i}}{d_n^{max}}\right\}$	Peak Interstory Drift Ratio of controlled maximum interstory drift to the uncontrolled value	$\mathbf{J_6}$	$max_{EQ}\left\{\frac{\max_{t,i}\frac{\lvert d_{RMS_i}(t)\rvert}{h_i}}{d_{RMS_n}{}^{max}}\right\}$	RMS Interstory Drift Ratio of controlled root mean square interstory drift to the uncontrolled value
$\mathbf{J_3}$	$max_{EQ}\left\{\frac{\max_{t,i}\lvert \ddot{x}_{ai}(t)\rvert}{\ddot{x}_a^{max}}\right\}$	Peak Floor Acceleration Ratio of controlled maximum absolute acceleration to the uncontrolled value	$\mathbf{J_7}$	$max_{EQ}\left\{\frac{\max_{t,i}\lvert \ddot{x}_{RMS_{ai}}(t)\rvert}{\ddot{x}_{RMS_a}{}^{max}}\right\}$	RMS Floor Acceleration Ratio of controlled maximum absolute acceleration to the uncontrolled value
$\mathbf{J_4}$	$max_{EQ}\left\{\max_{t,i}\lvert f^i(t)\rvert\right\}$	Peak Control Force Ratio of the maximum device output force to the weight of the structure	$\mathbf{J_8}$	$max_{EQ}\left\{\max_{t,i}\lvert f_{RMS}{}^i(t)\rvert\right\}$	RMS Control Force Ratio of the maximum device output force to the weight of the structure

Table 4.4: Comparison of Simulation/RTHS Results for various ground motions

Ground Motion	Controller		Evaluation Criteria							
			J1	J2	J3	J4 (kN)	J5	J6	J7	J8 (kN)
SAC Small EQ I PGA - 0.15 g	PON	Simulation	1.087	1.448	1.744	130	1.312	1.554	1.702	23
		RTHS	0.975	1.383	1.504	136	1.097	1.318	1.484	21
	COC	Simulation	1.045	1.180	**1.287**	**79**	1.091	1.215	1.303	**13**
		RTHS	0.937	0.989	0.987	**77**	0.892	0.973	1.366	12
	ODCOC	Simulation	**0.976**	**1.146**	1.351	99	**1.089**	**1.207**	**1.298**	14
		RTHS	**0.884**	**0.938**	**0.953**	78	**0.889**	**0.954**	**1.295**	**11**
SAC Small EQ II PGA - 0.325 g	PON	Simulation	0.638	0.697	0.872	158	0.657	0.787	0.918	42
		RTHS	**0.643**	**0.737**	0.870	162	0.607	0.727	0.813	41
	COC	Simulation	0.666	0.696	0.706	**120**	**0.624**	**0.698**	**0.786**	**28**
		RTHS	0.715	0.762	0.749	**145**	**0.596**	**0.638**	**0.669**	**26**
	ODCOC	Simulation	**0.616**	**0.652**	**0.672**	123	0.630	0.703	0.791	29
		RTHS	0.723	0.768	**0.745**	146	0.610	0.649	0.672	26
El Centro PGA - 0.3 g	PON	Simulation	0.725	0.753	0.977	168	0.641	0.762	0.911	40
		RTHS	**0.729**	0.820	0.932	182	**0.620**	0.745	0.822	39
	COC	Simulation	0.726	0.723	0.795	**126**	0.632	0.706	**0.807**	**28**
		RTHS	0.744	0.704	0.734	**154**	0.628	0.687	0.705	**27**
	ODCOC	Simulation	**0.670**	**0.685**	**0.759**	172	**0.619**	**0.701**	0.811	30
		RTHS	0.740	**0.701**	**0.681**	180	0.622	**0.680**	**0.695**	**27**
SAC Medium EQ I PGA - 0.5 g	PON	Simulation	**0.630**	**0.653**	1.078	166	**0.576**	0.677	0.790	33
		RTHS	**0.659**	**0.724**	1.078	179	**0.594**	0.704	0.774	34
	COC	Simulation	0.651	0.698	0.973	**124**	0.597	0.649	0.723	**22**
		RTHS	0.687	0.754	0.973	**156**	**0.621**	**0.666**	**0.679**	**22**
	ODCOC	Simulation	0.647	0.693	**0.939**	158	0.591	**0.643**	**0.717**	**22**
		RTHS	0.692	0.754	**0.939**	155	0.633	0.679	0.692	**22**
SSH (DBE) PGA - 0.75 g	PON	Simulation	**0.471**	0.571	0.885	173	**0.495**	0.593	0.735	50
		RTHS	**0.525**	**0.621**	0.862	185	**0.509**	**0.618**	**0.694**	50
	COC	Simulation	0.535	0.572	0.783	**139**	0.539	0.597	**0.691**	**35**
		RTHS	0.686	0.804	0.862	**182**	0.651	0.709	0.711	**35**
	ODCOC	Simulation	0.478	**0.536**	**0.782**	184	0.515	**0.587**	0.697	40
		RTHS	0.681	0.799	**0.847**	211	0.649	0.711	0.711	37
SAC Large EQ I PGA - 1 g	PON	Simulation	0.924	1.029	1.155	190	0.811	0.959	1.115	43
		RTHS	0.914	1.110	1.125	198	0.797	0.959	1.022	43
	COC	Simulation	0.906	**0.916**	0.976	**144**	0.807	0.895	**0.994**	**30**
		RTHS	0.857	**0.965**	0.890	**152**	**0.729**	**0.817**	**0.852**	**25**
	ODCOC	Simulation	**0.902**	0.933	**0.953**	198	**0.781**	**0.891**	1.019	34
		RTHS	**0.845**	0.991	**0.879**	176	0.737	0.827	0.859	**25**

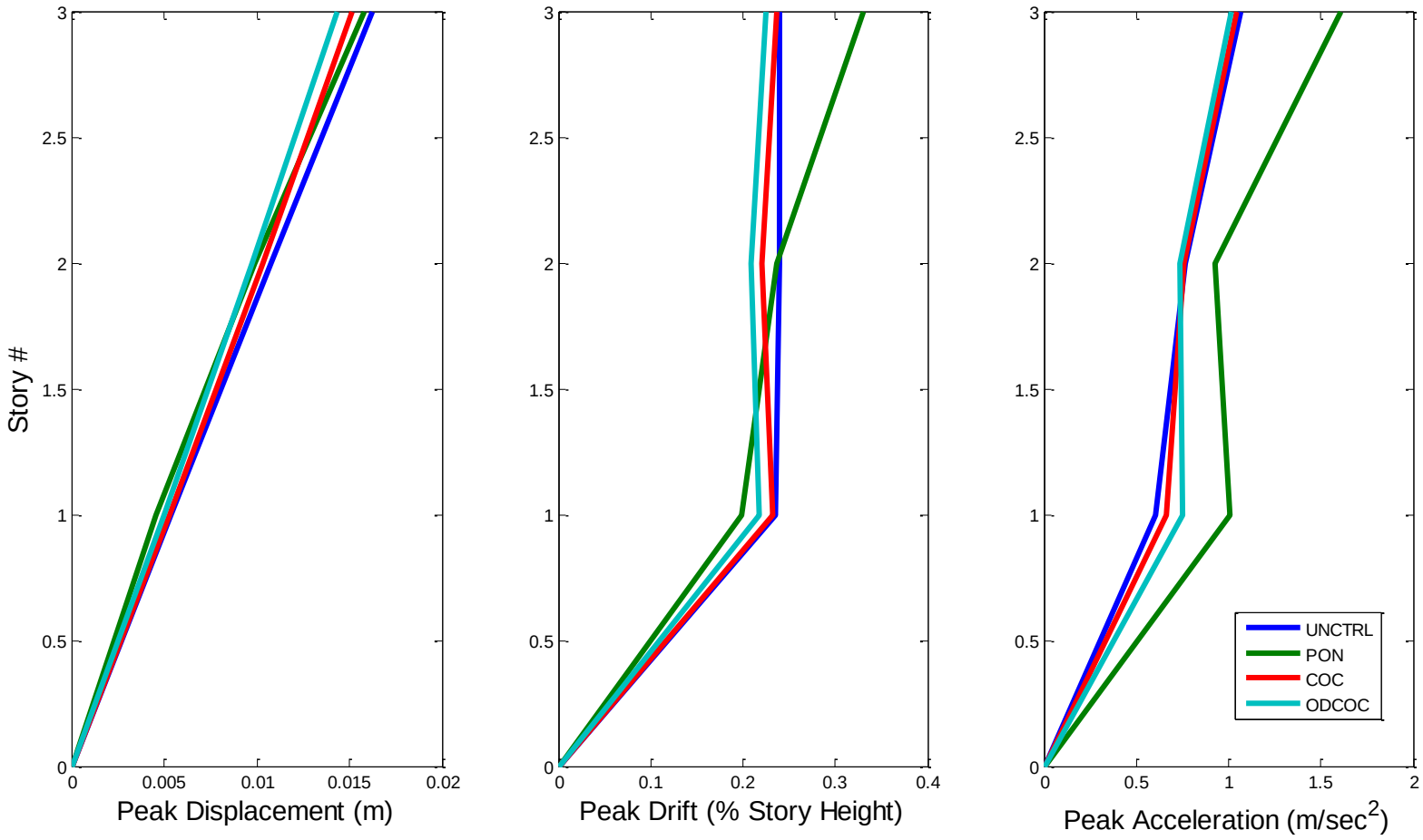

Figure 4.22: Response profiles for SAC Small EQ I

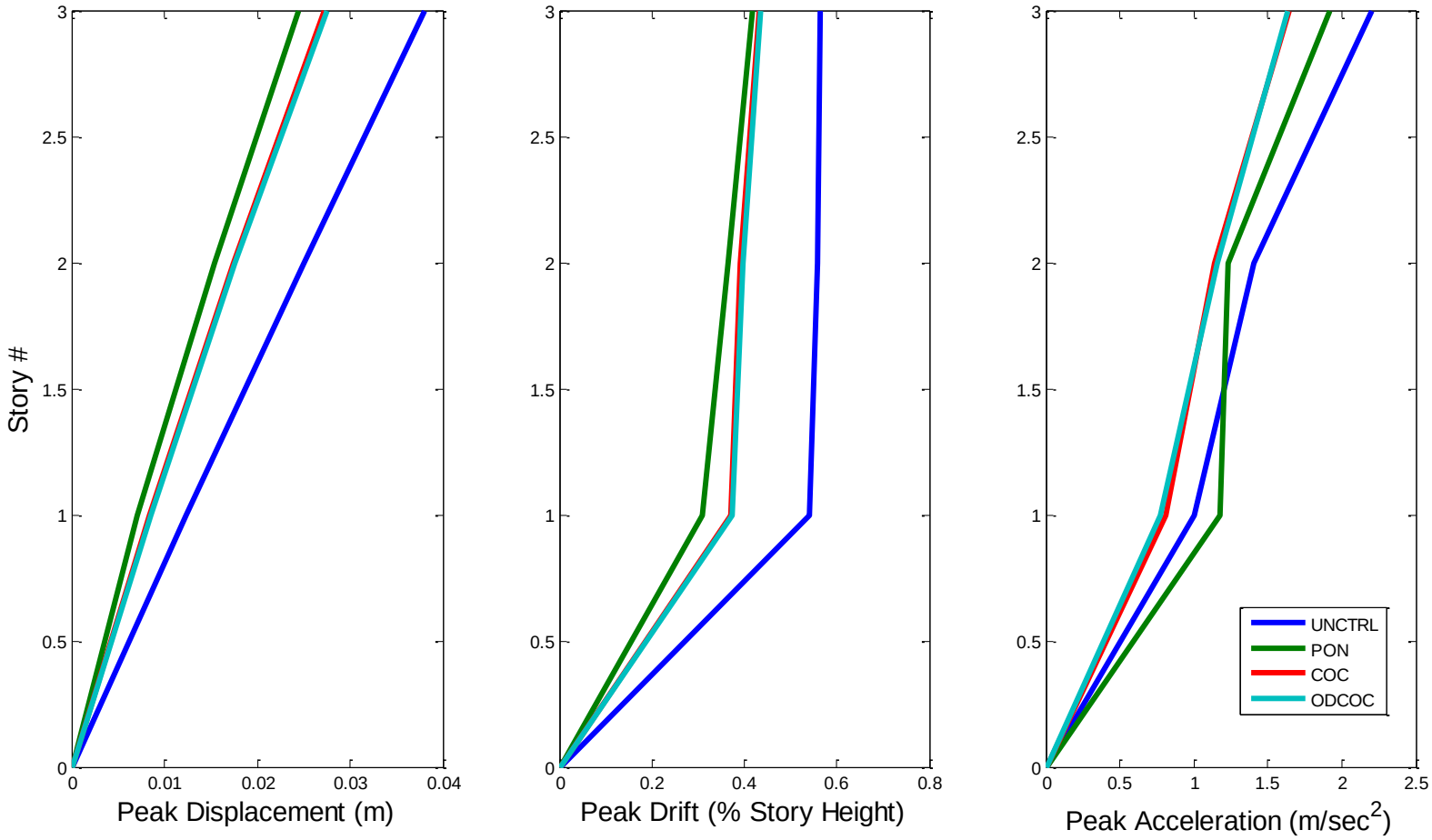

Figure 4.23: Response profiles for SAC Small EQ II

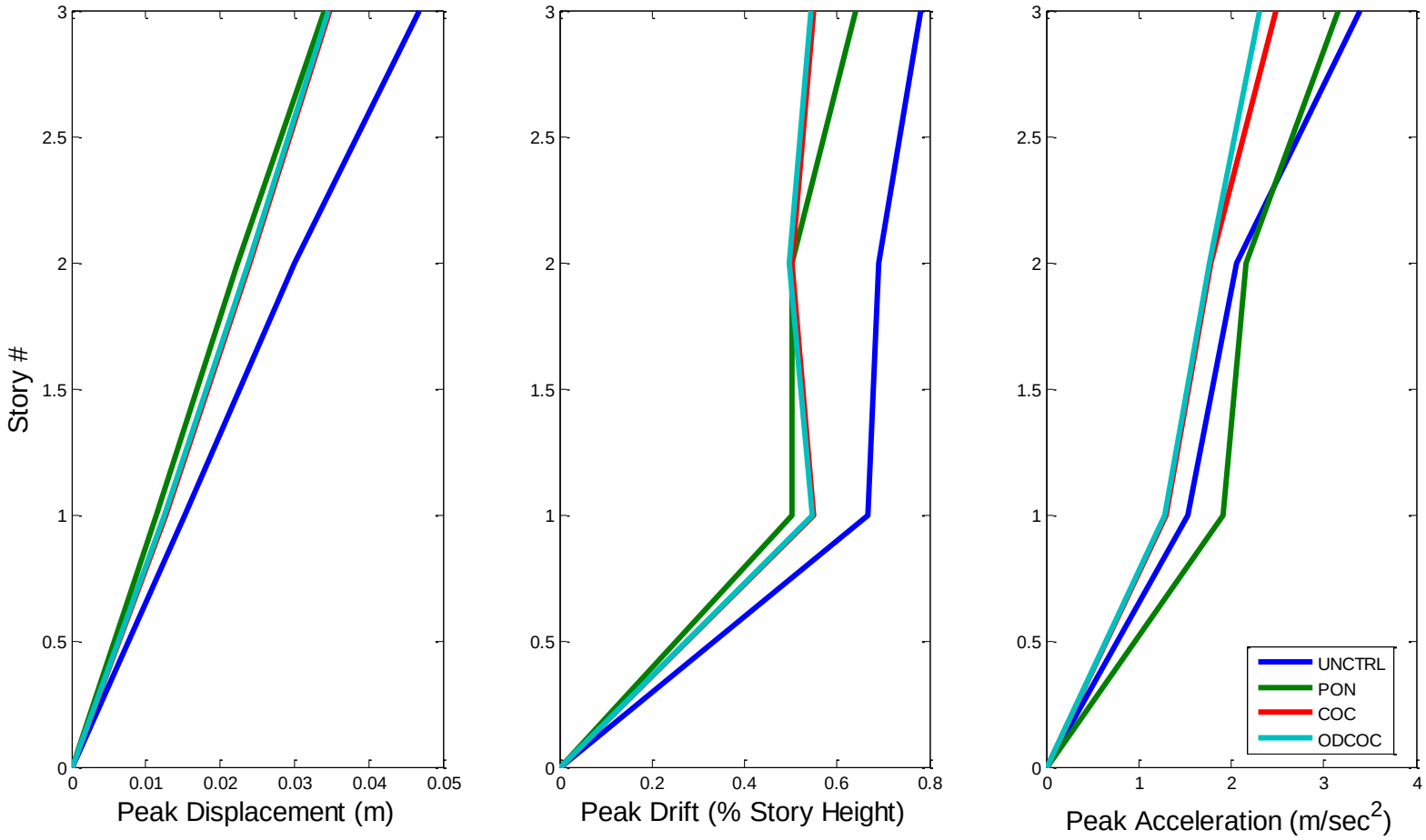

Figure 4.24: Response profiles for El Centro EQ

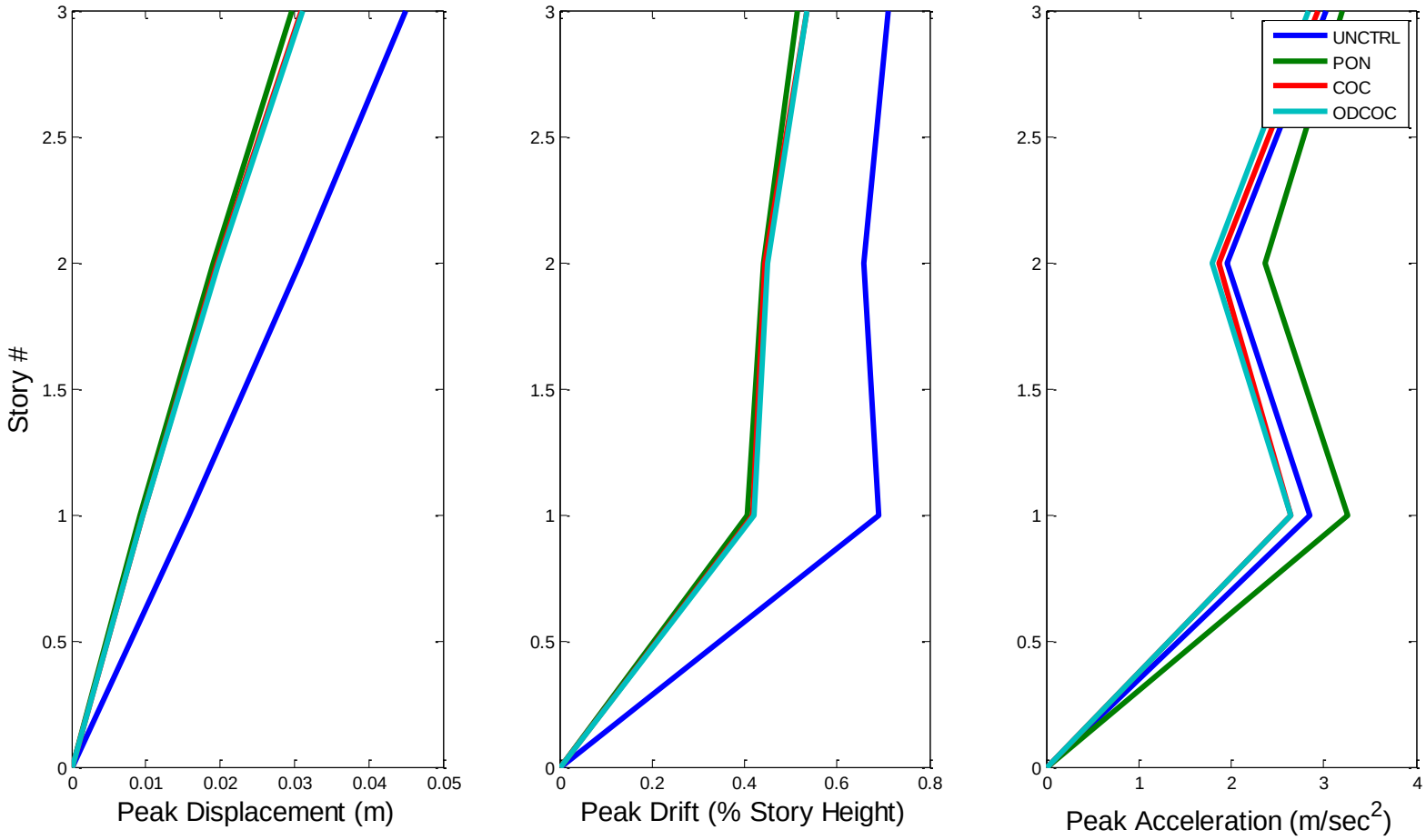

Figure 4.25: Response profiles for SAC Medium EQ I

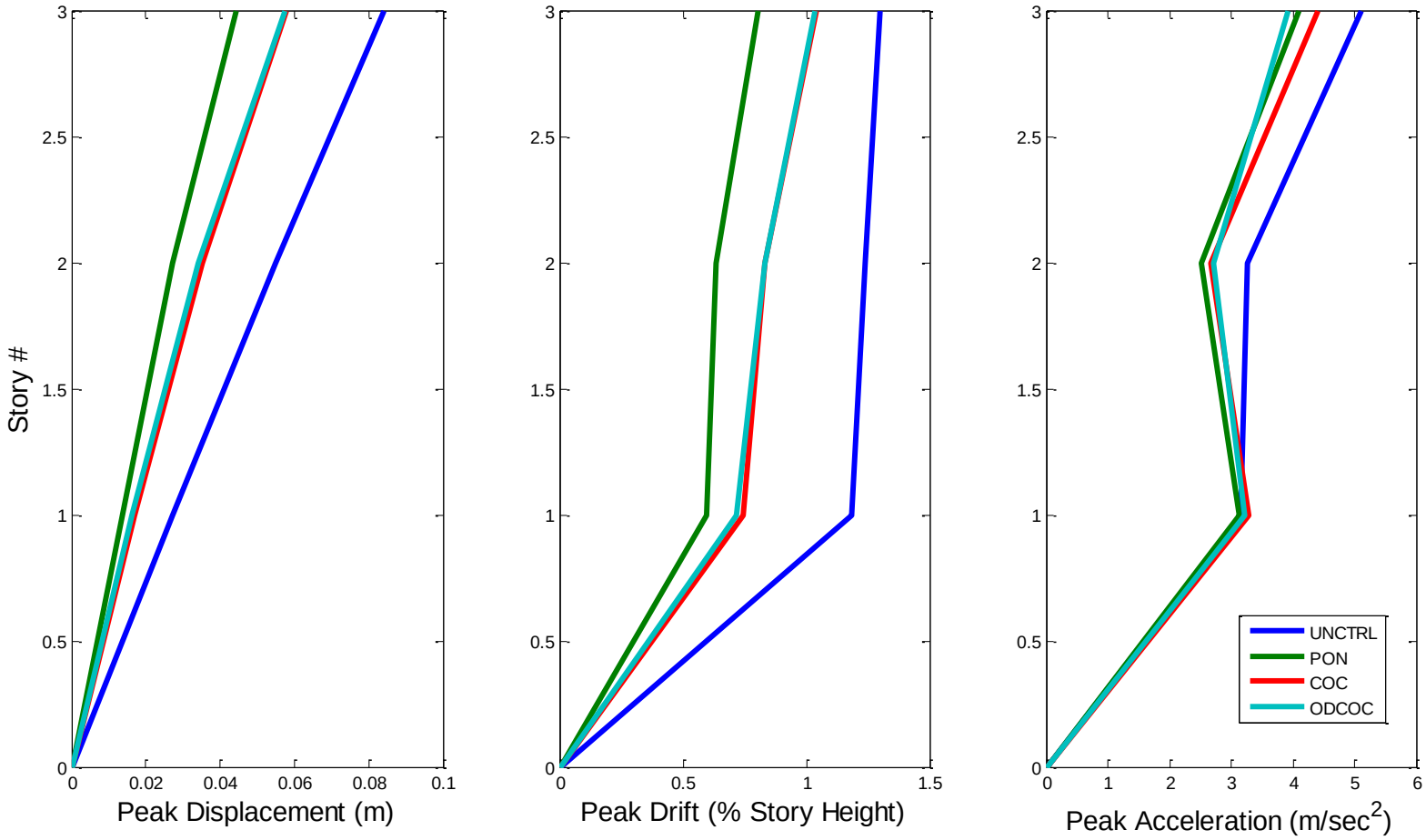

Figure 4.26: Response profiles for Superstition Hills EQ

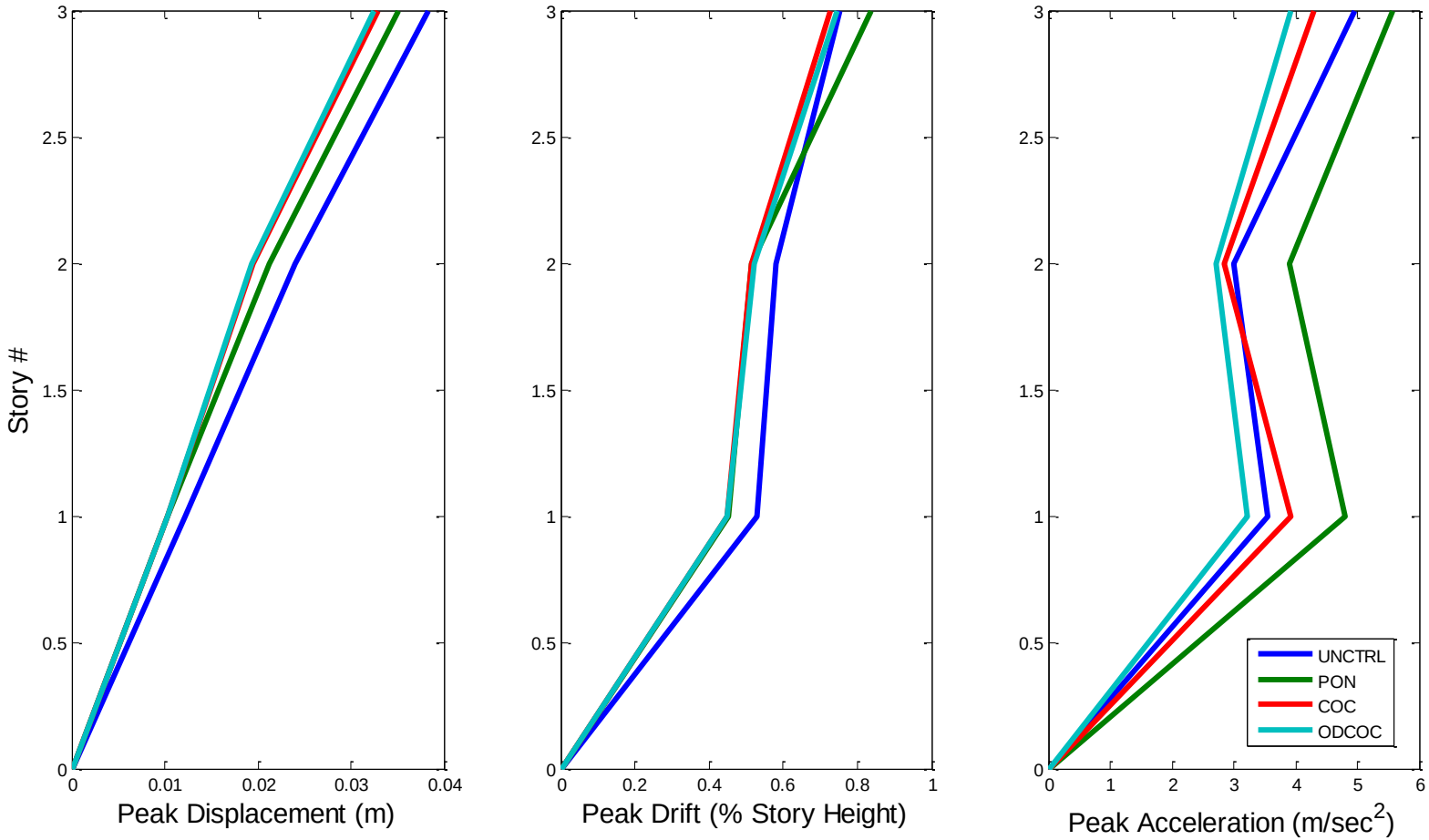

Figure 4.27: Response profiles for SAC Large EQ I

For control design purposes, the ***R*** matrix was selected to be an identity matrix of proper order, and a wide variety of ***Q*** matrices (with emphasis on different physical responses) were chosen and tested using a band-limited white noise input. Based on the performance of these controllers in pure simulation, the most effective weighting values were selected and implemented. Ultimately, both optimal controllers were designed to minimize the absolute acceleration, with equal weighting on all floors of the structure. Both the COC and the ODCOC controllers use a weighting value of 100000 m^2 on all floors for the ***Q*** matrix.

From Table 4.4, in the case of the smaller earthquakes, the PON and ODCOC controllers split achieving greater reduction in peak displacement and drift. However, the ODCOC results in lower responses than COC for these categories, by an average of 7% for displacement, and 5% for drift. For peak absolute acceleration, the COC and ODCOC approaches yield lower responses than the PON controller, by an average of ~25%, however the ODCOC is typically superior to COC by 5-6%. The COC does have the best performance in terms of peak and RMS force (indicating that this approach used the least amount of force to achieve response reduction), compared to the other two controllers. For the RMS response categories, ODCOC and COC are split in terms of superiority.

For the medium earthquakes cases, as before, the ODCOC algorithm performs much better than both PON (an average 15% improvement) and COC (an average 4% improvement) in peak acceleration reduction. ODCOC and PON again trade off for the best interstory drift and displacement reduction for both earthquakes. COC and ODCOC have much smaller peak and RMS forces associated with them.

Lastly, for the large earthquake cases, the optimal controllers perform much better for acceleration reduction compared to the passive control approach (~15% improvement). However, ODCOC is only marginally better than COC (2% improvement). ODCOC and PON again split the best peak displacement reduction, while the best drift reduction varies between all controllers. COC is the best control in terms of peak and RMS damper force.

The peak response profiles for displacement, interstory drift and acceleration are shown in Figures 4.22-4.27. In general, the PON approach proves to be superior for minimizing displacement and interstory drift. The ODCOC and COC approaches yield similar results for displacement and drift, with a slight edge to ODCOC (~3-4% average improvement). However, in every case, the ODCOC controller is clearly superior in reducing peak acceleration, especially at the top floor level. In several instances, the PON approach leads to peak acceleration levels that are larger than the uncontrolled case.

Overall, the ODCOC seems to be the superior controller in terms of peak acceleration response reduction, with an average improvement of 20% vs. PON control, and 4-5% vs. COC control. ODCOC and PON are close in terms of displacement and

drift reduction, with no clear trend across all earthquakes. COC and ODCOC also typically use about 25% less force than PON control.

4.3.4. Evaluating the Robust Performance of the Controllers

It is important for the performance of a controller to be robust, in face of many factors that may influence changes from the simulation design, such as uncertainties, modeling errors, etc. To assess robustness, the mass of the structure is varied in increments from 100% to 120% of the original design, and the *SAC Small EQ I* is used as the input excitation to the structure.

Table 4.5: Comparison of Simulation/RTHS Results to Evaluate Robust Performance

Ground Motion	% Mass	Controller		Evaluation Criteria							
				J1	J2	J3	J4 (kN)	J5	J6	J7	J8 (kN)
SAC Small I PGA - 0.15 g	100%	PON	Simulation	1.087	1.448	1.744	130	1.312	1.554	1.702	23
			RTHS	0.975	1.383	1.504	136	1.097	1.318	1.484	21
		ODCOC	Simulation	**0.976**	**1.146**	**1.351**	**99**	**1.089**	**1.207**	**1.298**	**14**
			RTHS	**0.884**	**0.938**	**0.953**	**78**	**0.889**	**0.954**	**1.295**	**11**
	105%	PON	Simulation	1.101	1.468	1.903	132	1.299	1.546	1.697	22
			RTHS	1.027	1.401	1.638	138	0.645	1.098	**0.995**	20
		ODCOC	Simulation	**0.981**	**1.118**	**1.394**	**95**	**1.071**	**1.186**	**1.279**	**13**
			RTHS	**0.932**	**0.961**	**1.076**	**86**	**0.587**	**0.899**	1.199	**11**
	110%	PON	Simulation	1.136	1.454	1.967	136	1.224	1.462	1.613	21
			RTHS	1.065	1.358	1.690	142	0.612	1.048	1.250	20
		ODCOC	Simulation	**0.991**	**1.082**	**1.462**	**94**	**1.031**	**1.142**	**1.232**	**12**
			RTHS	**0.945**	**0.940**	**1.138**	**85**	**0.583**	**0.888**	**1.181**	**11**
	120%	PON	Simulation	1.190	1.369	1.742	139	1.033	1.237	1.363	19
			RTHS	1.126	1.241	1.467	145	**0.532**	0.903	1.185	18
		ODCOC	Simulation	**1.007**	**1.000**	**1.284**	**83**	**0.929**	**1.024**	**1.092**	**12**
			RTHS	**0.982**	**0.911**	**1.048**	**83**	0.566	**0.847**	**1.128**	**11**

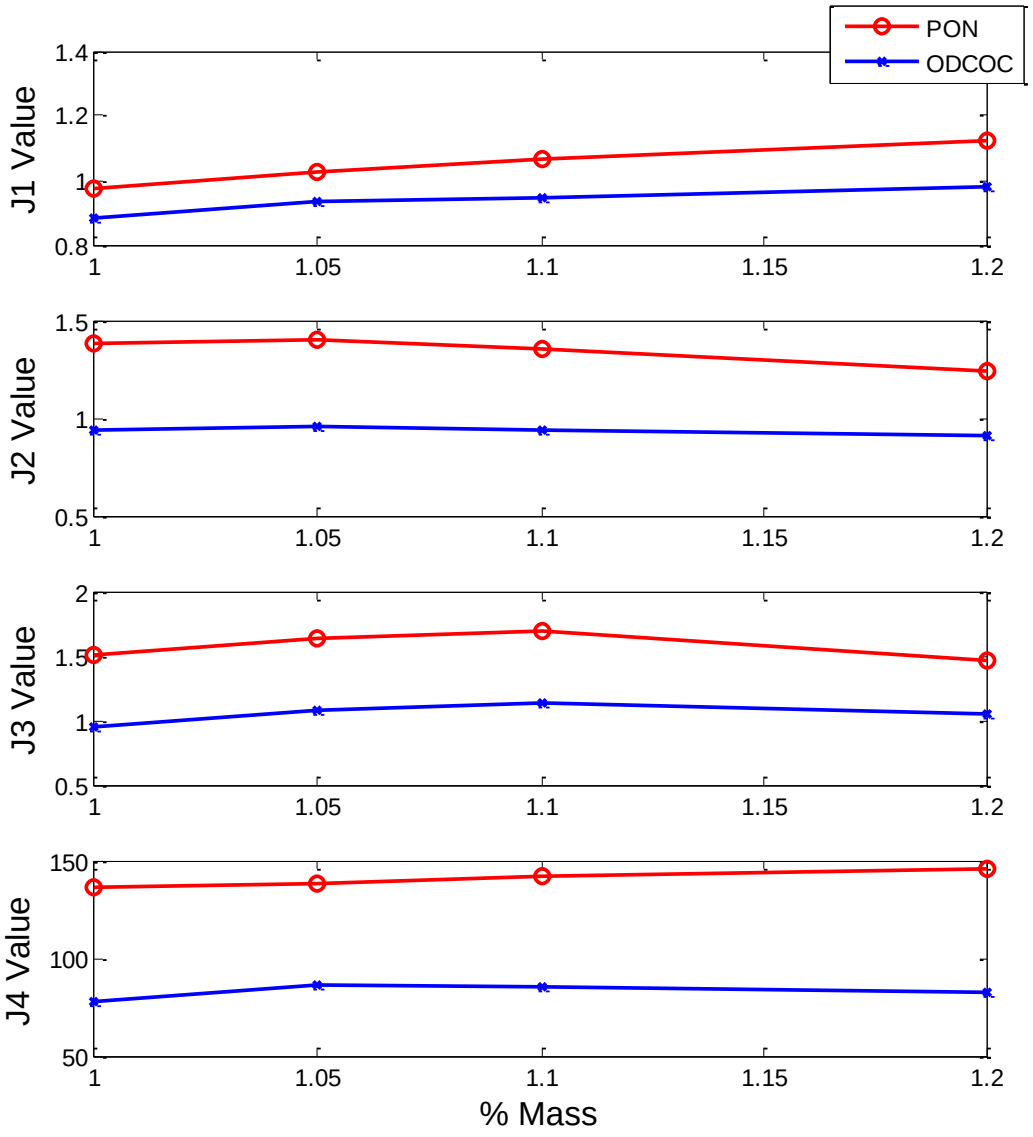

Figure 4.28: Variation of Peak Evaluation Criteria for Different Mass Cases

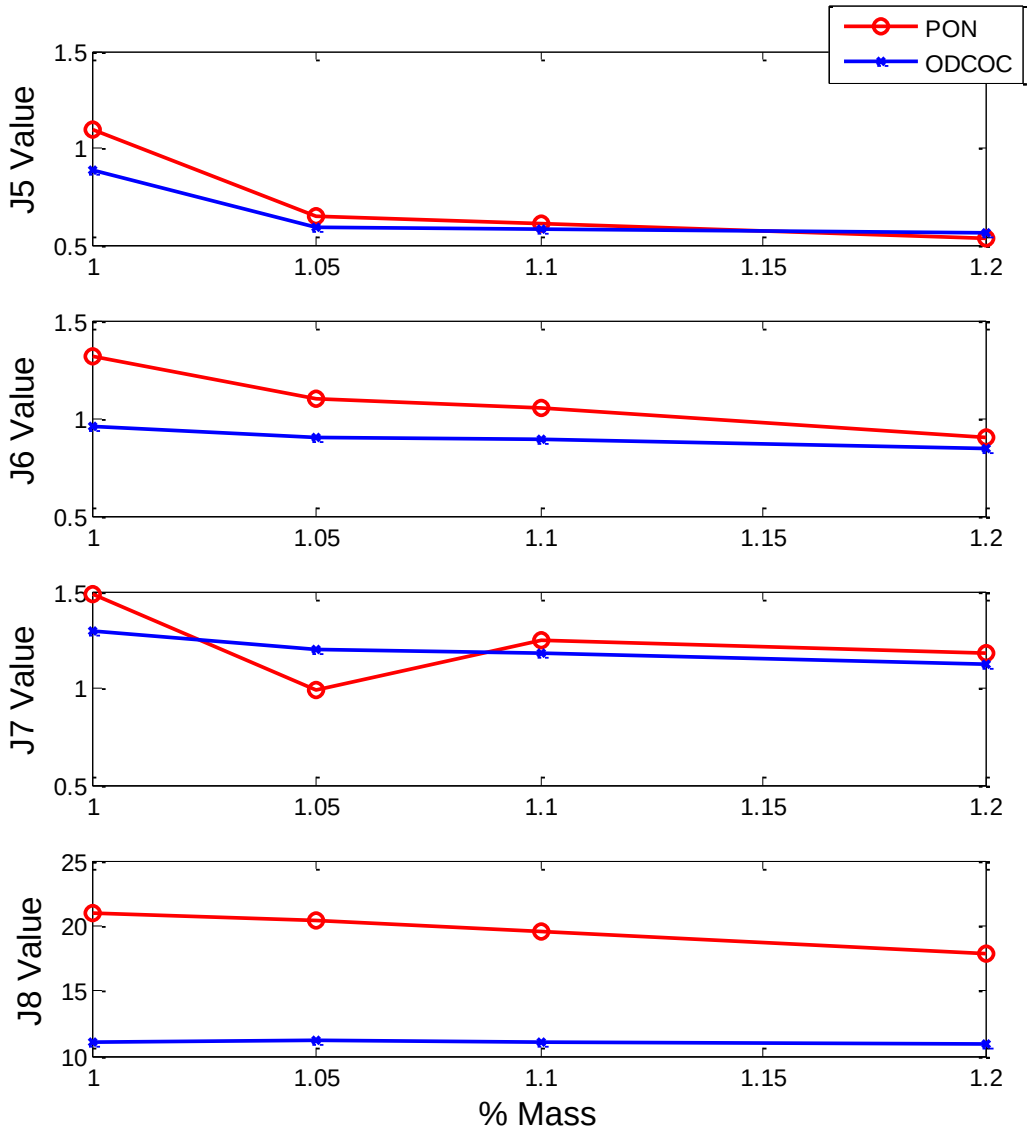

Figure 4.29: Variation of RMS Evaluation Criteria for Different Mass Cases

Based on the results in Table 4.5, it clear that the ODCOC controller outperforms the PON controller in virtually every category, for nearly every mass level. The peak displacement is reduced by an average of 15%, as compared to the PON case, and peak drift is reduced a further 30%. The peak acceleration is reduced by an average of 40% in comparison to the PON reduction, while using approx 70% of the peak force. All of the RMS categories favor the ODCOC control as well.

Further, as shown in Figure 4.28 and 4.29, the variation in the response criteria at different mass intervals is less severe for ODCOC in comparison to the PON controller. Generally, the results are more consistent for both peak and RMS responses when ODCOC is used. This reliability is a positive sign of robust performance for the controller, which shows that even in the face of changing conditions, the controller still yields reductions in response reductions. Robustness in control is a particularly desirable trait, as the actual-built structure is often different from the design and can change significantly over time. Controllers which can provide consistent levels of reduction are highly sought-after for real-world structural control applications.

4.4. Conclusions

To evaluate several damper control methods, a real-time hybrid simulation using a large-scale steel frame and a large-scale MR Damper (representing a typical three-story structure) is conducted at the NEES@Lehigh facility. System identification of the various components used in the RTHS, including the large-scale steel frame, large-scale MR damper, actuator controller, etc., are carried out using several experimental techniques, including: (1) pseudo-dynamic/hammer testing for the frame identification, (2) actuator excitation for the MR damper, and (3) actuator error tracking and model optimization for the actuator controller.

For MR damper controller evaluations, the available measurements, some of which were used for feedback in the semi-active controllers, included actuator and damper forces, relative displacements, relative velocities, and absolute accelerations at each floor level, strain gage readings from several points on the frame, etc. The global responses of the system to several ground motions were found for each controller and were compared to both pure numerical simulations and each other.

The RTHS using the large-scale steel frame was completed successfully and validated against numerical simulation results. In general, the semi-active control approaches proved to superior to the passive control approach for reduction in peak absolute acceleration. ODCOC proved to be the best option for each earthquake, with an average improvement of 25% versus the PON cases and 5% versus the COC case. Further, PON and ODCOC both performed well in terms of drift and displacement reduction, though no clear pattern or victor emerged from the earthquake subset. The COC approach was superior at utilizing the least damper force to achieve good results. In comparing the RTHS results to simulation, the structural responses for each were shown to track very well. Furthermore, the robust performance test results show that the

ODCOC outperformed the PON controller even in the face of unknown circumstances. For each instance of mass variation, the ODCOC shows improvements in responses.

Overall, the ODCOC has proven to be the superior controller, combining adaptability lacking in the passive control approach with improved response reduction compared to the clipped optimal controller.

CHAPTER 5: NINE-STORY BENCHMARK STRUCTURE EXPERIMENT (LINEAR)

In the previous chapter, a RTHS was conducted to test a 3-story structure using a 3-story large-scale steel frame. In this chapter, RTHS is used to test a nine-story benchmark structure. Three phases of RTHS testing are performed: (1) RTHS at the University of Illinois – Urbana/Champaign, where the MR damper is the physical substructure, and the structure is taken as the analytical substructure; (2) RTHS at Lehigh University, where a large-scale steel frame (used in the previous chapter) equipped with a large-scale MR damper in the first floor is the physical substructure and the remaining portion of the structure is the analytical substructure; and (3) the same setup as Phase 2 at Lehigh University with an additional large-scale MR damper installed in the second story of the steel frame. As in the previous chapter, the performance of each control algorithm is evaluated for each phase of RTHS and compared using a variety of general earthquake inputs in numerical simulation and real-time hybrid simulation. In addition, the best controller is analyzed regarding robust performance in the face of uncertainty.

5.1 Experimental Setup and Procedure

In this section, the benchmark structure featured in the various RTHS tests is described in detail. In addition, the RTHS test setup for both the Smart Structures Technology Lab (SSTL) at the University of Illinois – Urbana/Champaign (UIUC) and the RTMD facility at the NEES@Lehigh facility are described.

5.1.1. Benchmark Structure Description

The 9-story benchmark structure (Ohtori et al, 2004) used in this study was designed by Brandow & Johnston Associates for the SAC Phase II Steel Project. SAC is a joint venture of three non-profit organizations: The Structural Engineers Association of California (SEAOC), the Applied Technology Council (ATC) and California Universities for Research in Earthquake Engineering (CUREE). Although not actually constructed, the structure adheres to seismic code and represents a typical medium-rise building office building (for general commercial use) designed for the Los Angeles, California region.

The structure is 150 ft by 150 ft in plan, and 122 ft in elevation. The bays are 30 ft on-center, in both directions, with five bays each in the E–W direction and the N–S direction. Typical floor-to-floor heights (for analysis purposes measured from center of beam to center of beam) are 13 ft. The floor-to-floor height of the basement level is 12 ft and the first floor height is 18 ft. Lateral load resistance is achieved through the use of perimeter steel MRFs with simple framing on the furthest south E–W frame. The interior bays of the structure contain simple framing with composite floors. The levels of the 9-

story building are numbered with respect to the base level, which is located at the ground level. The ninth level is the roof. The building has an additional basement level denoted as B-1. In the design, column splices, which are seismic splices to carry bending and uplift forces, are located on the first, third, fifth, and seventh levels at 6 ft above the center line of the beam to column joint.

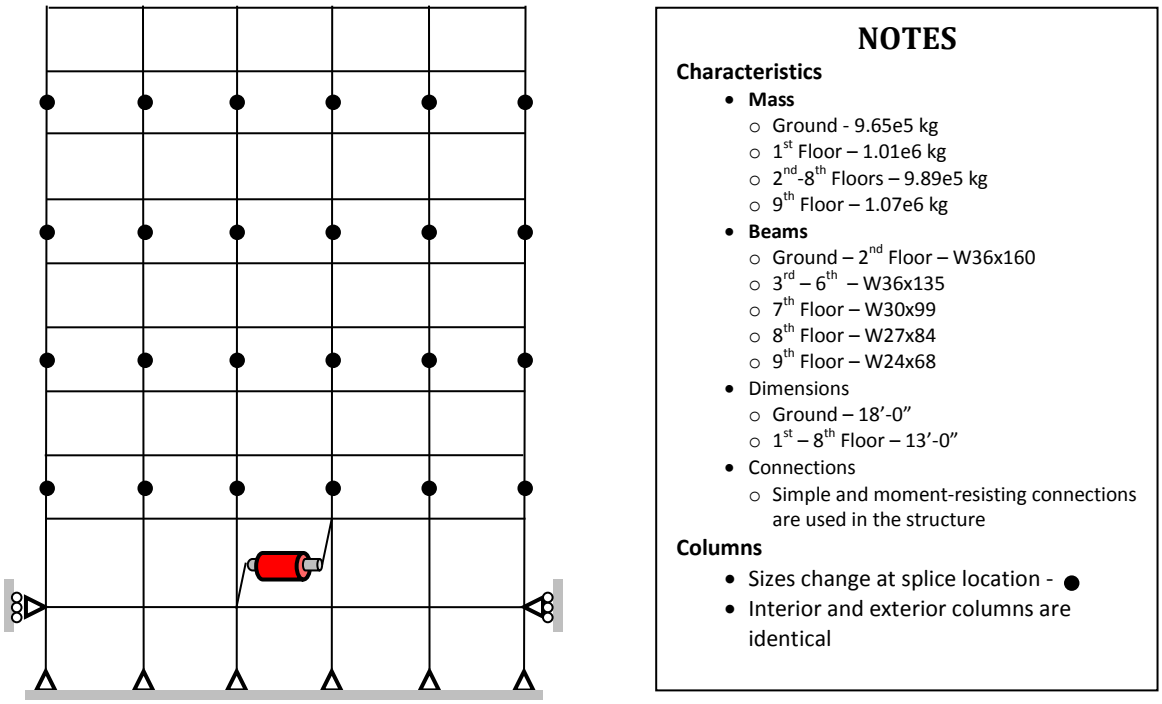

Figure 5.1: Benchmark Structure Details

Two different models are used for Phase 1 and Phase 2-3, respectively. In Phase 1 at UIUC, a linear finite-element 9DOF model of the benchmark structure is used as the analytical substructure. For Phase 2-3 at Lehigh, a simplified mass-spring-dashpot shear model of the structure is used as the analytical substructure.

For the finite-element-based model used in Phase I, initially, there are 198 DOFs. The structure is represented using 21 nodes connected using 28 structural elements. Nodes are located at beam-to-column joints and have 3 degrees-of-freedom (DOFs): horizontal, vertical, and rotational. Elements are created between nodes to represent the beams and columns in the structure. Each element has a pre-determined length, area, moment of inertia, modulus of elasticity, and density, and the consistent mass and stiffness matrices are assembled based on these properties

The global stiffness and mass matrices are constructed using a summation of the mass and stiffness of each element for the entire structure. Three separate model reductions are performed on the FE model, including: (1) reduction due to boundary

conditions, (2) reduction due to the assumption of rigidity of the floor slab in the horizontal plane using a Ritz transformation, and (3) Guyan reduction to eliminate the higher non-contributing modes. Though the higher modes do not have an impact on performance, they are computationally burdensome, so it is more efficient to eliminate them.

Beginning with the initial 198 DOF mode and applying the specified model reductions, the final model has 9 horizontal DOFs (one per floor). The characteristic matrices for this model are defined as

$$M = \begin{bmatrix} 5.32e5 & & & & & & & & \\ -3.94e5 & 5.17e5 & & & & & & & \\ -2.32e3 & -832 & 5.14e5 & & & & & & \\ 1.13e3 & 3.33e3 & -134 & 5.12e5 & & & & & \\ -400 & 1.41e3 & -3.45e3 & 127 & 5.11e5 & & & & \\ 124 & -519 & 1.48e3 & -3.29e3 & -261 & 5.1e5 & & & \\ 44 & 189 & -526 & 1.38e3 & -2.84e3 & -987 & 5.11e5 & & \\ 64 & -71 & 142 & -465 & 1.1e3 & -2.64e3 & -4.18e3 & 5.22e5 & \\ 76 & 36 & 4 & 111 & -118 & 524 & -337 & 1.18e4 & 5.49e5 \end{bmatrix} * \frac{kN * s^2}{m}$$

$$C = \begin{bmatrix} 3.65e6 & & & & & & & & \\ -1.86e6 & 4.11e6 & & & & & & & \\ -4.26e4 & -1.85e6 & 3.93e6 & & & & & & \\ -1.03e4 & -3.97e4 & -1.74e6 & 3.66e6 & & & & & \\ -5.e7e4 & -1.03e5 & -5.81e4 & -1.62e6 & 3.43e6 & & & & \\ -2.36e4 & -4.88e4 & -9.56e4 & -7.38e4 & -1.51e6 & 3.14e6 & & & \\ -3e3 & -1.18e4 & -3.75e4 & -8.59e4 & -7.73e4 & -1.41e6 & 2.97e6 & & \\ 9.02e3 & 9.15e3 & 2.63e3 & -1.87e4 & -6.07e4 & 4.82e3 & -1.37e6 & 2.62e6 & \\ 1.36e4 & 2.09e4 & 2.66e4 & 2.71e4 & 1.29e4 & -3.62e4 & -2.51e3 & -1.19e6 & 1.15e6 \end{bmatrix} * \frac{kN * s}{m}$$

$$K = \begin{bmatrix} 7.94e8 & & & & & & & & \\ -6.75e8 & 1.15e9 & & & & & & & \\ 1.66e8 & -7.13e8 & 1.07e9 & & & & & & \\ -2.72e7 & 1.71e8 & -6.36e8 & 9.38e8 & & & & & \\ 4.65e6 & -2.70e7 & 1.43e8 & -5.52e8 & 8.23e8 & & & & \\ -7.95e5 & 4.57e6 & -2.21e7 & 1.18e8 & -4.75e8 & 6.98e8 & & & \\ 2.59e5 & -8.39e5 & 3.76e6 & -1.76e7 & 9.74e7 & -4.12e8 & 6.20e8 & & \\ -4.32e4 & 1.84e5 & -7.67e5 & 3.37e6 & -1.72e7 & 1.03e8 & -3.67e8 & 4.80e8 & \\ 1.46e5 & 5.73e3 & 1.48e5 & -4.46e5 & 2.51e6 & -1.42e7 & 7.63e7 & -2.02e8 & 1.37e8 \end{bmatrix} * \frac{N}{m}$$

The first five natural frequencies of the reduced order model are 0.47, 1.27, 2.19, 3.31, and 4.55 Hz, which compare favorably with original benchmark model, and the damping is assumed to be 2%. This model is used to evaluate the proposed control strategies, based on criteria as described in a later section.

For the Phase II and III RTHS, the model of the nine-story benchmark structure is idealized as a collection of masses, dashpots, and springs with nine DOF (Marghareh et al., 2012). This simplification is due to the limitations using linear state-space representations a structure during a RTHS. It is noted that if the natural frequencies of a model are significantly higher than the operational frequency margin of the actuator control scheme, the RTHS may be difficult to perform. Thus, making this simplification allows for the model to be used effectively in the RTHS.

Each mass is as specified in Figure 5.1. To determine the interstory stiffness, the following equations are used:

$$\boldsymbol{\rho(i)} = \frac{\boldsymbol{I_b(i)}}{\boldsymbol{4 * I_c(i)}} \tag{5.1}$$

$$\boldsymbol{K(i)} = \frac{\left(\frac{\boldsymbol{12(12\rho(i)+1)}}{\boldsymbol{12\rho(i)+4}}\right)\boldsymbol{E \cdot I_c(i)}}{\boldsymbol{L(i)^3}} + \frac{\boldsymbol{4}\left(\frac{\boldsymbol{12(12*2\rho(i)+1)}}{\boldsymbol{(12*2\rho(i))+4}}\right)\boldsymbol{E \cdot I_c(i)}}{\boldsymbol{L(i)^3}} + \frac{\boldsymbol{3E \cdot I_c(i)}}{\boldsymbol{L(i)^3}} \tag{5.2}$$

where $\boldsymbol{I_b(i)}$ is the average moment of inertia for the beams at the i^{th} floor level, $\boldsymbol{I_c(i)}$ is the average moment of inertia for the columns at the i^{th} floor level, $\boldsymbol{E}$ is the modulus of elasticity for steel (200e^9 GPa), $\boldsymbol{L(i)}$ is the story height at the i^{th} floor level, and $\boldsymbol{K(i)}$ is the resulting interstory stiffness for the i^{th} floor level.

After obtaining each mass and stiffness, the characteristic matrices are then assembled in the following manner:

$$\boldsymbol{M} = \begin{bmatrix} \boldsymbol{m_1} & \boldsymbol{0} & \dots & \boldsymbol{0} \\ \boldsymbol{0} & \boldsymbol{m_2} & \ddots & \vdots \\ \vdots & \ddots & \ddots & \boldsymbol{0} \\ \boldsymbol{0} & \dots & \boldsymbol{0} & \boldsymbol{m_9} \end{bmatrix} \tag{5.3}$$

$$\boldsymbol{K} = \begin{bmatrix} \boldsymbol{k_1 + k_2} & \boldsymbol{-k_2} & \boldsymbol{0} & \dots & \boldsymbol{0} \\ \boldsymbol{-k_2} & \boldsymbol{k_2 + k_3} & \boldsymbol{-k_3} & \ddots & \vdots \\ \boldsymbol{0} & \boldsymbol{-k_3} & \boldsymbol{k_3 + k_4} & \ddots & \boldsymbol{0} \\ \vdots & \ddots & \ddots & \ddots & \boldsymbol{-k_9} \\ \boldsymbol{0} & \dots & \boldsymbol{0} & \boldsymbol{-k_9} & \boldsymbol{k_9} \end{bmatrix} \tag{5.4}$$

After determining $\boldsymbol{M}$ and $\boldsymbol{K}$, the $\boldsymbol{C}$ matrix can then be determined using modal damping, with the assumption of 2% damping in each mode.

Using the previously outlined procedure, the characteristic matrices for the shear model of the 9-story benchmark structure are defined as

$$\boldsymbol{M} = \begin{bmatrix} \boldsymbol{1.01e6} & \boldsymbol{0} & & & \dots & & & & \boldsymbol{0} \\ \boldsymbol{0} & \boldsymbol{9.89e5} & & & & & & & \\ & & \boldsymbol{9.89e5} & & & & & & \\ & & & \boldsymbol{9.89e5} & \ddots & & & & \\ \vdots & & & \ddots & \boldsymbol{9.89e5} & & & & \vdots \\ & & & & & \boldsymbol{9.89e5} & & & \\ & & & & & & \boldsymbol{9.89e5} & & \\ & & & & & & & \boldsymbol{9.89e5} \ddots & \boldsymbol{0} \\ \boldsymbol{0} & & & & \dots & & & \boldsymbol{0} & \boldsymbol{1.07e6} \end{bmatrix} * \frac{\boldsymbol{N * s^2}}{\boldsymbol{m}}$$

$$C = \begin{bmatrix} 9.29e5 & & & & & & & & \\ -3.66e5 & 1.05e6 & & & & & & & \\ -7.26e4 & -3.52e5 & 1.00e6 & & & & & & \\ -2.77e4 & -6.46e4 & -3.10e5 & 9.47e5 & & & & & \\ -1.43e4 & -2.67e4 & -6.19e4 & -3.18e5 & 8.91e5 & & & & \\ -8.18e3 & -1.37e4 & -2.49e4 & -5.97e4 & -2.78e5 & 8.02e5 & & & \\ -5.12e3 & -8.07e3 & -1.30e4 & -2.4e4 & -5.27e4 & -2.53e5 & 7.23e5 & & \\ -3.49e3 & -5.31e3 & -7.96e3 & -1.28e4 & -2.19e4 & -4.89e4 & -2.29e5 & 6.61e5 & \\ -3.02e3 & -4.50e3 & -6.52e3 & -9.87e3 & -1.51e4 & -2.66e4 & -5.86e4 & -2.58e5 & 4.57e5 \end{bmatrix} * \frac{N * s}{m}$$

$$K = \begin{bmatrix} 6.23e8 & -4.35e8 & 0 & & & \cdots & & & 0 \\ -4.35e8 & 8.62e8 & -4.27e8 & & & & & & \\ 0 & -4.27e8 & 7.81e8 & -3.54e8 & & & & & \\ & & -3.54e8 & 6.98e8 & -3.44e8 & \ddots & & & \vdots \\ & & & -3.44e8 & 6.20e8 & -2.76e8 & & & \\ \vdots & & & \ddots & -2.76e8 & 5.01e8 & -2.26e8 & & \\ & & & & & -2.26e8 & 4.09e8 & -1.83e8 & 0 \\ & & & & & & -1.83e8 & 3.50e8 & -1.67e8 \\ 0 & & & \cdots & & & 0 & -1.67e8 & 1.67e8 \end{bmatrix} * \frac{N}{m}$$

The first five natural frequencies of this model are 0.44 Hz, 1.18 Hz, 1.98 Hz, 2.74 Hz, and 3.44 Hz. As before, these frequencies compare well with the original finite-element model of the benchmark structure.

The intent of this experiment is to test two scenarios where the structure has 18 MR dampers installed in the first floor and 9 MR dampers installed in the 1st and 2nd floors, respectively. However, there is a physical limitation in that only one MR damper can be installed in the large-scale frame. Thus, rather than multiplying the damper force by the number of dampers present (done in the testing at UIUC), the structure (mass and stiffness) is further scaled to facilitate a single damper. In this case, the DBF stiffness is such that the maximum division that can be applied to the benchmark structure's total structural stiffness is nine. Thus, 1/9th of the full benchmark structure (mass, stiffness and damping) is tested, with the same dynamic characteristics. This reduction still allows for a small portion of the 1st floor stiffness to remain in the analytical model, while the DBF contributes the majority. Clearly, due to the relatively large portion of the complete specimen that resides in the physical structure, this configuration offers a new challenge to the RTHS implementation.

5.1.2. RTHS Methodology

In this section, the methodology for conducting the RTHS is discussed. An overview of the substructure breakdown is presented, including the free-body diagrams. Finally the equations of motion, including the interaction of the substructures with each other, are offered.

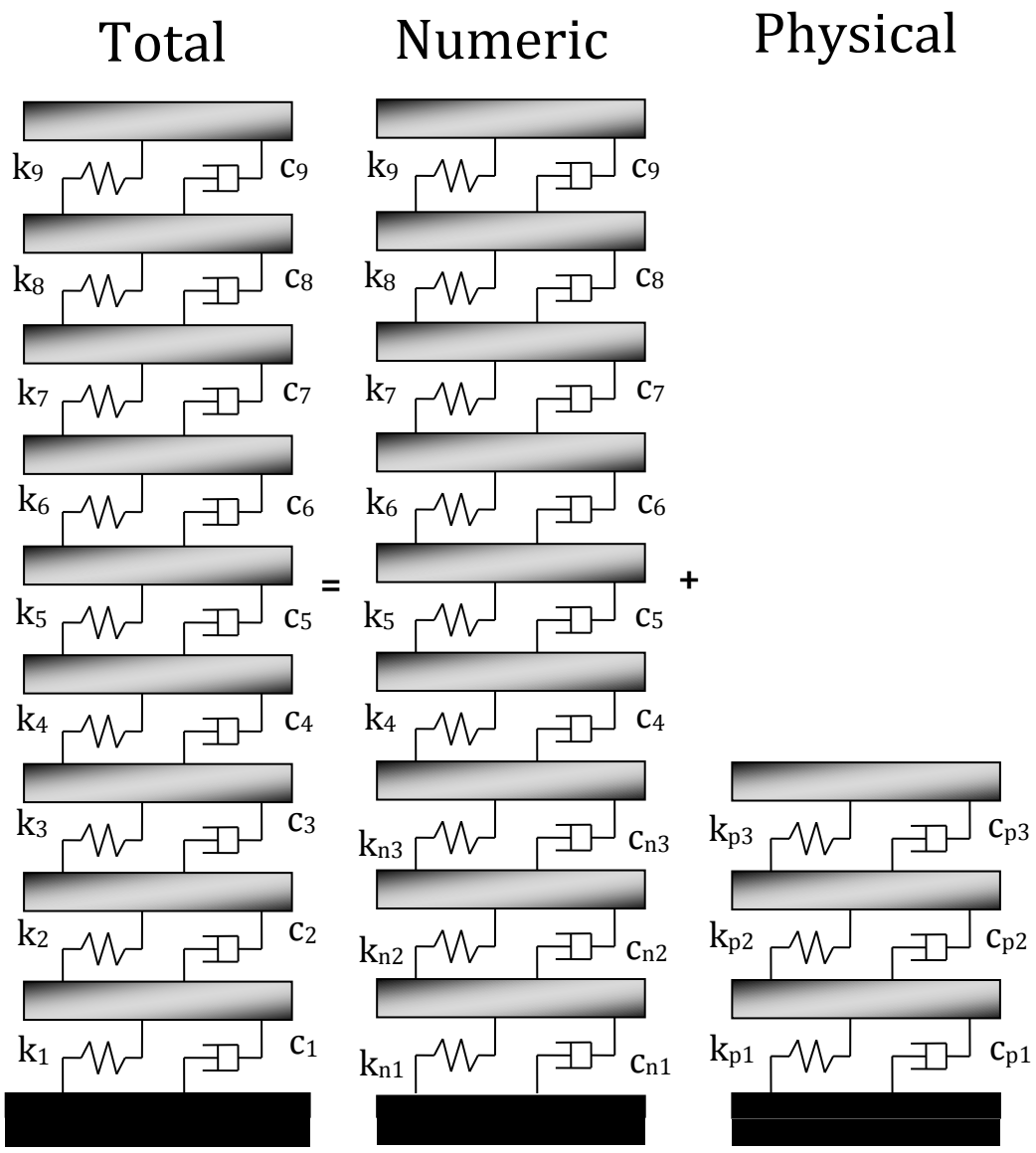

Figure 5.2: RTHS Structure Breakdown

The first step to developing a RTHS is to separate the total structure into components that will tested physically and modeled computationally. In this case, a portion of the first three stories will be tested physically using a large-scale steel frame. The rest of the structure will be modeled computationally. There is a feedback relationship between the two substructures in a RTHS (calculated displacement from the analytical model is imposed on the physical substructure, and the measured restoring forces from the physical substructure are fed back into the analytical model), and this relationship is established in the following way:

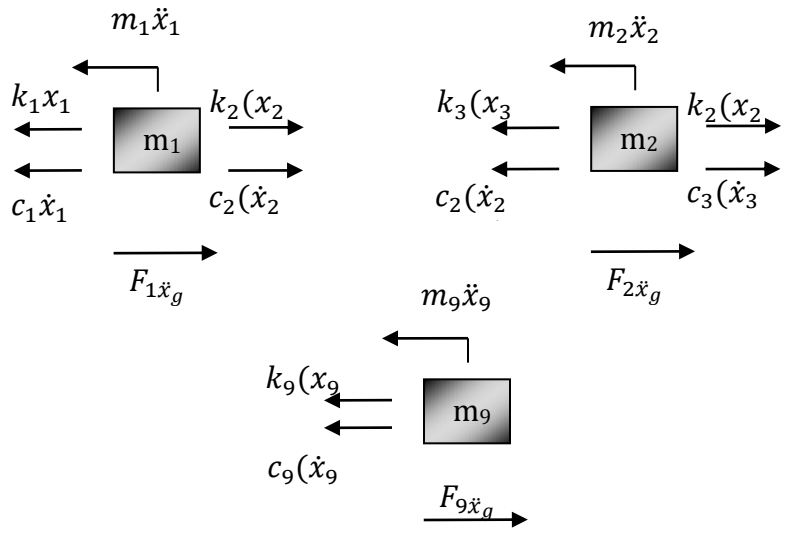

Figure 5.3: Free Body Diagrams of selected DOFs

Using the simplification of a shear structure, these FBDs lead to the equations of motion for the system, as outlined below:

$$\boldsymbol{F_{1\ddot{x}_g}} = \boldsymbol{m_1\ddot{x}_1 + c_1\dot{x}_1 - c_2(\dot{x}_2 - \dot{x}_1) + k_1x_1 - k_2(x_2 - x_1)} \quad \textbf{(5.2)}$$

$$\boldsymbol{F_{2\ddot{x}_g}} = \boldsymbol{m_2\ddot{x}_2 + c_2(\dot{x}_2 - \dot{x}_1) - c_3(\dot{x}_3 - \dot{x}_2) + k_2(x_2 - x_1) - k_3(x_3 - x_2)} \quad \textbf{(5.3)}$$

$$\boldsymbol{F_{3\ddot{x}_g}} = \boldsymbol{m_3\ddot{x}_3 + c_3(\dot{x}_3 - \dot{x}_2) - c_4(\dot{x}_4 - \dot{x}_3) + k_3(x_3 - x_2) - k_4(x_4 - x_3)} \quad \textbf{(5.4)}$$

$$\boldsymbol{F_{4\ddot{x}_g}} = \boldsymbol{m_4\ddot{x}_4 + c_4(\dot{x}_4 - \dot{x}_3) - c_5(\dot{x}_5 - \dot{x}_4) + k_4(x_4 - x_3) - k_5(x_5 - x_4)} \quad \textbf{(5.5)}$$

$$\boldsymbol{F_{5\ddot{x}_g}} = \boldsymbol{m_5\ddot{x}_5 + c_5(\dot{x}_5 - \dot{x}_4) - c_6(\dot{x}_6 - \dot{x}_5) + k_5(x_5 - x_4) - k_6(x_6 - x_5)} \quad \textbf{(5.6)}$$

$$F_{6\ddot{x}_g} = m_6\ddot{x}_6 + c_6(\dot{x}_6 - \dot{x}_5) - c_7(\dot{x}_7 - \dot{x}_6) + k_6(x_6 - x_5) - k_7(x_7 - x_6) \quad (5.7)$$

$$F_{7\ddot{x}_g} = m_7\ddot{x}_7 + c_7(\dot{x}_7 - \dot{x}_6) - c_8(\dot{x}_8 - \dot{x}_7) + k_7(x_7 - x_6) - k_8(x_8 - x_7) \quad (5.8)$$

$$F_{8\ddot{x}_g} = m_8\ddot{x}_8 + c_8(\dot{x}_8 - \dot{x}_7) - c_9(\dot{x}_9 - \dot{x}_8) + k_8(x_8 - x_7) - k_9(x_9 - x_8) \quad (5.9)$$

$$F_{9\ddot{x}_g} = m_9\ddot{x}_9 + c_9(\dot{x}_9 - \dot{x}_8) + k_9(x_9 - x_8) \quad (5.10)$$

In addition, due to the separation of physical and analytical substructures, several variables are composed of physical and analytical components:

$$m_1 = m_{n_1} + m_{p_1}, \quad c_1 = c_{n_1} + c_{p_1}, \quad k_1 = k_{n_1} + k_{p_1} \quad (5.11)$$

$$m_2 = m_{n_2} + m_{p_2}, \quad c_2 = c_{n_2} + c_{p_2}, \quad k_2 = k_{n_2} + k_{p_2} \quad (5.12)$$

$$m_3 = m_{n_3} + m_{p_3}, \quad c_3 = c_{n_3} + c_{p_3}, \quad k_3 = k_{n_3} + k_{p_3} \quad (5.13)$$

Also, the restoring forces from the physical substructure must be defined:

$$F_{m_1} = m_{p_1}\ddot{x}_1 + (c_{p_1} + c_{p_2})\dot{x}_1 - c_{p_2}\dot{x}_2 + (k_{p_1} + k_{p_2})x_1 - k_{p_2}x_2 \quad (5.14)$$

$$F_{m_2} = m_{p_2}\ddot{x}_2 - c_{p_2}\dot{x}_1 + (c_{p_2} + c_{p_3})\dot{x}_2 - c_{p_3}\dot{x}_3 - k_{p_2}x_1 + (k_{p_2} + k_{p_3})x_2 - k_{p_3}x_3 \quad (5.15)$$

$$F_{m_3} = m_{p_3}\ddot{x}_3 - c_{p_3}\dot{x}_2 + c_{p_3}\dot{x}_3 - k_{p_3}x_2 + k_{p_3}x_3 \quad (5.16)$$

By combining equations 5.1 - 5.15, we obtain the final equations of motion for the RTHS for the nine-story benchmark structure

$$F_{1\ddot{x}_g} = m_{n1}\ddot{x}_1 + c_{n_1}\dot{x}_1 - c_{n_2}(\dot{x}_2 - \dot{x}_1) + k_{n_1}x_1 - k_{n_2}(x_2 - x_1) + F_{m_1} \quad (5.17)$$

$$F_{2\ddot{x}_g} = m_{n_2}\ddot{x}_2 + c_{n_2}(\dot{x}_2 - \dot{x}_1) - c_{n_3}(\dot{x}_3 - \dot{x}_2) + k_{n_2}(x_2 - x_1) - k_{n_3}(x_3 - x_2) + F_{m_2} \quad (5.18)$$

$$F_{3\ddot{x}_g} = (m_{n_3} + m_{p_3})\ddot{x}_3 + c_{n_3}(\dot{x}_3 - \dot{x}_2) - c_4(\dot{x}_4 - \dot{x}_3) + k_{n_3}(x_3 - x_2) - k_4(x_4 - x_3) + F_{m_3} \quad (5.19)$$

$$F_{4\ddot{x}_g} = m_4\ddot{x}_4 + c_4(\dot{x}_4 - \dot{x}_3) - c_5(\dot{x}_5 - \dot{x}_4) + k_4(x_4 - x_3) - k_5(x_5 - x_4) \quad (5.20)$$

$$F_{5\ddot{x}_g} = m_5\ddot{x}_5 + c_5(\dot{x}_5 - \dot{x}_4) - c_6(\dot{x}_6 - \dot{x}_5) + k_5(x_5 - x_4) - k_6(x_6 - x_5) \quad (5.21)$$

$$F_{6\ddot{x}_g} = m_6\ddot{x}_6 + c_6(\dot{x}_6 - \dot{x}_5) - c_7(\dot{x}_7 - \dot{x}_6) + k_6(x_6 - x_5) - k_7(x_7 - x_6) \quad (5.22)$$

$$F_{7\ddot{x}_g} = m_7\ddot{x}_7 + c_7(\dot{x}_7 - \dot{x}_6) - c_8(\dot{x}_8 - \dot{x}_7) + k_7(x_7 - x_6) - k_8(x_8 - x_7) \quad (5.23)$$

$$F_{8\ddot{x}_g} = m_8\ddot{x}_8 + c_8(\dot{x}_8 - \dot{x}_7) - c_9(\dot{x}_9 - \dot{x}_8) + k_8(x_8 - x_7) - k_9(x_9 - x_8) \quad (5.24)$$

$$F_{9\ddot{x}_g} = m_9\ddot{x}_9 + c_9(\dot{x}_9 - \dot{x}_8) + k_9(x_9 - x_8) \quad (5.25)$$

5.1.3. SSTL RTHS Testing Facility Description

At the Smart Structures Technology Laboratory (SSTL, http://sstl.cee.illinois.edu), the RTHS setup utilizes a 125 kip actuator, manufactured by the Shore Western Corporation. A three-stage servo-valve, is used to control the actuator, constructed using both a Schenck-Pegasus model 1800 servo-valve and a model 20B two-stage servo-valve. The servo-valves are rated at 80 gpm and 0.86 gpm, respectively. The actuator and specimen (MR damper) are both mounted in a test frame designed to minimize backlash and elastic deformation under the high forces expected during testing. A Shore Western model 1104 digital servo-controller is used to control the actuator in displacement feedback mode. The actuator is controlled by using a model-based feed-forward feed-back control strategy (Phillips et al., 2011). The servo-controller accepts externally generated commands from a dSPACE model 1103 digital signal processing (DSP) board. This board is used to perform numerical integration of the equations of motion for the analytical substructure, apply the RTHS delay compensation techniques, and compute the desired current for the MR damper based on semi-active control laws. The Simulink model of the proposed RTHS is transferred to the DSP board. Real-time execution of the code is controlled and monitored from the host computer. The host computer also acts as the DAQ, logging data from specified channels within the Simulink model.

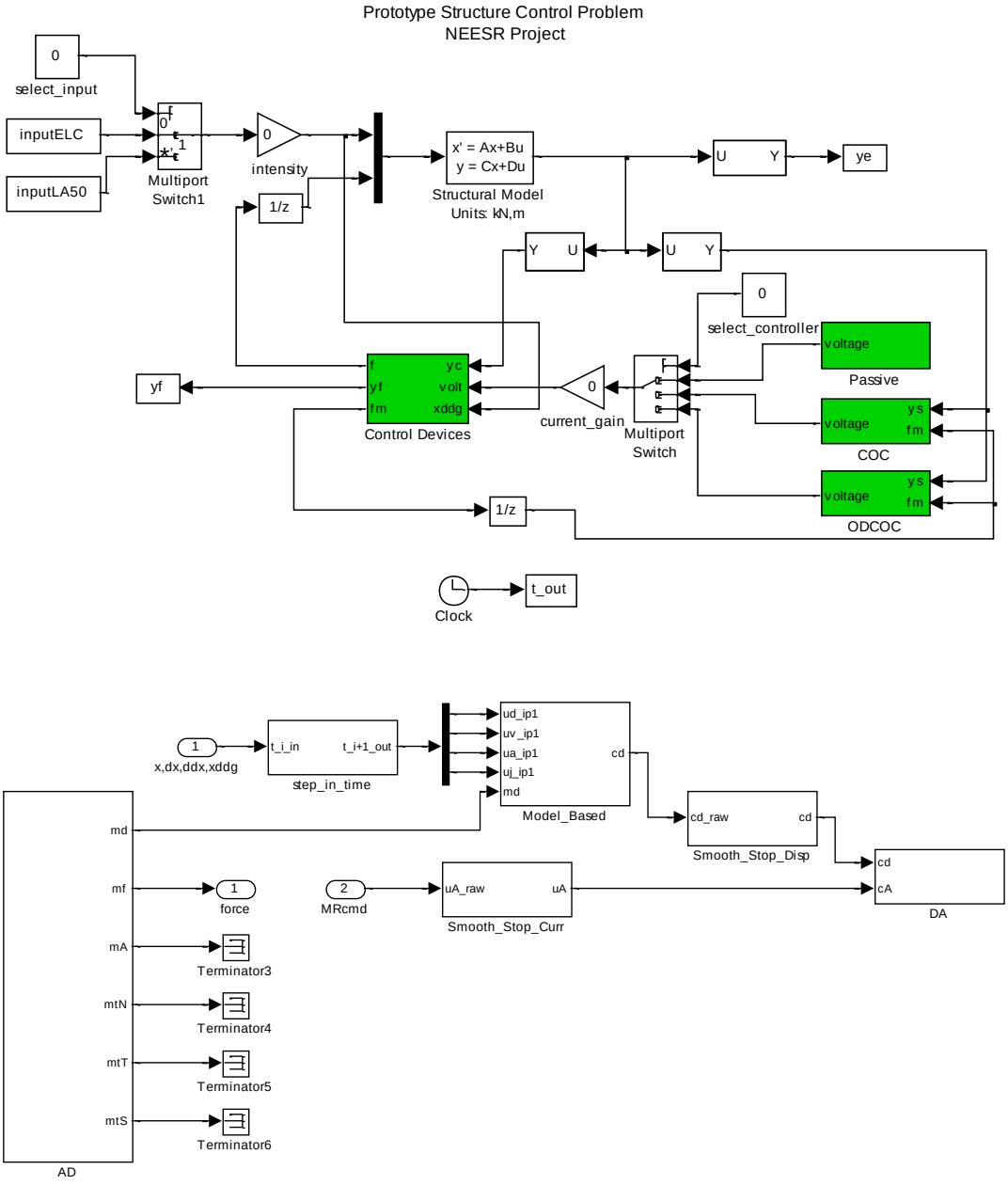

Figure 5.4: Representative RTHS Simulink Diagram

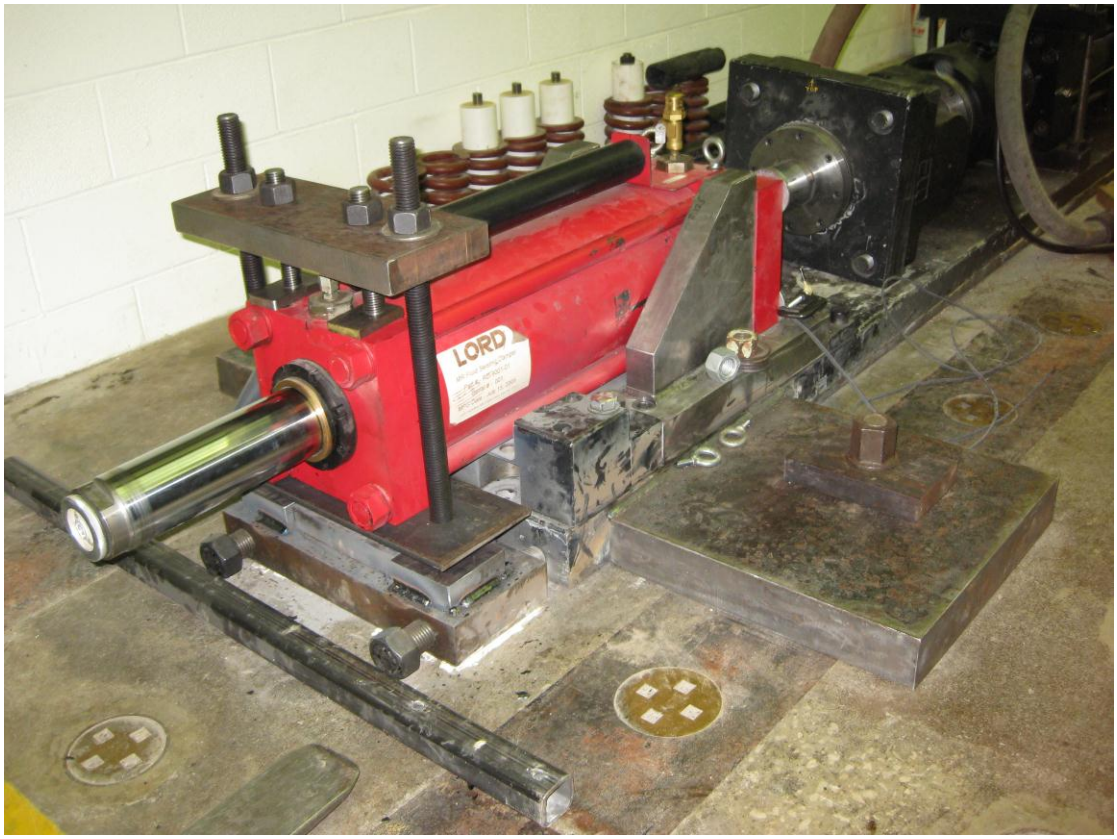

Figure 5.5: UIUC RTHS setup

5.1.4. NEES@Lehigh RTHS Testing Facility Description

The RTHS testing facility at Lehigh University used for the testing discussed in this chapter is described in Chapter 4. However, more instrumentation, including accelerometers, LVDTs, strain gages, etc. is installed to account for the required measurements associated with the additional MR damper between the first and second floors.

5.2. Phase I RTHS - MR Damper (UIUC)

In this section, the first phase of RTHS involving the nine-story benchmark structure is discussed. The RTHS is performed at the SSTL facility at the University of Illinois – Urbana/Champaign. The large-scale MR damper is taken as the physical substructure, and the nine story benchmark structure is modeled computationally using the finite-element approach previously described.

5.2.1. Phase I RTHS - MR Damper Identification

The large-scale MR damper used in the RTHS testing was identified using the procedure described in Chapter 4. It has been noted that although the dampers are all manufactured by Lord Corporation, there is some variance in performance between the dampers. As such, each damper model requires different parameters. The parameters for the large-scale damper at UIUC and a comparison of the performance of the model and the experimental damper are summarized in Table 5.1.

Table 5.1: MR Damper #3 model parameters

Phenomenological Bouc Wen Model Parameters			
Parameter	**Value**	**Parameter**	**Value**
α_A	950.4 kN	c_{1A}	100 kN·sec/m
α_B	-0.0098 kN	c_{1B}	28470 kN·sec/m
α_C	-934.3 kN	k_0	0.0559 kN/m
α_D	0.9376 kN	k_1	0.0641 kN/m
c_{0A}	277.4 kN·sec/m	x_0	0.01 m
c_{0B}	-0.0012 kN·sec/m	β	4430 m^{-1}
c_{0C}	-184.4 kN·sec/m	γ	4430 m^{-1}
c_{0D}	-1.13 kN·sec/m	A	336.56
		n	2

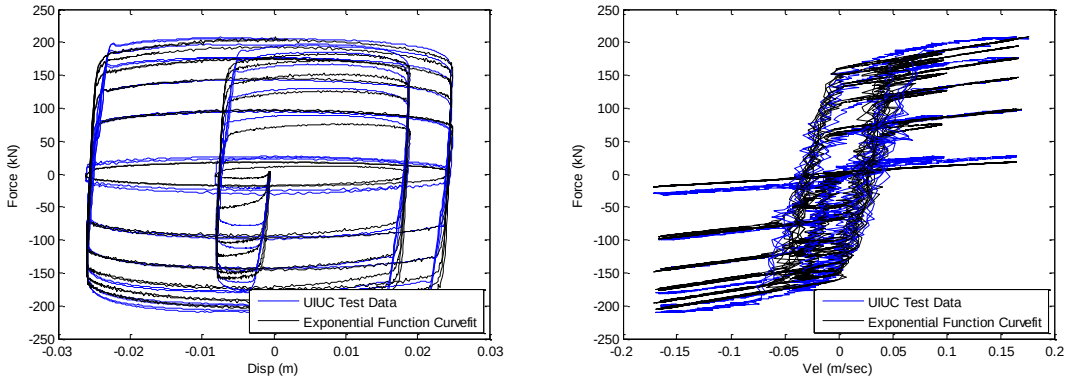

(a) **(b)**

Figure 5.6a-b: Comparison of (a) Force vs. Displacement and (b) Force vs. Velocity for the experimental damper and the numerical model

5.2.2. Phase I RTHS - Experimental Results

In this section, the results from the Phase I RTHS are presented and evaluated. Two separate types of experimental testing are conducted: (1) evaluation/validation of large-scale RTHS testing and (2) evaluation/validation of MR damper controller performance. The MR damper controller performances are evaluated under two conditions: (i) performance under general earthquake excitation, using seismic inputs of varying magnitudes, and (ii) robust performance in the face of uncertainties in the structural system. The uncertainties are manifested by varying the mass of the total structure in several increments by adjusting the analytical model. The classes of controllers considered for this phase of RTHS are the same as those listed in Chapter 4.

5.2.2.1. RTHS Validation

To validate the RTHS testing in Phase I, a comparison of results between a RTHS and an equivalent numerical simulation is made. Figure 5.5 and 5.6 show the comparison of several structural responses, including the 1st floor displacement and acceleration, for numerical simulation and RTHS. From this figure, it is clear that the RTHS simulations compare very well with the numerical simulation.

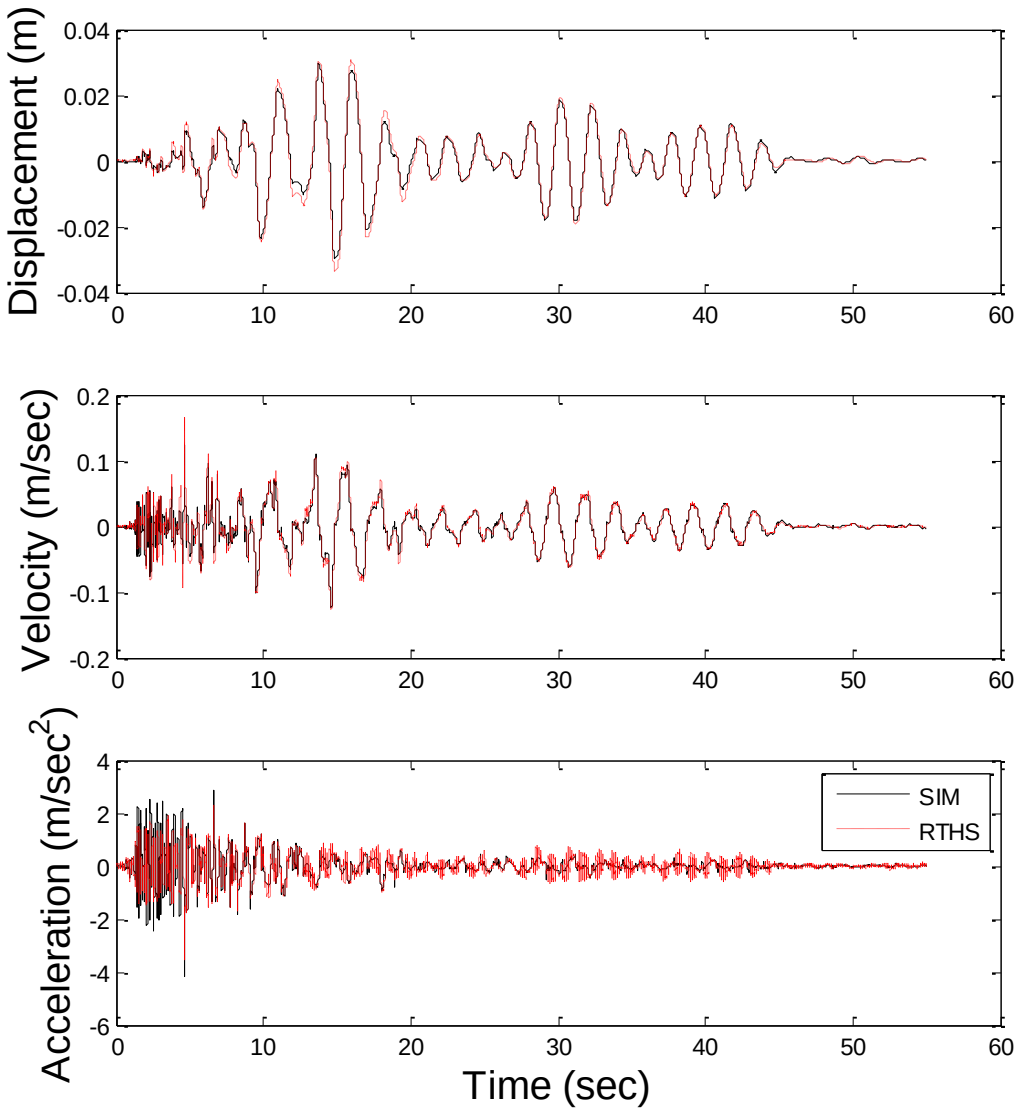

Figure 5.7: Time History Comparison of Simulation/RTHS 1st Floor Responses

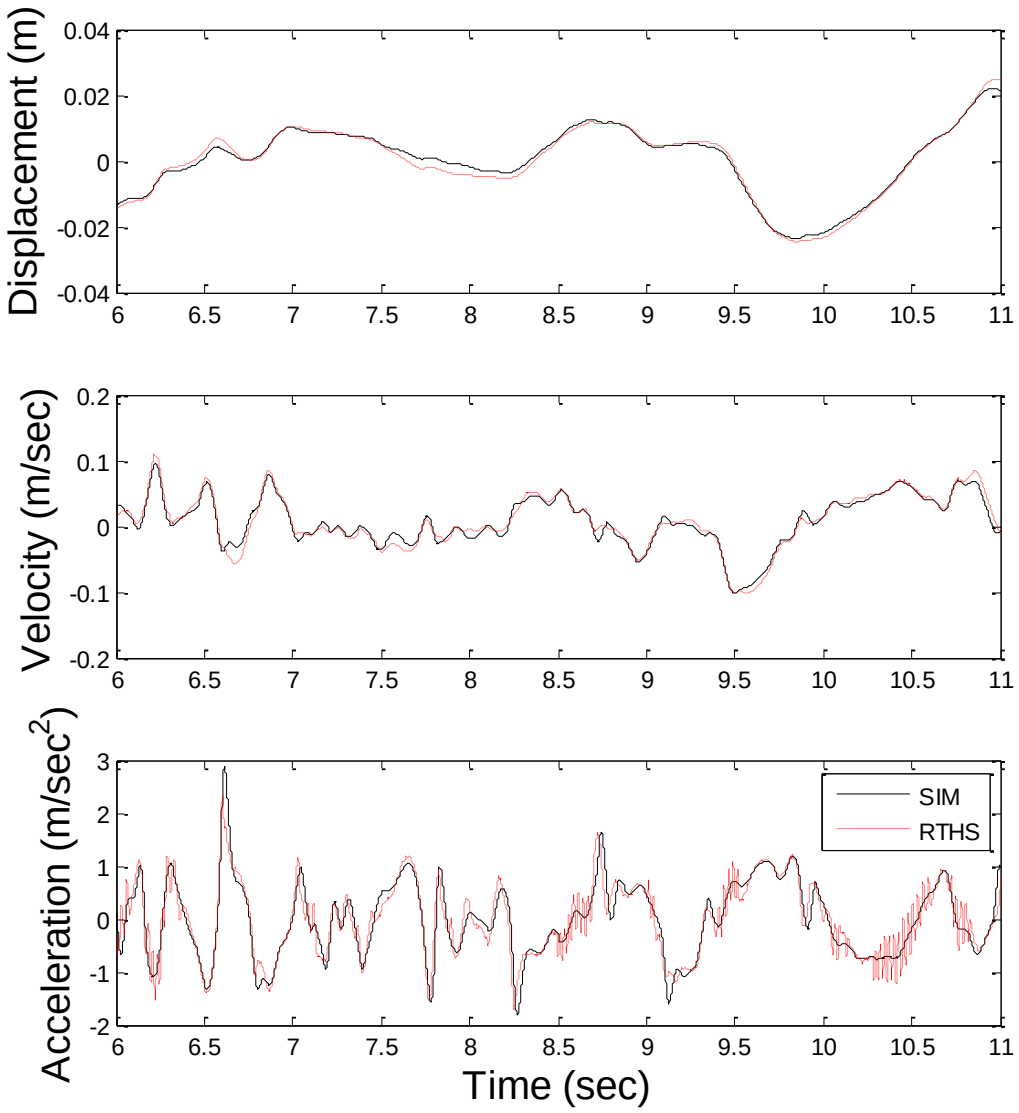

Figure 5.8: Time History Comparison of Simulation/RTHS 1st Floor Responses

5.2.2.2. MR Damper Controller Evaluation

The second test in the Phase I RTHS concerns evaluating the effectiveness of various control strategies for large-scale MR dampers. Several methods of appraisal are used, including: (1) numerical simulation using general earthquake excitation, (2) RTHS using a large-scale 200 kN MR damper as the physical substructure, and (3) numerical simulation to test the robust performance of the control strategies. All numerical simulations are performed using SIMULINK, a block diagram style tool included with MATLAB (Mathworks, 2012). Robust performance in a control strategy is a desirable trait because the as-built structure may vary from the intended design, or variations in the dynamics may occur over time. Because the control design is based on a model of the structure, there will be some differences between the design model and the structure on which the controller is implemented. Controllers which perform well despite these differences are more effective in practical applications. To simulate this difference, mass of the structure is varied from 80% to 120% of the original design,

Several input excitations, $\ddot{x}_g$, are used in the tests, including: (i) the NS component of the 1940 *El Centro* Earthquake, (ii) *SAC Small I Earthquake*, (iii) *SAC II Small Earthquake*, (iv) *SAC Medium I Earthquake*, (v) *SAC Medium II Earthquake*, and (vi) *SAC Large Earthquake.* The SAC ground motions are generated time histories for use in topical investigations, case studies, and trial applications in the SAC Phase 2 Steel Project (Los Angeles area, corresponding to seismic Zone 4).

The criteria for the evaluating controllers are based upon peak and RMS response characteristics of the structure, and in general, smaller values for the evaluation criteria are indicative of better performance. A summary of these criteria is presented in Table 5.2.

The test results are summarized in Tables 5.3-5.4 and Figures 5.9-5.10.

Table 5.2: Controller Evaluation Criteria

J Value	Equation	Description	J Value	Equation	Description
$\mathbf{J_1}$	$max_{EQ}\left\{\frac{\max_{t,i}\lvert x_i(t)\rvert}{x^{max}}\right\}$	Peak Floor Displacement Ratio of controlled maximum relative displacement to the uncontrolled value	$\mathbf{J_5}$	$max_{EQ}\left\{\frac{\max_{t,i}\lvert x_{RMS_i}(t)\rvert}{x_{RMS}{}^{max}}\right\}$	RMS Floor Displacement Ratio of controlled root mean square relative displacement to the uncontrolled value
$\mathbf{J_2}$	$max_{EQ}\left\{\frac{\max_{t,i}\frac{\lvert d_i(t)\rvert}{h_i}}{d_n^{max}}\right\}$	Peak Interstory Drift Ratio of controlled maximum interstory drift to the uncontrolled value	$\mathbf{J_6}$	$max_{EQ}\left\{\frac{\max_{t,i}\frac{\lvert d_{RMS_i}(t)\rvert}{h_i}}{d_{RMS_n}{}^{max}}\right\}$	RMS Interstory Drift Ratio of controlled root mean square interstory drift to the uncontrolled value
$\mathbf{J_3}$	$max_{EQ}\left\{\frac{\max_{t,i}\lvert \ddot{x}_{ai}(t)\rvert}{\ddot{x}_a^{max}}\right\}$	Peak Floor Acceleration Ratio of controlled maximum absolute acceleration to the uncontrolled value	$\mathbf{J_7}$	$max_{EQ}\left\{\frac{\max_{t,i}\lvert \ddot{x}_{RMS_{ai}}(t)\rvert}{\ddot{x}_{RMS_a}{}^{max}}\right\}$	RMS Floor Acceleration Ratio of controlled maximum absolute acceleration to the uncontrolled value
$\mathbf{J_4}$	$max_{EQ}\left\{\max_{t,i}\lvert f^i(t)\rvert\right\}$	Peak Control Force Ratio of the maximum device output force to the weight of the structure	$\mathbf{J_8}$	$max_{EQ}\left\{\max_{t,i}\lvert f_{RMS}{}^i(t)\rvert\right\}$	RMS Control Force Ratio of the maximum device output force to the weight of the structure

Table 5.3: Numerical Simulation Results Summary

Ground Motion	Controller	Evaluation Criteria							
		J1	J2	J3	J4 (kN)	J5	J6	J7	J8(kN)
El Centro PGA- 0.3g	PON	**0.67**	**0.457**	0.848	199	**0.419**	**0.331**	0.642	86
	COC	0.804	0.692	0.695	**183**	0.46	0.425	0.582	**51**
	ODCOC	0.766	0.646	**0.693**	214	0.434	0.402	**0.568**	57
SAC Small EQ I PGA - 0.15g	PON	**0.379**	0.417	0.843	176	**0.328**	**0.264**	0.523	78
	COC	0.411	0.409	0.697	**138**	0.374	0.348	0.473	**48**
	ODCOC	0.385	**0.39**	**0.634**	175	0.355	0.336	**0.463**	55
SAC Small EQ II PGA - 0.325g	PON	**0.838**	**0.628**	1.468	214	0.768	0.582	0.974	63
	COC	0.881	0.773	1.051	**170**	0.685	0.552	0.813	**37**
	ODCOC	0.848	0.759	**0.98**	186	**0.663**	**0.529**	**0.8**	39
SAC Medium EQ I PGA - 0.5g	PON	**0.457**	**0.369**	1.253	187	**0.388**	**0.303**	0.571	100
	COC	0.544	0.453	0.855	**164**	0.42	0.367	0.522	**58**
	ODCOC	0.53	0.446	**0.776**	182	0.403	0.354	**0.509**	60
SAC Medium EQ II PGA - 0.55g	PON	0.778	**0.618**	1.534	196	0.636	**0.466**	0.833	95
	COC	0.735	0.703	1.199	**160**	0.613	0.574	0.712	**52**
	ODCOC	**0.688**	0.649	**1.063**	177	**0.575**	0.535	**0.694**	61
SAC Large EQ I PGA - 1 g	PON	0.764	0.71	1.54	220	0.51	**0.412**	0.767	88
	COC	**0.709**	0.68	0.896	**168**	0.52	0.488	0.707	**50**
	ODCOC	**0.709**	**0.674**	**0.887**	212	**0.502**	0.481	**0.692**	56

Table 5.4: RTHS Results Summary

Ground Motion	Controller	Evaluation Criteria							
		J1	J2	J3	J4 (kN)	J5	J6	J7	J8 (kN)
El Centro PGA 0.3g	PON	**0.703**	**0.492**	0.841	199	**0.407**	**0.313**	0.609	71
	COC	0.844	0.759	0.736	**187**	0.466	0.46	0.57	**47**
	ODCOC	0.787	0.701	**0.707**	213	0.445	0.453	**0.56**	50
SAC Medium EQ II PGA 0.55g	PON	**0.712**	**0.587**	1.743	190	0.598	**0.427**	0.769	79
	COC	0.759	0.799	1.027	**172**	0.619	0.614	0.689	**51**
	ODCOC	0.721	0.72	**0.945**	188	**0.598**	0.607	**0.685**	56

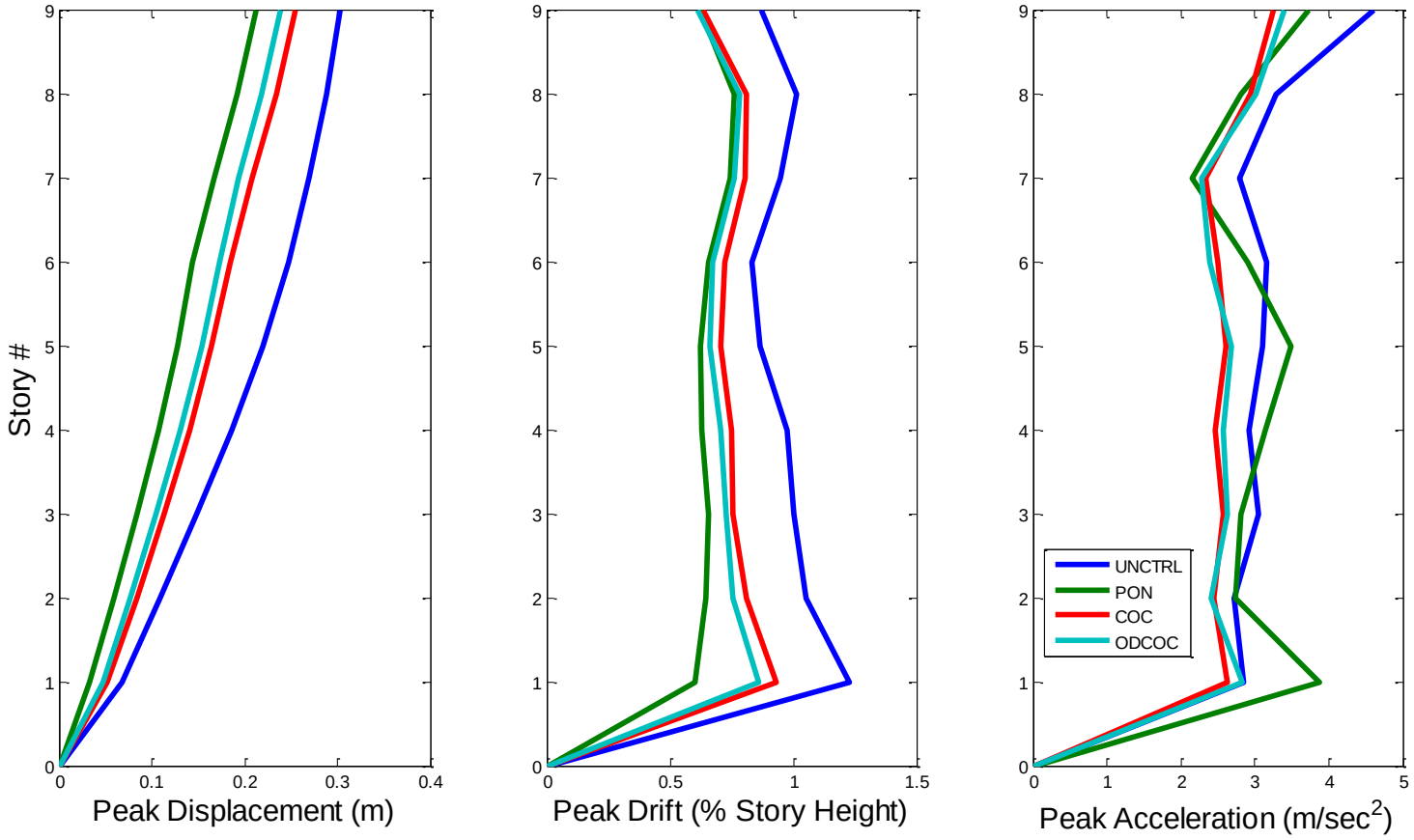

(a) **(b)** **(c)**

Figure 5.9: RTHS Response profiles for El Centro Earthquake

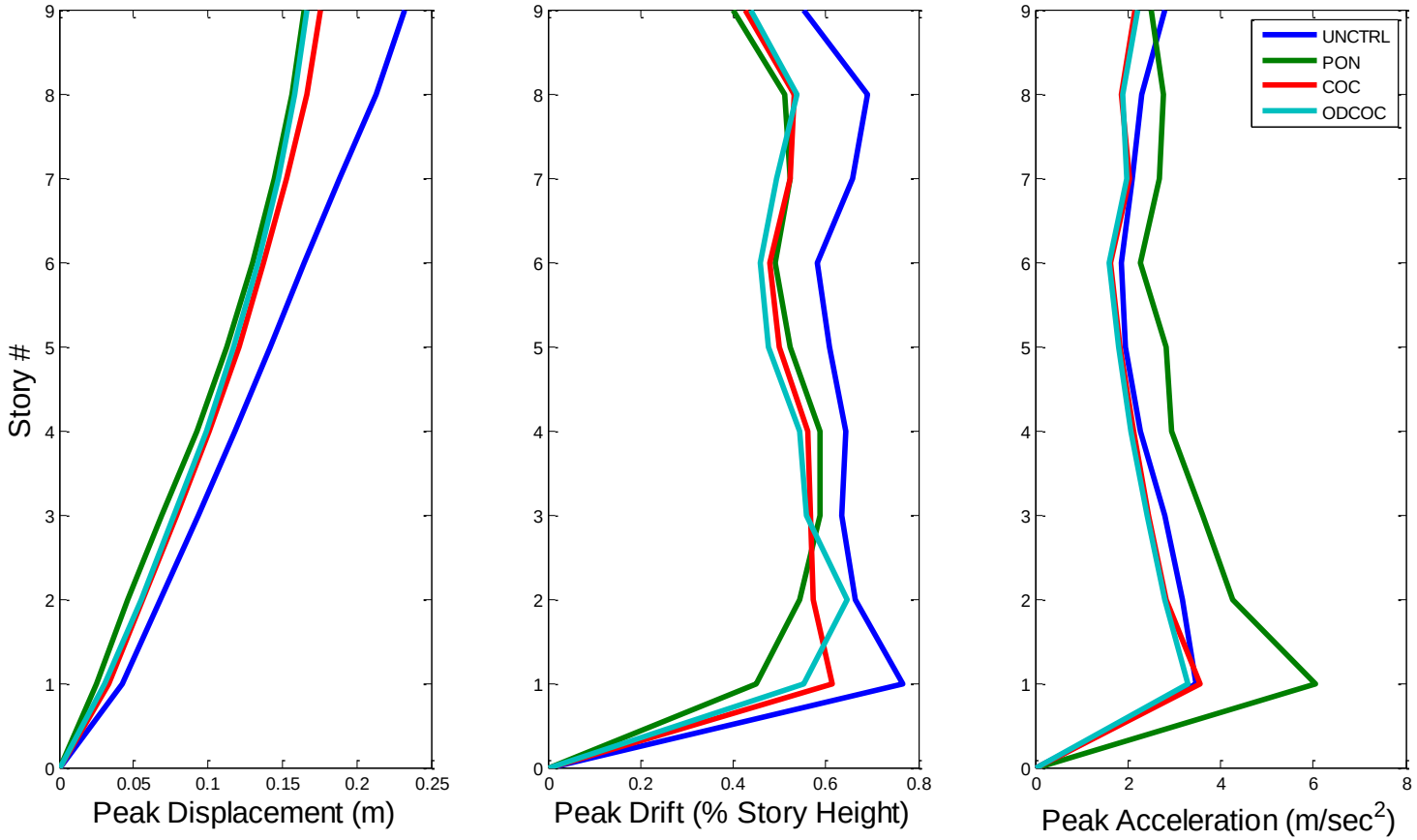

Figure 5.10: RTHS Response profiles for SAC Medium EQ II

Table 5.5: Robust Performance Simulation Results Summary

Ground Motion	% Mass	Controller	Evaluation Criteria							
			J1	J2	J3	J4 (kN)	J5	J6	J7	J8 (kN)
El Centro PGA 0.3g	**80%**	**PON**	**0.616**	**0.467**	0.957	**202**	**0.444**	**0.327**	0.616	83
		ODCOC	0.679	0.588	**0.768**	221	0.480	0.372	**0.568**	**68**
	90%	**PON**	**0.544**	**0.500**	0.755	**202**	**0.615**	**0.343**	0.671	85
		ODCOC	0.588	0.684	**0.611**	213	0.669	0.410	**0.604**	**64**
	95%	**PON**	**0.591**	**0.471**	0.744	**202**	**0.521**	**0.336**	0.656	88
		ODCOC	0.654	0.662	**0.605**	213	0.576	0.401	**0.574**	**60**
	100%	**PON**	**0.670**	**0.457**	0.848	**199**	**0.446**	**0.331**	0.642	86
		ODCOC	0.766	0.646	**0.695**	214	0.508	0.402	**0.568**	**57**
	105%	**PON**	**0.665**	**0.446**	0.857	200	**0.400**	**0.339**	0.643	82
		ODCOC	0.783	0.653	**0.705**	**215**	0.483	0.435	**0.587**	**54**
	110%	**PON**	**0.657**	**0.440**	0.862	**199**	**0.376**	**0.384**	0.687	79
		ODCOC	0.786	0.660	**0.709**	214	0.489	0.509	**0.644**	**53**
	120%	**PON**	**0.670**	**0.442**	0.890	**198**	**0.369**	**0.408**	0.696	78
		ODCOC	0.820	0.697	**0.736**	215	0.486	0.558	**0.657**	**51**
SAC Medium EQ II PGA 0.55g	**80%**	**PON**	0.473	0.397	1.263	**189**	**0.284**	0.358	0.656	108
		ODCOC	**0.425**	**0.394**	**0.977**	191	0.285	**0.332**	**0.551**	**75**
	90%	**PON**	**0.341**	**0.313**	1.047	**186**	**0.197**	**0.280**	0.541	102
		ODCOC	0.429	0.345	**0.654**	188	0.321	0.308	**0.474**	**67**
	95%	**PON**	**0.369**	**0.336**	1.117	**187**	**0.276**	**0.244**	0.477	101
		ODCOC	0.457	0.413	**0.687**	189	0.390	0.285	**0.426**	**64**
	100%	**PON**	0.778	**0.618**	1.534	196	0.573	**0.466**	0.833	95
		ODCOC	**0.688**	0.649	**1.063**	**177**	**0.481**	0.535	**0.694**	**61**
	105%	**PON**	**0.556**	**0.465**	1.232	186	**0.570**	**0.401**	0.717	99
		ODCOC	0.616	0.534	**0.787**	**181**	0.576	0.456	**0.629**	**59**
	110%	**PON**	**0.615**	**0.609**	1.269	**187**	0.605	**0.522**	0.870	101
		ODCOC	0.678	0.704	**0.842**	192	**0.539**	0.552	**0.733**	**55**
	120%	**PON**	0.897	0.794	1.503	186	0.741	0.834	1.158	109
		ODCOC	**0.822**	**0.788**	**0.761**	**173**	**0.533**	**0.714**	**0.848**	**46**

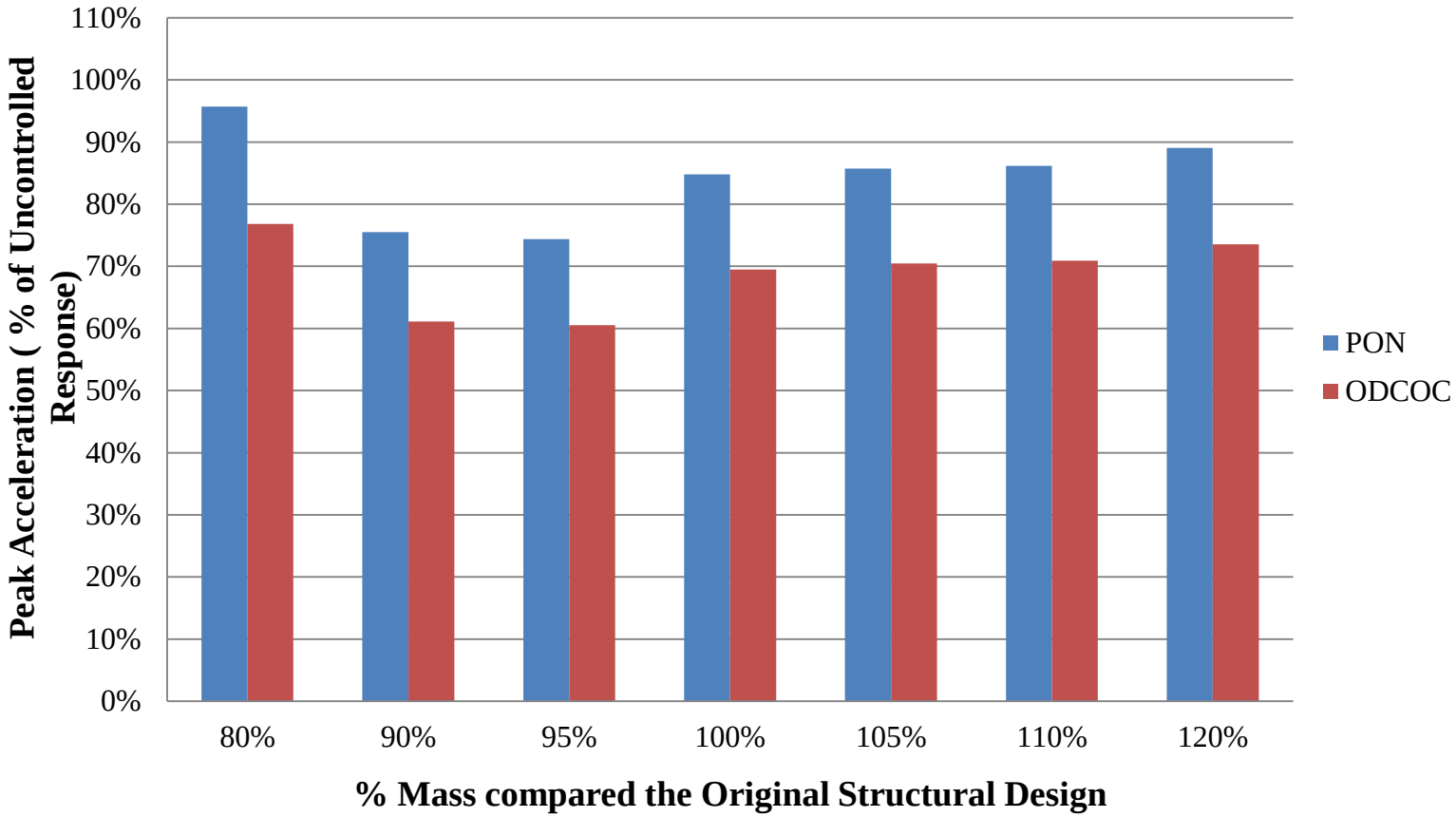

Figure 5.11: Simulation results to examine controller robustness

For control design purposes, the **R** matrix is selected to be an identity matrix of proper order, and a wide variety of **Q** matrices are arbitrarily chosen and tested using a 20 Hz band-limited white noise input. Based on the performance of these controllers, the weighting values are selected and implemented. Ultimately, both optimal controllers are designed to minimize the absolute acceleration output of all floors of the structure. The COC controller used a weighting value of 10000 m^2 on all floors for the **Q** matrix and the ODCOC used a more aggressive weighting value of 50000 m^2 on all floors for the **Q** matrix.

For the numerical simulations, in the case of the smaller earthquakes (including ELC and the Small SAC Earthquakes), the PON controller typically achieves greater reduction in peak relative displacement and drift. However, the ODCOC results in lower responses than COC for these categories, by an average of 3-4%. For peak absolute acceleration, the COC and ODCOC approaches yield lower responses than the PON controller, by an average of ~20%. The ODCOC is typically superior to COC by 5-6%. The COC does have the best performance in terms of peak and RMS force (indicating that this approach used the least amount of force to achieve response reduction), compared to the other two controllers. For peak total energy, there doesn't seem to be a clear trend, with PON and ODCOC being superior for different earthquakes. However, ODCOC is better than COC by 1-2% for each earthquake case, in each RMS category as well as total energy.

For the medium earthquakes cases, the ODCOC algorithm performs much better than both PON (an average 50% improvement) and COC (an average 15% improvement) in peak acceleration reduction. PON still has the edge in interstory drift reduction in both cases, by an average of 5%, though COC and ODCOC have much smaller RMS forces associated with them. COC has the best peak and RMS damper force, but as before, ODCOC achieves better reductions than COC in all other categories by an average of 3-4%.

For the SAC Large Earthquake case, the optimal control approaches achieve improved reductions in peak displacement and drift (5-6% vs. PON), peak absolute acceleration (~60% vs. PON), and RMS absolute acceleration (6-7% vs. PON). In all categories except force, ODCOC is better by a 2-3% average margin. Both semi-active controllers have smaller peak forces and RMS forces, as compared to PON.

When the mass of the structure is varied to demonstrate robustness, the ODCOC achieves a 15% greater reduction in peak absolute acceleration and uses lower peak forces as compared to the PON control approach. In addition, the RMS acceleration and damper force are much lower than PON, by average of 7% and 25 kN, respectively. In general, the PON control method is superior for displacement, drift, and total system energy.

The results of the RTHS tests confirm the controller performances shown in the numerical simulations. The PON control approach achieves the greatest reductions in peak displacement and interstrory drift. The ODCOC performs better than the COC by

an average of 5% in these categories. In terms of peak acceleration reduction, the ODCOC is the best controller by a wide margin (~20%). The reductions in RMS responses follow the same trends.

5.3. Phase II RTHS - Frame + Single MR Damper (Lehigh)

In this section, the second phase of hybrid testing is presented. For this RTHS, a portion of the first three floors of the structure, represented by a large-scale steel frame equipped with an MR damper, is utilized as the physical substructure. The rest of the structure, including the rest of the first three floors and the upper stories, is modeled computationally and included as the analytical substructure.

5.3.1. Phase II RTHS - MR Damper Identification

Through experimentation, it became apparent that there are noticeable differences in behavior between the MR damper installed at UIUC and the dampers being used at Lehigh University. The discrepancy is such that the parameters for the Bouc Wen model of the MR damper needed to be identified to better represent the dampers at Lehigh. The procedure for the identification is the same as described in Section 5.2.2. A summary of these parameters is presented in Table 5.6.

Table 5.6: Lehigh MR Damper Model Parameters

Phenomenological Bouc Wen Model Parameters			
Parameter	**Value**	**Parameter**	**Value**
α_A	687.7 kN	c_{1A}	100 kN·sec/m
α_B	0.006 kN	c_{1B}	15000 kN·sec/m
α_C	-697.6 kN	k_0	0.0559 kN/m
α_D	-0.91 kN	k_1	0.0641 kN/m
c_{0A}	201.3 kN·sec/m	x_0	0.01 m
c_{0B}	0. 1229 kN·sec/m	β	3000 m^{-1}
c_{0C}	-109 kN·sec/m	γ	3000 m^{-1}
c_{0D}	-2.116 kN·sec/m	A	336.56
		n	2

5.3.2. Phase II RTHS - Experimental Results

In this section, the results from the evaluation of the controllers, using numerical simulation and RTHS testing, are presented. Several control algorithms are considered for the MR damper, including: (1) PON, (2) COC, and (3) ODCOC. Two different types of experimental testing are conducted: (1) evaluation/ validation of large-scale RTHS testing and (2) evaluation/validation of MR damper controller performance. The MR damper controller performances are evaluated under general earthquake excitation, using seismic inputs of varying magnitudes.

5.3.2.1. RTHS Validation

To validate the RTHS testing, a comparison of test results for a RTHS test and an equivalent numerical simulation is made. Several structural responses, including the 1st floor displacement, acceleration, and the bracing displacement, are plotted both for numerical simulation and RTHS. From these figures, it is clear that the RTHS simulations compare very well with the numerical simulation.

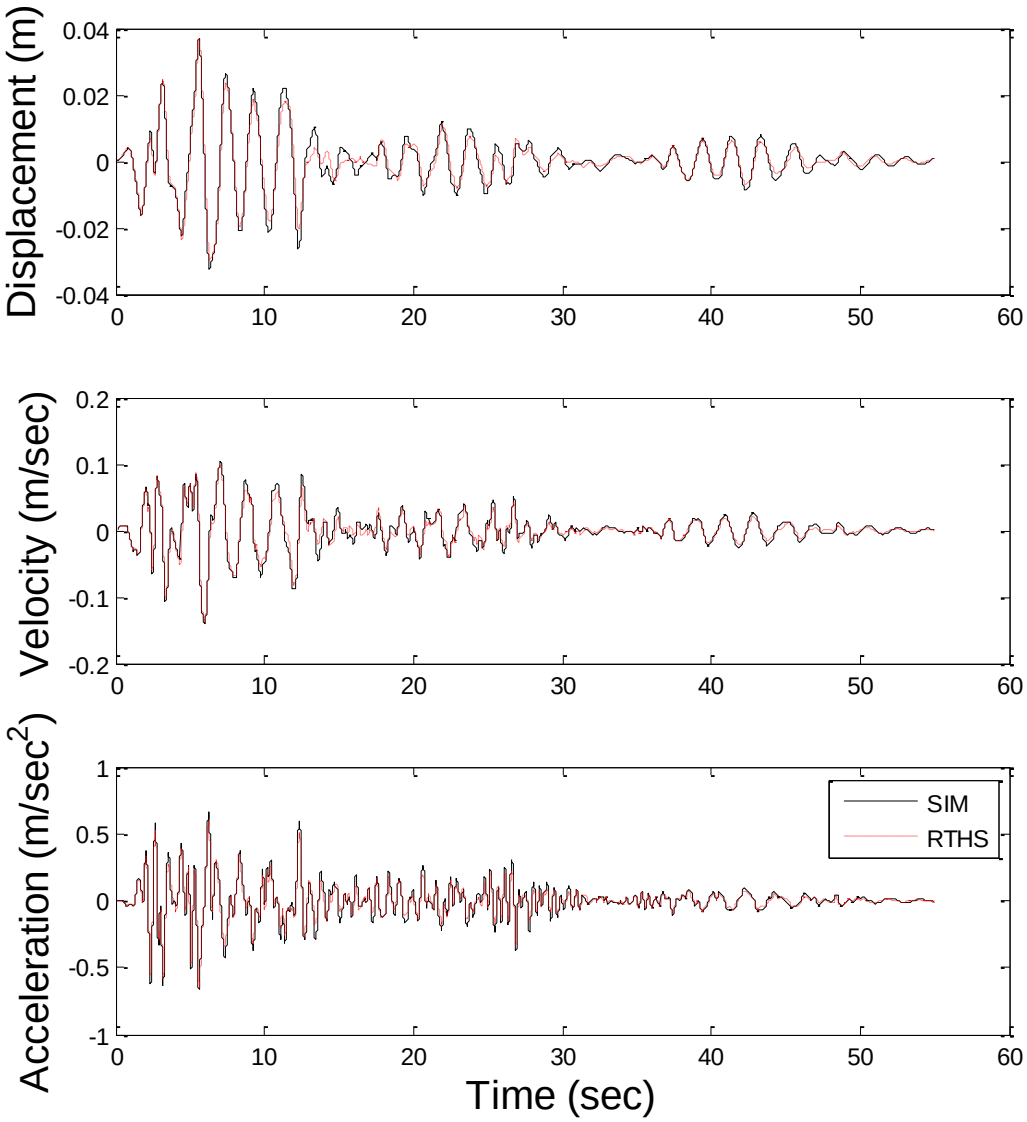

Figure 5.12: Time History Comparison of Phase II Simulation/RTHS 9th Floor Responses

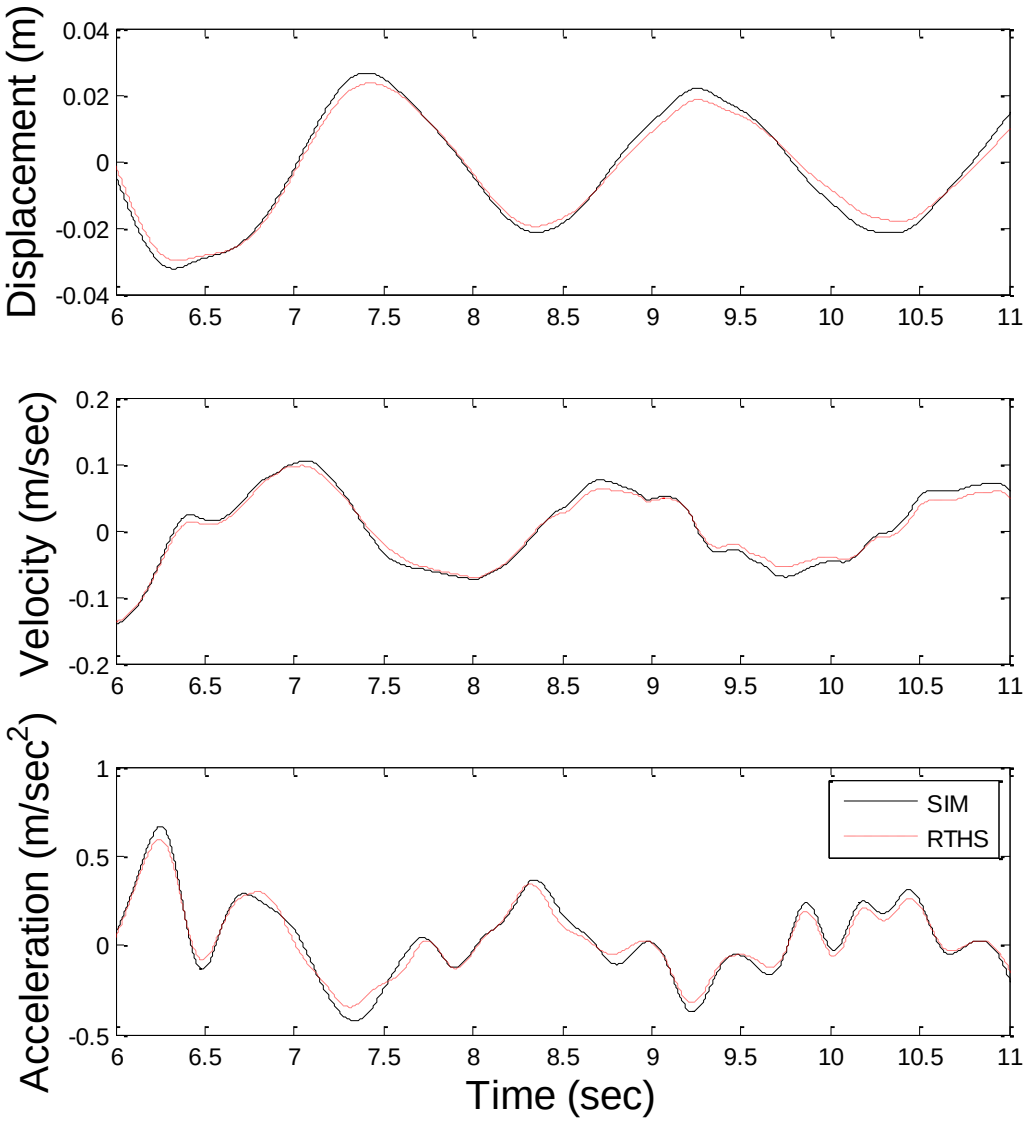

Figure 5.13: Time History Comparison of Phase II Simulation/RTHS 9th Floor Responses

5.3.2.2. MR Damper Controller Evaluation

To further validate the MR damper controller performance, a RTHS test using a large-scale steel frame (the same as previously described in Chapter 4) equipped with a single MR damper between the ground and 1st floor is used as the experimental substructure. The rest of the prototype structure (the portion of mass, damping, and stiffness not accounted for with the steel frame) is modeled as the analytical substructure, using a linear, finite element-based 3DOF model.

To evaluate the efficiency of the proposed controllers, several input excitations, $\ddot{x}_g$, are used in simulation, including: (i) *SAC Small I Earthquake*, (ii) *SAC II Small Earthquake*, (iii) the NS component of the 1940 *El Centro* Earthquake, (iv) *SAC Medium I Earthquake*, (v) *SAC Medium II Earthquake*, and (vi) *SAC Large Earthquake*. The SAC ground motions are generated time histories for use in topical investigations, case studies, and trial applications in the SAC Phase 2 Steel Project (Los Angeles area, corresponding to seismic Zone 4). The evaluation criteria are the same as described in Table 5.2.

Table 5.7: Numerical Simulation Results

Ground Motion	Controller	Evaluation Criteria							
		J1	J2	J3	J4 (kN)	J5	J6	J7	J8 (kN)
SAC Small EQ I PGA - 0.15 g	**PON**	1.087	1.448	1.744	130	1.312	1.554	1.702	23
	COC	1.045	1.18	**1.287**	**79**	1.091	1.215	1.303	**13**
	ODCOC	**0.976**	**1.146**	1.351	99	**1.089**	**1.207**	**1.298**	14
SAC Small EQ II PGA - 0.325 g	**PON**	0.638	0.697	0.872	158	0.657	0.787	0.918	42
	COC	0.666	0.696	0.706	**120**	**0.624**	**0.698**	**0.786**	**28**
	ODCOC	**0.616**	**0.652**	**0.672**	123	0.63	0.703	0.791	29
El Centro PGA - 0.3 g	**PON**	0.725	0.753	0.977	168	0.641	0.762	0.911	40
	COC	0.726	0.723	0.795	**126**	0.632	0.706	**0.807**	**28**
	ODCOC	**0.67**	**0.685**	**0.759**	172	**0.619**	**0.701**	0.811	30
SAC Medium EQ I PGA - 0.5 g	**PON**	**0.63**	**0.653**	1.078	166	**0.576**	0.677	0.79	33
	COC	0.651	0.698	0.973	**124**	0.597	0.649	0.723	**22**
	ODCOC	0.647	0.693	**0.939**	158	0.591	**0.643**	**0.717**	**22**
SAC Medium EQ II PGA - 0.55 g	**PON**	**0.471**	0.571	0.885	173	**0.495**	0.593	0.735	50
	COC	0.535	0.572	**0.743**	**139**	0.539	0.597	**0.691**	**35**
	ODCOC	0.478	**0.536**	0.782	184	0.515	**0.587**	0.697	40
SAC Large EQ I PGA - 1 g	**PON**	0.924	1.029	1.155	190	0.811	0.959	1.115	43
	COC	0.906	**0.916**	0.976	**144**	0.807	0.895	**0.994**	30
	ODCOC	**0.902**	0.933	**0.953**	198	**0.781**	**0.891**	1.019	34

Table 5.8: RTHS Results

Ground Motion	Controller	Evaluation Criteria							
		J1	J2	J3	J4 (kN)	J5	J6	J7	J8 (kN)
SAC Small EQ I PGA - 0.15 g	PON	0.975	1.383	1.504	136	1.097	1.318	1.484	21
	COC	0.937	0.989	0.987	**77**	0.892	0.973	1.366	12
	ODCOC	**0.884**	**0.938**	**0.953**	78	**0.889**	**0.954**	**1.295**	**11**
SAC Small EQ II PGA - 0.325 g	PON	**0.643**	0.737	0.87	162	0.607	0.727	0.813	41
	COC	0.715	**0.762**	0.749	**145**	**0.596**	**0.638**	**0.669**	**26**
	ODCOC	0.723	0.768	**0.745**	146	0.61	0.649	0.672	26
El Centro PGA - 0.3 g	PON	**0.729**	0.82	0.932	182	**0.62**	0.745	0.822	39
	COC	0.744	0.704	0.734	**154**	0.628	0.687	0.705	**27**
	ODCOC	0.74	**0.701**	**0.681**	180	0.622	**0.68**	**0.695**	**27**
SAC Medium EQ I PGA - 0.5 g	PON	**0.659**	**0.724**	1.078	179	**0.594**	0.704	0.774	34
	COC	0.687	0.754	0.973	**156**	**0.621**	**0.666**	**0.679**	**22**
	ODCOC	0.692	0.754	**0.939**	155	0.633	0.679	0.692	**22**
SAC Medium EQ II PGA - 0.55 g	PON	**0.525**	**0.621**	**0.802**	185	**0.509**	**0.618**	**0.694**	50
	COC	0.686	0.804	0.862	**182**	0.651	0.709	0.711	**37**
	ODCOC	0.681	0.799	0.847	211	0.649	0.711	0.711	37
SAC Large EQ I PGA - 1 g	PON	0.914	1.11	1.125	198	0.797	0.959	1.022	43
	COC	0.857	**0.965**	0.89	**152**	**0.729**	**0.817**	**0.852**	25
	ODCOC	**0.845**	0.991	**0.879**	176	0.737	0.827	0.859	25

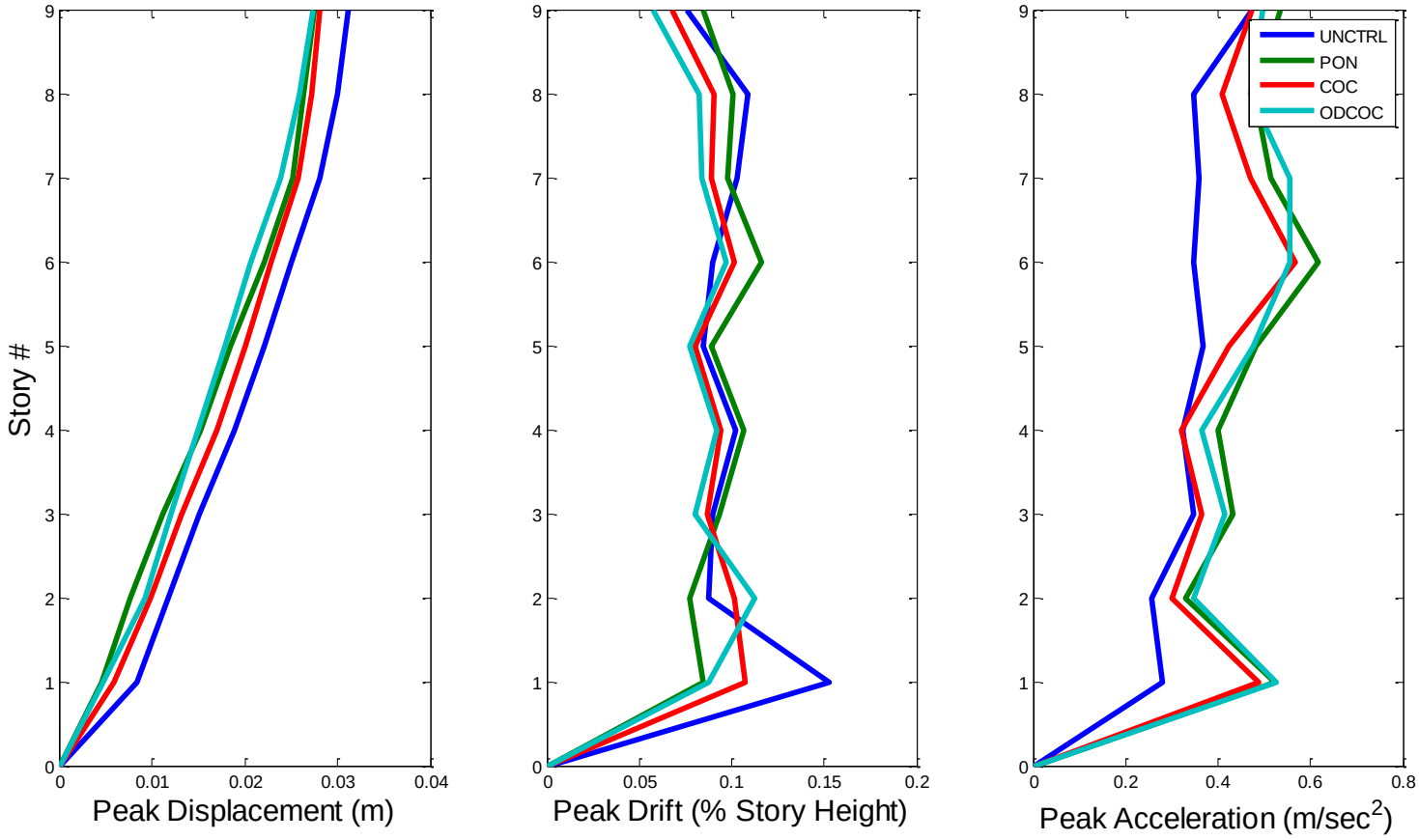

Figure 5.14: Response profiles for SAC Small EQ I

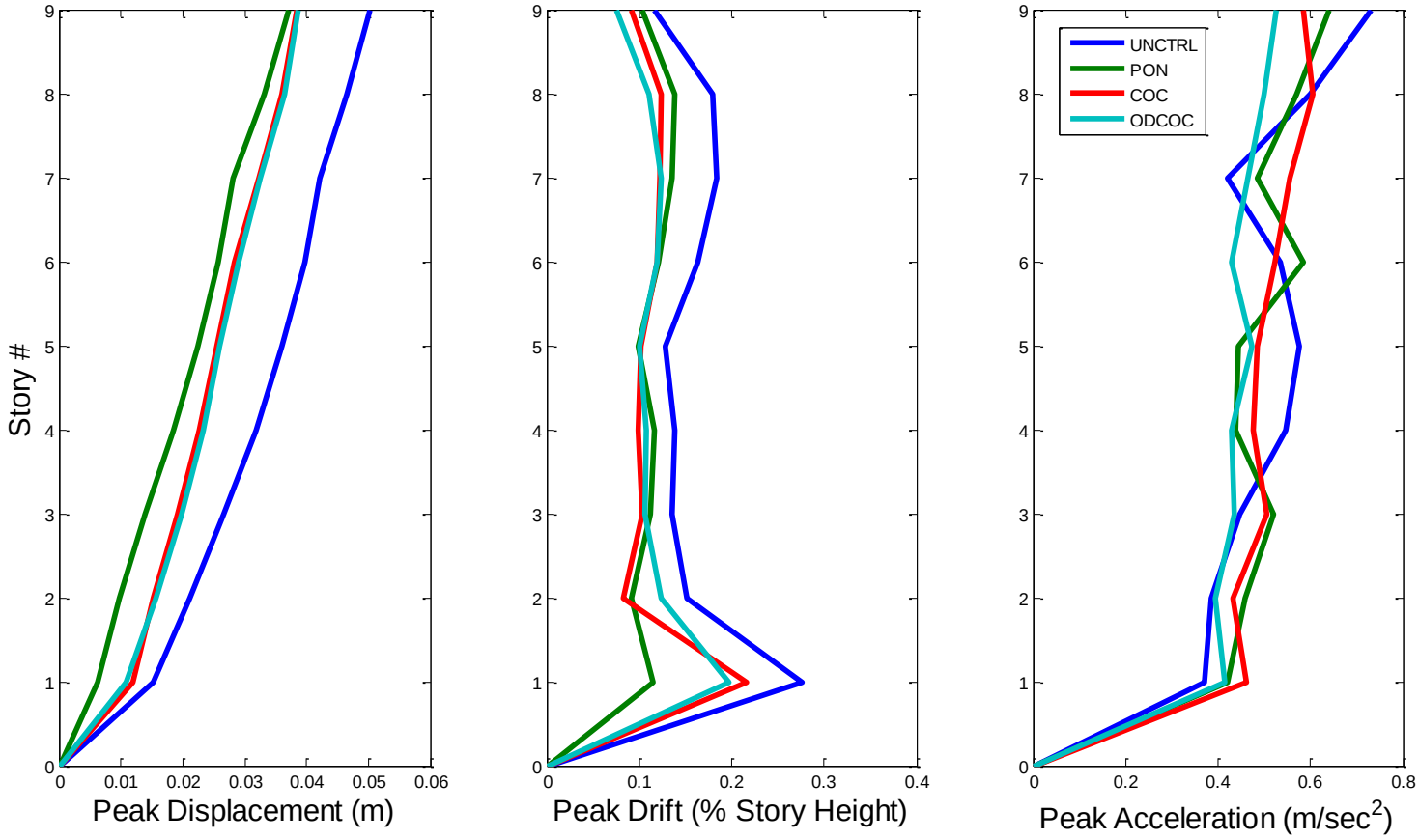

Figure 5.15: Response profiles for El Centro EQ

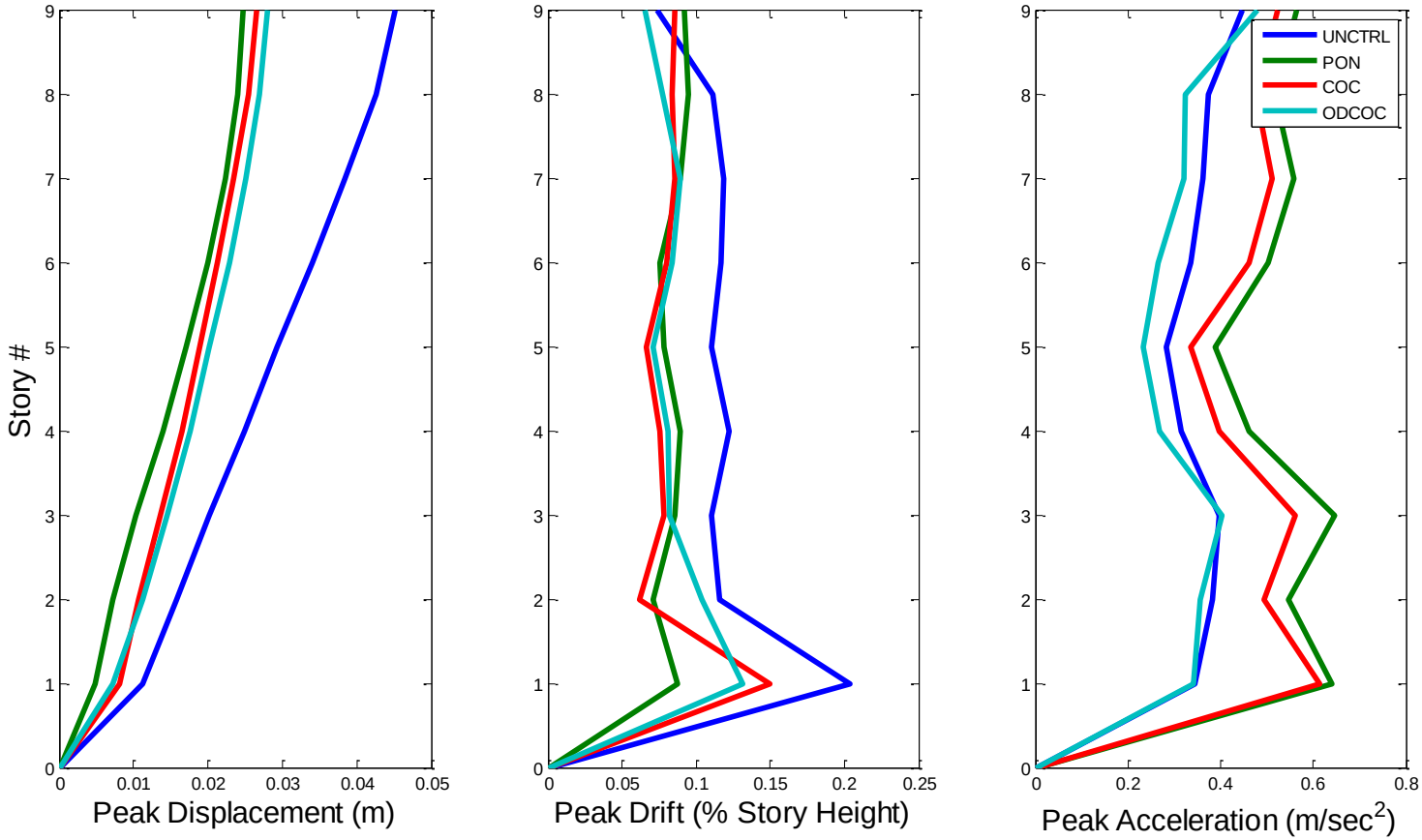

Figure 5.16: Response profiles for SAC Medium EQ I

The results of this study show that the ODCOC is the superior controller for acceleration response reduction. In general, there is an approximate 20% improvement in response as compared to the PON control approach, and a 10% improvement as compared to the COC control approach.

In terms of peak and RMS damper force, the semi-active controllers are always superior to the passive case, with a 25% reduction. COC uses a slightly lower peak force in every case, when compared to the ODCOC. However, both controllers have essentially the same RMS force over the course of each earthquake.

For the peak displacement and drift, there does not seem to be a clear trend that emerges from the data. The best performance varies between PON and ODCOC based on the earthquake input, and in general, the best controller maintains a 10% superior reduction versus the other controllers.

Though only a few representative plots are shown, comparisons show good agreement between the numerical simulation and RTHS time history results with each controller for each structural response.

5.4. Phase III RTHS - Frame + Dual MR Damper (Lehigh)

In this section, the third phase of hybrid testing is presented. For this RTHS, as before, a portion of the first three floors of the 9-story structure, as represented by a large-scale steel frame, is utilized as the physical substructure. In this case, two MR dampers are installed in the first floor and the second floor, respectively. The rest of the structure including the rest of the first three floors and the upper stories, is modeled computationally and included as the analytical substructure. RTHS simulation is performed using the same setup at the Lehigh RTHS facility, and the performance of each controller is evaluated.

5.4.1. Phase III RTHS - MR Damper / Brace Identification

To conduct this phase of testing, an additional two components had to be identified on the physical frame: the second MR damper, installed between the second and third floors of the frame, and the stiffness of the bracing between the second and third floors of the frame.

The MR damper is found to be sufficiently modeled using the previous Bouc Wen parameters specified in Section 5.3.3. In the same fashion, using the histogram plotting method previously outlined in Section 4.3.2.2, the stiffness of the bracing in the second floor is found to be the same as the first floor bracing, 48,615 kN/m. Both the MR Damper model and the bracing stiffness value are used in performing numerical simulation and developing the analytical models for the RTHS.

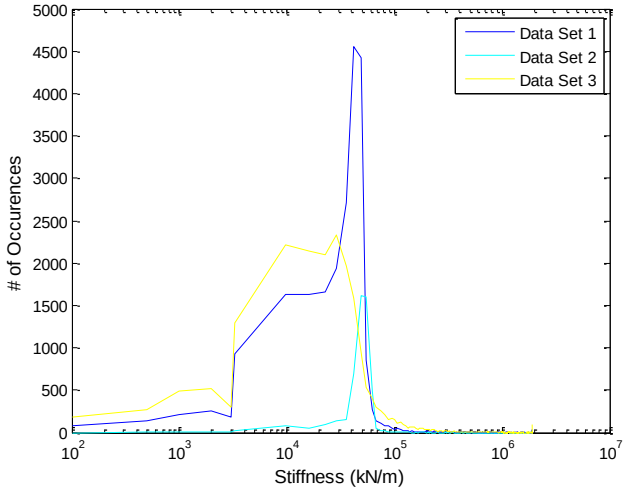

Figure 5.17: 2nd Floor Bracing Stiffness Histogram

5.4.2. Phase III RTHS - Experimental Results

In this section, the results from the evaluation of the controllers, using numerical simulation and RTHS testing, are presented. As before, two separate types of experimental testing are conducted: (1) evaluation/ validation of large-scale RTHS testing and (2) evaluation/validation of MR damper controller performance. The validation of the RTHS is performed using two different test scenarios: (1) comparisons between the RTHS and an equivalent numerical simulation and (2) testing to determine the repeatability of the RTHS testing method. The MR controllers are evaluated under two different conditions, including: (1) general earthquake excitation testing using seismic ground motions of different magnitudes and (2) testing to evaluate the robust performance of the controllers in uncertain circumstances (mass variation, in this case). Several control algorithms are considered for the MR damper, including: (1) PON, (2) COC, and (3) ODCOC. The evaluation criteria and the earthquake records remain the same.

5.4.2.1. RTHS Validation

To validate the RTHS testing, a comparison of test results for a RTHS test and an equivalent purely numerical simulation is made. Figures 5.18 and 5.19 shows the comparison of the 1st floor displacement and acceleration, respectively, for numerical simulation and RTHS. From this figure, it is clear that the RTHS simulations compare very well with the numerical simulation.

In addition, the results for the repeatability test show (Table 5.9 and Figure 5.20) that RTHS generates the same results during multiple runs of the same test.

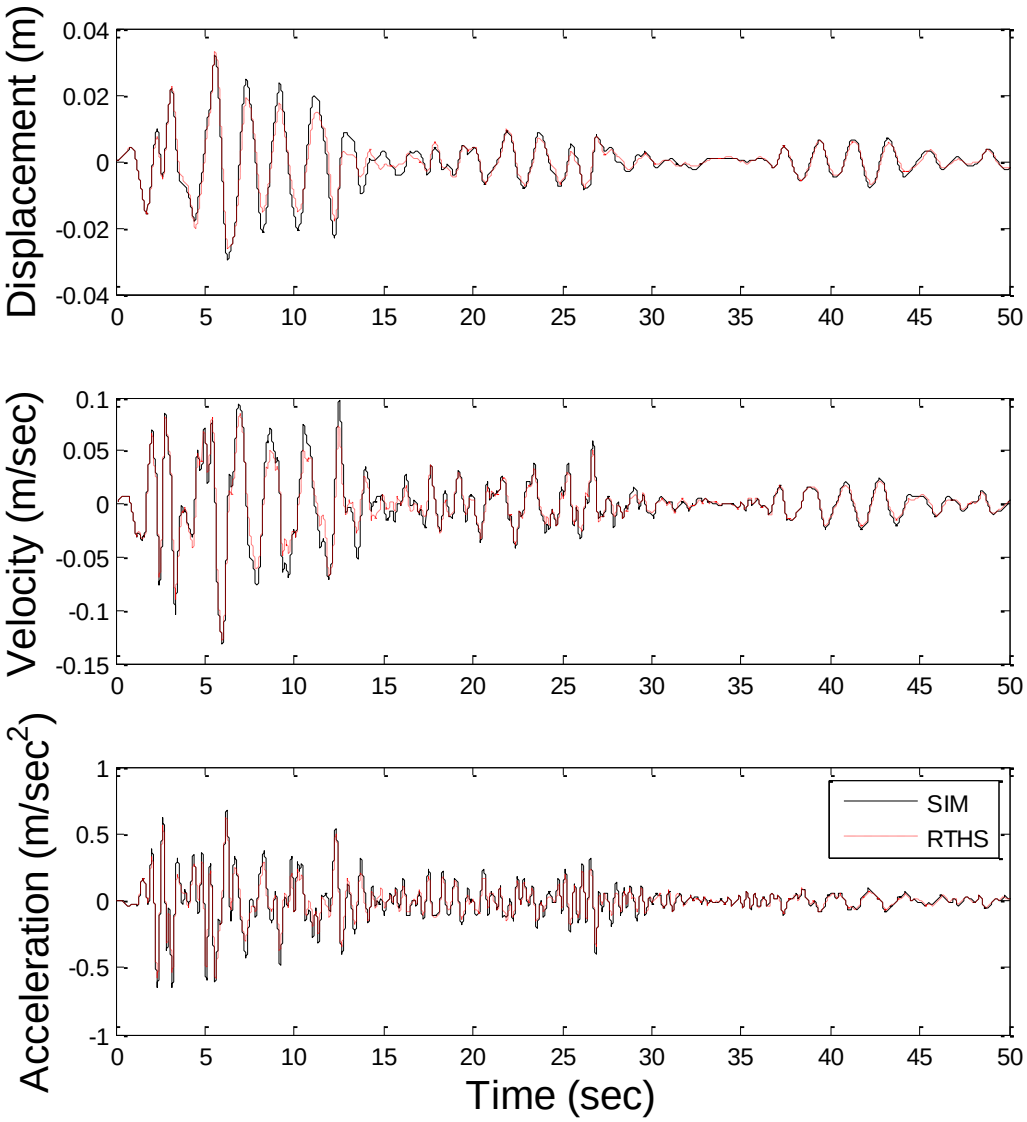

Figure 5.18: Time History Comparison of Phase III Simulation/RTHS 9st Floor Responses

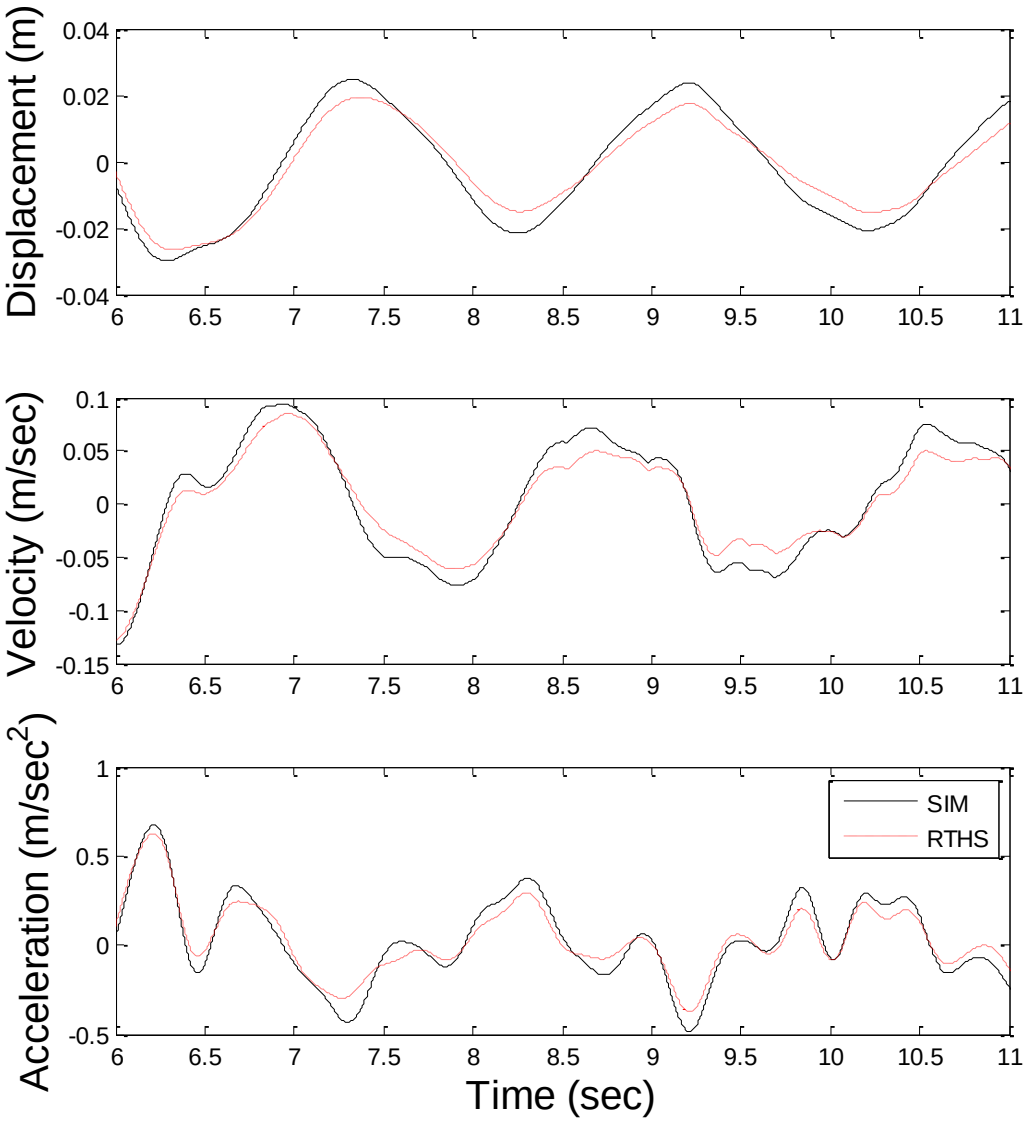

Figure 5.19: Time History Comparison of Phase III Simulation/RTHS 9st Floor Responses

Table 5.9: Comparison of RTHS Results to Evaluate Repeatability

Ground Motion	Controller		Evaluation Criteria							
			J1	J2	J3	J4 (kN)	J5	J6	J7	J8 (kN)
ELC PGA - 0.3 g	ODCOC	RTHS 1	0.830	0.606	0.747	72	0.694	0.634	0.735	15
		RTHS 2	0.833	0.606	0.767	68	0.694	0.638	0.741	15
		RTHS 3	0.851	0.619	0.780	71	0.704	0.648	0.744	14

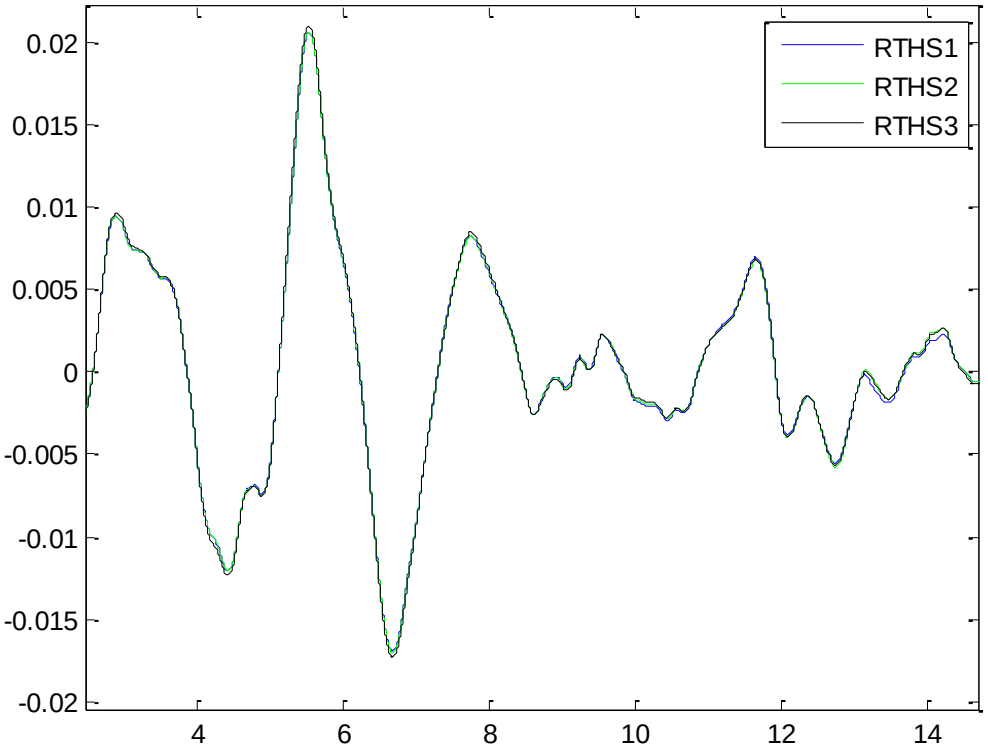

Figure 5.20: Time History Comparison for Three Identical RTHSs

5.4.2.2. MR Damper Controller Evaluation

To validate the MR damper controller performance, a RTHS test using the 9-story benchmark structure equipped with a two dampers is used. A large-scale steel frame equipped with two MR dampers between the ground / 1st floor and the 1st / 2nd floor is used as the experimental substructure. The rest of the benchmark structure (the portion of mass, damping, and stiffness not accounted for with the steel frame) is modeled as the analytical substructure, using a 9DOF model.

Table 5.10: Phase II Numerical Simulation Results

Ground Motion	Controller	Evaluation Criteria							
		J1	J2	J3	J4 (kN)	J5	J6	J7	J8 (kN)
SAC Small EQ I PGA - 0.15 g	**PON**	0.937	0.66	1.7	112	0.846	**0.5**	1.197	19
	COC	0.916	0.683	1.301	**86**	0.761	0.511	0.997	13
	ODCOC	**0.914**	**0.633**	**1.082**	93	**0.744**	0.524	**0.927**	**12**
SAC Small EQ II PGA - 0.325 g	**PON**	**0.54**	**0.39**	1.02	74	**0.624**	**0.348**	0.946	24
	COC	0.57	0.498	0.809	**58**	0.683	0.542	0.866	17
	ODCOC	0.653	0.607	**0.801**	68	0.752	0.659	**0.864**	**15**
El Centro PGA - 0.3 g	**PON**	**0.642**	**0.398**	1.027	125	0.684	**0.406**	1.001	30
	COC	0.719	0.578	0.851	**95**	**0.664**	0.531	0.806	19
	ODCOC	0.749	0.626	**0.797**	99	0.693	0.591	**0.791**	**17**
SAC Medium EQ I PGA - 0.5 g	**PON**	**0.525**	**0.378**	1.851	106	**0.513**	**0.284**	0.875	29
	COC	0.574	0.617	1.588	59	0.545	0.474	**0.781**	17
	ODCOC	0.658	0.642	**1.355**	**58**	0.597	0.541	**0.782**	**15**
SAC Medium EQ II PGA - 0.55 g	**PON**	1.021	0.622	1.001	143	0.976	**0.564**	1.059	37
	COC	0.96	**0.596**	**0.854**	99	0.884	0.623	0.901	23
	ODCOC	**0.928**	0.792	**0.855**	**74**	**0.851**	0.677	**0.86**	**18**
SAC Large EQ I PGA - 1 g	**PON**	0.858	0.97	1.828	150	**0.517**	**0.386**	1.21	30
	COC	**0.8**	0.724	1.216	**69**	0.552	0.48	0.894	19
	ODCOC	0.811	**0.721**	**1.179**	83	0.619	0.555	**0.886**	**18**

Table 5.11: Phase II RTHS Results

Ground Motion	Controller	Evaluation Criteria							
		J1	J2	J3	J4 (kN)	J5	J6	J7	J8 (kN)
SAC Small EQ I PGA - 0.15 g	**PON**	**0.851**	**0.581**	1.374	115	0.768	**0.484**	1.155	18
	COC	**0.851**	0.794	1.287	84	**0.706**	0.605	1.005	13
	ODCOC	0.872	0.813	**0.867**	**79**	0.719	0.644	**0.957**	**11**
SAC Small EQ II PGA - 0.325 g	**PON**	**0.518**	**0.353**	0.845	71	**0.611**	**0.391**	0.858	22
	COC	0.575	0.599	0.737	57	0.635	0.602	0.785	17
	ODCOC	0.649	0.557	**0.701**	**54**	0.685	0.679	**0.775**	**15**
El Centro PGA - 0.3 g	**PON**	**0.663**	**0.338**	0.983	134	**0.628**	**0.401**	0.891	28
	COC	0.765	0.619	0.848	81	0.644	0.615	0.754	18
	ODCOC	0.83	0.606	**0.747**	**72**	0.694	0.634	**0.735**	**15**
SAC Medium EQ I PGA - 0.5 g	**PON**	**0.512**	**0.413**	1.684	105	**0.479**	**0.343**	0.755	26
	COC	0.583	0.694	1.442	59	0.528	0.541	0.7	18
	ODCOC	0.608	0.738	**1.224**	**54**	0.562	0.595	**0.685**	**16**
SAC Medium EQ II PGA - 0.55 g	**PON**	0.977	**0.54**	0.974	142	0.898	**0.546**	0.959	32
	COC	0.939	0.588	0.803	84	**0.754**	0.654	**0.733**	20
	ODCOC	**0.934**	0.829	**0.757**	**57**	0.774	0.731	0.761	**16**
SAC Large EQ I PGA - 1 g	**PON**	**0.797**	0.833	1.877	152	0.5	**0.39**	1.197	29
	COC	0.808	0.838	1.201	80	**0.538**	0.554	0.865	18
	ODCOC	0.856	**0.692**	**1.123**	**66**	0.573	0.563	**0.833**	**16**

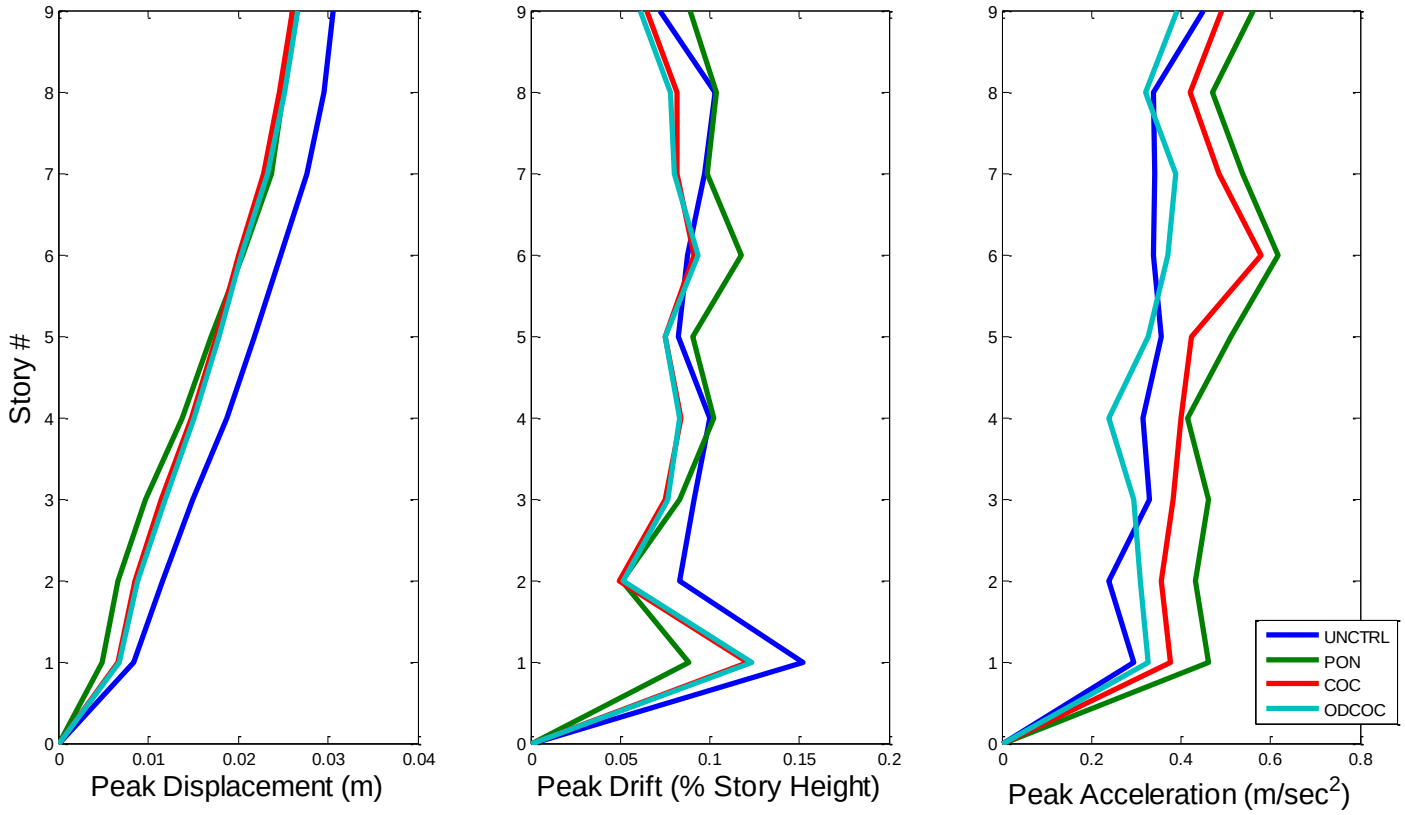

Figure 5.21: Response profiles for SAC Small EQ I

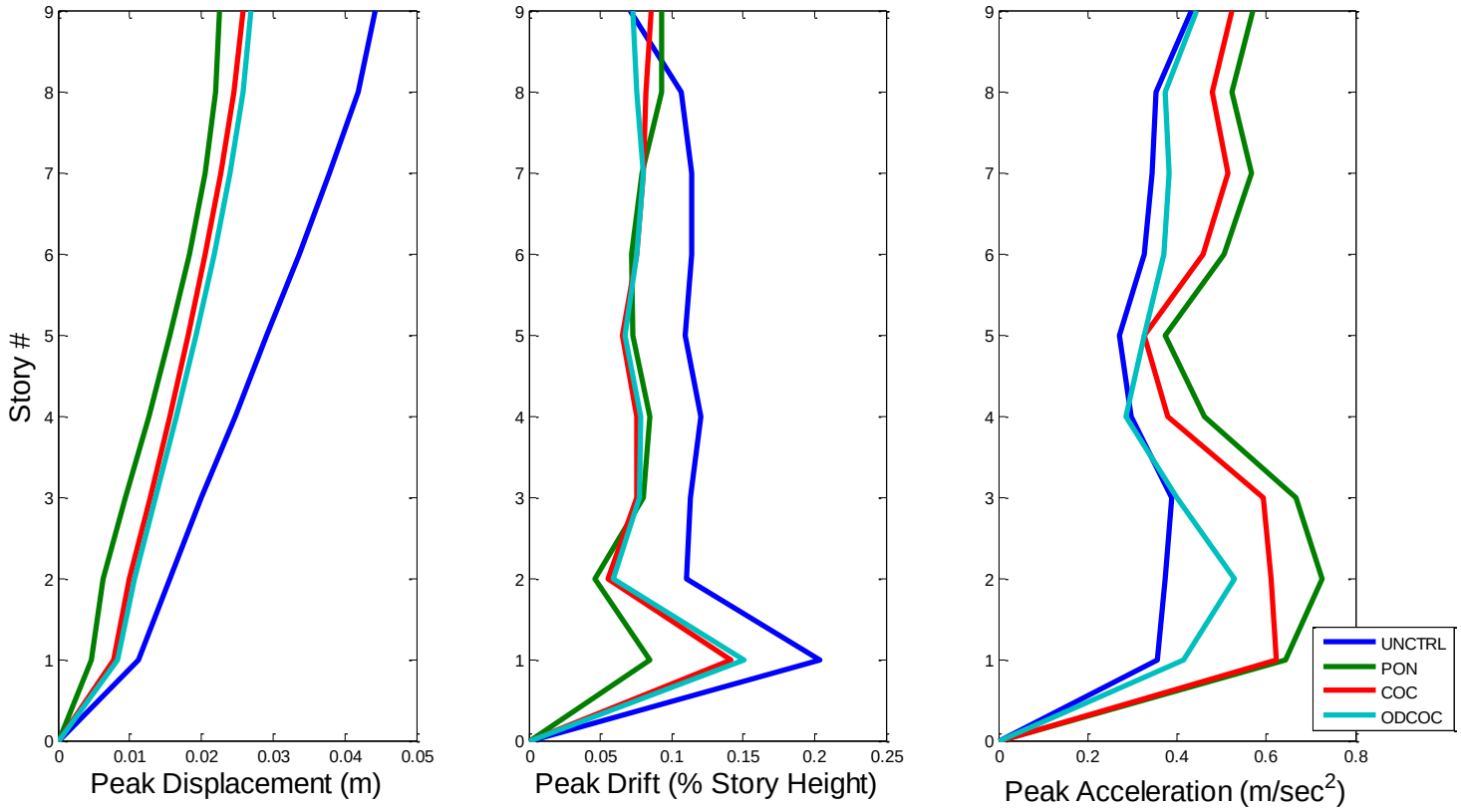

Figure 5.22: Response profiles for El Centro EQ

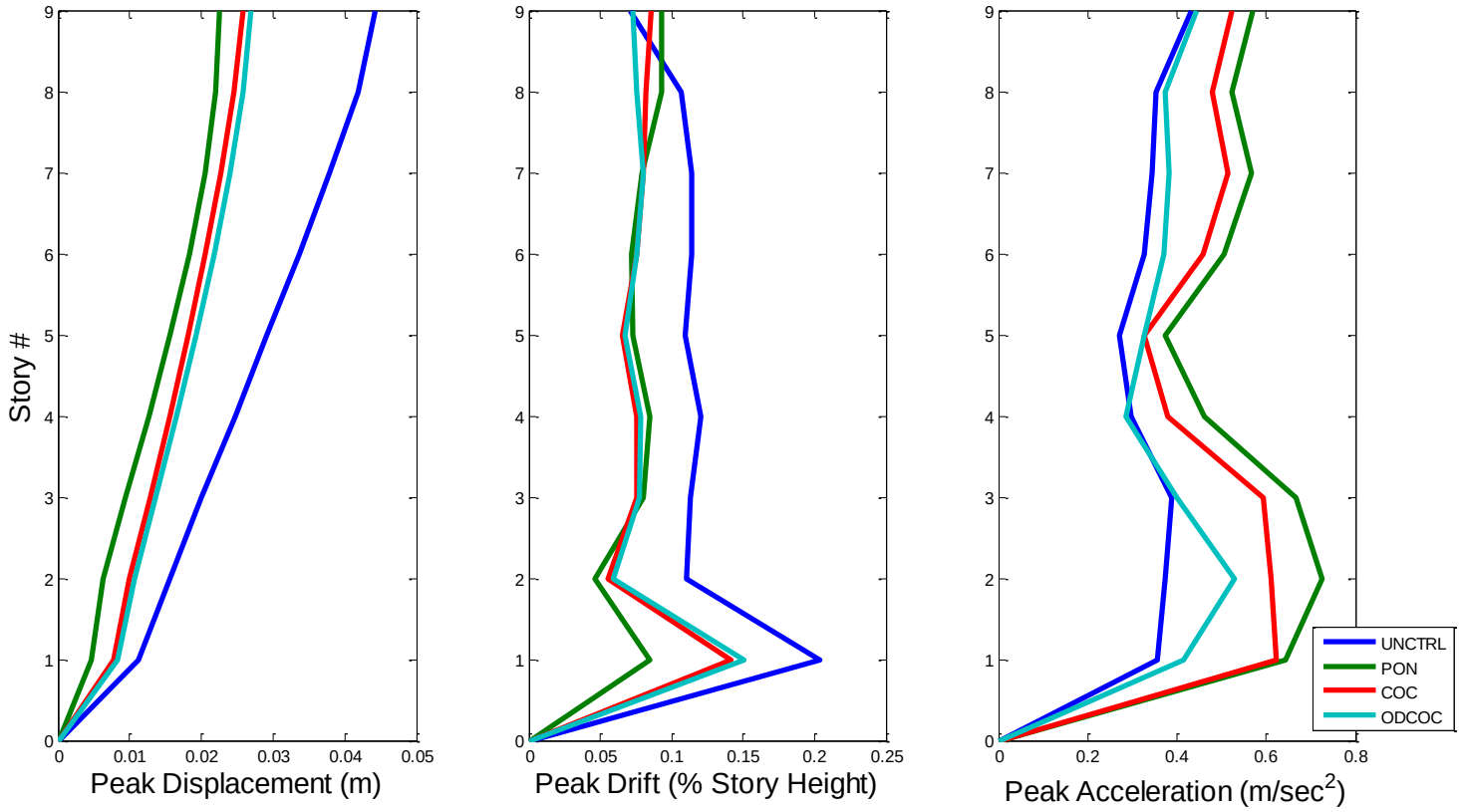

Figure 5.23: Response profiles for SAC Medium EQ I

Table 5.12: Robust Performance Test Results

Ground Motion	% Mass	Controller	Evaluation Criteria							
			J1	J2	J3	J4 (kN)	J5	J6	J7	J8 (kN)
SAC Small EQ I PGA 0.15g	80%	PON	0.861	**0.584**	1.410	118	0.837	**0.551**	0.995	20
		ODCOC	**0.825**	0.788	**1.036**	**76**	**0.792**	0.689	**0.942**	**13**
	90%	PON	**0.838**	**0.583**	1.464	116	0.798	**0.521**	0.924	18
		ODCOC	0.842	0.812	**0.948**	**79**	**0.744**	0.659	**0.860**	**12**
	95%	PON	**0.836**	**0.593**	1.447	113	0.773	**0.504**	0.884	18
		ODCOC	0.853	0.824	**0.885**	**77**	**0.726**	0.654	**0.825**	**11**
	100%	PON	**0.851**	**0.581**	1.374	115	0.768	**0.484**	0.867	18
		ODCOC	0.872	0.813	**0.867**	**79**	**0.719**	0.644	**0.802**	**11**
	105%	PON	**0.860**	**0.578**	1.178	107	0.744	**0.490**	0.823	17
		ODCOC	0.876	0.796	**0.776**	**76**	**0.715**	0.660	**0.773**	**11**
	110%	PON	**0.872**	**0.569**	1.107	119	0.741	**0.478**	0.802	17
		ODCOC	0.895	0.811	**0.800**	**76**	**0.718**	0.692	**0.759**	**10**
	120%	PON	**0.891**	**0.541**	1.090	121	**0.731**	**0.503**	0.760	16
		ODCOC	0.918	0.807	**0.767**	**70**	0.735	0.743	**0.744**	**10**

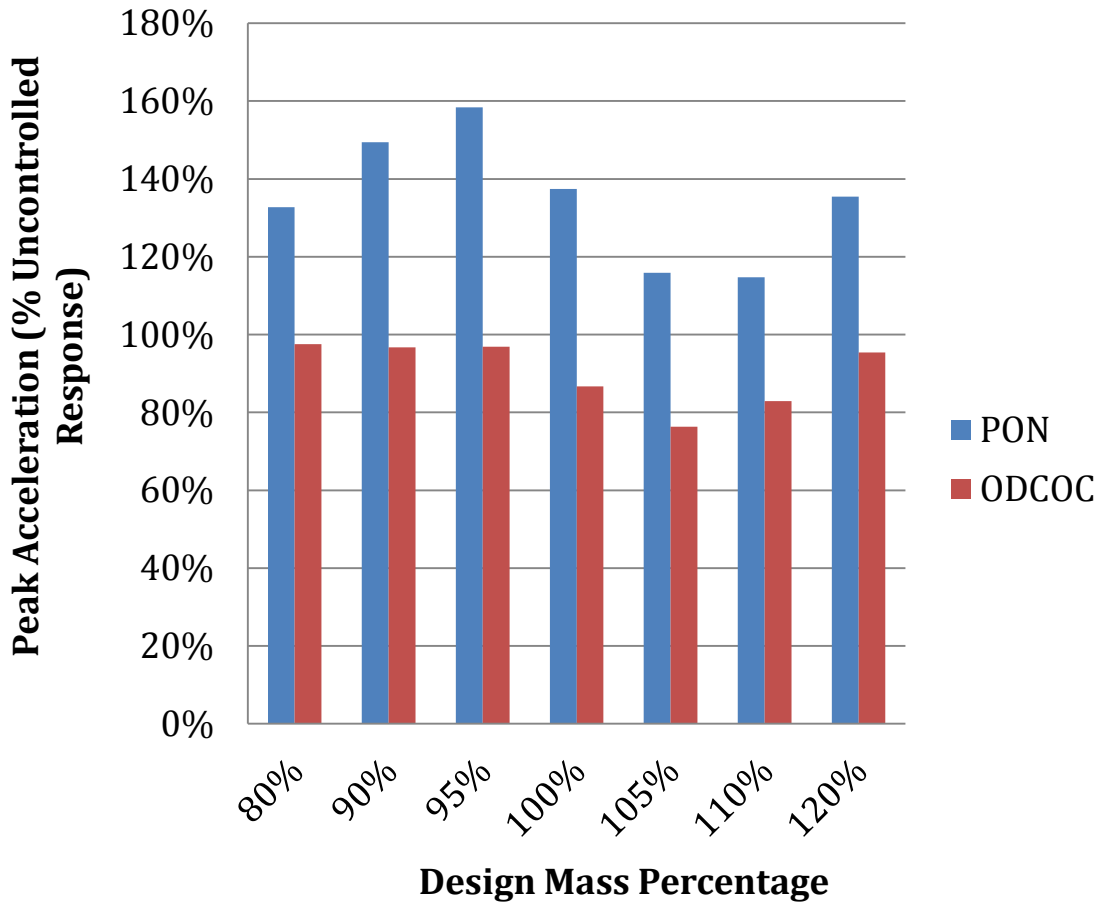

Figure 5.24: Comparison of RTHS Results to Examine Controller Robustness – Peak Absolute Acceleration

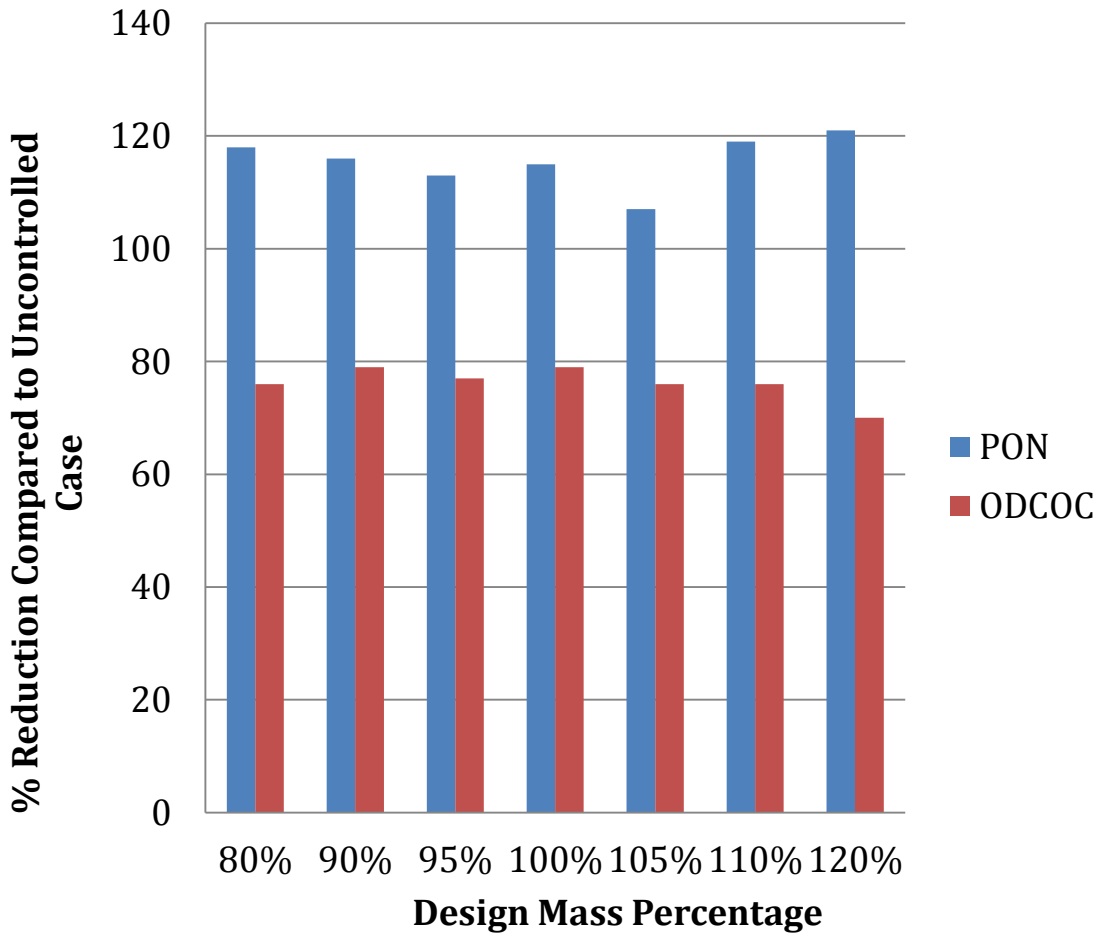

Figure 5.25: Comparison of RTHS Results to Examine Controller Robustness – Peak Damper Force

To design the optimal controllers, 20 Hz band-limited white noise single is used as the excitation for the structure. The **R** matrix is selected as an identity matrix of proper order and the **Q** matrix is chosen using a large set of weighting values. Both controllers (COC and ODCOC) are designed to minimize the absolute acceleration output of the structure, with equaling emphasis on all floors. Based on the performance of the structure, the COC controller used a weighting value of 70000 m^2 and the ODCOC used a value of 50000 m^2 for the **Q** matrix.

Based on the general earthquake input test results, several important trends emerge. For the smaller earthquake cases, the ODCOC controller achieves a greater reduction in peak absolute acceleration, with an average 25% improvement as compared to the PON controller, and an average 10% improvement when compared to the COC controller. In addition, the semiactive control methods utilize significantly less peak and RMS damper forces to achieve their respective performances, as compared to the passive approach. However, using PON control did yield greater reduction in peak relative displacement and drift. It should be noted that while the semiactive methods could not match the PON performance, the ODCOC results in lower responses than COC for these categories, by an average of 2-3%.

For the medium earthquakes cases, the ODCOC algorithm again performs much better than both PON (an average 25% improvement) and COC (an average 13% improvement) in peak acceleration reduction. PON still has the edge in interstory drift reduction in both cases, by an average of 10%, though COC and ODCOC still have much smaller forces (peak and RMS) associated with them.

For the SAC Large Earthquake case, ODCOC is clearly superior controller, with improved reductions in peak drift, peak acceleration, and damper force (both peak and RMS) compared to both PON and COC. Both semi-active controllers have smaller peak forces and RMS forces, as compared to PON.

These trends continue in the tests to evaluate controller robustness. In each test, ODCOC is the superior controller in terms of peak and RMS acceleration as well as peak and RMS damper force, by a wide margin. The PON control is superior for peak and RMS drift in all cases, and the best controller for peak and RMS displacement varies as the mass increases.

It should be noted that the interstory drift performance is a bit misleading. This particular structure has a "soft" story at the first floor, due to the increased height at this level. Thus, for every earthquake, the peak interstory drift occurs at the first floor. For the PON case, the damper uses greater force and essentially locks up the floor. Because the optimal controllers are designed to generate the best acceleration response for the overall structure, they generally allow a higher degree of flexibility in the first floor so the global response of the structure is improved. If this soft story is eliminated from consideration, the optimal controllers actually outperform the passive controller for both displacement and interstory drift, in general.

Finally, the results for the repeatability test show that the RTHS method is capable of generating the same results with multiple runs of the same test. The small variations can be explained from the noise in various components within the RTHS setup.

5.5. Conclusions

To further demonstrate the improved performance made possible with the ODCOC algorithm for the large-scale MR damper, a real-time hybrid simulation using a large-scale steel frame and a large-scale MR Damper (representing a nine-story benchmark structure designed in a previous study) is conducted. The study was conducted in three phases: (1) RTHS using a single MR damper as the physical substructure at the NEES@UIUC facility, (2) RTHS using a single damper mounted within a large-scale three-story steel frame at the first floor as the physical substructure at the NEES@Lehigh facility and (3) RTHS using a two MR dampers mounted within a large-scale three-story steel frame at the first and second floors as the physical substructure at the NEES@Lehigh facility. As before, the available measurements, some of which were used for feedback in the semi-active controllers, included actuator and damper forces, relative displacements, relative velocities, and absolute accelerations at each floor level, strain gage readings from several points on the frame, etc. Over the course of the phases of RTHS, three types of testing were conducted, including: (1) general earthquake excitation to determine the global responses of the system in order to evaluate the MR damper control performances, (2) testing to determine the robust performance of selected damper controllers in the face of uncertainty in the structural system, and (3) repeatability testing, to validate the results of the RTHS test method.

In general, the semi-active control approaches are superior to the passive control approach for reductions in absolute acceleration and damper force. ODCOC proved to be the best option for each earthquake, with an average improvement of 25% versus the PON cases and 5% versus the COC case. Further, PON and ODCOC both performed well in terms of drift and displacement reduction, with PON being the best option for drift reduction and both controllers achieving good results for displacement. In comparing the RTHS results to simulation, the structural responses for each were shown to track very well, validating the performance of the controllers seen in simulation.

For the robustness testing, the ODCOC outperformed the PON controller even in the face of unknown circumstances for acceleration and damper force. While the PON case yielded scattered results depending on the mass variation, the ODCOC responses stayed consistent, with improvements in responses occurring at each instance of mass variation.

Overall, the ODCOC has proven to be the superior controller for both the linear 3-story prototype structure and the linear 9-story benchmark structure. In the next chapter,

the performance of a non-linear model of the nine-story benchmark structure equipped with MR dampers using ODCOC control is examined.

CHAPTER 6: NINE-STORY BENCHMARK STRUCTURE EXPERIMENT (NON-LINEAR)

In the previous chapter, RTHS was performed to evaluate the controller performance using a linear model of a 9-story benchmark structure and a 3-story large-scale steel frame. In this chapter, numerical simulations are conducted using a real-time non-linear computational tool to evaluate the controller performance on a non-linear model of the 9-story benchmark structure equipped with MR dampers. Several damper configurations are considered, with multiple earthquake inputs. Each controller is evaluated based on general earthquake input and robust performance when facing unknown conditions.

6.1. Benchmark Structure Description

As in the previous chapter, the 9-story structure used in this study was designed by Brandow & Johnston Associates for the SAC Phase II Steel Project (Ohtori et al, 2004). Although not actually constructed, the structure adheres to seismic code and represents a typical medium-rise building office building (for general commercial use) designed for the Los Angeles, California region. Details on the structural design are found in Chapter 5.

6.2. RT-Frame 2D Description

In this section, the main features of the RT Frame 2D modeling tool, developed by Castaneda (2012), and presented and described. This real-time structural modeling and computation tool is implemented using an embedded MATLAB subset function format (Mathworks 2009). This configuration allows the user to take advantage of the embedded inference engine, which can more efficiently generates codes and accelerate the execution of the algorithm. Using a user-defined modeling options and a preset scheme to characterize different elements of a given structure, the source code (dynamic language – MATLAB *script*) is compiled into a real-time executable function (static language – *C script*) to perform on the given RTHS platform.

The built-in user options for this computational tool are extensive. Mass is modeled using a concentrated-lumped scheme, with distribution evenly spread through global translational degrees-of-freedom (DOF). Several types of damping can be specified, including Rayleigh damping or proportional damping with either the mass or stiffness. Modeling elements allows even more freedom, with different choices for three different elements: columns, beams, and joints.

Column elements can only be modeled as linear-elastic elements, but there is an option to include zero-length rotational springs, which have user-defined hysteretic properties to evaluate the moment-rotation interaction of the spring. Beam elements are

modeled in two ways: a linear/non-linear element with the optional zero-length springs or a moment-curvature non-linear beam element with a hysteretic model that represents yielding. This element can be modeled with either a spread- or concentrated-plasticity model. If an element includes a hysteretic component, three models are available, including a bi-linear hysteretic model with kinematic hardening, a tri-linear hysteretic model with kinematic hardening, and the Frederick-Armstrong hysteretic model with both kinematic and isotropic hardening. Joints are modeled using a combination of two elements, connectivity areas and panel zones, which are defined in the following manner: (1) connectivity is the region where the beam and column elements connect to the panel zone and (2) the panel zone consists of the region where forces from adjacent members are transfer. The panel zones are constructed using the model developed by Hjelmstad and Haikal (2006), which consists of a rotational DOF in conjunction with two translational DOFs at the center of the panel zone, with three possible deformation modes.

Efficiency in computation is paramount for the tool to stay within the "real-time" constraints, and so the geometric stiffness approach (commonly referred to as P-Delta analysis) is used to simplify the analysis. Non-linear analysis, in contrast, is done by solving temporarily discretized equations of motions. To discretize these equations, two options are available: (1) an implicit integration scheme or (2) an explicit integration scheme. The difference between the two lies in the fact that for explicit scheme, the displacement in the next time step is a function of the current displacement, velocity, and acceleration, while in an implicit scheme, the displacement in the next time step requires solving a non-linear equation and is a function of velocity and acceleration. This tool offers the option of using either scheme: (1) implicit, unconditionally-stable Newmark method and the (2) explicit, unconditionally-stable CR algorithm, which is the standard selection. The equations for the CR algorithm are presented in the following sections.

6.2.1. CR Algorithm Description

The CR algorithm (Cheng and Ricles, 2008) calculates the displacement and velocity states of a system in an explicit form based on the value of those states at the previous time-step. The algorithm is unconditionally-stable and shows a high level of accuracy, similar to the Newmark approach. The integration scheme is defined as

$$\dot{\boldsymbol{x}}_{\boldsymbol{t+\Delta t}} = \dot{\boldsymbol{x}}_{\boldsymbol{t}} + \boldsymbol{\alpha_1}(\boldsymbol{\Delta t})\ddot{\boldsymbol{x}}_{\boldsymbol{t}} \tag{2.30}$$

$$\boldsymbol{x}_{\boldsymbol{t+\Delta t}} = \boldsymbol{x}_{\boldsymbol{t}} + (\boldsymbol{\Delta t})\dot{\boldsymbol{x}}_{\boldsymbol{t}} + \boldsymbol{\alpha_2}(\boldsymbol{\Delta t})^{\boldsymbol{2}}\ddot{\boldsymbol{x}}_{\boldsymbol{t}} \tag{2.31}$$

$$\boldsymbol{\alpha_1} = \boldsymbol{\alpha_2} = \boldsymbol{4}(\boldsymbol{4M} + \boldsymbol{2\Delta tC} + \boldsymbol{\Delta tK})^{\boldsymbol{-1}}\boldsymbol{M} \tag{2.32}$$

From these equations, the corresponding acceleration at the next time step can be calculated, using the following equation

$$\ddot{x}_{te\Delta t} = M^{-1}\left(-MG\ddot{x}_{g,t+\Delta t} + Pf_{t+\Delta t} - C\dot{x}_{t+\Delta t} - R_{t+\Delta t}\right) \qquad \textbf{(2.33)}$$

where M, C, K are the global mass, damping, stiffness matrices. $x_{t+\Delta t}, \dot{x}_{t+\Delta t}$, and $\ddot{x}_{t+\Delta t}$ are the vectors of the displacement, velocity, and acceleration states of the structure at time, $t + \Delta t$. $\ddot{x_g}$ and f are the ground acceleration input to the structural system, and the control forces (if external control devices are being used). G and P are loading vectors, and $R_{t+\Delta t}$ is the vector of restoring forces at the $t + \Delta t$ time step.

6.3 Modeling of the Structural System

The structure is modeled using the RT-Frame2D platform. RT-Frame2D offers many advantages for simulating non-linear systems, including: (1) flexible modeling options for multiple structural elements, including beam-columns, panel zones, etc., (2) a convenient, open source platform that is compatible with and accessible from any computer equipped with MATLAB software, and (3) further compatibility with real-time hybrid simulation (using the MATLAB xPC Target) for any future physical experimentation. For these reasons, RT-Frame2D is an optimal tool for conducting the non-linear numerical simulations.

The steel used in the structure is taken as A992 steel. A tri-linear hysteresis model with kinematic hardening was selected for this steel type. The second and third flexural stiffness values are taken as 90% and 3.5% of the original flexural stiffness value for each element, respectively, which is typical of A992 steel. Mass is modeled as a lumped system, and the damping effect is recreated with a Rayleigh damping model. Beam-columns in the structure are modeled as non-linear elements, with yielding represented using the concentrated plasticity model. The model for the panel zones in the structure is taken as the rigid-body version. The integration scheme utilized in the simulation was selected to be the CR algorithm. These selections are made to keep the analysis as thorough as possible while remaining viable, from a simulation time and computational-intensity perspective. Based on the parameters of the structure, the variables summarizing the model inputs used in this study for RT-Frame2D (Castaneda et al, 2012) are defined as the following (Units: N-m)

$section\_idx =$

Sect.	EI1	EI2	EI3	EA	GA	Curve 1	Curve 2	Plast.	Shear
1	6.83E+08	6.15E+08	2E+07	1.9E+10	8.90E+15	0.0095	0.01	1	0
2	6.38E+08	5.74E+08	2E+07	1.81E+10	8.90E+15	0.0096	0.0101	1	0
3	5.99E+08	5.39E+08	2E+07	1.73E+10	8.90E+15	0.0097	0.0101	1	0
4	5.2E+08	4.68E+08	2E+07	1.56E+10	8.90E+15	0.0099	0.0104	1	0
5	4.53E+08	4.08E+08	2E+07	1.41E+10	8.90E+15	0.0101	0.0106	1	0
6	3.81E+08	3.43E+08	1E+07	1.23E+10	8.90E+15	0.0103	0.0108	1	0
7	3.2E+08	2.88E+08	1E+07	1.07E+10	8.90E+15	0.0105	0.011	1	0
8	3E+08	2.7E+08	1E+07	1.02E+10	8.90E+15	0.0106	0.0111	1	0
9	2.83E+08	2.55E+08	1E+07	9.75E+09	8.90E+15	0.0106	0.0112	1	0
10	8.12E+08	7.31E+08	3E+07	6.06E+09	8.90E+15	0.00406	0.00429	1	0
11	6.49E+08	5.84E+08	2E+07	5.12E+09	8.90E+15	0.00414	0.00437	1	0
12	3.32E+08	2.99E+08	1E+07	3.75E+09	8.90E+15	0.00496	0.00524	1	0
13	2.37E+08	2.13E+08	8E+06	3.2E+09	8.90E+15	0.00543	0.00571	1	0
14	1.52E+08	1.37E+08	5E+06	2.59E+09	8.90E+15	0.00614	0.00646	1	0

$PZ\_node =$

Node	a	b	t	E	v	Plane Stress
8	0.2	0.2	0.01	2E+11	0.3	1

(Typical)

To verify the model, a simulation of an uncontrolled structure (i.e. equipped with no MR dampers) is completed. The results of this simulation are compared with an uncontrolled simulation using the original benchmark structure files (Ohtori et al, 2004). A comparison of the 1st floor displacement is shown, and the results of the simulations match each other well.

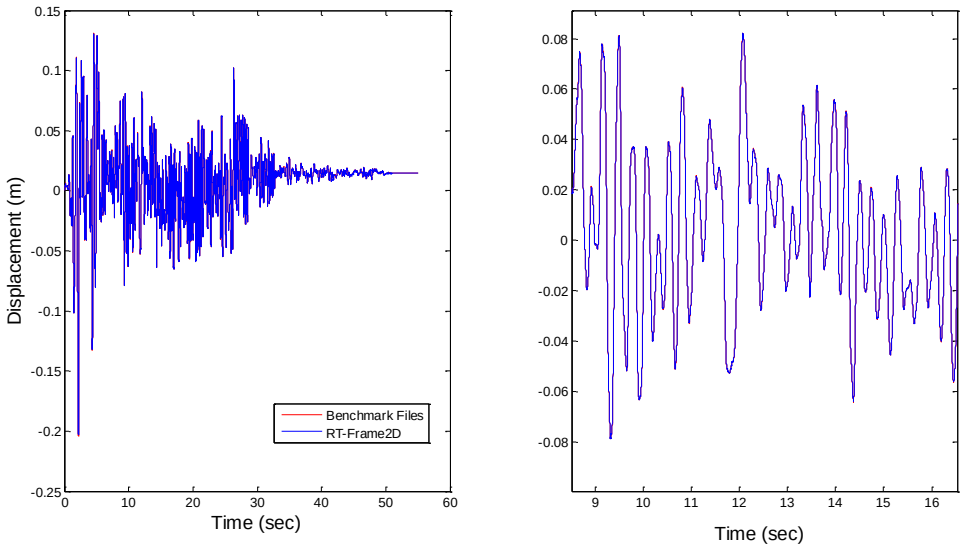

Figure 6.1: Comparison of Simulation Platform Results

6.3.1. Modeling of the MR Damper

The model of the large-scale MR damper used in the numerical simulation was identified using the procedure outlined in Chapter 4. The parameters for the Bouc Wen MR Damper model are the same as those specified in Chapter 5, Table 5.1.

6.4. Numerical Simulations

In this section, the results of the non-linear numerical simulations are discussed. Several different damper deployment schemes are considered for simulation, and the evaluation criteria for the controllers are proposed. Different control algorithms for the MR damper are compared using multiple seismic excitations. Reductions in the structural responses are determined to assess the best controller performance.

6.4.1. Controller Evaluation Criteria

Several controllers will be evaluated using these numerical simulations, including Passive Off (POFF) control, Passive On (PON) control, Clipped Optimal (COC) control, and Over-Driven Clipped Optimal (ODCOC) control. In addition, several different schemes are considered for deploying the dampers, including eighteen (18) dampers on the first floor (18-0-0-0-0-0-0-0-0-0), nine (9) dampers on the first and second floors (9-9-0-0-0-0-0-0-0-0), six dampers on the first three floors (6-6-6-0-0-0-0-0-0-0), and two

dampers on every floor (2-2-2-2-2-2-2-2-2) of the structure. For a structure of this size, prior simulation studies found that 18 MR dampers (200 kN force capacity) are needed to achieve the level of restoring force necessary to affect the responses of the structure.

To assess the performance of the controllers, as in previous chapters, the criteria are based upon peak and RMS response characteristics of the structure from several seismic inputs. In addition, because of the non-linear nature of the structural model, the residual drift, defined as the permanent displacement of a floor as a result of the seismic excitation, is also considered for these simulations. Because results are given as a ratio of the controlled response to the uncontrolled response, smaller values for the evaluation criteria are indicative of better performance. A summary of these criteria is presented in Table 6.2.

Lastly, another measure of controller performance is the amount of energy dissipated by the device/control strategy. For the MR damper, the energy dissipation occurs as the piston strokes through the MR fluid when the structure is subjected to seismic loading. Thus, the relationship between piston displacement and energy dissipation can be used to compare the controllers. From Chopra (2000), the energy dissipated by the MR damper during a displacement interval is given as

$$\boldsymbol{E_D} = \int \boldsymbol{f_D} * \boldsymbol{d}(\boldsymbol{x_d}), \ \ \boldsymbol{x} \in [\boldsymbol{x_1}, \boldsymbol{x_2}] \qquad \textbf{(2.34)}$$

where $\boldsymbol{f_D}$ is the damper force, $\boldsymbol{x_d}$ is the damper displacement (which can be taken as the interstory drift), $\boldsymbol{x_1}$ and $\boldsymbol{x_2}$ are a displacement interval, and $\boldsymbol{E_D}$ is the total energy dissipation. Equation 6.5 can also be written in a discrete form, as

$$\boldsymbol{E_D} = \sum (|\boldsymbol{f_D}(\boldsymbol{t_i})| * |\boldsymbol{x_d}(\boldsymbol{t_i}) - \boldsymbol{x_d}(\boldsymbol{t_{i-1}})|), \ \ \boldsymbol{x} \in [\boldsymbol{x_1}, \boldsymbol{x_2}] \qquad \textbf{(2.35)}$$

where $\boldsymbol{f_D}(\boldsymbol{t_i})$ and $\boldsymbol{x_d}(\boldsymbol{t_i})$ are the damper force and piston displacement (taken as the interstory drift) at the time $\boldsymbol{t_i}$. Because the time interval is small, the difference between the continuous integration and discrete summation is negligible.

The seismic ground motions used in this study include several records used in the previous chapters, as well as some additional earthquakes. In total, there 10 separate records covering a variety of peak ground acceleration (PGA) levels, including: (i) *SAC Small I Earthquake (0.15g – PGA)*, (ii) *El Centro Earthquake (0.3 g), (iii) SAC II Small Earthquake II (0.325g)*, (iv) *Small Earthquake III (0.35g)*, (v) *SAC Medium I Earthquake (0.55g)*, (vi) *Northridge Earthquake (0.65g), (vii) SAC Medium II Earthquake (0.7g)*, (viii) *SAC Large Earthquake I (0.8g), (ix) Kobe Earthquake (0.9g), and (x) SAC Large Earthquake II (1.0g).* The time histories of these ground motions are included in the index.

Table 6.1 Controller evaluation criteria

J Value	Equation	Description	J Value	Equation	Description
J_1	$max_{EQ}\left\{\frac{\max_{t,i}\lvert x_i(t)\rvert}{x^{max}}\right\}$	Peak Floor Displacement Ratio of controlled maximum relative displacement to the uncontrolled value	J_5	$max_{EQ}\left\{\frac{\max_{t,i}\lvert x_{RMS_i}(t)\rvert}{{x_{RMS}}^{max}}\right\}$	RMS Floor Displacement Ratio of controlled root mean square relative displacement to the uncontrolled value
J_2	$max_{EQ}\left\{\frac{\max_{t,i}\frac{\lvert d_i(t)\rvert}{h_i}}{d_n^{max}}\right\}$	Peak Interstory Drift Ratio of controlled maximum interstory drift to the uncontrolled value	J_6	$max_{EQ}\left\{\frac{\max_{t,i}\frac{\lvert d_{RMS_i}(t)\rvert}{h_i}}{{d_{RMS}}_n^{max}}\right\}$	RMS Interstory Drift Ratio of controlled root mean square interstory drift to the uncontrolled value
J_3	$max_{EQ}\left\{\frac{\max_{t,i}\lvert \ddot{x}_{ai}(t)\rvert}{\ddot{x}_a^{max}}\right\}$	Peak Floor Acceleration Ratio of controlled maximum absolute acceleration to the uncontrolled value	J_7	$max_{EQ}\left\{\frac{\max_{t,i}\lvert \ddot{x}_{RMS_{ai}}(t)\rvert}{{\ddot{x}_{RMS}}_a^{max}}\right\}$	RMS Floor Acceleration Ratio of controlled maximum absolute acceleration to the uncontrolled value
J_4	$max_{EQ}\left\{\max_{t,i}\lvert f^i(t)\rvert\right\}$	Peak Control Force Ratio of the maximum device output force to the weight of the structure	J_8	$max_{EQ}\left\{\max_{tei}\lvert {f_{RMS}}^i(t)\rvert\right\}$	RMS Control Force Ratio of the maximum device output force to the weight of the structure
			J_9	$max_{EQ}\left\{\frac{\max_{t,i}\frac{\lvert d_{RD_i}(t)\rvert}{h_i}}{{d_{RD}}_n^{max}}\right\}$	Residual Drift Ratio of the maximum residual drift to the uncontrolled value

6.4.2. Results Summary

For the purposes of control, two different optimization schemes were considered in the design of the semi-active controllers, one to minimize the floor absolute accelerations and one to minimize the relative floor displacements. In both cases, equal weight was given to every floor and the **R** matrix was selected to be an identity matrix of proper order. Values for the **Q** matrices were arbitrarily chosen and tested using a band-limited white noise input. Based on the performance of these controllers in simulations with this general input, the best weighting values for each of the two design cases were identified and implemented. A summary of each simulation case, including **Q** matrix weights, is presented in Table 6.2.

Table 6.2: Simulation Case Summary

Case #	Damper Placement Scheme	Controller Optimization	COC Weighting	ODCOC Weighting
1	18-0-0-0-0-0-0-0-0	ACC	1e6	4e6
2	18-0-0-0-0-0-0-0-0	DISP	3e5	1e6
3	9-9-0-0-0-0-0-0-0	ACC	1e8	8e7
4	9-9-0-0-0-0-0-0-0	DISP	7e8	7e8
5	6-6-6-0-0-0-0-0-0	ACC	5e8	1e8
6	6-6-6-0-0-0-0-0-0	DISP	5e7	9e7
7	2-2-2-2-2-2-2-2-2	ACC	7.5e8	3e9
8	2-2-2-2-2-2-2-2-2	DISP	8e9	1e10

Table 6.3: Case 1 Nonlinear Simulation Results

Ground Motion	Controller	Evaluation Criteria								
		J1	J2	J3	J4 (kN)	J5	J6	J7	J8 (kN)	J9
SAC Small EQ I PGA - 0.15g	PON	0.845	0.746	0.918	239	0.798	0.696	0.872	118	0.270
	COC	0.862	0.779	0.931	203	0.821	0.735	0.877	101	0.479
	ODCOC	0.872	0.745	0.822	217	0.820	0.726	0.792	105	0.262
El Centro PGA - 0.3g	PON	0.915	0.915	0.942	247	0.990	1.023	0.902	121	1.795
	COC	0.930	0.929	0.930	221	0.959	0.948	0.907	104	1.678
	ODCOC	0.915	0.915	0.851	238	0.952	0.958	0.823	111	0.877
SAC Small EQ II PGA - 0.325g	PON	0.998	0.993	0.983	285	0.847	0.872	0.910	80	0.030
	COC	0.997	0.993	0.984	220	0.846	0.848	0.917	68	0.037
	ODCOC	1.018	1.006	0.915	246	0.861	0.866	0.860	71	0.021
SAC Small EQ III PGA - 0.35g	PON	0.984	0.999	0.943	279	1.187	1.267	0.918	97	0.612
	COC	0.988	0.999	0.966	223	1.143	1.224	0.917	82	0.495
	ODCOC	0.977	0.989	0.895	246	1.178	1.249	0.855	85	0.468
SAC Medium EQ I PGA - 0.55g	PON	0.975	0.986	0.955	300	1.190	1.333	0.916	89	1.301
	COC	0.977	0.987	0.960	259	1.180	1.319	0.920	76	1.287
	ODCOC	0.969	0.981	0.859	244	1.172	1.306	0.834	80	1.172
Northridge PGA - 0.65g	PON	0.946	0.948	0.953	277	0.964	0.971	0.914	100	1.260
	COC	0.958	0.961	0.966	207	0.970	0.978	0.919	85	0.929
	ODCOC	0.965	0.966	0.869	202	0.975	0.982	0.829	89	0.965
SAC Medium EQ II PGA - 0.7 g	PON	0.937	0.928	0.934	228	0.942	0.976	0.943	140	1.108
	COC	0.946	0.938	0.941	198	0.949	0.980	0.947	120	1.060
	ODCOC	0.939	0.930	0.843	239	0.946	0.976	0.854	131	0.998
SAC Large EQ I PGA - 0.8g	PON	0.942	0.929	0.930	246	0.937	0.935	0.920	142	0.034
	COC	0.954	0.943	0.941	192	0.949	0.947	0.926	119	0.028
	ODCOC	0.973	0.970	0.962	192	0.959	0.955	0.932	123	0.031
Kobe PGA - 0.9g	PON	0.973	0.973	0.936	295	0.950	0.954	0.932	125	0.311
	COC	0.979	0.978	0.942	236	0.960	0.963	0.939	108	0.515
	ODCOC	0.976	0.975	0.940	238	0.954	0.957	0.936	117	0.262
SAC Large EQ II PGA - 1g	PON	0.962	0.952	0.972	286	0.984	1.051	0.903	115	0.944
	COC	0.969	0.960	0.976	238	0.991	1.064	0.912	99	0.957
	ODCOC	0.964	0.955	0.875	263	0.985	1.043	0.822	104	0.861

Table 6.4: Case21 Nonlinear Simulation Results

Ground Motion	Controller	Evaluation Criteria								
		J1	J2	J3	J4 (kN)	J5	J6	J7	J8 (kN)	J9
SAC Small EQ I PGA - 0.15g	PON	0.845	0.746	0.918	239	0.798	0.696	0.872	118	0.270
	COC	0.919	0.926	1.002	205	0.903	0.878	0.904	46	0.454
	ODCOC	0.832	0.806	0.918	234	0.792	0.708	0.902	96	0.201
El Centro PGA - 0.3g	PON	0.984	0.999	0.943	279	1.187	1.267	0.918	97	0.612
	COC	0.993	0.998	0.989	187	0.992	1.048	0.929	44	0.476
	ODCOC	0.920	0.923	0.961	223	1.070	1.110	0.920	72	0.414
SAC Small EQ II PGA - 0.325g	PON	0.998	0.993	0.983	285	0.847	0.872	0.910	80	0.030
	COC	1.000	0.993	0.984	123	0.912	0.931	0.946	34	0.059
	ODCOC	0.885	0.884	0.995	267	0.757	0.764	0.922	59	0.019
SAC Small EQ III PGA - 0.35g	PON	0.915	0.915	0.942	247	0.990	1.023	0.902	121	1.795
	COC	0.964	0.960	0.927	147	0.932	0.917	0.936	45	1.667
	ODCOC	0.889	0.881	0.924	231	0.934	0.911	0.915	101	0.871
SAC Medium EQ I PGA - 0.55g	PON	0.975	0.986	0.955	300	1.190	1.333	0.916	89	1.301
	COC	0.981	0.988	0.972	201	1.077	1.128	0.931	42	1.131
	ODCOC	0.899	0.907	0.965	248	1.052	1.155	0.929	64	1.134
Northridge PGA - 0.65g	PON	0.946	0.948	0.953	277	0.964	0.971	0.914	100	1.260
	COC	0.967	0.967	0.966	197	0.982	0.994	0.944	48	0.930
	ODCOC	0.865	0.871	0.984	238	0.868	0.877	0.928	73	0.846
SAC Medium EQ II PGA - 0.7 g	PON	0.937	0.928	0.934	228	0.942	0.976	0.943	140	1.108
	COC	0.965	0.961	0.961	232	0.974	0.983	0.964	60	1.080
	ODCOC	0.863	0.858	0.958	208	0.860	0.891	0.952	109	0.950
SAC Large EQ I PGA - 0.8g	PON	0.942	0.929	0.930	246	0.937	0.935	0.920	142	0.034
	COC	0.967	0.959	0.957	218	0.962	0.967	0.946	61	0.061
	ODCOC	0.978	0.970	0.964	244	0.966	0.961	0.937	103	0.031
Kobe PGA - 0.9g	PON	0.973	0.973	0.936	295	0.950	0.954	0.932	125	0.311
	COC	0.981	0.982	0.969	208	0.969	0.971	0.959	61	0.513
	ODCOC	0.986	0.987	0.945	214	0.971	0.973	0.950	88	0.227
SAC Large EQ II PGA - 1g	PON	0.962	0.952	0.972	286	0.984	1.051	0.903	115	0.944
	COC	0.979	0.973	0.985	251	0.987	1.040	0.941	49	0.843
	ODCOC	0.867	0.857	0.980	217	0.885	0.954	0.926	93	0.725

Table 6.5: Case 3 Nonlinear Simulation Results

Ground Motion	Controller	Evaluation Criteria								
		J1	J2	J3	J4 (kN)	J5	J6	J7	J8 (kN)	J9
SAC Small EQ I PGA - 0.15g	PON	0.849	0.794	0.939	242	0.811	0.758	0.854	127	0.841
	COC	0.882	0.832	0.955	192	0.847	0.805	0.875	101	0.860
	ODCOC	0.922	0.824	0.888	200	0.880	0.840	0.833	92	0.723
El Centro PGA - 0.3g	PON	0.902	0.897	0.901	248	0.972	0.944	0.898	128	1.957
	COC	0.922	0.920	0.905	212	0.930	0.883	0.914	102	1.272
	ODCOC	0.910	0.905	0.814	248	0.916	0.895	0.844	95	1.191
SAC Small EQ II PGA - 0.325g	PON	0.996	0.989	0.983	290	0.839	0.848	0.914	86	0.233
	COC	0.998	0.992	0.987	204	0.857	0.886	0.931	68	0.131
	ODCOC	1.004	0.999	0.891	218	0.873	0.911	0.848	62	0.152
SAC Small EQ III PGA - 0.35g	PON	0.984	0.985	0.965	278	1.062	1.094	0.910	104	1.319
	COC	0.987	0.989	0.988	207	1.040	1.072	0.920	81	1.233
	ODCOC	0.982	0.985	0.916	228	1.028	1.097	0.855	74	1.170
SAC Medium EQ I PGA - 0.55g	PON	0.986	0.992	0.980	229	1.175	1.321	0.913	95	1.274
	COC	0.989	0.993	0.982	189	1.153	1.262	0.924	77	1.241
	ODCOC	0.988	0.992	0.907	183	1.147	1.202	0.867	68	1.131
Northridge PGA - 0.65g	PON	0.946	0.948	0.961	289	0.963	0.973	0.913	107	1.646
	COC	0.967	0.970	0.982	218	0.975	0.985	0.926	84	1.436
	ODCOC	0.974	0.975	0.917	216	0.981	0.990	0.872	81	1.218
SAC Medium EQ II PGA - 0.7 g	PON	0.936	0.930	0.943	228	0.936	0.958	0.943	146	1.016
	COC	0.950	0.944	0.954	189	0.949	0.967	0.952	117	0.979
	ODCOC	0.954	0.948	0.893	204	0.959	0.974	0.895	116	1.001
SAC Large EQ I PGA - 0.8g	PON	0.937	0.930	0.937	240	0.933	0.934	0.921	149	0.497
	COC	0.959	0.956	0.962	178	0.953	0.954	0.936	113	0.323
	ODCOC	0.969	0.965	0.967	184	0.962	0.962	0.945	108	0.294
Kobe PGA - 0.9g	PON	0.969	0.971	0.944	237	0.946	0.950	0.931	131	0.499
	COC	0.977	0.977	0.956	195	0.960	0.963	0.943	105	0.582
	ODCOC	0.974	0.974	0.955	243	0.954	0.958	0.947	103	0.483
SAC Large EQ II PGA - 1g	PON	0.961	0.950	0.980	231	0.980	1.030	0.904	122	1.801
	COC	0.976	0.966	0.988	157	0.989	1.042	0.923	95	1.687
	ODCOC	0.973	0.963	0.877	184	0.981	1.010	0.834	90	1.454

Table 6.6: Case 4 Nonlinear Simulation Results

Ground Motion	Controller	Evaluation Criteria								
		J1	J2	J3	J4 (kN)	J5	J6	J7	J8 (kN)	J9
SAC Small EQ I PGA - 0.15g	PON	0.849	0.794	0.939	242	0.811	0.758	0.854	127	0.841
	COC	0.919	0.926	1.002	228	0.903	0.878	0.904	91	0.854
	ODCOC	0.819	0.793	0.918	234	0.779	0.697	0.902	192	0.503
El Centro PGA - 0.3g	PON	0.902	0.897	0.901	248	0.972	0.944	0.898	128	1.957
	COC	0.964	0.960	0.927	220	0.932	0.917	0.936	91	1.367
	ODCOC	0.879	0.871	0.924	231	0.923	0.901	0.915	201	1.106
SAC Small EQ II PGA - 0.325g	PON	0.996	0.989	0.983	290	0.839	0.848	0.914	86	0.233
	COC	1.000	0.993	0.984	246	0.912	0.931	0.946	69	0.190
	ODCOC	0.890	0.889	0.995	267	0.762	0.768	0.922	118	0.020
SAC Small EQ III PGA - 0.35g	PON	0.984	0.985	0.965	278	1.062	1.094	0.910	104	1.319
	COC	0.993	0.998	0.989	291	0.992	1.048	0.929	87	1.176
	ODCOC	0.898	0.902	0.961	267	1.045	1.085	0.920	145	1.081
SAC Medium EQ I PGA - 0.55g	PON	0.986	0.992	0.980	229	1.175	1.321	0.913	95	1.274
	COC	0.981	0.988	0.972	201	1.077	1.128	0.931	83	1.131
	ODCOC	0.887	0.895	0.965	248	1.038	1.140	0.929	128	1.119
Northridge PGA - 0.65g	PON	0.946	0.948	0.961	289	0.963	0.973	0.913	107	1.646
	COC	0.967	0.967	0.966	276	0.982	0.994	0.944	96	1.303
	ODCOC	0.857	0.863	0.984	285	0.859	0.868	0.928	146	1.122
SAC Medium EQ II PGA - 0.7 g	PON	0.936	0.930	0.943	228	0.936	0.958	0.943	146	1.016
	COC	0.965	0.961	0.961	232	0.974	0.983	0.964	121	1.080
	ODCOC	0.872	0.867	0.958	233	0.869	0.900	0.952	218	0.960
SAC Large EQ I PGA - 0.8g	PON	0.937	0.930	0.937	240	0.933	0.934	0.921	149	0.497
	COC	0.967	0.959	0.957	231	0.962	0.967	0.946	123	0.513
	ODCOC	0.978	0.970	0.964	231	0.966	0.961	0.937	206	0.131
Kobe PGA - 0.9g	PON	0.969	0.971	0.944	237	0.946	0.950	0.931	131	0.499
	COC	0.981	0.982	0.969	277	0.969	0.971	0.959	122	0.613
	ODCOC	0.986	0.987	0.945	260	0.971	0.973	0.950	176	0.447
SAC Large EQ II PGA - 1g	PON	0.961	0.950	0.980	231	0.980	1.030	0.904	122	1.801
	COC	0.979	0.973	0.985	206	0.987	1.040	0.941	98	1.484
	ODCOC	0.872	0.862	0.980	243	0.890	0.960	0.926	185	1.336

Table 6.7: Case 5 Nonlinear Simulation Results

Ground Motion	Controller	Evaluation Criteria								
		J1	J2	J3	J4 (kN)	J5	J6	J7	J8 (kN)	J9
SAC Small EQ I PGA - 0.15g	PON	0.855	0.830	0.951	243	0.820	0.794	0.853	132	0.569
	COC	0.900	0.894	0.980	163	0.879	0.862	0.890	86	0.800
	ODCOC	0.917	0.921	0.928	180	0.916	0.896	0.854	71	0.563
El Centro PGA - 0.3g	PON	0.889	0.877	0.895	250	0.958	0.910	0.903	132	2.423
	COC	0.919	0.912	0.916	183	0.925	0.911	0.931	85	1.826
	ODCOC	0.902	0.890	0.835	221	0.928	0.925	0.871	69	0.833
SAC Small EQ II PGA - 0.325g	PON	1.003	0.988	0.982	292	0.842	0.879	0.924	90	0.536
	COC	1.003	0.992	0.992	167	0.896	0.927	0.949	55	0.539
	ODCOC	1.000	0.994	0.919	224	0.943	0.946	0.889	51	0.474
SAC Small EQ III PGA - 0.35g	PON	0.982	0.978	0.991	278	1.014	1.010	0.913	108	1.198
	COC	0.987	0.984	0.998	192	1.000	0.992	0.932	70	1.113
	ODCOC	0.999	1.002	0.907	252	1.003	1.019	0.853	62	1.079
SAC Medium EQ I PGA - 0.55g	PON	0.993	0.992	0.995	218	1.160	1.278	0.918	99	1.247
	COC	0.999	0.997	0.991	197	1.103	1.118	0.935	66	1.164
	ODCOC	0.997	0.996	0.916	192	1.110	1.128	0.867	57	1.074
Northridge PGA - 0.65g	PON	0.944	0.946	0.959	245	0.963	0.973	0.916	111	1.785
	COC	0.964	0.966	0.976	238	0.978	0.989	0.937	73	1.486
	ODCOC	0.962	0.962	0.888	231	0.979	0.994	0.873	65	1.248
SAC Medium EQ II PGA - 0.7 g	PON	0.932	0.927	0.941	255	0.927	0.940	0.947	150	0.937
	COC	0.954	0.949	0.958	208	0.951	0.953	0.962	97	0.946
	ODCOC	0.952	0.948	0.892	208	0.956	0.954	0.908	82	1.005
SAC Large EQ I PGA - 0.8g	PON	0.933	0.927	0.938	259	0.931	0.930	0.927	153	0.738
	COC	0.957	0.954	0.963	237	0.954	0.956	0.947	96	0.611
	ODCOC	0.957	0.954	0.962	234	0.958	0.962	0.958	89	0.585
Kobe PGA - 0.9g	PON	0.966	0.968	0.945	253	0.940	0.944	0.931	135	0.765
	COC	0.974	0.974	0.967	216	0.956	0.958	0.949	93	1.000
	ODCOC	0.969	0.970	0.982	246	0.948	0.951	0.954	101	0.686
SAC Large EQ II PGA - 1g	PON	0.959	0.947	0.982	245	0.972	0.996	0.909	126	1.605
	COC	0.980	0.971	0.992	208	0.983	1.014	0.938	80	1.346
	ODCOC	0.979	0.971	0.913	218	0.984	1.010	0.874	73	1.240

Table 6.8: Case 6 Nonlinear Simulation Results

Ground Motion	Controller	Evaluation Criteria								
		J1	J2	J3	J4 (kN)	J5	J6	J7	J8 (kN)	J9
SAC Small EQ I PGA - 0.15g	PON	0.855	0.830	0.951	243	0.820	0.794	0.853	132	0.569
	COC	0.904	0.915	0.981	188	0.887	0.870	0.896	83	0.831
	ODCOC	0.796	0.800	0.971	211	0.762	0.739	0.868	117	0.586
El Centro PGA - 0.3g	PON	0.889	0.877	0.895	250	0.958	0.910	0.903	132	2.423
	COC	0.924	0.915	0.906	186	0.918	0.912	0.935	79	1.261
	ODCOC	0.840	0.821	0.896	239	0.887	0.827	0.913	114	1.100
SAC Small EQ II PGA - 0.325g	PON	1.003	0.988	0.982	292	0.842	0.879	0.924	90	0.536
	COC	1.002	0.989	0.987	234	0.894	0.925	0.946	58	0.579
	ODCOC	0.893	0.878	0.979	292	0.782	0.809	0.933	75	0.418
SAC Small EQ III PGA - 0.35g	PON	0.982	0.978	0.991	278	1.014	1.010	0.913	108	1.198
	COC	0.983	0.980	0.995	214	0.956	0.970	0.932	71	1.005
	ODCOC	0.859	0.857	0.997	227	0.863	0.906	0.922	89	0.946
SAC Medium EQ I PGA - 0.55g	PON	0.993	0.992	0.995	218	1.160	1.278	0.918	99	1.247
	COC	0.996	0.994	0.994	192	1.085	1.093	0.937	66	1.141
	ODCOC	0.899	0.899	0.993	209	1.004	0.985	0.932	81	1.062
Northridge PGA - 0.65g	PON	0.944	0.946	0.959	245	0.963	0.973	0.916	111	1.785
	COC	0.956	0.958	0.967	201	0.973	0.985	0.938	75	1.270
	ODCOC	0.871	0.873	0.967	203	0.884	0.893	0.928	96	0.949
SAC Medium EQ II PGA - 0.7 g	PON	0.932	0.927	0.941	255	0.927	0.940	0.947	150	0.937
	COC	0.955	0.953	0.961	199	0.955	0.959	0.964	92	0.965
	ODCOC	0.843	0.842	0.956	219	0.837	0.847	0.956	124	0.773
SAC Large EQ I PGA - 0.8g	PON	0.933	0.927	0.938	216	0.931	0.930	0.927	153	0.738
	COC	0.954	0.951	0.958	186	0.950	0.954	0.947	100	0.720
	ODCOC	0.959	0.959	0.956	239	0.946	0.947	0.937	129	0.525
Kobe PGA - 0.9g	PON	0.966	0.968	0.945	253	0.940	0.944	0.931	135	0.765
	COC	0.974	0.976	0.963	232	0.957	0.960	0.957	83	0.886
	ODCOC	0.977	0.980	0.958	231	0.958	0.961	0.951	105	0.634
SAC Large EQ II PGA - 1g	PON	0.959	0.947	0.982	245	0.972	0.996	0.909	126	1.605
	COC	0.971	0.962	0.989	204	0.978	1.011	0.936	82	1.354
	ODCOC	0.897	0.890	0.999	218	0.896	0.925	0.923	108	1.143

Table 6.9: Case 7 Nonlinear Simulation Results

Ground Motion	Controller	Evaluation Criteria								
		J1	J2	J3	J4 (kN)	J5	J6	J7	J8 (kN)	J9
SAC Small EQ I PGA - 0.15g	PON	0.893	0.919	1.043	246	0.840	0.863	0.853	139	0.826
	COC	0.925	0.952	1.031	175	0.903	0.913	0.906	88	0.921
	ODCOC	0.932	0.955	0.938	226	0.897	0.911	0.833	102	0.763
El Centro PGA - 0.3g	PON	0.906	0.945	0.978	288	0.959	0.935	0.892	136	2.496
	COC	0.926	0.954	0.975	240	0.937	0.945	0.931	87	2.226
	ODCOC	0.915	0.947	0.876	295	0.945	0.944	0.831	100	1.637
SAC Small EQ II PGA - 0.325g	PON	1.003	0.988	0.982	250	0.842	0.879	0.924	135	0.736
	COC	1.003	0.992	0.992	143	0.896	0.927	0.949	164	0.539
	ODCOC	1.000	0.994	0.919	192	0.943	0.946	0.889	152	0.504
SAC Small EQ III PGA - 0.35g	PON	0.978	0.988	1.001	284	1.028	1.060	0.871	116	1.220
	COC	0.980	0.989	1.021	228	0.989	1.013	0.913	76	1.073
	ODCOC	0.972	0.982	0.937	280	0.990	1.018	0.833	85	1.091
SAC Medium EQ I PGA - 0.55g	PON	0.985	0.998	0.926	235	1.127	1.261	0.888	108	1.203
	COC	0.985	0.995	0.948	196	1.076	1.117	0.927	71	1.126
	ODCOC	0.977	0.993	0.849	239	1.079	1.135	0.840	82	1.129
Northridge PGA - 0.65g	PON	0.942	0.910	0.914	255	0.963	0.975	0.906	119	2.226
	COC	0.950	0.920	0.921	228	0.968	0.986	0.933	82	2.167
	ODCOC	0.944	0.906	0.821	275	0.968	0.982	0.847	91	1.806
SAC Medium EQ II PGA - 0.7 g	PON	0.932	0.927	0.941	287	0.927	0.940	0.947	150	0.937
	COC	0.954	0.949	0.958	268	0.951	0.953	0.962	292	0.946
	ODCOC	0.952	0.948	0.892	277	0.956	0.954	0.908	246	0.905
SAC Large EQ I PGA - 0.8g	PON	0.926	0.887	0.917	215	0.931	0.947	0.901	159	0.332
	COC	0.936	0.901	0.927	182	0.943	0.958	0.929	112	0.616
	ODCOC	0.923	0.877	0.908	202	0.935	0.952	0.924	129	0.339
Kobe PGA - 0.9g	PON	0.959	0.946	0.917	300	0.936	0.949	0.925	142	1.017
	COC	0.962	0.949	0.932	250	0.943	0.953	0.945	102	0.948
	ODCOC	0.956	0.944	0.927	313	0.933	0.945	0.940	117	0.878
SAC Large EQ II PGA - 1g	PON	0.936	0.892	0.937	237	0.967	0.955	0.891	133	1.422
	COC	0.947	0.910	0.950	185	0.970	0.964	0.926	93	1.198
	ODCOC	0.938	0.897	0.854	226	0.969	0.980	0.840	107	1.150

Table 6.10: Case 8 Nonlinear Simulation Results

Ground Motion	Controller	Evaluation Criteria								
		J1	J2	J3	J4 (kN)	J5	J6	J7	J8 (kN)	J9
SAC Small EQ I PGA - 0.15g	PON	0.893	0.919	1.043	246	0.840	0.863	0.853	139	0.826
	COC	0.904	0.915	0.981	235	0.887	0.870	0.896	124	0.831
	ODCOC	0.790	0.794	0.971	253	0.757	0.734	0.868	140	0.681
El Centro PGA - 0.3g	PON	0.906	0.945	0.978	288	0.959	0.935	0.892	136	2.496
	COC	0.924	0.915	0.906	279	0.918	0.912	0.935	119	2.261
	ODCOC	0.813	0.795	0.896	287	0.859	0.801	0.913	114	1.368
SAC Small EQ II PGA - 0.325g	PON	1.003	0.988	0.982	250	0.842	0.879	0.924	135	0.736
	COC	1.002	0.989	0.987	234	0.894	0.925	0.946	88	0.579
	ODCOC	0.911	0.895	0.979	251	0.797	0.825	0.933	113	0.426
SAC Small EQ III PGA - 0.35g	PON	0.978	0.988	1.001	284	1.028	1.060	0.871	116	1.220
	COC	0.983	0.980	0.995	257	0.956	0.970	0.932	107	1.005
	ODCOC	0.867	0.864	0.997	265	0.870	0.914	0.922	134	0.954
SAC Medium EQ I PGA - 0.55g	PON	0.985	0.998	0.926	235	1.127	1.261	0.888	108	1.203
	COC	0.996	0.994	0.994	230	1.085	1.093	0.937	98	1.141
	ODCOC	0.901	0.901	0.993	239	1.007	0.987	0.932	121	1.065
Northridge PGA - 0.65g	PON	0.942	0.910	0.914	255	0.963	0.975	0.906	119	2.226
	COC	0.956	0.958	0.967	268	0.973	0.985	0.938	112	2.270
	ODCOC	0.890	0.892	0.967	271	0.904	0.914	0.928	144	1.138
SAC Medium EQ II PGA - 0.7 g	PON	0.932	0.927	0.941	287	0.927	0.940	0.947	150	0.937
	COC	0.955	0.953	0.961	266	0.955	0.959	0.964	138	0.965
	ODCOC	0.838	0.838	0.956	246	0.832	0.843	0.956	124	0.769
SAC Large EQ I PGA - 0.8g	PON	0.926	0.887	0.917	215	0.931	0.947	0.901	159	0.332
	COC	0.954	0.951	0.958	233	0.950	0.954	0.947	150	0.720
	ODCOC	0.959	0.959	0.956	239	0.946	0.947	0.937	155	0.325
Kobe PGA - 0.9g	PON	0.959	0.946	0.917	300	0.936	0.949	0.925	142	1.017
	COC	0.974	0.976	0.963	290	0.957	0.960	0.957	124	0.886
	ODCOC	0.977	0.980	0.958	289	0.958	0.961	0.951	126	0.634
SAC Large EQ II PGA - 1g	PON	0.936	0.892	0.937	237	0.967	0.955	0.891	133	1.422
	COC	0.971	0.962	0.989	255	0.978	1.011	0.936	123	1.354
	ODCOC	0.890	0.883	0.999	272	0.889	0.918	0.923	162	1.134

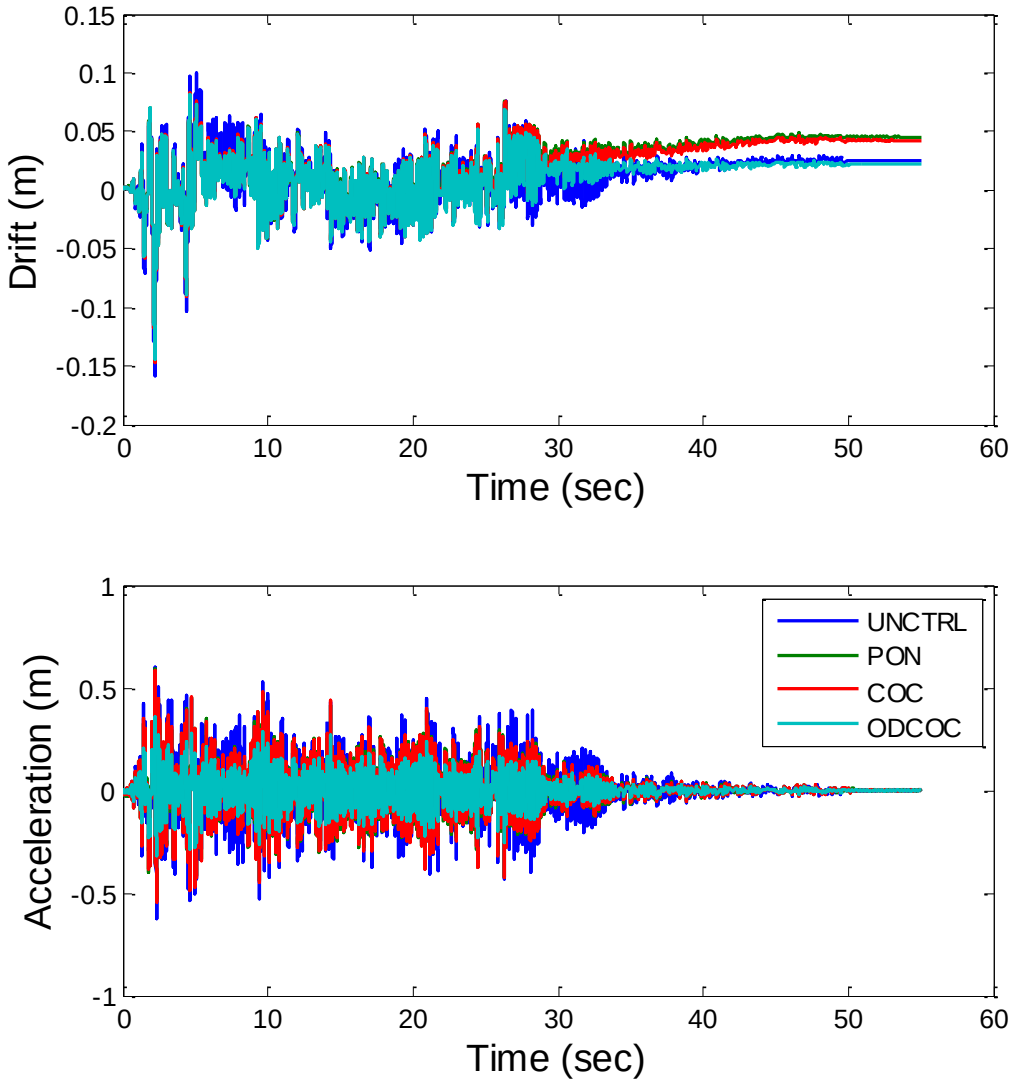

Figure 6.2: 1st Floor Time History Comparison – ELC EQ – Case 1

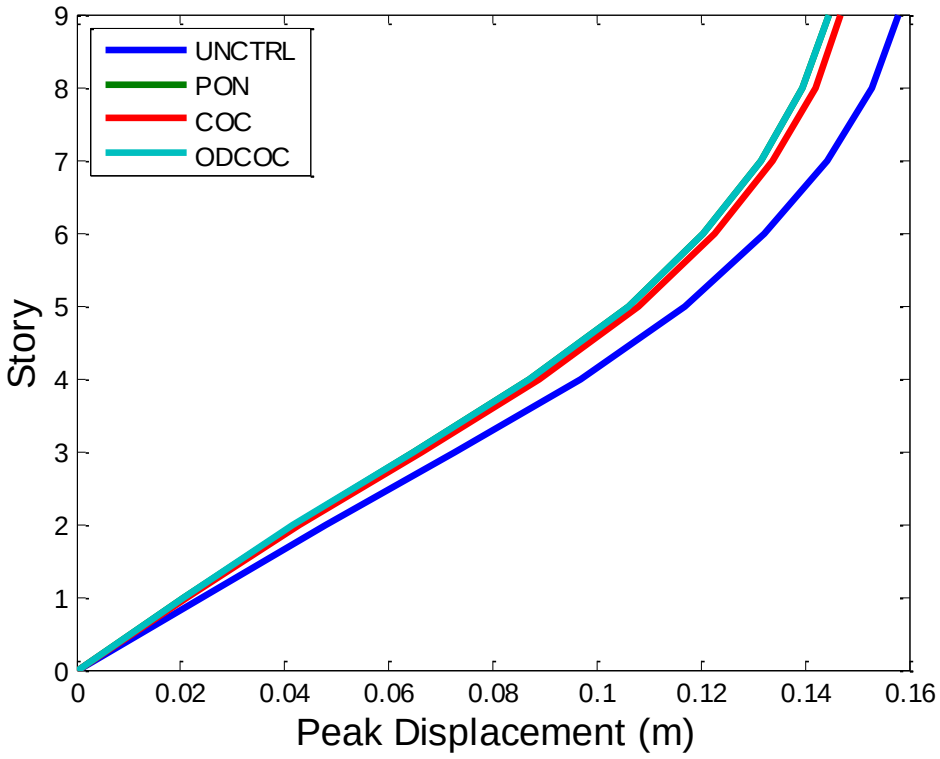

Figure 6.3: Peak Displacement Profile – ELC EQ – Case 1

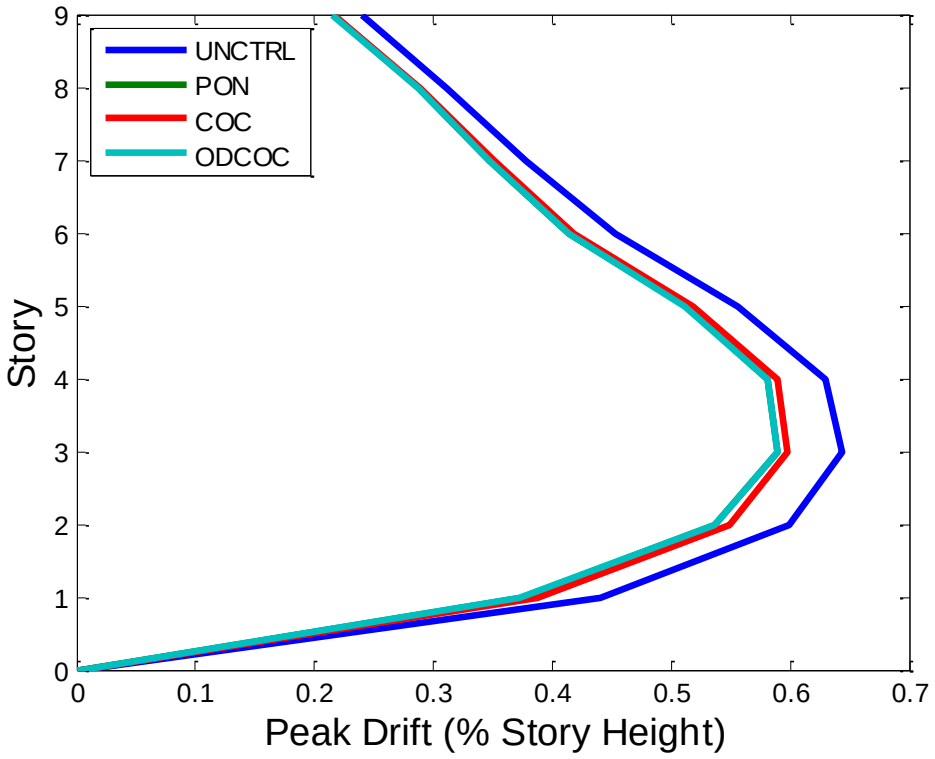

Figure 6.4: Peak Drift Profile – ELC EQ – Case 1

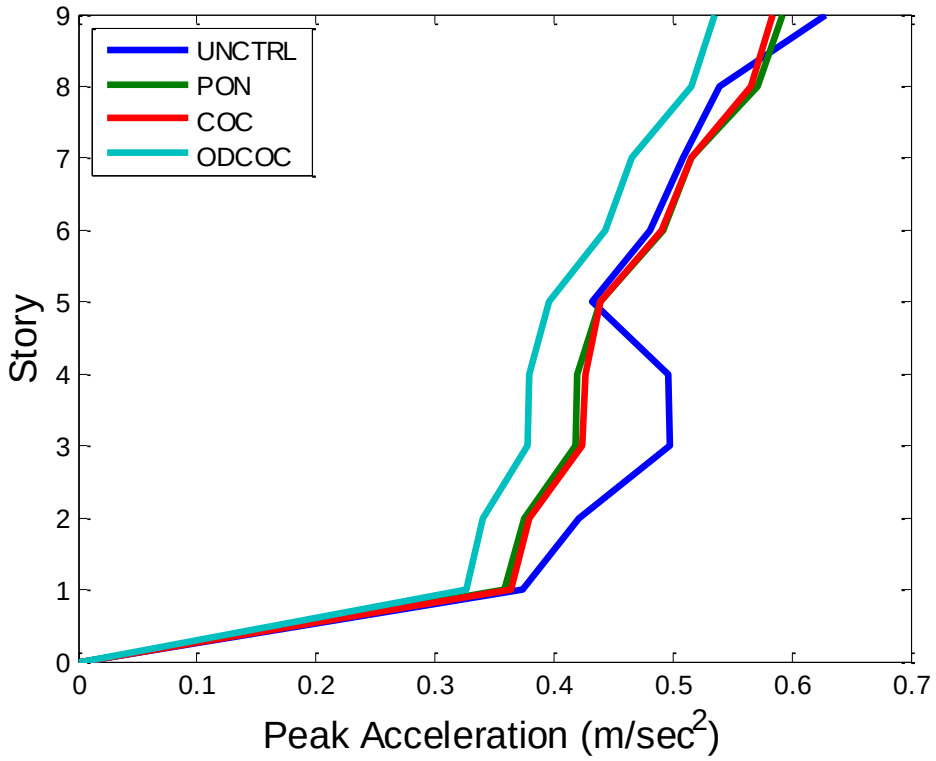

Figure 6.5: Peak Acceleration Profile – ELC EQ – Case 1

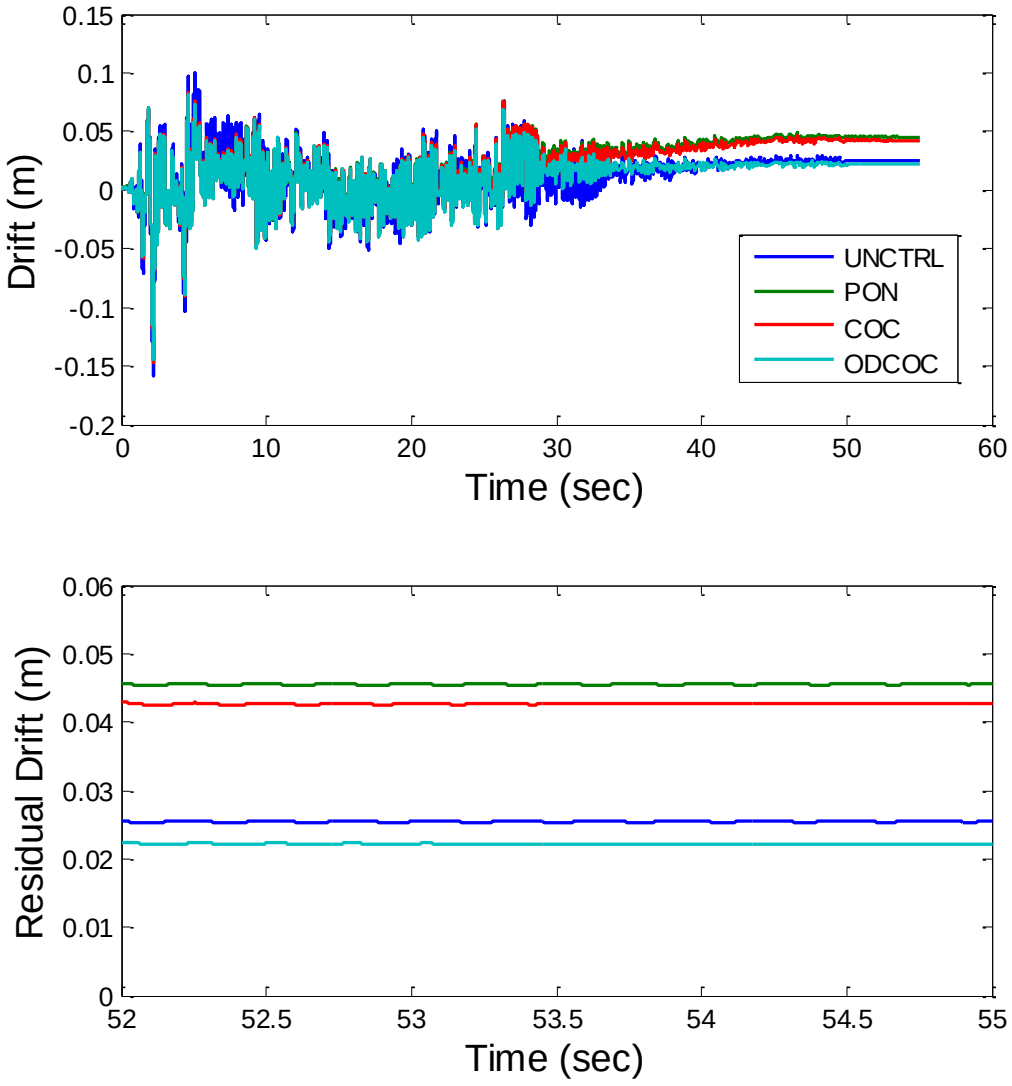

Figure 6.6: Residual Drift Comparison – ELC EQ – Case 1

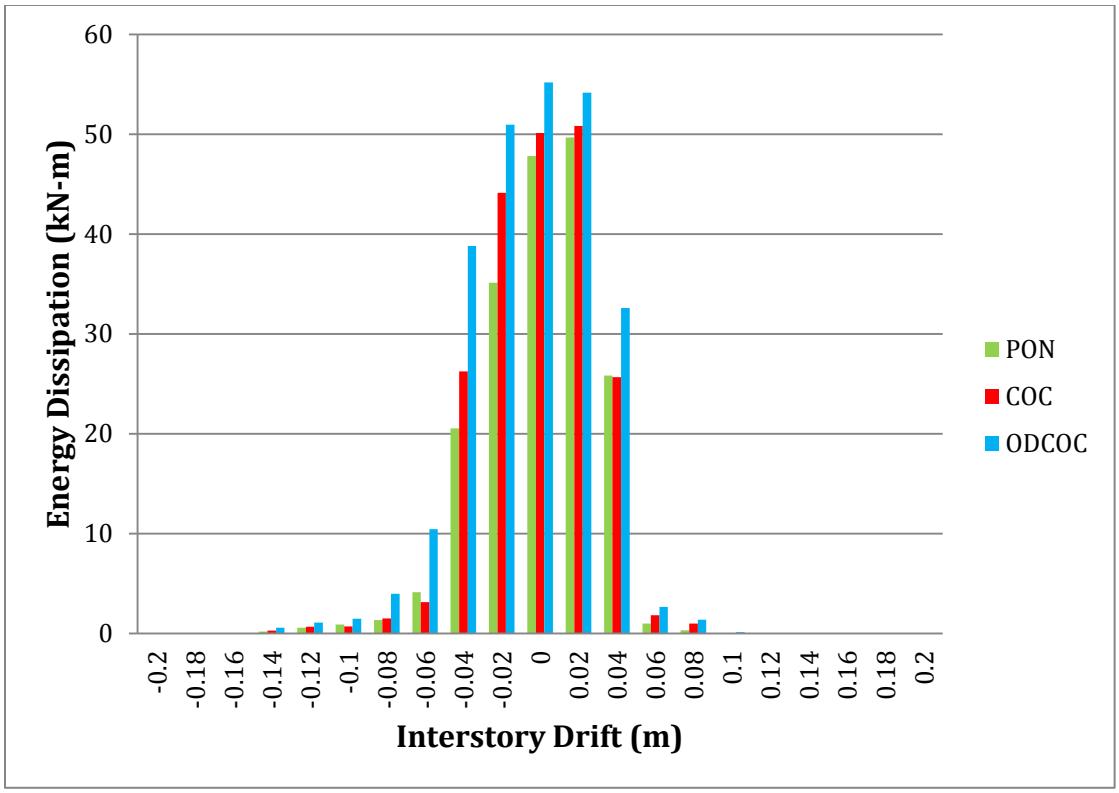

Figure 6.7: Energy Dissipation Comparison – ELC EQ – Case 1

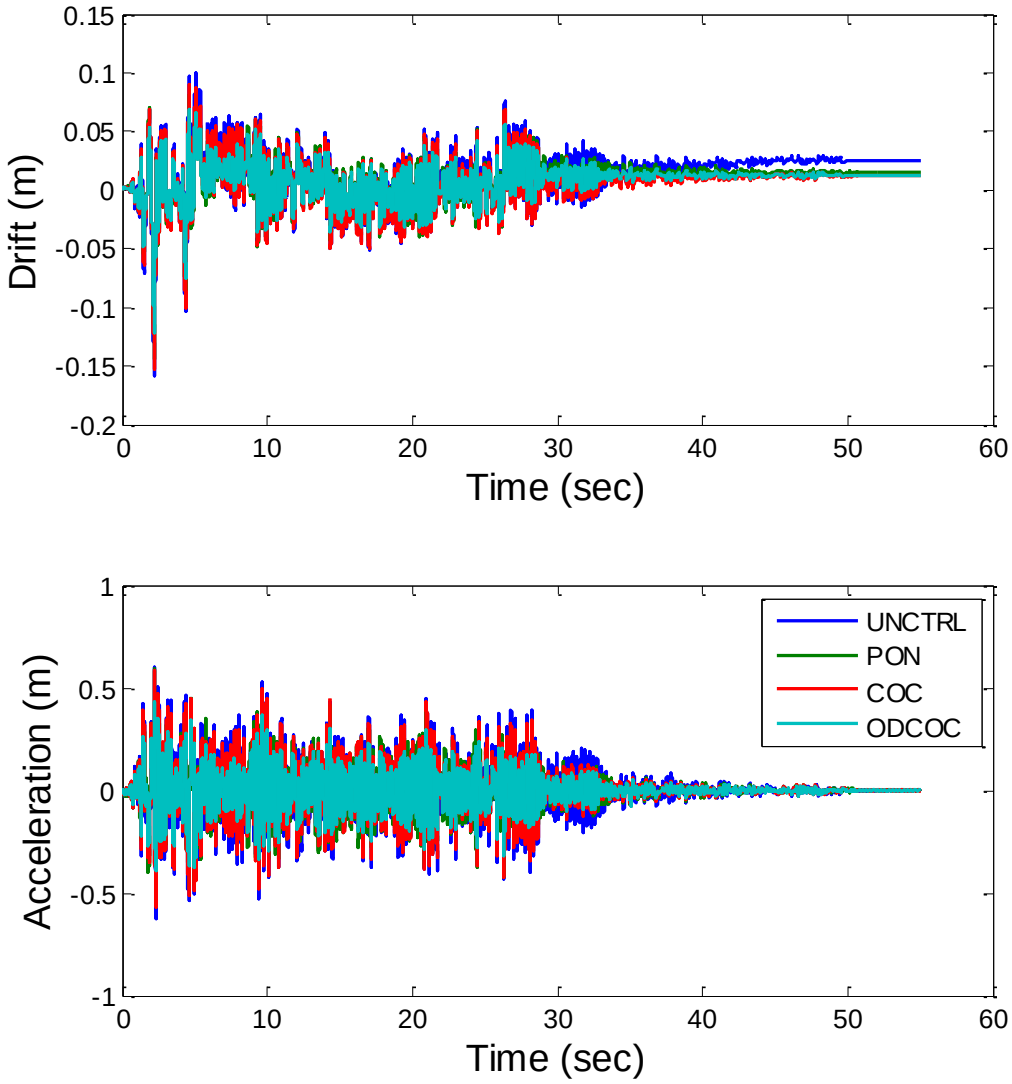

Figure 6.8: 1st Floor Time History Comparison – ELC EQ – Case 2

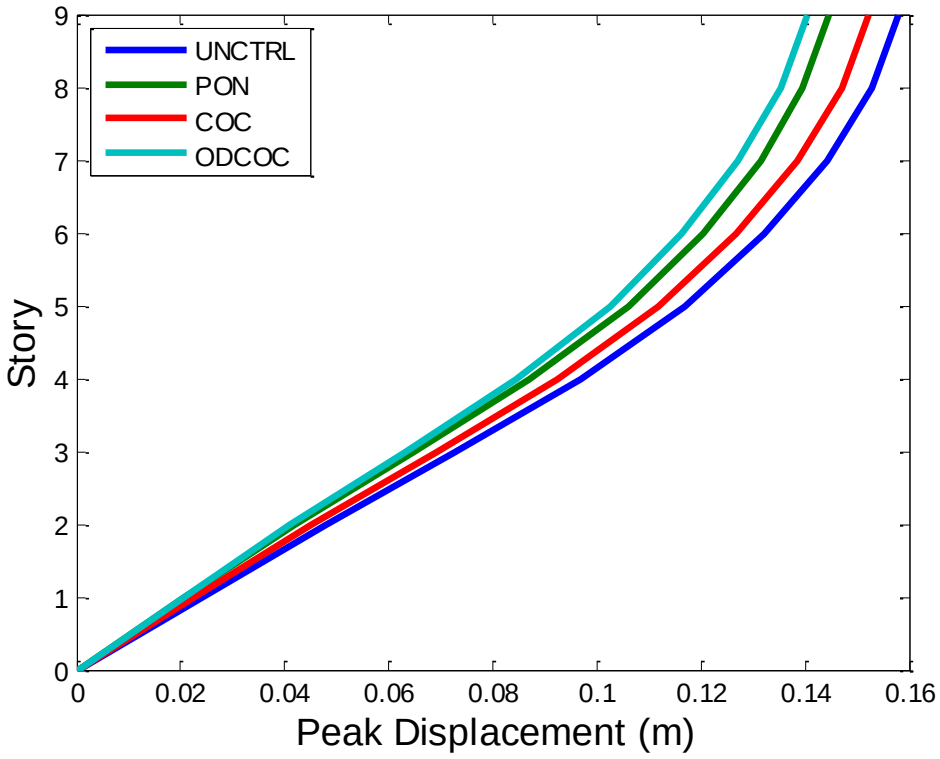

Figure 6.9: Peak Displacement Profile – ELC EQ – Case 2

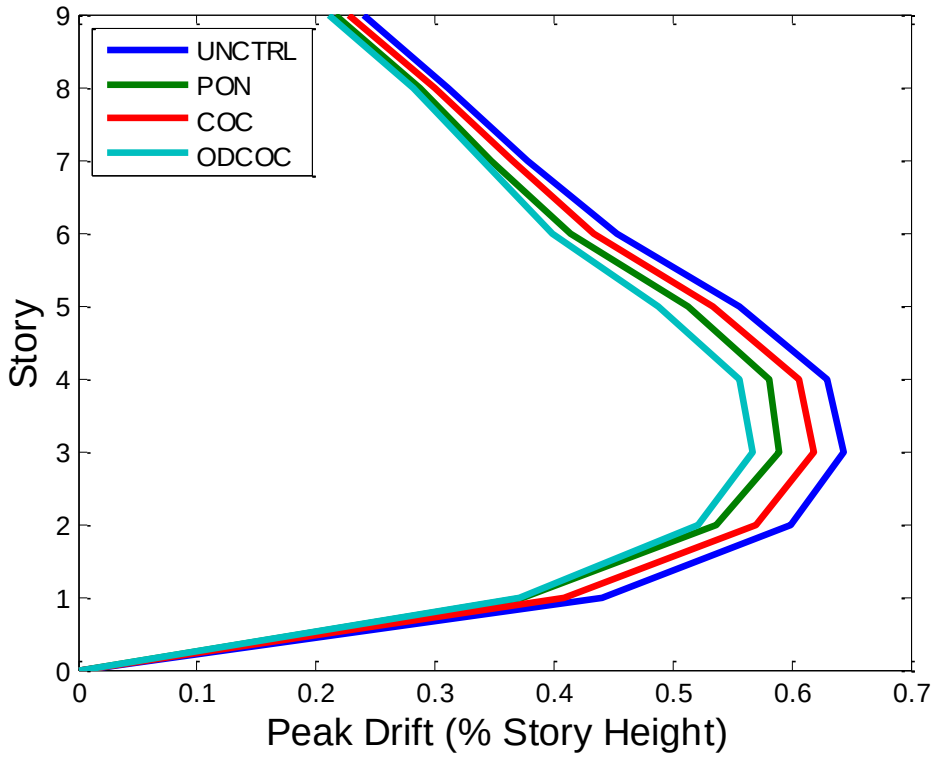

Figure 6.10: Peak Drift Profile – ELC EQ – Case 2

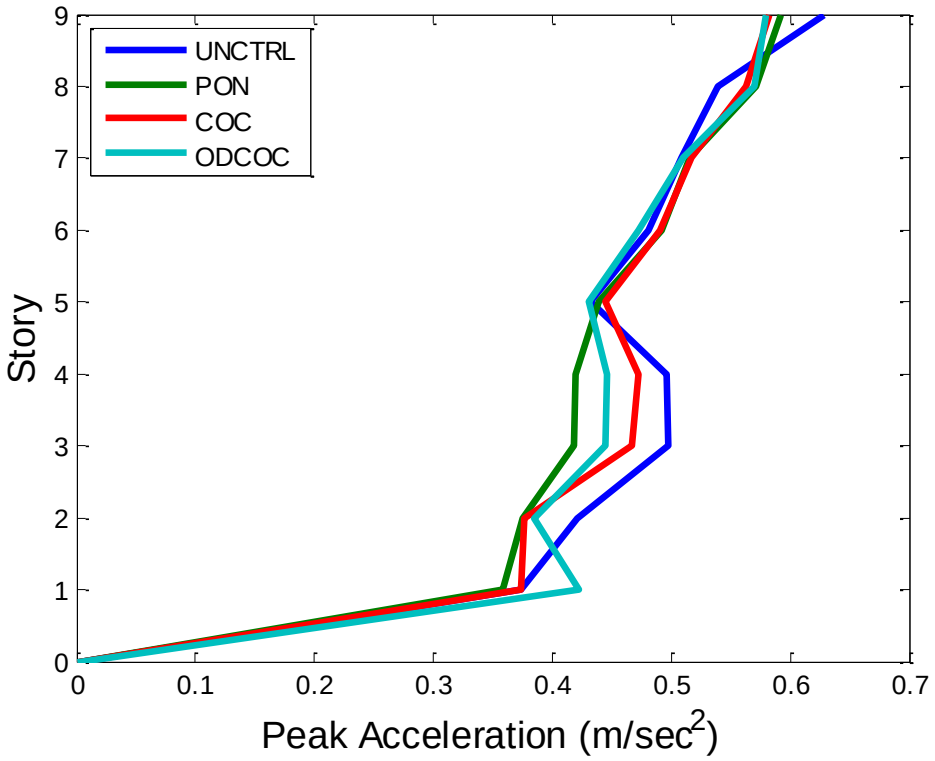

Figure 6.11: Peak Acceleration Profile – ELC EQ – Case 2

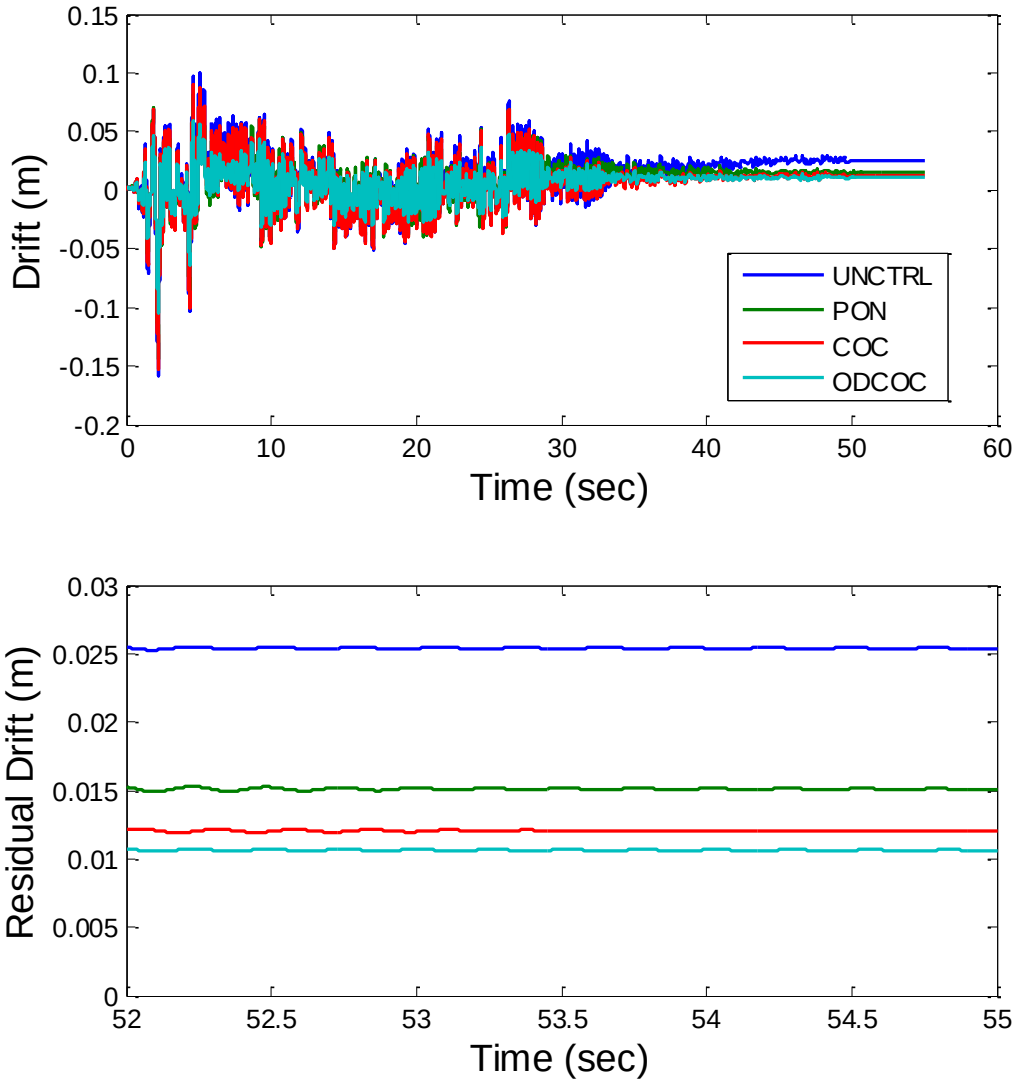

Figure 6.12: Residual Drift Comparison – ELC EQ – Case 2

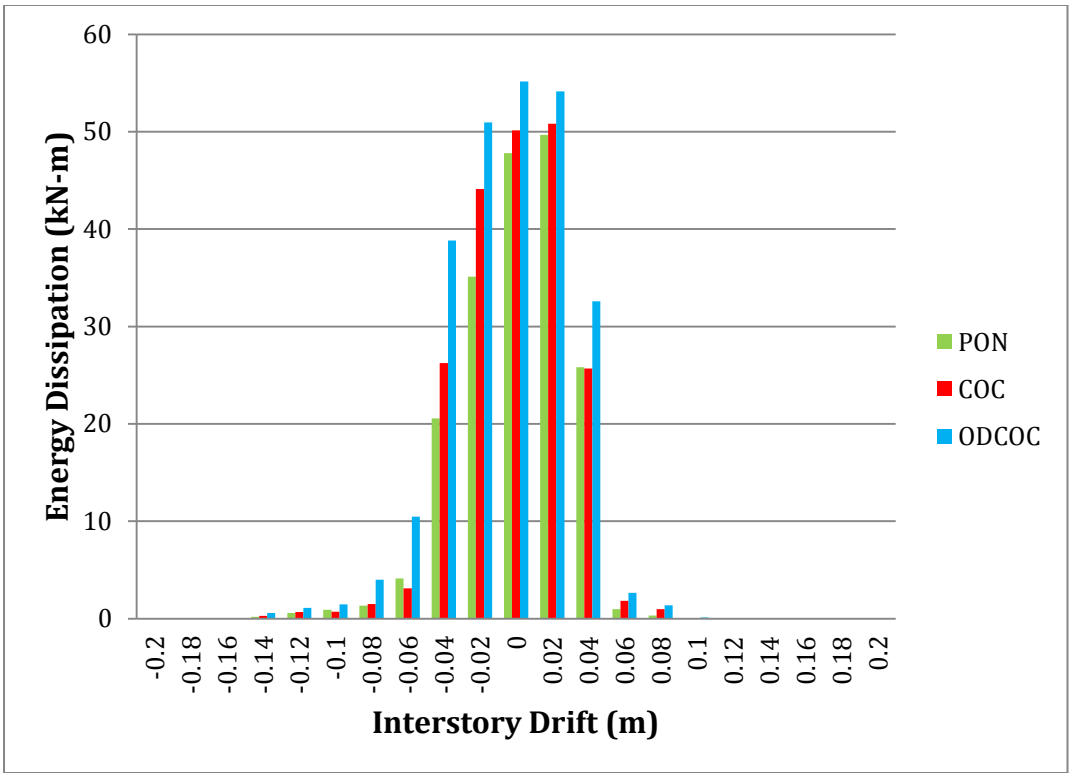

Figure 6.13: Energy Dissipation Comparison – ELC EQ – Case 2

For completeness, all of the results for each simulation case are shown in Tables 6.3-10. Several important trends have emerged from the simulation results. Regarding peak displacement (J1), in general, the controllers all achieve modest reductions compared to the uncontrolled case for each earthquake in each case (with the exception of the SAC Small EQ II). When comparing PON to the semi-active (SA) control approaches (with acceleration optimization), PON typically achieves the best results by ~1-2%. Between the SA controllers, ODCOC is typically better than COC by ~1-2%, as well. However, when displacement optimization is used for the SA approaches, the ODCOC fares much better for peak displacement reduction, by an average of 10-15% improvement when compared to both the PON and COC controllers. In general, the controllers achieve slightly higher reductions for the smaller earthquakes as compared to the medium and larger seismic excitations. In addition, the peak displacement seems to increase slightly as the dampers become less concentrated at the base of the structure, due to the presence of the "soft" first story. Focusing the dampers in that one story allows for improved responses due to the higher level of restoring force from the dampers.

The peak drift response reduction results tell the same story. When using SA controllers geared towards acceleration optimization, PON typically achieves the largest response reductions, though all controllers are within a few percent of each other. However, if displacement optimization is used, ODCOC again achieves better results than both PON and COC, usually with a 7-10% margin of improvement. There is not a direct relationship between the damper placement and the magnitude of the earthquake and controller performance in terms of peak drift response reduction.

The peak acceleration response reduction is also affected by the response optimization scheme. The PON approach, in general, tends to have larger absolute accelerations in comparison to the SA approaches. When acceleration optimization weighting is used in the control design, the ODCOC controller again performs much better than PON or COC, with a 7-10% improvement in reduction. In general, the peak acceleration, like the displacement, increases as the dampers are further distributed through the building. Across the various earthquakes, the ODCOC outperforms the other controllers in virtually every case, regardless of the earthquake input.

The peak force utilized by the dampers is typically higher for the PON control, as compared to the SA approaches. This behavior is due to the fact that the PON controller puts the damper in a constant "On" state, while the SA approaches can change the current applied to the damper depending on the situation. Of the two approaches, COC uses the smallest amount of force in most cases, when compared to ODCOC and PON. However, ODCOC is able to achieve better results (superior to COC and PON) while using a lower force than PON. So, there is a trade-off between using slightly higher forces to achieve better results. Typically, the peak damper forces are higher for the SA controllers when the displacement optimization scheme is used as opposed the acceleration optimization scheme, but the forces are still smaller than the PON approach for virtually every earthquake. Using less force to achieve better results is significant because smaller capacity devices may be used in conjunction with these control approaches. Smaller devices are less costly, so there is a clear economic advantage for any control approach that is can achieve improved response reductions with a smaller capacity damper. The

damper placement scheme does not appear to have an effect on the amount of force output for the dampers, as the average force is approximately the same across all the cases.

The RMS response values follow the same trends as the peak forces, with ODCOC being superior for displacement/drift when the displacement optimization is used and acceleration when the acceleration optimization is used. Again, the COC controller tends to utilize the least amount of force, but the ODCOC controller is typically able to achieve the best performance.

Regarding the residual displacement, one of the limitations regarding RT-Frame2D is the necessity to perform computation within the time limits necessary to achieve real-time hybrid testing. With current computing power, the non-linear behavior of each member cannot be calculated and output within the time limit required to be considered "real-time". Thus, the exact locations and severity of the non-linearities that develop is not possible to determine. However, the level of non-linearity a structure develops is also seen in the residual displacement the structure exhibits. Residual displacement is the plastic (permanent) yeilding the structure experiences due to non-linearity developing as a result of the seismic excitation. In virtually every earthquake for every case, the ODCOC achieved a smaller level of residual displacement as compared to the other controllers. For individual earthquakes, on average, the difference between ODCOC and the other controllers is approximately 20%. Overall, considering all cases and earthquakes, the ODCOC yields an average of 20%, 30%, and 20% improvement in residual drift compared to the uncontrolled, PON, and COC control cases, respectively. Therefore, it is evident that the ODCOC is superior to the other control methods at reducing the level of residual displacement within a structure under seismic loading. In addition, the results indicate that in general, the size of the earthquake did not have a discernible impact on the residual displacement, as evidenced by the large discrepancy in final displacement between the various earthquakes. However, the distribution of the dampers did have an effect, as the residual displacement increases (on average) as the dampers become more distributed. Clustering them on near the bottom of the structure had a greater impact on residual drift reduction than spreading the dampers evenly throughout the structure, as demonstrated in Figure 6.14. While residual displacement still occurs in the structure, the average controlled residual drift reduction for the 18-0-0-0-0-0-0-0-0 damper case (compared to the uncontrolled structure) is far superior to every other deployment scenario.

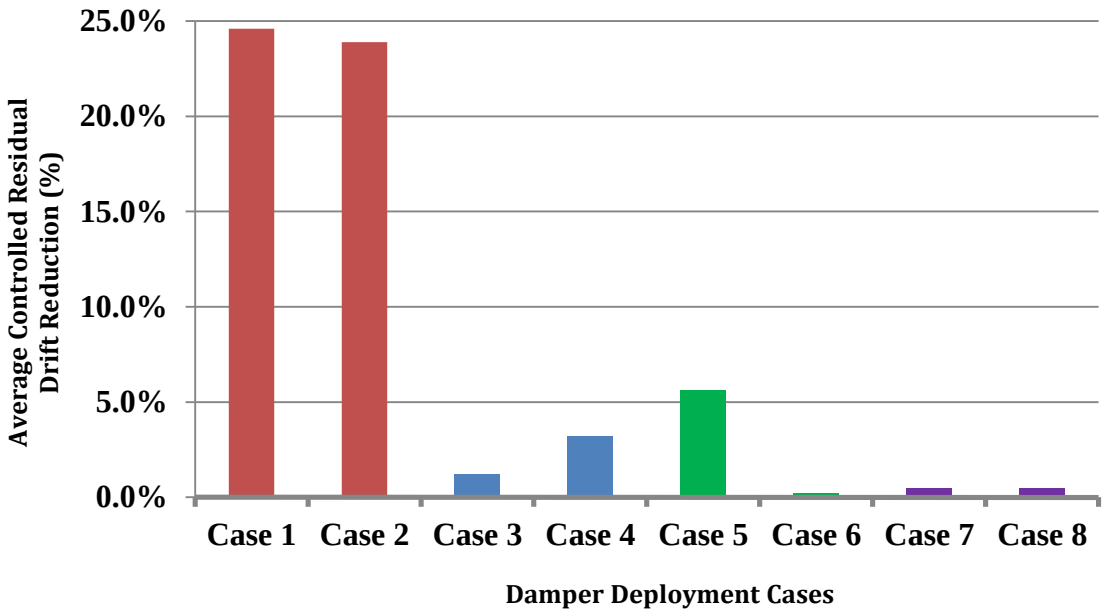

Figure 6.14: Average Controlled Residual Drift Reduction Comparison

The last measure of the controller performance is the energy dissipation. Again, in virtually every case, the ODCOC controller was able to dissipate more energy within the structural system. For each controller, the pattern of energy dissipation was triangular in form, with the maximum dissipation occurring when the interstory drift is nearly 0 m (and the corresponding velocity is at the maximum value for each cycle). The average total energy dissipated by the MR damper when using PON control is 187 kN•m, compared to 237 kN•m and 270 kN•m for COC and ODCOC control, respectively. Thus, the ODCOC approach is able to dissipate more energy (40% increase compared to PON and 15% increase compared to COC) within the structure.

In addition to the tables of results, several representative plots are shown, including time histories and response profiles. The time history plots show the reduction in peak drifts and accelerations that the Based on the profiles, there are clear differences in responses at each level of the structure for each controller when differing response weighting schemes are used in control design for the SA controllers.

Based on the results of this study, the ODCOC approach is clearly superior for displacement/drift when displacement weighting is used, acceleration when acceleration weighting is used, and is able to achieve the most significant residual drift reduction among the control approaches.

6.5. Conclusions

In this final evaluation of the proposed control algorithm developed for use with large-scale MR dampers, numerical simulations were conducted using MATLAB (Version R2011b) and the RT-Frame2D Computational Tool. RT-Frame2D is a modeling/simulation tool developed to aid researchers in conducting real-time hybrid simulations more efficiently by taking advantages of the capabilities of the MATLAB software platform. A nonlinear model of the nine-story benchmark structure was developed using this tool. Based on a linearized model of the nine story structure, several controllers for the MR dampers were developed and employed in simulation. A total of eight (8) cases were considered, including acceleration and displacement optimization control schemes and various placement schemes for the MR dampers. The performances of the controllers in each case were assessed using criteria established on the global performance of the structure.

In general, the ODCOC control approach proved to be superior to the other control approaches, depending on the response optimization scheme used in the control design. When the displacement optimization method was employed, ODCOC proved to be the best controller in virtually all cases for both displacement and drift, often by a margin of approximately 10% versus the other controllers. Alternatively, when the acceleration optimization approach was utilized, ODCOC proved again to be the best controller, with an average of 7% improvement in the acceleration response reduction as compared to PON and COC. In terms of the force utilized by the dampers, the COC approach used the smallest amount of control force, although the ODCOC was able to achieve the best performance while using less force than the PON approach. Lastly, in comparing the residual displacement of the structure, the ODCOC approach showed an increased ability to protect the structure against permanent displacement. On an individual earthquake basis, the ODCOC achieved an average 20% reduction in residual drift compared to the other controllers. When considering all earthquakes and damper deployment cases, the ODCOC achieved an average of 23% reduction in peak residual drift (over the entire structure), compared to the other approaches, including the uncontrolled case.

Overall, this study further established the ODCOC as a superior controller in non-linear applications using large-scale MR dampers.

CHAPTER 7: CONCLUSIONS AND FUTURE WORK

In this report, a new control strategy specifically intended for use with large-scale magneto-rheological (MR) dampers has been developed and experimentally validated using numerical simulation and real-time hybrid simulation.

The dynamics of the large-scale MR devices were investigated first. From experimentation, it was determined that the force response time of the damper was dependent on the level of voltage commanded to the damper. Commanding a higher voltage level (or over-driving the damper) resulted in the measured damper force rising to the peak value at a faster rate. Similarly, if the damper force was at the maximum value, commanding a higher level *negative* voltage generates a current in the opposite direction (back-driving the damper) and breaks the bonds between the MR fluid particles, which reduces the measured force at a faster rate. The amplified voltage commands can only be applied for a short duration for two reasons: (1) safety concerns for the damper and (2) when back-driving, the opposite-direction current will eventually generate a magnetic field, and the force will rise again. Thus, time limitations on the higher level commands are also considered in the proposed controller.

To maximize the effectiveness of the device in real-world applications, these characteristics (over-driving and back-driving) and device dynamics were exploited in proposing a new semi-active controller for large-scale MR devices. The Over-Driven Clipped Optimal Controller (ODCOC) utilizes a LQG regulator, designed to determine a desired restoring force based on acceleration feedback, in conjunction with a control law, designed to select a command voltage for the MR damper to track the desired force. By commanding higher voltage levels for short durations, the ability of large-scale dampers to accurately track a desired force is increased. This was demonstrated in both numerical simulation and a real-time hybrid simulation, using a force-tracking exercise with a comparison to an established semi-active control method (Clipped Optimal Control. Because the COC only commands voltages within the operational range of the damper, the damper cannot respond as quickly and does not track the force as well as the ODCOC. Over-driving and back-driving, even in short bursts, makes a large difference in the performance of large-scale devices.

The ability of the ODCOC to reduce the global responses of buildings equipped with MR dampers was investigated using three experiments and two different structures: (1) a prototype 3-story structure representing a typical low-rise office building in Los Angeles and (2) a 9-story benchmark structure representing a mid-rise office building in Los Angeles. A new Bouc-Wen model for the large-scale MR dampers was developed for use in numerical simulation and real-time hybrid simulation. Several controllers, including the proposed controller, were designed and compared. Their performance in reducing both peak and RMS responses was evaluated under various seismic ground motions. In addition, robust performance of the controllers was examined under various conditions. The main conclusions of each experiment are summarized in the following paragraphs.

The first successful implementation of the controller was conducted using the 3-story prototype structure. Using numerical simulation, the semi-active controllers were designed to optimize the acceleration response of the structure, with equal weighting on all floors for the optimal controller design. Real-time hybrid simulation (RTHS) was performed using a large-scale steel frame and a large-scale MR damper at the NEES RTMD facility at Lehigh University. The first outcome of these tests was that the RTHS results compared quite well to pure numerical simulation, validating the performance of the RTHS. In general, the semi-active control approaches proved to be superior to the passive control in several areas. For reductions in peak absolute acceleration, ODCOC proved to be the best option for each earthquake, with an average improvement of 25% and 5% compared to PON and COC control, respectively. Though drift and displacement reductions showed no clear frontrunner between PON and ODCOC, the semi-active approaches were vastly superior at utilizing the least amount damper force to achieve good results. In evaluating robust performance of the controllers, ODCOC was found to be quite robust, achieving good results when the structural mass was varied significantly.

The second experiment considered a 9-story benchmark structure. The experiment consisted of several phases using multiple facilities: (1) RTHS using a single MR damper as the physical substructure at the Smart Structures Technology Lab at the University of Illinois, (2) RTHS using a large-scale three-story steel frame with a single MR damper mounted between the base and first floor as the physical substructure at the NEES@Lehigh RTMD facility and (3) RTHS using a large-scale three-story steel frame with two MR dampers mounted at the first and second floors as the physical substructure at the NEES@Lehigh RTMD facility. To validate the RTHS method, three types of testing were conducted (though not every test type was completed for each phase), including: (1) general earthquake excitation, (2) robust performance testing, and (3) repeatability testing.

In comparing the RTHS results to simulation, the structural responses for each were shown to track very well for all phases of testing, validating the performance of the controllers seen in simulation. In addition, the RTHS repeatability tests confirm that the differences in the test results are within acceptable tolerances.

In general, for this structure given the damper deployment schemes, the semi-active control approaches are superior to the passive control approach for reductions in absolute acceleration and damper force. ODCOC again proved to be the best option for each earthquake, with an average improvement of 20% versus the PON cases and 8% versus the COC case across the three phases. Further, PON and ODCOC both performed well in terms of drift and displacement reduction, with PON being the best option for drift reduction and both controllers achieving good results for displacement. For the robustness testing, the ODCOC outperformed the PON controller for acceleration and damper force. In addition, while the PON control case yielded somewhat scattered results depending on the mass chosen, the reduction with the ODCOC responses stayed consistent, which is a desirable result. Lastly, in testing the RTHS approach for repeatability, the three test results matched extremely well, showing that RTHS can be implemented in a reliable and repeatable way with the proper equipment.

Finally, the third investigation used a simulation tool developed specifically for the MATLAB platform to conduct numerical simulations of a non-linear model of the 9-story benchmark structure. The results of this numerical study show that the ODCOC achieves superior response reductions in comparison to the other controllers, both passive and semi-active. Two different controllers, focusing on acceleration and displacement response reduction, respectively, were designed for both ODCOC and COC. When displacement response weighting was used, the ODCOC yielded ~10% reduction in the displacement and interstory drift responses as compared to other control approaches. When acceleration response weighting was used, the ODCOC had a 7% improvement in the acceleration responses (peak and RMS) as compared to the other controllers. In addition, the ODCOC showed a greater ability (20% improvement) to reduce the residual drift (i.e. permanent drift the structure experiences as a result of the earthquake) in comparison of the other control methods.

The results of these three experiments demonstrate that the proposed controller is quite capable of effectively reducing the global responses in various structures under seismic loading, providing improved performance and protection.

Overall, there are several contributions to the field of civil engineering that have resulted from this research. They include:

- Development of a new semi-active control algorithm designed for use with large-scale MR dampers. The algorithm incorporates the specific features of over- and back-driving current control to increase the rate at which the device can respond. The improved response time is important for the large-scale device to be able to track a desired force and maintain the ability to control the structure.
- Successful performance of a real-time hybrid simulation using a large-scale steel frame equipped with MR dampers as the physical substructure. In various phases of the RTHS, two different large-scale structures were represented by the same frame and dampers, including a 3-story office structure and a 9-story benchmark structure.
- Demonstrated improved response reductions for several structures using MR dampers and the proposed semi-active control strategy. Evaluations were based on several seismic inputs to the structures (with various levels of PGA) and robust performance testing, in which the mass of the structure was varied in comparison to the original design mass. The proposed controller was found to perform well, even in the face of uncertainties in the structural system, compared to other approaches.

All data pertaining to this study is available in the NEES Project Warehouse, nees.org), including data sets related to the identification of the large-scale MR damper (Chae et al. 2013a-b, Phillips 2013), identification of the large-scale steel test frame (Ozdagli et al. 2013a-e), and the RTHS data (Friedman et al. 2013a-e).

7.1. Future Work

Based on this research, some future avenues of research include:

- Prefiltered Clipped Optimal Control

There are dynamics associated with the current driver used to apply current to the damper and the MR fluid reaching rheological equilibrium, which results in a time lag between the application of the commanded signal to the damper and the corresponding force output from the damper. The situation that arises from this is that the controller is outputting a desired force based upon the current structural responses, which is then used to determine a corresponding desired voltage level. The voltage is applied to the damper, and after a delay to reach the corresponding force output, the force is then applied to the structure. In this manner, the damper is effectively controlling an event that has already occurred. In the time that passed between the command voltage and the corresponding force output, the structural responses have changed and as such, the desired restoring force has changed as well. It is readily apparent that if the delay in the control device were of sufficient length, problems in stability and performance degradation could arise, without proper compensation.

In conventional semi-active control algorithms, this delay is not considered in the controller design. With PCOC, a single order filter is included in the system plant used in the LQG regulator design to account for this delay. In this way, the controller considers the presence of the delay and can account for it in the optimal force output. A summary of this control approach is presented herein

Consider a system, as shown in the block diagram in Figure 4a. The state space equations for plant in this system, which consists only of the structure in this case, are

$$\dot{\boldsymbol{x}} = \boldsymbol{A}\boldsymbol{x} + \boldsymbol{B}\boldsymbol{f} + \boldsymbol{E}\ddot{\boldsymbol{x}}_{\boldsymbol{g}}$$

$$\boldsymbol{y} = \boldsymbol{C}\boldsymbol{x} + \boldsymbol{D}\boldsymbol{f} + \boldsymbol{F}\ddot{\boldsymbol{x}}_{\boldsymbol{g}}$$

Now consider the same system with the addition of a filter which represents a time delay, as seen in Figure 4b. The state space equations of the filter are as follows

$$\dot{\boldsymbol{z}} = \boldsymbol{A}_{\boldsymbol{filt}}\boldsymbol{z} + \boldsymbol{B}_{\boldsymbol{filt}}\boldsymbol{u}$$

$$\boldsymbol{f} = \boldsymbol{C}_{\boldsymbol{filt}}\boldsymbol{z} + \boldsymbol{D}_{\boldsymbol{filt}}\boldsymbol{u}$$

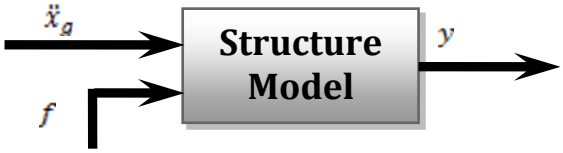

(a)

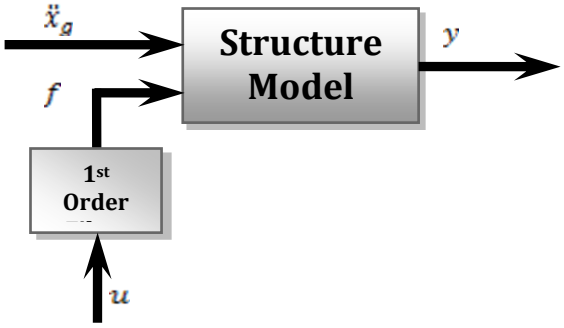

(b

Figure 7.1: (a) System Plant and (b) System Plant with filer to account for force time lag

If both the structure and the filter are considered to comprise the plant of the system, then the state space equations for both components must be combined. This is done in the following manner

$$\dot{\boldsymbol{x}} = \boldsymbol{A}\boldsymbol{x} + \boldsymbol{B}(\boldsymbol{C}_{\boldsymbol{filt}}\boldsymbol{z} + \boldsymbol{D}_{\boldsymbol{filt}}\boldsymbol{u}) + \boldsymbol{E}\ddot{\boldsymbol{x}}_{\boldsymbol{g}}$$

$$\boldsymbol{y} = \boldsymbol{C}\boldsymbol{x} + \boldsymbol{D}(\boldsymbol{C}_{\boldsymbol{filt}}\boldsymbol{z} + \boldsymbol{D}_{\boldsymbol{filt}}\boldsymbol{u}) + \boldsymbol{F}\ddot{\boldsymbol{x}}_{\boldsymbol{g}}$$

$$\dot{\boldsymbol{z}} = \boldsymbol{A}_{\boldsymbol{filt}}\boldsymbol{z} + \boldsymbol{B}_{\boldsymbol{filt}}\boldsymbol{u}$$

These equations can be reorganized into a final state space form

$$\begin{bmatrix}\dot{\boldsymbol{x}}\\ \dot{\boldsymbol{z}}\end{bmatrix} = \underbrace{\begin{bmatrix}\boldsymbol{A} & \boldsymbol{B}\cdot\boldsymbol{C}_{\boldsymbol{filt}}\\ \boldsymbol{0} & \boldsymbol{A}_{\boldsymbol{filt}}\end{bmatrix}}_{\mathrm{A_{pf}}}\begin{bmatrix}\boldsymbol{x}\\ \boldsymbol{z}\end{bmatrix} + \underbrace{\begin{bmatrix}\boldsymbol{E} & \boldsymbol{B}\cdot\boldsymbol{D}_{\boldsymbol{filt}}\\ \boldsymbol{0} & \boldsymbol{B}_{\boldsymbol{filt}}\end{bmatrix}}_{\mathrm{B_{pf}}}\begin{bmatrix}\ddot{\boldsymbol{x}}_{\boldsymbol{g}}\\ \boldsymbol{u}\end{bmatrix}$$

$$[\boldsymbol{y}] = \underbrace{[\boldsymbol{C} \quad \boldsymbol{D} \cdot \boldsymbol{C}_{filt}]}_{C_{pf}} \begin{bmatrix} \boldsymbol{x} \\ \boldsymbol{z} \end{bmatrix} + \underbrace{[\boldsymbol{F} \quad \boldsymbol{D} \cdot \boldsymbol{D}_{filt}]}_{D_{pf}} \begin{bmatrix} \ddot{\boldsymbol{x}}_{\boldsymbol{g}} \\ \boldsymbol{u} \end{bmatrix}$$

These new state space matrices, A_{pf}, B_{pf}, C_{pf}, and D_{pf} are used during the LQG regulator design process, and produce a regulator that will compensate for the time lag in the system.

This regulator could be paired with control laws from either COC or ODCOC. The benefits of those approaches would also extend to this control approach.

- Further RTHS Validation

The results of this research provide an important validation step between real-time hybrid simulation and numerical simulation. However, a full experimental analysis using three separate approaches (numerical simulation, fully-physical experimental testing, and real-time hybrid simulation) would provide comprehensive proof that the method is valid.

- Damper Placement Optimization

Several different options for the deployment of the dampers were considered for the 9-story benchmark structure. More work is needed in determining procedures and protocols for placing these dampers within a structure during the design period.

LIST OF REFERENCES

Abdel-Rohman, M., and Leipholz, H. H. (1979). General approach to active structural control. *Journal of the Engineering Mechanics Division*, *105*(6), 1007-1023.

Al-Dawod M., Samali, B., Kwok, K., and Naghdy, F., (2004) "Fuzzy Controller for Seismically Excited Nonlinear Buildings" Journal of Engineering Mechanics, 130, 407 (2004); doi10.1061/(ASCE) 0733-9399(2004) 130:4 (407)

American Red Cross Multi-Disciplinary Team, 2011, "Report on the 2010 Chilean earthquake and tsunami response": U.S. Geological Survey Open-File Report 2011-1053, v. 1.1, 68 p., available at http://pubs.usgs.gov/of/2011/1053/Earthquake and Tsunami of 2011," http://www.britannica.com/EBchecked/topic/1761942/Japan-earthquake-and-tsunami-of-2011.

Asano, K., and Nakagawa, H., (1993) "Seismic Random Response of Elasto-Plastic Systems Under Active Saturation Control Force." *Proceedings of the US National Workshop on Structural Control Research*. 1993.

Bass, B. and R.E. Christenson (2007), "System Identification of 200 kN Magneto-Rheological Fluid Damper for Structural Control in Large-Scale Smart Structures," American Control Conference, New York City, July 11-13, 2007. Proceedings, 2690-2695.

Bertero, V. V., and S. W. Zagajeski. "Optimal inelastic design of Seismic-Resistant Reinforced Concrete framed structures." *Nonlinear Design of Concrete Structures, CSCE-ASCE-ACI-CEB International Symposium*. 1979.

Bitaraf, M., Ozbulut, O., Hurlebaus, S., and Barroso, L., (2010) "Application of semi-active control strategies for seismic protection of buildings with MR dampers" Engineering Structures, Vol 32:10 pp 3040-3047

Boada, M.J., Calvo, J.A., and Boada, B.L. (2009) "A new non-parametric model based on a neural network for a MR damper". Proceedings of the 9th Biennial Conf. on Engineering Systems Design and Analysis, Vol 2, pp. 597-602

Bonnet, P.A., Lim, C.N., Williams, M.S., Blakeborough, A., Neild, S.A., Stoten, D.P., and Taylor, C.A., (2007) "Real-time hybrid experiments with Newmark integration, MCSmd outer-loop control and multi-tasking strategies. Earthquake Engineering and Structural Dynamics 2007; 36(1):119–141.

Bouc (1971) "Mathematical model of hysteresis: Application to systems with a degree of freedom" Acustica 24 pp 16-25

Carlson, J.D., Catanzarite, D.M., and St. Clair, K.A. (1995) "Commercial Magneto-rheological fluid devices" 5th Int. Conf. on ER, MR Suspensions and Assoc. Technology, Sheffield, 10-14 July 1995

Carrion, J.E., and Spencer, B.F., (2006) "Real-time hybrid testing using model-based delay compensation." Proceedings of the Fourth International Conference on Earthquake Engineering, Taipei, Taiwan, 2006.

Castaneda, N. (2012) "Development and Validation of a Real-Time Computational Framework for Hybrid Simulation of Dynamically-Excited Steel Frame Structure." *Ph.D. Dissertation*, Purdue University, 2012

Chae, Y., Ricles, J., and Sause, R., (2010) "Evaluation of structural control strategies for improving seismic performance of buildings with MR Dampers using real-time large-scale hybrid simulation" Proceedings of the 19th Analysis and Computation Specialty Conference, pp 335-346

Chae, Y., (2011) *Seismic hazard mitigation of building structures using magneto-rheological dampers*. Lehigh University, 2011.

Chae, Y., Jiang, Z., Ricles, J., Christenson, R., and Dyke, S.J. (2013a). "MR Damper Characterization - Lehigh - Damper 1", Network for Earthquake Engineering Simulation (database), Dataset, DOI:10.4231/D3DV1CN1D

Chae, Y., Jiang, Z., Ricles, J., Christenson, R., and Dyke, S.J. (2013b). "MR Damper Characterization - Lehigh - Damper 2", Network for Earthquake Engineering Simulation (database), Dataset, DOI: Pending

Chang, C. and Yang, H. (1995), "Control of Buildings Using Active Tuned Mass Dampers," Journal of Engineering Mechanics, Vol. 121, No. 3 (355)

Chang, K., and Lin, Y. (2004) "Seismic Response of Full-Scale Structure with Added Viscoelastic Dampers" *Journal of Structural Engineering 130*: 600 (2004); http://dx.doi.org/10.1061/(ASCE)0733-9445(2004)130:4(600) (9 pages)

Chantranuwathana, S., and Huei, P. (1999) "Adaptive robust control for active suspensions." *American Control Conference, 1999. Proceedings of the 1999*. Vol. 3. IEEE, 1999.

Chen, Z.Q., Wang, X.Y., Ko, J.M., Ni, Y., Spencer, B.F., and Yang G., (2003) "MR Damping system on Dongting Lake cable-stayed bridge" Journal of Smart Structures and Materials, Vol 5057, pp. 229-235

Chen, C., and Ricles, J.M., (2008) "Development of direct integration algorithms for structural dynamics using discrete control theory. Journal of Engineering Mechanics 2008; 134(8):676–683.

Chen, C., and Ricles, J.M. (2010) "Tracking error-based servohydraulic actuator adaptive compensation for real-time hybrid simulation." *Journal of structural engineering* 136.4 (2010): 432-440.

Christenson, R., et al., (2008). "Large-Scale Experimental Verification of Semiactive Control through Real-Time Hybrid Simulation", Presented at the 2006 Structures Congress & 17th Analysis and Computation Specialty Conference, May 18–20, 2006, St. Louis. Journal of Structural Engineering 134, 522 (2008); http://dx.doi.org/10.1061/(ASCE)0733-9445(2008)134:4(522)

Christenson, R. and Lin, Y.Z., "Real-Time Hybrid Simulation of a Seismically Excited Structure with Large-Scale Magneto-Rheological Fluid Dampers", *Hybrid Simulation Theory: Implementations and Applications, ISBN 978-0-415-46568-7*, 2008.

Chopra, A.K., (2000) Dynamics of Structures: Theory and Applications to Earthquake Engineering (2nd Edition), Prentice Hall, 2000

Darby, A.P., Blakeborough, A., and Williams, M.S.. (1999) "Real-time substructure tests using hydraulic actuators." Journal of Engineering Mechanics 1999; 125:1133–1139.

Darby, A. P., Blakeborough, A., and M. S. Williams. "Improved control algorithm for real-time substructure testing." *Earthquake engineering & structural dynamics* 30.3 (2001): 431-448.

Dermitzakis, S.N. and Mahin, S.A. (1985) "Development of substructuring techniques for on-line computer controlled seismic performance testing." Report UBC/EERC-85/04, Earthquake Engineering Research Center, University of California, Berkeley

Dyke S.J. (1996) "Acceleration Feedback Control Strategies for Active and Semi-active Control Systems: Modeling, Algorithm Development, and Experimental Verification" Ph.D. Dissertation, University of Notre Dame, 1996

Dyke, S.J., Spencer, B.F., Jr., Sain, M.K., and Carlson, J.D., (1995) "Modeling and control of magneto-rheological dampers for seismic response reduction," *Smart Mater. Struct.* 5 565

Earthquake Engineering Research Center, "Action Plan for Performance-Based Seismic Design" , Report No. FEMA-349, Federal Emergency Management Agency, 1998

ENR. (Aug. 1977), Tuned Mass Dampers Steady Sway of Skyscrapers in Wind:14-15.

Erguven, et al http://www.eedmi.itu.edu.tr/Van_Depremi/index_en.html

Fediw, A.A., Isyumov, N., and Vickery, BJ., "Performance of a Tuned Sloshing Water Damper", Journal of Wind Engineering and Industrial Aerodynamics, Vol. 57, 1995, pp. 237-247.

FEMA P695 (2009) http://www.fema.gov/library/viewRecord.do?id=3736

Fierro, E. A., and Perry, C. L.(1993). "San Francisco retrofit design using added damping and stiffness (ADAS) elements."Proc., Seminar on Seismic Isolation, Passive Energy Dissipation and Active Control, Appl. Technol. Council, Redwood City, Calif., ATC 17–1,**2**, 593–604.

Friedman, A.J. (2012). "Development and Validation of a New Control Strategy Considering Device Dynamics for Large-Scale MR Dampers Using Real-time Hybrid Simulation", *Ph.D. Dissertation*, Purdue University, December, 2012

Friedman, A, Dyke, S.J., and Phillips, B. (2013) "Over-Driven Control For Large-Scale MR Dampers." *Smart Mater. Struct.* 22 (2013) 045001.

Friedman, A., Phillips, B., Ahn, R., Chae, Y., Zhang, Z., Cha, Y., Dyke, S.J., Ricles, J.M., Spencer, B.F., Christenson, R.E., and Sause, R., (2013a). "RTHS (Damper) - 3StoryPS - Single MR Damper (Floor 1)" Network for Earthquake Engineering Simulation (database), Dataset, DOI:Pending

Friedman, A., Phillips, B., Ahn, R., Chae, Y., Zhang, Z., Cha, Y., Dyke, S.J., Ricles, J.M., Spencer, B.F., Christenson, R.E., and Sause, R., (2013b). "RTHS (Damper) - 3StoryPS - Single MR Damper (Floor 1)" Network for Earthquake Engineering Simulation (database), Dataset, DOI:Pending

Friedman, A., Phillips, B., Ahn, R., Chae, Y., Zhang, Z., Cha, Y., Dyke, S.J., Ricles, J.M., Spencer, B.F., Christenson, R.E., and Sause, R., (2013c). "RTHS (Frame + Damper) - 3StoryPS - Single MR Damper (Floor 1)" Network for Earthquake Engineering Simulation (database), Dataset, DOI:Pending

Friedman, A., Phillips, B., Ahn, R., Chae, Y., Zhang, Z., Cha, Y., Dyke, S.J., Ricles, J.M., Spencer, B.F., Christenson, R.E., and Sause, R., (2013d). "RTHS (Frame + Damper) - 9StoryBM - Single MR Damper (Floor 1)" Network for Earthquake Engineering Simulation (database), Dataset, DOI:Pending

Friedman, A., Phillips, B., Ahn, R., Chae, Y., Zhang, Z., Cha, Y., Dyke, S.J., Ricles, J.M., Spencer, B.F., Christenson, R.E., and Sause, R., (2013e). "RTHS (Frame + Damper) - 9StoryBM - Two MR Dampers (Floor 1 + 2)" Network for Earthquake Engineering Simulation (database), Dataset, DOI:Pending

Gamota, D.R. and Filisko, F.E., (1991) "Dynamic mechanical studies of electrorheological materials: moderate frequencies" Journal of Rheology Vol 35:3 pp 339-425

Gao, X., Castaneda, N., & Dyke, S. (Accepted). “Real-time Hybrid Simulation: from Dynamic System, Motion Control to Experimental Error.” Earthquake Engineering and Structural Dynamics.

Gavin, H.P. (2001) “Multi-duct ER Dampers,” Journal of Intelligent Material Systems and Structures. Vol 12:5, pp 353-366

Ghaboussi, J., and Abdolreza, J., (1995) "Active control of structures using neural networks." *Journal of Engineering Mechanics* 121.4 (1995): 555-567.

Gu, Z., Oyadiji, S., (2008) “Application of MR damper in structural control using ANFIS method,” Computers & Structures, Volume 86, Issues 3-5, February 2008, Pages 427-436, ISSN 0045-7949, 10.1016/j.compstruc.2007.02.024

Hatamoto, H., Chung, Y.S. and Shinozuka, M. (1990) “Seismic Capacity Enhancement of RC Frames by Means of Damage Control Design”, Proc., 4 USNCEE (Palm Springs, CA), 2, p279-288.

Horiuchi, T., Nakagawa, M., Sugano, M. and Konno, T. (1996). “Development of a real-time hybrid experimental system with actuator delay compensation,” In Proc. 11th World Conf. Earthquake Engineering, Paper No. 660.

Hu, J.L., Li, Y., and Gang, Y., (2009) “Experimental study on fuzzy-semi-active structural control using MR dampers”. Journal of Vibration and Shock, doi CNKI:SUN:ZDCJ.0.2009-03-033

Jiang, Z., and R. Christenson. (2011) "A comparison of 200 kN magneto-rheological damper models for use in real-time hybrid simulation pretesting." *Smart Materials and Structures* 20.6 (2011): 065011.

Jiang, Z., (2012) *Increasing Resilience in Civil Structures Using Smart Damping Technology*. Diss. UNIVERSITY OF CONNECTICUT, 2012.

Jiang, X., and Hojjat A., (2008) "Neuro-genetic algorithm for non-linear active control of structures." *International Journal for Numerical Methods in Engineering* 75.7 (2008): 770-786.

Jibson, R.W., and Harp, E.L., 2011, “Field reconnaissance report of landslides triggered by the January 12, 2010, Haiti earthquake”: U.S. Geological Survey Open-File Report 2011–1023, 19 p.

Kane, M., Lynch, J.P., and Law, K. (2011) “Market-based control of shear structures utilizing magnetorheological dampers” Proceedings of the American Control Conference, ACC 2011. June 29-July 1, San Francisco, CA

Kareem, A., Kijewski, T. and Tamura, Y., (1999), "Mitigation of Motions of Tall Buildings with Specific Examples of Recent Applications," Wind and Structures: An International Journal, Vol. 2, No.3, pp. 201-251

Karnopp, D., & Allen, R. R. (1975, September). Semiactive control of multimode vibratory systems using the ilsm concept. In *American Society of Mechanical Engineers, Design Engineering Technical Conference, Washington, DC, Sept. 17-19, 1975, 5 p.* (Vol. 1).

Kaynia, A. M., Daniele, V. and Biggs, J. M. (1981). "Seismic effectiveness of tuned mass dampers." Journal of Structural Division, ASCE, 107, No. ST8, 1465-1484

Kim, D.H., Seo, S.-N., and Lee, I.-W. (2004) "Optimal Neurocontroller for Nonlinear Benchmark Structure" Journal of Engineering Mechanics, 130, 424 (2004); doi10.1061/(ASCE)0733-9399(2004) 130:4 (424)

Kim, Y., Hurlebaus, S., and Langari, R., (2010) "Model-based multi-input, multi-output supervisory semi-active nonlinear fuzzy controller" Computer-aided civil and infrastructure engineering, Vol 25:5 pp 387-393

Klinger, Y., Ji, C., Shen, Z.-K, and Bakun, W.H. (2010) "Introduction to the Special Issue on the 2008 Wenchuan, China, Earthquake Bulletin of the Seismological Society of America", Vol. 100, No. 5B, pp. 2353–2356, November 2010, doi: 10.1785/012010017

Kobori, T. (1996) "Future Direction on Research and Development of Seismic Response-Controlled Structures." *Computer-Aided Civil and Infrastructure Engineering* 11.5 (1996): 297-304.

Kottapalli, S et al., (2010) "Analytical, First Principles Modeling of Elastomeric Dampers", *Presented at the American Helicopter Society Aeromechanics Specialists' Conference.* San Francisco, CA, January 20-22, 2010.

Lee T. Y. and Chen, P.-C. (2011) "Experimental and Analytical Study of Sliding mode control for isolated bridges with MR Dampers" Journal of Earthquake Engineering 15:564-581

Lee, K.S., Fan, C.P., Sause, R., and Ricles, J. (2005) "Simplified design procedure for frame buildings with viscoelastic or elastomeric structural dampers", *Earthquake Engineering and Structural Dynamics.* 2005; 34:1271-1284 DOI: 10.1002/ eqe.479

Li, H., and Huo, L., (2010). "Advances in Structural Control in Civil Engineering in China," *Mathematical Problems in Engineering*, vol. 2010, Article ID 936081, 23 pages, 2010. doi:10.1155/2010/936081

Li, Q., Zhi, L., Tuan, A., Kao, C., Su, S., and Wu, C. (2011). ”Dynamic Behavior of Taipei 101 Tower: Field Measurement and Numerical Analysis.” *J. Struct. Eng.*, 137(1), 143–155. doi: 10.1061/(ASCE)ST.1943-541X.0000264

Liu, P., Liu, H., Teng, J., and Cao, T., (2006) “Parameter Identification for smart dampers based on simulation and genetic algorithms” Proceedings of the 2006 IEEE Intl’ Conference on Mechatronics and Automation pp 2199-2204

Maghareh, A., Barnes, M.J., and Sun, Z., (2012), "Evaluation of 9-Story Benchmark Building Shear Model," http://nees.org/resources/4103.

MATLAB 2010a, Mathworks, Inc., Natick, MA

McClamroch, N. Harris, and H. P. Gavin. "Closed loop structural control using electrorheological dampers." *American Control Conference, 1995. Proceedings of the*. Vol. 6. IEEE, 1995.

McKenna, F., Fenves, G.L., and Scott, M.H. (2006) "OpenSees: Open system for earthquake engineering simulation." *Pacific Earthquake Engineering Center, University of California, Berkeley, CA., http://opensees. berkeley. edu* (2006).

Metered, H., Bonello, P., and Oyadiji, S., (2009) “Nonparametric identification modeling of magnetorheological damper using chebyshev polynomials fits” SAE International Journal of Passenger Cars – Mechanical Systems, Vol 2:1 pp 1125-1135

Nakashima, M., Kato, H., Takaoka, E., (1992) “Development of real-time pseudo dynamic testing.” Earthquake Engineering and Structural Dynamics 1992; 21(1):79–92.

Nakata, N., and Stehman, M., (2012). "Substructure shake table test method using a controlled mass: formulation and numerical simulation." Earthquake Engineering and Structural Dynamics, DOI:10.1002/eqe.2169.

Nilkhamhang, I., Mori, T., and Sano, A., (2008) “Direct and indirect stable adaptive control for suspensions with MR Dampers” IFAC Proceedings, Vol 17:1

Nishitani, A., and Yutaka I., (2001) "Overview of the application of active/semiactive control to building structures in Japan." *Earthquake engineering & structural dynamics* 30.11 (2001): 1565-1574.

Ohtori, Y., Christenson, R.E., Spencer, B.F., and Dyke, S.J. (2004) "Benchmark control problems for seismically excited nonlinear buildings." *Journal of Engineering Mechanics* 130.4 (2004): 366-385.

Ozdagli, A., Friedman, A., Ahn, R., Dong, B., Dyke, S.J., and Ricles, J.M., (2013a). "Dynamic System Identification on DBF - Rigid Links ON - Ground Links ON -

Loading Beams OFF", Network for Earthquake Engineering Simulation (database), Dataset, DOI:10.4231/D3599Z13P

Ozdagli, A., Friedman, A., Ahn, R., Dong, B., Dyke, S.J., and Ricles, J.M., (2013b). "Dynamic System Identification on DBF - Rigid Links OFF - Ground Links ON - Loading Beams OFF", Network for Earthquake Engineering Simulation (database), Dataset, DOI:10.4231/D31J9770D

Ozdagli, A., Friedman, A., Ahn, R., Dong, B., Dyke, S.J., and Ricles, J.M., (2013c). "System Identification on DBF - Rigid Links ON/OFF - Ground Links ON - Loading Beams ON - Actuator @ Floor 1", Network for Earthquake Engineering Simulation (database), Dataset, DOI:10.4231/D3WS8HK5D

Ozdagli, A., Friedman, A., Ahn, R., Dong, B., Dyke, S.J., and Ricles, J.M., (2013d). "System Identification on DBF - Rigid Links ON/OFF - Ground Links ON - Loading Beams ON - Actuator @ Floor 2", Network for Earthquake Engineering Simulation (database), Dataset, DOI:10.4231/D3S46H549

Ozdagli, A., Friedman, A., Ahn, R., Dong, B., Dyke, S.J., and Ricles, J.M., (2013e). "System Identification on DBF - Rigid Links ON/OFF - Ground Links ON - Loading Beams ON - Actuator @ Floor 3", Network for Earthquake Engineering Simulation (database), Dataset, DOI:10.4231/D3NC5SC05

Paulay, T. and Priestley, MJN (1992) "Seismic Design of Reinforced Concrete and Masonry Buildings", John Wiley and Sons, New York, 744 p.

Phillips, B. and Spencer, B.F. (2011). "Model-based Feedforward-feedback tracking control for real-time hybrid simulation," Newmark Structural Engineering Laboratory Report 028: ISSN 1940-9826; August 15, 2011.

Phillips, B., (2012) "Model-based feedforward-feedback control for real-time hybrid simulation of large-scale structures." (2012). Ph.D. Dissertation, University of Illinois – Urbana/Champaign 2012

Phillips, B., Jiang, B., Spencer, B.F., Christenson, R., and Dyke, S.J., (2013). "MR Damper Characterization - UIUC - Damper 3", Network for Earthquake Engineering Simulation (database), Dataset, DOI:10.4231/D3PC2T80D

Rao, M., (2001) "Recent applications of Viscoelastic Damping for Noise Control in Automobiles and Commercial Airplanes." *Journal of Sound and Vibration*, Vol 262:3 PP 457-474 http://dx.doi.org/10.1016/S0022-460X(03)00106-8

SANZ (1992) NZS4203 "Code of Practice for General Structural Design and Design Loadings for Buildings", NZ Standards Association, Wellington.

Shook, D., Lin, P.Y., Lin, T.K., and Roschke, P. (2007) "A comparative study in the semi-active control of isolated structures" Journal of Smart Materials and Structures 16(2007) pp 1433-1446

Skinner, R. I., Beck, J. L., & Bycroft, G. N. (1974). A practical system for isolating structures from earthquake attack. *Earthquake Engineering & Structural Dynamics*, *3*(3), 297-309.

Song, W., (2005) "Modeling MR Dampers with application of nonparametric approach" Journal of Intelligent Material Systems and Structures, Vol 16:5 pp 421-432

Soong, T. T., and Spencer, B.F. (2002) "Supplemental energy dissipation: state-of-the-art and state-of-the-practice." *Engineering Structures* 24.3 (2002): 243-259.

Soong, T., Masri, S.F., and Housner, G.W., (1991) "An overview of active structural control under seismic loads" Engineering Structures, Vol 10:2, April 1988, pp 74-84

Shing, P.B. (2002) "Development of High-Speed On-line Substructuring testing system at the University of Colorado" CASCADE Technical Workshop, Oxford, U.K., 2002

Spencer, B.F., Dyke, S.J., Sain, M.K., and Carlson, J.D., (1997) "Phenomenological model of a magnetorheological damper" Journal of Engineering Mechanics, ASCE Vol 123:3 pp 230-238

Spencer, B.F. and Nagarajaiah, S. "State of the Art of Structural Control" J. Struct. Eng. 129, 845 (2003); doi 10.1061/(ASCE)0733-9445(2003)129:7(845) (12 pages)

Spencer Jr, B. F., and Sain, M.K. (1997) "Controlling buildings: a new frontier in feedback." *Control Systems, IEEE* 17.6 (1997): 19-35.

Stanway, R., Sproston, J.L., and Stevens, N.G., (1987) "Non-linear modeling of an electrorheological vibration damper" Journal of Electrostatics, Vol 20:2, pp 167-184

Stengel, R.F. (1986) *Stochastic optimal control: theory and application*. John Wiley & Sons, Inc., 1986.

Structural Engineers of Association of Northern California, (2005) San Francisco City Hall, http://www.celebratingeqsafety.com/sf-city-hall

Structural Engineers Association of California (1999) "Guidelines for performance-based seismic engineering", SEAOC Blue Book - draft of Appendix I.

Suhardjo, J., B. F. Spencer Jr, and A. Kareem. "Frequency domain optimal control of wind-excited buildings." *Journal of Engineering Mechanics* 118.12 (1992): 2463-2481.

Symans, M.D. and Constantinou, M.C. (1997) "Semi-active control systems for seismic protections of structures: State-of-the-art review" Engineering Structures 21 (1999) 469-487

Tena-Collunga, A., and Vergara, A., (1997) "Seismic Retrofit of a Mid-Rise Building using Steel Bracing or ADAS Energy Dissipation Devices: A Comparative Study." *11th World Conference on Earthquake Engineering,* Paper #20 ISBN: 0 08 042822 3

Ural, D. "The Effects of a Tuned Mass *Damper* on a Building", International Journal for Housing Science and Its Applications, Vol.19, No. 1, pp.033-044, *1995*.

Xu, Z.D., Shen, P.Y., and Guo, Y.Q. (2003) "Semi-active control of structures incorporated with magnetorheological dampers using neural networks" *Journal of Smart Mater. Struct.* 12 80 doi:10.1088/0964-1726/12/1/309

Xue, X., Sun, Q., Zhang, L., and Wu, X., (2011) "Semi-active Control Strategy using Genetic Algorithm for Seismically Excited Structure Combined with MR Damper" *Journal of Intelligent Material Systems and Structures* February: Vol 22, Pages 291-302

Wang, D.H. and Liao, W.H., (2005) "Modeling and control of magnetorheological fluid dampers using neural networks" Smart Material Structures Vol 14:1

Warnitchai, P., et al (1993), "An experimental study on active tendon control of cable-stayed bridges," Earthquake Engineering and Structural Dynamics, Vol. 22, No. 2. pp 93-111

Wen (1976) "Method of random vibration of hysteretic systems" Journal of Engineering Mechanics Division ASCE Vol 102 pp 249-263

Wu, B., Wang, Q., Shing, P.B., Ou, J. (2007) "Equivalent force control method for generalized real-time substructure testing with implicit integration" Earthquake Engineering and Structural Dynamics 2007; 36(9):1127–1149.

Yang, G. (2001). "Large-Scale Magnetorheological Fluid Damper for Vibration Mitigation: Modeling, Testing and Control," *Ph.D dissertation,* University of Notre Dame, 2001

Yoshida, O. and Dyke, S.J. (2004) “Seismic Control of a Nonlinear Benchmark Building Using Smart Dampers” Journal of Engineering Mechanics, 130, 393 (2004); doi10.1061/(ASCE) 0733-9399(2004) 130:4 (386)

Yoshimura, T., Nakaminami, K., Kurimoto, M., and Hino, J.. (1999) "Active suspension of passenger cars using linear and fuzzy-logic controls." *Control Engineering Practice* 7.1 (1999): 41-47.

Zapatiero, M., Luo, N.S., and Harimi, H.R., (2009) “Neural network-backstepping control for vibration reduction in a magnetorheological suspension system” *Diffusion and Defect Data Pt.B: Solid State Phenomena*, v 147-149, p 839-844, 2009, *Mechatronic Systems and Materials III*